Numerical Renormalization Group studies of Correlation effects in Phase Coherent Transport through Quantum Dots

Theresa Hecht

München 2008

Numerical Renormalization Group studies of Correlation effects in Phase Coherent Transport through Quantum Dots

Theresa Hecht

Dissertation
an der Fakultät für Physik
der Ludwig–Maximilians–Universität
München

vorgelegt von
Theresa Hecht
aus Friedberg

München, den 21. Mai 2008

Erstgutachter: Prof. Dr. Jan von Delft
Zweitgutachter: Priv. Doz. Dr. Ralf Bulla
Tag der mündlichen Prüfung: 18. Juli 2008

To my sister and my parents

Contents

II   Results   43

List of Figures

Abstract

This thesis contributes to the field of transport through quantum dots. These devices allow for a controlled study of quantum transport and fundamental physical effects, like the Kondo effect [1]. In this thesis we will focus on dots that are well described by generalized Anderson impurity models, where the discrete levels of the quantum dot are tunnel-coupled to fermionic reservoirs. The model parameters, like level energy and width, can be tuned in experiments. Therefore these systems constitute a valuable arena for testing experiment against theory and vice versa. In order to describe these strongly correlated systems, we employ the numerical renormalization group method [2]. This allows us to address both longstanding questions concerning experimental results and new physical phenomena in these fundamental models.

This thesis consists of three major projects. The first and most extensive one is concerned with the phase of the transmission amplitude through a quantum dot. Measurements of many-electron quantum dots with small level spacing reveal universal phase behaviour [3, 4, 5], a result not fully understood for almost 10 years. Recent experiments [5] have seen that, contrarily, for dots with only a few electrons, i.e. large level spacing, the phase depends on the mesoscopic dot parameters. Analyzing a multi-level Anderson model, we show that the generic feature of the two regimes can be reproduced in the regime of overlapping levels or well separated levels, respectively. Thereby the universal character follows from Fano-type antiresonances of the renormalized single-particle levels. Moderate temperature supports the universal character. In the mesoscopic regime, we also investigate the effect of Kondo correlations on the transmission phase. In a second project we analyze a quantum dot coupled to a superconducting reservoir. In contrast to previous belief, the energy resolution of our method is not restricted by the energy scale of the superconducting gap, leading to new insights into the method. The high resolution allows us to resolve sharp peaks in the spectral function that emerge for a certain regime of parameters. A third project deals with a quantum dot coupled to two independent channels, a system known to exhibit non-Fermi liquid behaviour. We investigate the existence of the non-Fermi liquid regime when driving the system out of the Kondo regime by emptying the dot. We find that the extent of the non-Fermi liquid regime strongly depends on the mechanisms that couple impurity and reservoirs but prevent mixing of the latter.

Part I

General Introduction

Chapter 1

Introduction

The vast progress in nanofabrication during the last decades made it possible to study basic physical effects in a very controlled manner. One example of these highly controllable devices are quantum dots [6]. In a quantum dot electrons are confined in a small two-dimensional region coupled to external reservoirs (often called leads). Due to the spatial confinement, transport through the quantum dot (triggered by a small voltage difference between the leads) is determined by both energy and charge quantization inside the dot. Both quantization effects are directly observable in transport measurements, including elaborate setups, or the detailed analysis of basic physical effects like the Kondo effect [1, 7, 8, 9, 10].

In the Kondo effect, below a critical temperature (Kondo temperature T_K), a local moment gets screened by reservoir electrons within an energy window T_K around the Fermi energy. The Kondo effect was observed experimentally [11] in the 1930's, far before quantum dots could be built. It emerged in the data as an anomalous behaviour of the resistivity of metals below a certain temperature. Only in the 1960's Kondo [1] was able to explain the experimental curves with the existence of magnetic impurities inside the metal. Scattering of electrons at these local moments does not die out with decreasing temperature but gets enhanced, resulting in strongly correlated electron systems. Even though well understood meanwhile, the Kondo effect received new interest for the study of transport phenomena with the fabrication of devices on a micro or nano scale, where now localized electrons in the quantum dot can provide the local moment to be screened: On the one hand the Kondo effect strongly affects the transport properties of these systems at low temperatures, on the other hand side quantum dots constitute a testing ground for studying this prime example of a many-body effect in all its facets.

In order to analyze these strongly correlated systems theoretically, elaborate methods beyond mean-field or perturbation theory have to be employed. In this thesis we study quantum impurity models by means of Wilson's numerical renormalization group method [2] (NRG). The key idea of this method is the logarithmic discretization of the conduction band, allowing all relevant energy scales to be considered in the calculation. Thermodynamic and dynamic quantities like the linear conductance can be calculated in linear response at zero and finite temperature.

This thesis contributes to the understanding of transport phenomena through quantum impurity systems. It describes three major projects. The first and most extensive one is motivated by measurements of the phase of the transmission amplitude through a multi-level quantum dot done in the Heiblum group [3, 4, 12, 13, 5, 14]. Experiments proved coherence of transport but where not fully explained theoretically for almost 10 years. It turns out that it is the ratio of mean level spacing to mean level width that governs the generic properties of the system. Secondly, an impurity model with superconducting leads is investigated. This study is motivated both by the high quality analyzis of the spectral function and the quest for new insight into the mechanisms of NRG to that model. In a third project, we investigate the existence of the non-Fermi liquid regime in two different two-channel Kondo systems apart from half filling.

In the following, we give an overview of the content of this thesis. It is organized into four parts. **Part I** provides an overview for the field of transport through quantum impurity systems and the NRG method. In Chapter 2, some fundamental properties of transport through quantum dots is summarized, and the standard models used to describe these systems, the Anderson and the Kondo model, are introduced. The Kondo effect is discussed and different ways to calculate the transmission amplitude through an impurity system are motivated. A pedagogical introduction to the NRG method is given in Chapter 3, covering also recent developments like the concept of a complete basis (within the framework of NRG) and sum-rule conserving calculation of spectral functions.
The NRG method is applied in **Part II** to several quantum impurity problems. All models involved are schematically depicted in their NRG representation in Fig. 3.8. A majority of the results are published in this Part have been published.
Chapter 4 is motivated by measurements of the transmission phase through a quantum dot, all performed in the Heiblum group [3, 4, 12, 13, 5, 14]. They find that in large quantum dots, the phase exhibits universal behaviour, i.e. between any two electrons that successively enter the quantum dot, the phase sharply drops by π (phase lapse), whereas for a small number of electrons in the dot, the occurrence of the phase lapse depends on the parameters of the successive levels (mesoscopic behaviour). In Sec. 4.2 we analyze the transmission amplitude through a spinless multi-level Anderson model and find universal phase behaviour when the level spacing is small compared to the mean level widths, as well as a crossover to mesoscopic behaviour when increasing ratio or level spacing to level width, in accordance with experiments. The universal phase lapse behaviour follows from Fano-type antiresonances between the renormalized single-particle levels, that are obtained by use of the functional renormalization group [15]. Section 4.3 contains a more detailed study of both a spinful and spinless two-level Anderson model with both the NRG and functional renormalization group method. The effect of spin and temperature in the mesoscopic regime is investigated in Sec. 4.4 for up to three levels. For odd occupation of the quantum dot, Kondo correlations dominate the physics in the low-temperature limit. We investigate the consequence of the decrease of Kondo correlations with increasing temperature on phase and magnitude of the transmission amplitude, focusing on the influence of the neighbouring

level.

A model of a local impurity coupled to a superconducting reservoir is investigated in Chapter 5. We show that NRG is able to resolve energy differences that are much smaller than the energy scale of the superconducting gap. This is contrary to intuition, since energy scales like a finite magnetic field or finite temperature act as a lower bound on the energy resolution possible with NRG. This high resolution allows us to calculate the impurity spectral function very accurately, and to resolve sharp peaks in the spectral function close to the gap edge in case of the gap much smaller than T_K.

The extent of the non-Fermi liquid regime in two-channel Kondo systems away from the local moment regime is discussed in Chapter 6. We study two theoretical models that allow for a tuning of the energy of the local level and thereby a control of the local occupation. We are interested in the existence of non-Fermi liquid behaviour when emptying the local level. The two models are motivated by the proposal [16], realized only recently [17].

At the end of this part, a short summary and outlook are given.

The Appendix, **Part III**, contains technical details relevant for the studies carried out in Part II. App. A elucidates procedure and tricks to obtain a smooth spectral function from the raw NRG output. The equation of motion method (self-energy trick) can be applied to improve the accuracy of the spectral functions, as explained and illustrated in App. A.2. The mapping from the Anderson to the Kondo model is performed in App. B for the example of a two-channel model related to Sec. 6.2. At $T = 0$, standard Kondo systems exhibit Fermi liquid behaviour and their transport properties are fully characterized by the scattering matrix. Accordingly, the low lying energy levels of the converged NRG flow diagrams can be understood in terms of the scattering phases defined by the eigenvalues of the scattering matrix, as explained in App. C. Some useful fermionic commutator relations are summarized in App. D.

The last part, **Part IV**, contains various miscellaneous items, the bibliography, a list of publications, the acknowledgements, the "Deutsche Zusammenfassung" and finally the author's curriculum vitae.

Chapter 2

Quantum dots (QDs)

The Kondo effect is one of the prime examples of strongly correlated many-body phenomenon. After the first experimental signatures in 1934 and Kondo's explanation in 1964 (sketched in the following Section), it attracted new interest with the development of nanotechnology. The second Section of this Chapter is about the basics of QDs. QDs are experimental devices which allow for the study of scattering mechanisms (like the Kondo effect) via transport measurements in a highly controllable manner. In the last Section of this Chapter we introduce the Anderson impurity model. This is one of the standard models for describing QDs tunnel-coupled to external reservoirs, as needed for transport.

2.1   History of the Kondo effect

In 1934, de Haas, de Boer and van den Berg [11] presented puzzling experimental data of the resistivity of gold samples that were assumed to be pure. Their measurements revealed a minimum of the resistance at about $\sim 10K$, as well as a finite resistance in the zero temperature limit. The results are sketched in Fig. 2.1. The striking behaviour was confirmed also for other metals like silver or copper. This observation contradicted the then known theories of resistance, predicting a monotonous increase with temperature.

   The resistance of metals was known to be determined by different kind of scattering mechanisms, all yielding a monotonous increase with temperature: (i) The low-temperature limit is dominated by temperature independent potential scattering of conduction electrons at impurity atoms embedded in the lattice structure of the solid. This results in a finite resistance at zero temperature. (ii) Electron-electron scattering increases with temperature as $\rho_{\mathrm{el}}^{\mathrm{el}} \propto T^2$. Clearly, this gives only a minor contribution at low temperatures, vanishing for $T \to 0$. (iii) The same holds for scattering of electrons with phonons (lattice distortions), which goes as $\rho_{\mathrm{phonon}}^{\mathrm{el}} \propto T^5$, therefore dominating the resistance with increasing temperature. Obviously, the scattering mechanisms (i)-(iii) cannot explain the minimum in resistance observed by de Haas *et al*.

   From its observation in 1934, this low-temperature anomaly was an open question for 30 years, until Jun Kondo solved the problem of the resistance minimum in 1964 [1]. The

key to the solution was that the potential scattering (i) does not cover all electron-impurity scattering processes. If the impurities possess a magnetic moment (typical examples are ferrum, manganese or cobalt), also spin-spin scattering of the spin-1/2 conduction electrons with the magnetic moment of the impurities has to be taken into account. Even a very low concentration of these local moments (remember, the probes were assumed to be "pure") is enough to change the low-temperature properties dramatically.

The spin-spin interaction allows for spin-flip scattering, clearly not covered by the scattering processes (i)-(iii). Kondo showed, using perturbation theory, that the novel scattering mechanism results in logarithmic divergences for decreasing temperature, $\rho^{\mathrm{el}}_{\mathrm{magn.imp}} \propto \ln(T_K/T)$. T_K is the Kondo temperature, i.e. the energy scale were the spin-flip scattering starts to dominate the physics of the system. Including all four scattering mechanisms, the resistance can be expressed as

$$\rho^{\mathrm{el}}(T) = ac_{\mathrm{imp}}\rho^{\mathrm{el}}_0 + bT^2 + cT^5 + c_{\mathrm{imp}}\rho^{\mathrm{el}}_1 \ \ln \frac{T_K}{T}, \tag{2.1}$$

with the characteristic resistances ρ^{el}_0 and ρ^{el}_1, the impurity concentration c_{imp} and the constants a, b, c. The equation reproduces the experimental findings for $T \sim T_K$, where the resistance minimum is at $\sim T_K$.

In Chapter 2.4 we will dwell on the higher order scattering processes leading to the Kondo effect and sketch both a perturbative as well as a simple scaling method to estimate the Kondo temperature and the logarithmic divergences. For temperatures $T \ll T_K$, these approaches fail (*Kondo problem*). More elaborate methods (like the numerical renormalization group method (NRG), see Chapter 3) yield a screening of the local moments by the surrounding bulk electrons of energy $E \approx E_F \pm T_K$ around the Fermi energy E_F. Therefore, the local spins are screened and the ground state is a singlet (*Kondo singlet*). Spin-flip scattering and consequently also the logarithmic divergence are suppressed, resulting in a finite resistance at zero temperature, in accordance with experiments.

2.2   Quantum dot basics

Due to the confinement of electrons on small spatial scales, QDs reveal both charge and energy quantization. Accordingly, they are ideal devices to study quantum impurity physics. Following up on the preceding Section, we introduce (lateral) QDs as artificial impurities with experimentally adjustable properties. Therefore they are ideal devices for the study of quantum transport phenomenon like the Kondo effect.

2.2.1   Quantum dots and the Kondo effect

The Kondo effect, which was initially observed for magnetic impurities in a metallic reservoir, experienced a revival with the improvement of nanofabrication. In 1998, Goldhaber-Gordon *et al.* [9] were the first to measure the Kondo effect in one of these highly controllable nano devices, namely in a QD, which at that time still was called single-electron transistor.
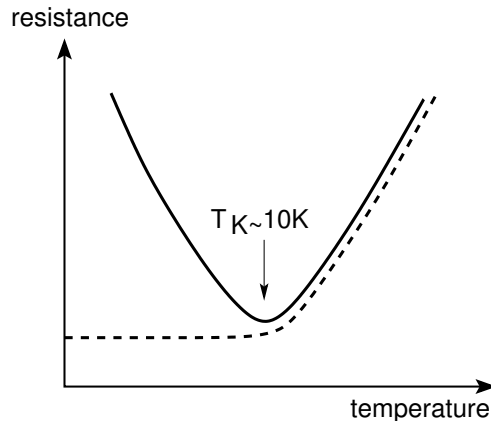
Figure 2.1: Sketch of the temperature dependence of the resistance of a gold sample with a small concentration of magnetic impurities, as measured by de Haas *et al.* [11]. The resistance minimum at $\sim T_K$ was a puzzle for 30 years, until Kondo related the non-monotonicity with spin-flip scattering of electrons at magnetic impurities (*Kondo effect*). For $T \lesssim T_K$, this results in a resistance $\propto \log(T_K/T)$. At temperatures above T_K the resistance is dominated by electron-phonon scattering $\propto T^5$.

In a QD, electrons are confined within a very small area (a "dot"). The constraint on mobility in all three spatial dimensions results in a discrete energy spectrum for the electrons (and holes). Additionally, due to the spatial confinement, the Coulomb repulsion between all electrons occupying the QD is an important energy scale, so that electrons can only enter one by one. Therefore, QDs reveal both charge and energy quantization. The discrete local levels of a QD are tunnel-coupled to the surrounding material. This is usually a semiconductor (or rarely a metal) with continuous band structure, thus providing a reservoir of electrons. An graphical energy representation of a QD setup is sketched in Fig. 2.2(b).

If the total spin of the electrons confined in the QD is finite (in the simplest case one electron occupies the QD), this localized magnetic moment acts like a magnetic impurity. Therefore, as discussed in the preceding section, spin-flip scattering between the reservoir electrons and the spin of the QD dominates the low-temperature physics and the Kondo effect emerges.

The enhancement of the scattering rate due to the Kondo effect can be studied by transport measurements. For this purpose the QD is coupled to two reservoirs (left and right or source and drain) at slightly different chemical potential (achieved by applying a small voltage bias V_{sd} between source and drain). Therefore the Kondo effect results in an enhanced forward scattering, leading to an increase in current through the QD. Compare the situation to a magnetic impurities in a bulk, where the direction of scattering is not restricted. Then the enhanced scattering due to the Kondo effect effectively decreases the flow of electrons in forward direction, thus it is the resistance and not the current that increases for temperatures below T_K.

QDs not only enable a "man made" Kondo effect, but allow for its controlled study.

The energy of the local levels can be shifted via the control of the potential depth of the QD by a gate voltage V_g. Therefore the number of electrons on the QD can be changed by simply tuning a voltage, thereby switching the Kondo effect on (finite spin, e.g. one or odd number of electrons) or off (zero spin, e.g. zero or even number of electrons). Further, the coupling to the reservoirs can be controlled and it is possible to study the effect of a magnetic field or the dependence of the strength of the source-drain voltage. It is also possible to couple several QDs [18] or to integrate them into larger structures like an Aharonov-Bohm interferometer [19], a geometry studied in Chapter 4.
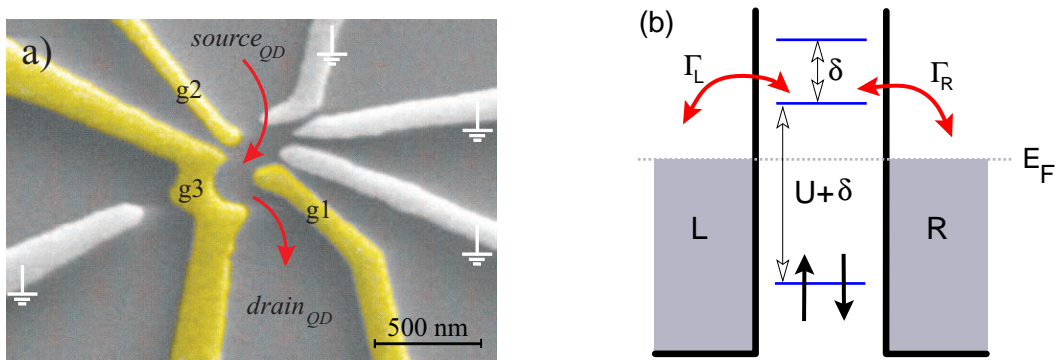
Figure 2.2: Lateral quantum dot. (a) Scanning electron microscope micrograph of a lateral QD (courtesy by Clemens Rössler, LMU Munich). Electrons can tunnel from the source through the QD to the drain lead. The electrostatic potential defining the quantum dot is defined by gate electrodes. (b) Sketch of the relevant energy scales of a QD in equilibrium. The continuous bands of the left (L) and right (R) reservoirs are filled up to the Fermi energy, thus $\mu_L = \mu_R = E_F$. Due to the spatial confinement of electrons inside the QD, the local energy levels are discretized. Electrons can tunnel from the leads into the QD and occupy the levels below the Fermi energy. Also the Coulomb interaction between the localized electrons has to be paid.

2.2.2 Scales

For quantum mechanical effects to occur, the size of a QD is restricted by the thermal wavelength $\lambda_T = \sqrt{\frac{h^2}{2m^\star k_B T}}$ and the de Broglie wavelength $\lambda_B = \frac{h}{p}$ of the electrons. m^* is the effective mass of an electron. At low temperatures, the electron energy can be approximated by the Fermi energy, thus $p \approx m^\star v_F$, with the Fermi velocity v_F. Because of much the smaller Fermi velocities of semiconductors compared to metals, the de Broglie wavelength of semiconductors ($\lambda_B \sim 100nm$) is much larger than for metals ($\lambda_B \sim 0.1nm$). Therefore standard QDs are of semiconducting material with a diameter $L \lesssim 100nm$.

The corresponding energy quantization results in a finite spacing δ of the local levels. Approximating the QD as a two-dimensional box (square) of length L, it can be estimated

to behave as

$$\delta \propto 1/L^2. \tag{2.2}$$

The second energy scale important due to the spatial confinement, is the Coulomb repulsion between the negatively charged electrons in the QD. An electron added to the QD which acts as a capacitor, has to pay the charging energy $U = e^2/2C$, where C denotes the capacitance of the QD. For a disc capacitor of diameter L and dielectric constant ε_0, it can be estimated by $C \sim \varepsilon_0 L$, yielding

$$U \approx \frac{e^2}{2\varepsilon_0 L}. \tag{2.3}$$

Additional interaction between localized electrons is given by the spin-spin exchange interaction. In most cases this is a minor effect and can thus be neglected.

For typical QDs, the Coulomb repulsion is the dominant energy scale, $U > \delta$. In principal, both the level spacing and the Coulomb energy for a specific setup are fixed by the material and the size[1]. A third energy scale of the system which can be varied more easily in experiment is given by the coupling strength Γ between the reservoir and the local levels. Usually $\delta > \Gamma$ so that the levels (that are broadened by Γ) do not overlap and the levels get occupied one by one when lowering the energy of the local levels. Due to energy and charge quantization, QDs are sometimes referred to as "artificial atoms". The filling of symmetric QDs is even known to obey a periodic table [6] according to two-dimensional electron orbits and obeying Hund's rule, i.e. maximizing the spin of each orbit.

2.2.3 Fabrication

The most commonly used QDs for transport measurements are lateral QDs. A scanning electron microscope micrograph is shown in Fig. 2.2(a). In a semiconductor heterostructure, a potential minimum near the interface of the two different materials (e.g. GaAs/AlGaAs) leads to the formation of a two-dimensional electron gas. Metallic gates on top of the structure deplete the region below them when a negative voltage is applied. With the proper design of these top gates, a small electron island (i.e. the QD) and a left and right reservoir can be defined in the two-dimensional electron gas below the surface. By control of the gates the tunnel coupling between dot and reservoirs can be adjusted. A voltage bias applied between the reservoirs (acting as source and drain) results in transport through the QD. Moreover, a gate electrode controls the potential depth of the QD, thereby shifting the local levels so that the occupation of the QD can be changed.

As mentioned above, with progress of nano-fabrication methods, also more complicated structures like several QDs coupled to each other [18] or a QD in one arm of an Aharonov-Bohm geometry, see Fig. 4.1, can be realized.

Other standard types of QDs (for different fields of application) are e.g. vertical QDs, where the QD is defined by chemical etching, or self assembled QDs which accumulate

---

[1]Depending on the type of QD, the size of the dot can be changed by adjusting the confining potential.

at the barrier layer between two semiconducting materials with different lattice constant, thereby reducing the lattice tension.

2.3   Anderson model

The Anderson model is commonly used to describe localized levels with local interaction that are tunnel-coupled to one or several reservoirs – as realized in the above described impurity or QD systems [9]. Initially, the model was invented by P.W. Anderson [20] to explain the existence of local moments in metals.

The Hamiltonian of the Anderson model can be split into three parts,

$$H = H_{\text{imp}} + H_{\text{res}} + H_{\text{imp-res}}, \tag{2.4a}$$

specifying the properties of the bare impurity, the reservoirs and the coupling between the two systems, respectively. For M local levels coupled to N electronic reservoirs, these terms are given by

$$H_{\text{imp}} = \sum_{j=1}^{M} \sum_{\sigma} \varepsilon_{dj} n_{dj\sigma} + \sum_{\{j\sigma\} \neq \{j'\sigma'\}} U_{jj'} n_{dj\sigma} n_{dj'\sigma'} \tag{2.4b}$$

$$H_{\text{res}} = \sum_{\alpha=1}^{N} \sum_{\mathbf{k}\sigma} \varepsilon_{\alpha\mathbf{k}} c_{\alpha\mathbf{k}\sigma}^{\dagger} c_{\alpha\mathbf{k}\sigma} \tag{2.4c}$$

$$H_{\text{imp-res}} = \sum_{j=1}^{M} \sum_{\alpha=1}^{N} \sum_{\mathbf{k}\sigma} V_{j\alpha\mathbf{k}} c_{\alpha\mathbf{k}\sigma}^{\dagger} d_{j\sigma} + V_{j\alpha\mathbf{k}}^{\star} d_{j\sigma}^{\dagger} c_{\alpha\mathbf{k}\sigma}. \tag{2.4d}$$

Electrons occupying the local level j with energy ε_{dj} and spin $\sigma = \{\uparrow, \downarrow\}$ are created by the operator $d_{j\sigma}^{\dagger}$. The level energies are measured w.r.t. the Fermi energy E_F. The local electrons interact via the Coulomb repulsion U with each other, where $n_{dj\sigma} = d_{j\sigma}^{\dagger} d_{j\sigma}$ is the charge operator. Additional local terms may be added, for example to take into account the effect of an external magnetic field or exchange interaction.

An electron in reservoir α with momentum $\mathbf{k}$ and spin σ is created by the creation operator $c_{\alpha\mathbf{k}\sigma}^{\dagger}$. The reservoirs – also called leads or baths in the case of QDs – are assumed to be identical, non-interacting and in equilibrium. The dispersion relation is then given by $\varepsilon_{\alpha\mathbf{k}} = \varepsilon_{\mathbf{k}}$ for all α. The creation and annihilation operators obey the standard fermionic anti-commutation relations $[a_i, a_{i'}^{\dagger}]_+ = \delta_{ii'}$, $[a_i, a_{i'}]_+ = 0$ and $[a_i^{\dagger}, a_{i'}^{\dagger}]_+ = 0$, where $a_i = d_{j\sigma}, c_{\alpha\mathbf{k}\sigma}$, respectively.

The tunnelling between lead α and level j is characterized by the tunnelling matrix element $V_{j\alpha\mathbf{k}}$, usually assumed to be momentum independent and real, $V_{j\alpha\mathbf{k}} = V_{j\alpha}$. Finite level-lead coupling results in a broadening of the local levels. Each coupling term contributes a width

$$\Gamma_{j\alpha} = \pi \rho |V_{j\alpha}|^2, \tag{2.5}$$

where $\rho = \sum_{\mathbf{k}} \delta(\omega - \varepsilon_{\mathbf{k}})$ is the density of states of the leads. The broadening is additive, thus the total width of level j (due to tunnel coupling) is given for each spin channel by $\Gamma_j = \sum_\alpha \Gamma_{j\alpha}$. We do not take into account other broadening mechanisms (e.g. due to thermal fluctuations).

To summarize, the Anderson model (and therefore transport through a QD), as described by Eq. (2.4), is characterized by the Coulomb interaction U, the local level energies ε_{dj} and the tunnel couplings $V_{j\alpha}$. As mentioned above, these parameters are well controllable by electrode voltages in experiments. There one usually measures transport from source (say left reservoir) to drain (say right reservoir), thus $N = 2$.

In case of two leads and symmetric coupling ($\Gamma_{jL} = \lambda^2 \Gamma_{jR}$ for all level j), a unitary rotation of the lead operators results in an eventually simpler structure of the Anderson Hamiltonian (2.4). The basis transformation u given by

$$\begin{pmatrix} c_{1\mathbf{k}\sigma} \\ c_{2\mathbf{k}\sigma} \end{pmatrix} = \frac{1}{\sqrt{V_L^2 + V_R^2}} \begin{pmatrix} V_L & V_R \\ V_R & -V_L \end{pmatrix} \begin{pmatrix} c_{L\mathbf{k}\sigma} \\ c_{R\mathbf{k}\sigma} \end{pmatrix} \tag{2.6}$$

decouples the system into part 1 and 2, respectively. The situation is sketched in Fig. 2.3. Levels where the matrix elements for coupling to the left and right lead have the same sign, $s_j = \text{sign}(V_{jL} V_{jR}) = +$, couple only to channel 1 (depicted in yellow), whereas levels with $s_j = -$ couple exclusively to channel 2 (red). The effective couplings are given by $V_j' = \sqrt{1 + \lambda^2} V_{Lj}$.

Obviously, the condition of symmetric coupling holds always for the single level Anderson model (where we drop the index j). Then one of the channels (say channel 2) decouples completely and all relevant physics is contained in system 1. Same holds if all s_j have the same sign. Therefore the dimension of the Hilbert space to treat is almost halved, reducing the computational effort to solve the system considerably.
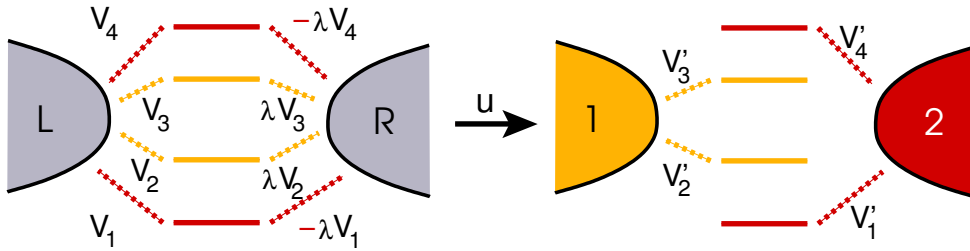
Figure 2.3: Sketch of the action of the unitary rotation u diagonalizing the scattering matrix for the case $\Gamma_{Lj} = \lambda^2 \Gamma_{Rj}$, see Eq. (2.6). Then the system decouples into part 1 and 2, respectively. This means that levels with $s_j = \text{sign}(V_{jL} V_{jR}) = +$ couple only to channel 1, whereas levels with $s_j = -$ couple exclusively to channel 2. Therefore the scattering phase shift of each of the effective channels is related by the Friedel sum rule [21] to the total occupation of the levels it couples to, see Sec. 2.6.5. The effective couplings are given by $V_j' = \sqrt{1 + \lambda^2} V_j$.

2.4   Transport processes in the Anderson model

The characteristic parameters of a QD (like Coulomb energy U or level spectrum) directly influence its transport properties. Therefore they can be extracted from tunnelling spectroscopy, where the current I is measured as a function of gate voltage V_g shifting the local level energies and source-drain voltage V_{sd}. Typical experimental data, with colour coded differential conductance dI/dV_{sd} [22], is presented in Fig. 2.4(a). The temperature fulfils $T \ll \delta, U$; otherwise thermal fluctuations smear out features due to energy and charge quantization.

The basic features of Fig. 2.4(a) can be explained by first order tunnelling processes, as will be done in the next paragraph. We focus on the regime $V_{sd} \to 0$ of linear response, which can be treated with NRG, see Chapter 3 and Part II of this thesis. We then address the issue of higher order tunnelling processes as well as their importance for the emergence of the Kondo effect.

2.4.1   Sequential tunnelling

In first order, current flow across the QD is possible if at least one local level lies within the transport window. The latter is defined by the shift of the chemical potentials $\mu_{L,R}$ of the left and the right lead when a finite source-drain voltage V_{sd} is applied between them. Therefore $\mu_{L,R} = E_F \pm eV_{sd}/2$, see Fig. 2.4(b), where $e = |e|$. We define the Fermi energy $E_F = 0$ as the Fermi energy of the system at $V_{sd} = 0$ and assume the leads large enough so that the chemical potentials are not perturbed by the flow of the current. For a level within that transport window, electrons can hop on and off the dot levels sequentially (sequential tunnelling), leading to a net current from source to drain for $V_{sd} > 0$. Thereby each local level within the transport window opens up a transport channel that contributes up to $2e^2/h$ to the differential conductance. The factor 2 accounts for the two possible spin orientations. In the experimental data, see Fig. 2.4(a), the thin lines parallel to the diamonds mark the excitation energies of the QD, whereas the lines elongating the diamonds confine the regions where several levels contribute to the current.

If *no* level lies within the transport window, electron hopping is suppressed by Coulomb repulsion (*Coulomb blockade*) and level spacing, therefore $I = dI/dV_{sd} \to 0$. In the experimental data, this leads to the so-called Coulomb diamonds aligned along $V_{sd} = 0$. Clearly, within each diamond the number of electrons is fixed. The next electron can populate the QD for V_g tuning a level inside the transport window. First scans of the differential conductance

Only recently, first success for applying NRG to non-equilibrium systems [23] is reported. In this thesis we use the standard NRG to solve Anderson-like impurity models in equilibrium. An introduction to the method is given in Chapter 3. Therefore we focus on the regime of linear response ($V_{sd} \to 0$), with the linear conductance defined as

$$G = \lim_{V_{sd} \to 0} \frac{dI}{dV_{sd}}. \tag{2.7}$$

Figure 2.5 shows an example for the V_g-dependence of the linear conductance, i.e. the profile of dI/dV_{sd} measurements as shown in Fig. 2.4(a) at $V_{sd} = 0$. Transport only occurs when a level of the QD is aligned with the Fermi energy. At these charge degeneracy points, there is no energy difference if an electron enters (or leaves) the level from (or to) the leads, therefore current flow is possible even in the linear response limit. The resulting conductance peaks at the charge degeneracy points are called Coulomb peaks.

At low temperature where all single-particle levels below the Fermi energy are filled, the charge degeneracy points, and therefore the conductance peaks are separated by the Coulomb energy; if a new level gets involved, also the level spacing has to be taken into account. At the Coulomb peaks, the conductance may reach the unitary limit $G = 2e^2/h$. The width of a peak reflects the broadening of the corresponding level (due to thermal fluctuations and coupling Γ of the level with the lead).

In the Coulomb valleys between two consecutive peaks, sequential transport is suppressed exponentially with decreasing temperature: The probability that the QD gets populated by an additional electron (energy cost $U/2$ in the middle of the valley) goes as $\propto \exp(-U/2T)$.
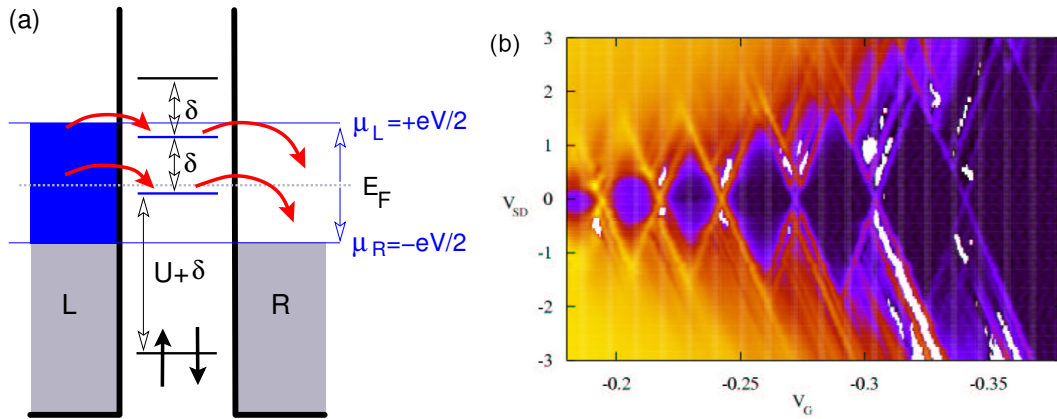
Figure 2.4: Transport for finite V_{sd}. (a) Sketch of a QD with V_g adjusted such that two electrons occupy the QD. Transport occurs through the two levels lying within the transport window $E_F \pm V_{sd}/2$ (blue). We assume constant level spacing δ. (b) Conductance measurement: Differential conductance dI/dV_{sd} colour coded versus the source-drain (V_{sd}) and gate voltage (V_g) (courtesy by A.K. Hüttel, TU Delft). Clearly, first order transport processes only occur for at least one level within the transport window.

For sequential tunnelling, transport necessarily involves real scattering processes inside the QD, randomizing the transmission phase. Therefore sequential tunnelling is incoherent, contrary to higher order processes (presented in the next Section), that may well be coherent. In Chapter 4 we analyze measurements that for the first time proved experimentally that transport across a QD has a coherent component.

Furthermore, at low temperatures, where sequential tunnelling is suppressed in the Coulomb blockade valleys, it is the higher order processes that govern the transport properties of the system. In the following, we introduce examples of higher order co-tunnelling
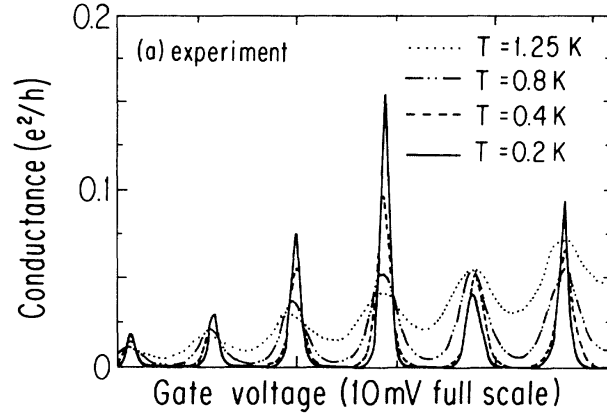
Figure 2.5: Linear conductance $G = \lim_{V \to 0} dI/dV_{sd}$ versus gate voltage V_g [24]. The Coulomb blockade peaks are separated alternately by U and $\delta + U$. In the Coulomb valleys in between, transport is suppressed. The Coulomb peaks are broadened due to the level broadening and temperature.
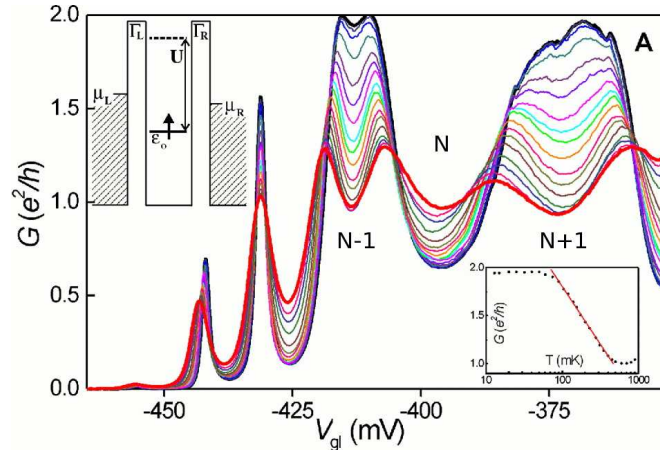
Figure 2.6: Measurement of the linear conductance G through a Kondo QD upon lowering the temperature T from $800mK$ (thick red line) to $15mK$ (thick black line) (carried out by van der Wiel *et al.* [10]). For odd occupation of the QD (the number of electrons is indicated, thereby N is an even number), the conductance increases with decreasing temperature, saturating slightly below the theoretical maximum of $2e^2/h$ (unitary limit), see also the inset. In case of even occupation, the conductance decreases as T is lowered, as in standard Coulomb blockade.

processes. Particular attention is given to spin-flip processes related to the Kondo effect. For brevity we restrict the discussion to electron-like processes (dominant for example in the regime $|\varepsilon_d| \gg |\varepsilon_d + U|$). The same argument holds for the hole-like analogues.

2.4.2 Second order co-tunnelling

We present both inelastic and elastic second order co-tunnelling processes. Due to energy conservation, the former are only possible at finite temperature or finite source-drain voltage. For details we refer to the review of Pustilnik and Glazman [25] and reverences therein. Figures 2.7 and 2.8 sketch examples of second order virtual co-tunnelling processes deep inside the Coulomb blockade.
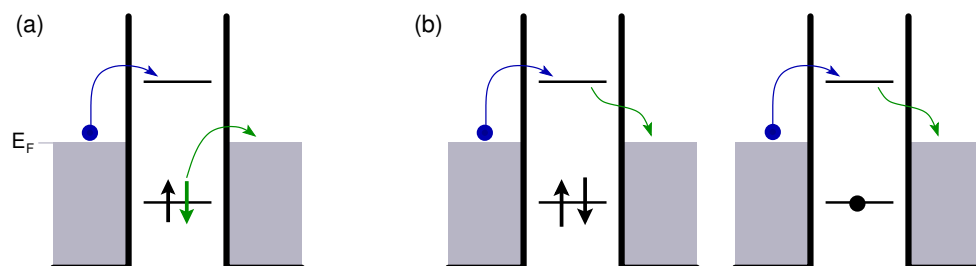
Figure 2.7: Examples of second order co-tunnelling processes deep in the Coulomb blockade regime. The first tunnelling process is indicated in blue, the second one in green. The filled circles stand for either spin up or down. (a) Inelastic co-tunnelling leaving an electron-hole pair of energy $\gtrsim \delta$ on the QD. (b) Elastic co-tunnelling for even (left) and odd (right) occupation of the QD. Transport occurs through an initially empty level. Therefore, the spin of the incoming electron does not depend on the spin configuration of the QD which remains unchanged.
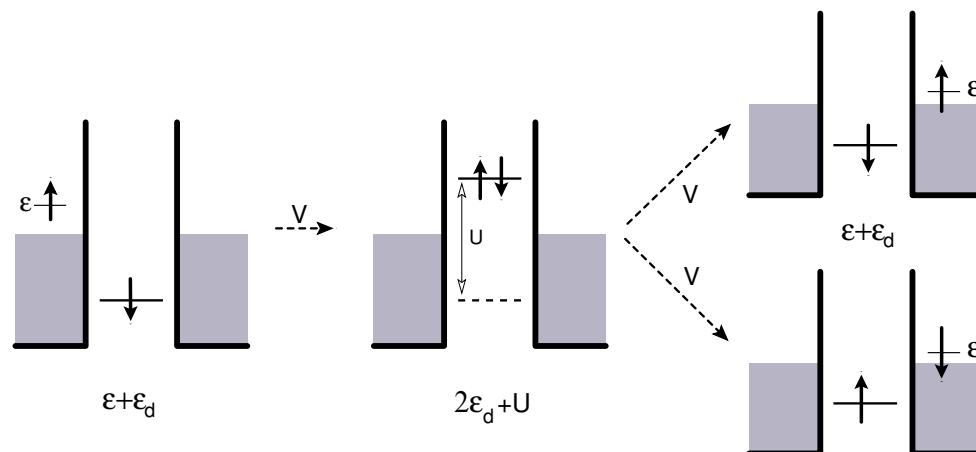
Figure 2.8: Example of elastic second order co-tunnelling processes deep in the Coulomb blockade regime which is only possible for initially odd occupation of the QD. The spin of the incoming electron is opposite to the local spin in the QD. Spin-flip of the local spin is possible. The energy of the system at the different states are indicated.

Inelastic co-tunnelling

A typical example for second order inelastic co-tunnelling is sketched in Fig. 2.7(a). An electron from the left lead tunnels into the QD occupying some local level. An electron from another level hops off the QD (to the right lead), leaving an electron-hole pair in the dot.

Elastic co-tunnelling

Elastic co-tunnelling processes are not accompanied by the creation of an electron-hole pair, implying that the occupation of each level of the QD is the same before and after the virtual process. For second order processes, this condition is fulfilled if only one level is involved. Examples for an electron transfer via an initially empty level is shown in Fig. 2.7(b). All other local levels remain unchanged in every step and the spin of the QD is conserved.

For odd number of local electrons the QD provides a local moment (*local moment regime*). In this case, additional elastic processes may occur if the spin of the incoming electron is opposite to the local spin on the QD. Then the lead electron can tunnel onto the singly occupied level. In the second step, a spin-flip of the local spin is possible, as sketched in Fig. 2.8. Note that these processes are *only* possible for opposite spin alignment of the incoming and the initial local electron, whereas the previous examples were independent of the spin orientation (and the local moment of the QD). Consequently, for opposite spin alignment and local moment regime, the energy of the system is lowered by the *additional* processes by

$$\Delta E_e(\varepsilon) = \frac{V^2}{\varepsilon_d + U - \varepsilon} \quad \text{and} \quad \Delta E_h(\varepsilon) = \frac{V^2}{\varepsilon - \varepsilon_d}, \tag{2.8}$$

where ΔE_h stands for the corresponding hole-like process. Therefore anti-alignment of the lead and dot spin is favourable, resulting in a singlet ground state, the so called *Kondo singlet*.

Transmission amplitude

The transmission amplitude (for an initial lead electron of energy ε) for all presented second order processes is given by

$$A^{(2)} = -\frac{V^2}{\Delta E}, \tag{2.9}$$

where we assume left-right symmetric and energy independent coupling, $V = V_L = V_R$. The energy difference between the virtual and the initial (final) state is denoted by ΔE. For processes mediated by a singly occupied level it is given by $\Delta E = \varepsilon_d + U - \varepsilon$. If the first unoccupied level is involved, the level distance has to be taken into account, thus $\Delta E = \varepsilon_d + U + \delta - \varepsilon$. Note that the sign depends on the chosen order of the fermionic states. Then in Coulomb blockade, where $\varepsilon_d + U \gg E_F$ (and assuming $\varepsilon \approx E_F$), the transmission amplitude is negative.

2.4.3 Next order corrections

In the previous Section we saw that in the Coulomb blockade regime, the lowest order co-tunnelling processes do not lead to any divergence of the co-tunnelling amplitude. In the following we present corrections to the amplitude in next order $(O(V^4))$ that contribute to a logarithmic divergence in the tunnelling amplitude for the QD in the local moment regime. This logarithmic divergence is characteristic for the Kondo effect. We discuss the relation of this divergence to the Kondo temperature and the breakdown of perturbation theory for energy scales smaller than the Kondo temperature. The full argument for the Kondo model (Sec. 2.5) can be found for example in [26].

The dominant fourth order process leading to Kondo physics is depicted in Fig. 2.9. It involves a virtual state with the local electron flipped and an electron of energy ε' in the leads. This intermediate state is essential for the emergence of the Kondo effect. The similar process without intermediate spin-flip cancels a transition that involves the virtual creation of an electron-hole pair [27].

The transmission amplitude of the fourth order process with virtual spin flip is given by

$$A_K^{(4)}(\varepsilon) = -\int_{-\varepsilon_c}^{\varepsilon_c} d\varepsilon' \left[1 - f(\varepsilon')\right] \rho(\varepsilon') \frac{V^4}{\Delta E \cdot (\varepsilon' - \varepsilon) \cdot \Delta E}. \tag{2.10}$$

The integration is done over all lead levels of energy ε' available for the intermediate state. For temperature $T \to 0$, the Fermi function $f(\varepsilon') = 1/(e^{(\varepsilon' - E_F)/k_B T} + 1)$ turns to a step function and integration starts at the Fermi energy E_F. $\varepsilon_c \gg E_F$ is some high-energy cutoff; usually $\varepsilon_c < |\varepsilon_d|, |\varepsilon_d + U|$. $\Delta E = \varepsilon_d + U - \varepsilon$, as above. For constant lead density of states ρ and zero temperature, the amplitude yields

$$A_K^{(4)}(\varepsilon) = -\rho \frac{V^4}{\Delta E^2} \int_{E_F}^{\varepsilon_c} d\varepsilon' \frac{1}{\varepsilon' - \varepsilon} = -\rho \frac{V^4}{\Delta E^2} \ln \left| \frac{\varepsilon_c}{\varepsilon - E_F} \right|. \tag{2.11}$$

As the second order amplitude $A^{(}2)$ for the transitions leading to the Kondo singlet, $A_K^{(4)}$ is always negative, therefore it enhances the co-tunnelling contribution to the conductance. Consequently, transport across a QD is not only possible at the Coulomb blockade peaks, but also in the local moment regime, i.e. for odd occupation of the QD.

At finite temperature, the energy of the incoming electron can be approximated by the temperature, $\varepsilon - E_F \approx T$, and the correction is proportional to $\ln \left[\frac{\varepsilon_c}{T}\right]$. For $T \to 0$ and $\varepsilon \to 0$, the tunnelling correction diverges logarithmically. Clearly, perturbation theory breaks down for $A_K^{(4)}$ comparable to the second order amplitude $A^{(2)}$ given in Eq. (2.9), $\frac{V^4 \rho}{\Delta E^2} \ln \left[\frac{\varepsilon_c}{T}\right] \sim \frac{V^2}{\Delta E}$. This is the case for the temperature of the order of $T_K \sim \varepsilon_c \exp \left[-c \frac{\Delta E}{V^2 \rho}\right]$, also called Kondo temperature. Consequently, below T_K, physics is dominated by higher order processes (as the one presented in Fig. 2.9) and the perturbative treatment is no longer justified. This is the Kondo effect.

Consequently, for temperatures below the Kondo temperature, transport across the QD is no longer suppressed in the regime between two Coulomb blockade peaks if an odd number of electrons occupies the QD (local moment regime). A plateau (*Kondo plateau*)

in the conductance forms between the neighbouring Coulomb peaks. It may reach the unitary limit of conductance, see Sec. 2.6. Typical experimental data in the Kondo regime are presented in Fig. 2.6. The Kondo temperature for the Anderson model – accounting for all possible processes and giving the right prefactor – can be estimated in the framework of the exact Bethe-Ansatz [28] or poor man's scaling [29] to be

$$
T_K = \sqrt{\frac{\Gamma U}{2}} e^{-\pi \frac{\varepsilon_d - E_F}{2U} \frac{(\varepsilon_d + U - E_F)}{\Gamma}}.
\tag{2.12}
$$

The last term in the exponent accounts for the processes presented above, the other term stems from the effect of processes not described here (e.g. hole-like processes).

The poor man's scaling method for the Kondo model will be introduced in Sec. 2.5.1. As perturbation theory, it fails for energy scales below T_K. An ingenious scheme for solving the Kondo problem also for energies well below T_K was devised by K.G. Wilson in the 1970's: the numerical renormalization group method [2]. This method will be introduced in Chapter 3 and used to solve various impurity problems in Part II of this thesis.
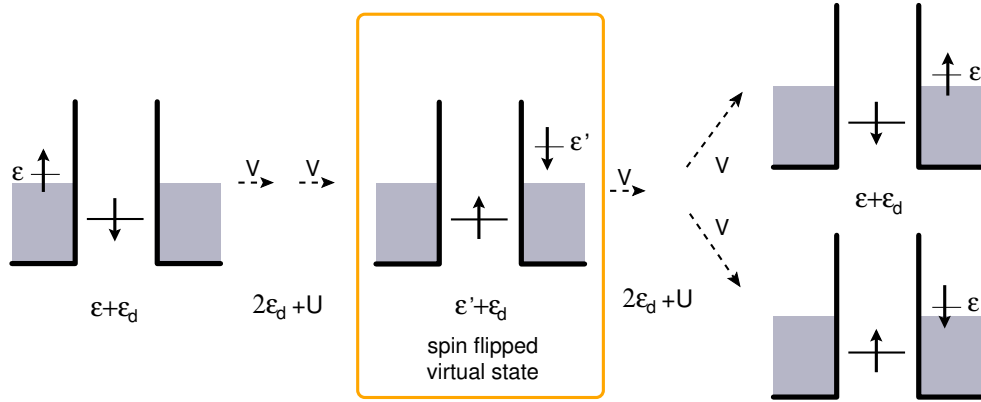
Figure 2.9: Fourth order processes leading to Kondo physics. The doubly occupied intermediate states of energy $2\varepsilon_d + U$ are not drawn explicitly. The intermediate spin-flipped state is crucial for the emergence of the Kondo effect.

2.5 Kondo model

In the preceding Section we saw that Kondo physics occurs in the local moment regime were the QD is occupied by an odd number of electrons. At low enough temperature $(T \ll \delta \ll U)$ all levels except the one directly below the Fermi energy are either double or not occupied, thus provide net spin zero. The spin of the QD is therefore determined by the one singly occupied level and as explained above, for low temperature the tunnelling amplitude is dominated by higher order spin-flip processes mediated by the singly occupied local level.

In this regime the QD can be described by the Kondo model: A single magnetic moment $\mathbf{S}$ interacts via second order coupling with the spin $\mathbf{s} = \sum_{\mathbf{k}\mathbf{k}'\sigma\sigma'} \frac{1}{2}\mathbf{c}_{\mathbf{k}\sigma}^\dagger \sigma_{\sigma\sigma'} \mathbf{c}_{\mathbf{k}'\sigma'}$ of the lead electrons (to be precise: of the even combination of the lead electrons). Since no additional local level is provided, only processes as were depicted in Fig. 2.8 are possible. This leads to an effective spin-spin coupling $\mathbf{S} \cdot \mathbf{s}$. The coupling constant is determined by the energy gain due to the second order virtual processes,

$$J = \frac{V^2}{E_F - \varepsilon_d} + \frac{V^2}{\varepsilon_d + U - E_F}, \tag{2.13}$$

see Eq. (2.8). In order to obtain an energy independent coupling constant, we assumed that $\varepsilon \approx E_F$. Summing up all possible processes, the Kondo Hamiltonian reads

$$H_K = 2J\, \mathbf{S} \cdot \mathbf{s} + \sum_{k\sigma} \varepsilon_k c_{k\sigma}^\dagger c_{k\sigma}. \tag{2.14}$$

A rigorous transformation from the Anderson model to the Kondo model is given by the Schrieffer-Wolff transformation [30], see Appendix B Eq. (B.14).

Two short checks against the results of Sec. 2.4.2: (i) Since $\mathbf{S} \cdot \mathbf{s} = [S^z s^z + \frac{1}{2}(S^+ s^- + S^- s^+)]$, H_K contains all relevant second order processes in V. We use the usual definition of the ladder operators $S^\pm$ and $s^\pm$, respectively. (ii) In the local moment regime the level energy fulfils $\varepsilon_d < E_F < \varepsilon_d + U$, thus the interaction is antiferromagnetic, $J > 0$, and the ground state is a spin singlet.

2.5.1 Poor man's scaling for the Kondo model

Since it is a very intuitive introduction to scaling or renormalization methods, we introduce the poor man's scaling method. This method was proposed in 1970 by P.W. Anderson [31] to solve the Kondo problem. The key idea is to arrive at an effective Hamiltonian that (i) captures the low-energy properties of the system but (ii) still has the same structure than the initial Hamiltonian. This is achieved by successively reducing the bandwidth, always including the effect of the virtual transitions via this narrow band-strip into the coupling constant of the new effective Hamiltonian with reduced (effective) bandwidth. When the effective bandwidth reaches the energy scale of interest, the physics at that scale is covered by lowest order perturbation theory in the effective coupling, since higher order processes are negligible for energies of the order of the effective bandwidth.

Let us sketch the poor man's scaling for the Kondo model described by the Hamiltonian (2.14). For details, see Ref. [32] or [26]; poor man's scaling for the Anderson model can be found in [29, 33].

Consider a second order transition that involves as intermediate state a level of energy ε close to the band edge D, say $D - |\delta D| < |\varepsilon| < D$, where $0 < |\delta D| ll D$. This corresponds to high energy excitations of order $\sim D$, therefore such transitions can only occur virtually, i.e. to higher order in J. Each such process contributes $\sim J^2/D$ to the second order

correction of the tunnelling amplitude. For all $\rho\,|\delta D|$ electronic states contained in the narrow strips the correction sums to [31]

$$A_J^{(2)} \sim 2\rho J^2 \frac{|\delta D|}{D}. \tag{2.15}$$

The factor 2 accounts for electron and hole-like processes. Therefore, a renormalization of the coupling constant

$$J_D \to J_{\tilde{D}} = J + 2\rho J^2 \frac{|\delta D|}{D} \tag{2.16}$$

includes the second order transitions under consideration into the first order processes of an effective system of bandwidth $\tilde{D} = D - \delta D$. The new situation is described by the effective Hamiltonian

$$\tilde{H}_K = 2J_{\tilde{D}}\mathbf{S}\cdot\mathbf{s} + \sum_{k\sigma} \varepsilon_k c_{k\sigma}^\dagger c_{k\sigma}, \qquad \text{with} \quad |\varepsilon_k| < \tilde{D} < D, \tag{2.17}$$

having the same structure than the original Kondo Hamiltonian (2.14).

For successive infinitesimal reduction of the bandwidth, Eq. (2.16) leads to the scaling equation of the Kondo model

$$\frac{dJ_{\tilde{D}}}{d\ln\tilde{D}} = -2\rho J_{\tilde{D}}^2. \tag{2.18}$$

Note that δD negative here. Integration yields

$$J_{\tilde{D}} = \frac{J_D}{1 + 2\rho J_D \ln(\tilde{D}/D)}, \tag{2.19}$$

which is a continuously growing function for decreasing $\tilde{D}$ if one starts in the weak coupling regime, $\rho J \ll 1$. This means that by reducing the bandwidth, the system tends towards strong coupling.

The properties of the system at temperature T are described for $\tilde{D} \approx T$, with an effective coupling $J_T = \frac{J}{1+2\rho J \ln(T/D)}$. This is a logarithmically diverging function, where the divergence at $1 + 2\rho J \ln(T/D) = 0$ yields an estimate of the Kondo temperature of the Kondo model

$$T_K^{O(J^2)} \sim D e^{-1/(2\rho J)}. \tag{2.20}$$

Applying poor man's scaling to third order in the coupling J, the estimate of the Kondo temperature can be improved to [26]

$$T_K^{O(J^3)} \sim D|2J\rho|^{1/2} e^{-1/(2\rho J)}, \tag{2.21}$$

which is the result that reasonably agrees with the solution of the Kondo model obtained with NRG, see Appendix B.1. There we also relate the Kondo temperature of the Anderson model to the Kondo temperature of the Kondo model.

2.6 Conductance

In the preceding Section we discussed some of the most important tunnelling processes contributing to transport across a QD. Let us now present the theoretical framework (or a formulary) for calculating the experimentally accessible quantities, i.e. the current I and the differential conductance $G = lim_{V_{sd} \to 0} dI/dV_{sd}$. Typical experimental curves were presented in Figs. 2.4 and 2.5.

The current is defined as change in time of the relative charge in the left and right lead. The current operator is given by

$$I = \frac{d}{dt} \frac{e}{2} (N_L - N_R), \tag{2.22}$$

where $N_\alpha = \sum_{k\sigma} c^\dagger_{\alpha k \sigma} c_{\alpha k \sigma}$ is the occupation number operator for lead $\alpha = L, R$, respectively. For an Anderson-like Hamiltonian with hopping term $H_{\text{imp-res}} = \sum_{\mathbf{k}\sigma,\alpha} V_\alpha (c^\dagger_{\alpha \mathbf{k} \sigma} d_\sigma + \text{h.c.})$, we use $\frac{d}{dt} N_\alpha = \frac{i}{\hbar}[H, N_\alpha] = \frac{i}{\hbar}[H_{\text{imp-res}}, N_\alpha]$ to rewrite the current operator as

$$I = \frac{ie}{\hbar} \sum_{k\alpha j} (V_{k\alpha j} \, c^\dagger_{k\alpha} d_j - V^\star_{k\alpha j} \, d^\dagger_j c_{k\alpha}), \tag{2.23}$$

with the level index j. Note that in the following we use the same symbol for the current ($I = \langle I_{\text{operator}} \rangle$) and the current operator.

2.6.1 Meir-Wingreen

Meir and Wingreen [33] showed (using the Keldysh formalism [34]) that the current through an interacting region can be expressed in terms of the Fermi functions of the leads $f_\alpha(\varepsilon) = 1/(e^{(\varepsilon + \mu_\alpha)/T} + 1)$ together with purely local properties of the interacting region like the occupation and the spectral function $A = -1/\pi \text{Im} \mathcal{G}^R$. $\mathcal{G}^R = -i\theta(t)\langle [d(t), d^\dagger]_+ \rangle$ is the local retarded Green's function. For the single-level Anderson model this yields

$$I = \frac{e}{h} \sum_\sigma \int d\varepsilon \; (f_L(\varepsilon) - f_R(\varepsilon)) \; 4\pi^2 \rho \frac{|V_L|^2 |V_R|^2}{|V_L|^2 + |V_R|^2} \left[-\frac{1}{\pi} \text{Im} \mathcal{G}^R(\varepsilon) \right], \tag{2.24}$$

leading to the differential conductance

$$G = \frac{dI}{dV_{sd}} = \frac{e^2}{h} \sum_\sigma \int d\varepsilon \left(-\frac{df(\varepsilon)}{d\varepsilon} \right) 4\pi^2 \rho \frac{|V_L|^2 |V_R|^2}{|V_L|^2 + |V_R|^2} \left[-\frac{1}{\pi} \text{Im} \mathcal{G}^R(\varepsilon) \right]. \tag{2.25}$$

Note that the Green's function covers all possible tunnelling processes, including inelastic processes and spin flips. In case of more than one level, a similar equation holds if the couplings to the left and right lead differ only by a factor λ for all levels j, $V_{Lj} = \lambda V_{Rj}$. Note that this condition also restricts the signs of the couplings. Therefore Meir-Wingreen does not hold for the $s = -$ case studied in connection with the many-level Anderson model, see Chapter 4.

In order to evaluate Eq. (2.25), the Green's function has to be calculated in presence of the source-drain voltage V_{sd}. In this thesis, we focus on the linear response regime $V_{sd} \to 0$, where the local Green's function can be evaluated in equilibrium. An example of a spectral function $A \propto \mathrm{Im}\mathcal{G}^R$ of a one level Anderson model calculated with NRG is given in Chapter 3.5.

2.6.2 Kubo formula

For arbitrary couplings, the linear conductance can be calculated using the Kubo formula [35]. It expresses the linear response of a system to some perturbation (here the applied source-drain voltage) in terms of the unperturbed system. Here it relates G with the current-current correlator,

$$G = \lim_{\omega \to 0} \frac{1}{\hbar\omega} \int_0^\infty dt e^{i\omega t} \langle [I(t), I] \rangle, \tag{2.26}$$

where the current-current correlator is evaluated in equilibrium. For $V_{Lj} = \lambda V_{Rj}$, Eq. (2.25) is recovered.

2.6.3 Landauer formula

In case of zero temperature and linear response, only single-electron, elastic processes are allowed by energy conservation. The system can be assumed to be a Fermi liquid and the Landauer formula

$$G = \frac{e^2}{h} \sum_\sigma |t_{LR}|^2, \tag{2.27}$$

originally derived for non-interacting systems [36], holds even in the presence of local interactions [33]. The transmission amplitude from lead α to α' is given by

$$t_{\alpha\alpha'} = 2 \sum_{ij} \pi\rho \, V_{\alpha i} \, \mathcal{G}^R_{ij} \, V^\star_{\alpha' j}, \tag{2.28}$$

were the spin index is suppressed.

2.6.4 Scattering theory

In the Fermi liquid regime, the transmission is completely characterized by the scattering phase shifts $\delta_{0\sigma}$ for lead electrons with spin σ at the Fermi energy. Therefore, the Landauer formula (2.27) can be reformulated in terms of these phase shifts.

The scattering matrix S and the transmission amplitude t are related by

$$S_{\alpha\alpha'} = \delta_{\alpha\alpha'} + it_{\alpha\alpha'}, \tag{2.29}$$

thus $S_{LR} = it_{LR}$. The scattering matrix can be diagonalized by a unitary rotation in the $L - R$ lead space,

$$S_\sigma = u^\dagger \begin{pmatrix} e^{i2\delta_{1\sigma}} & 0 \\ 0 & e^{i2\delta_{2\sigma}} \end{pmatrix} u, \quad \text{with} \quad u = \begin{pmatrix} e^{i\phi}\cos\theta & e^{i\phi}\sin\theta \\ -e^{-i\phi}\sin\theta & e^{-i\phi}\cos\theta \end{pmatrix}. \tag{2.30}$$

Therefore the transmission amplitude (2.28) from the left to the right lead reads

$$t_{LR} = \sin(2\theta) \ \sin(\delta_{1\sigma} - \delta_{2\sigma}) \ e^{i(\delta_{1\sigma} + \delta_{2\sigma}) + i\phi}. \tag{2.31}$$

Note that this result holds for arbitrary signs of the couplings $V_{j\alpha}$, contrary to Meir-Wingreen. Eq. (2.31) further simplifies in case of $\Gamma_{jL} = \lambda^2 \Gamma_{jR}$. The angles θ and ϕ of the unitary transformation u are then given by $\cos\theta = V_{jL}$, $\sin\theta = V_{jR}$ and $\phi = 0$ (This is the same transformation given by Eq. (2.6), which was shown to decouple the system into two parts). Therefore, an alternative representation of the Landauer formula (2.27) is given by

$$G = \frac{2e^2}{h} \ 4\frac{|V_L|^2|V_R|^2}{(|V_L|^2 + |V_R|^2)^2} \ \sin(\delta_{1\sigma} - \delta_{2\sigma})^2. \tag{2.32}$$

In case of a single level Anderson model, only one scattering channel (say channel 1) is coupled to the impurity, therefore the scattering phase shift of the decoupled channel is zero, $\delta_{2\sigma} = 0$. Additionally, the spectral function at zero frequency is known by the Friedel sum rule to be $A(\omega = 0) = \frac{\sin(\delta_{1\sigma})^2}{\pi(\Gamma_L + \Gamma_R)}$. Then, at zero temperature where the Fermi functions becomes δ-functions[2], the Meir-Wingreen formula given by Eq. (2.25) agrees with the scattering representation of the Landauer formula.

For fixed couplings, the maximum of the linear conductance is reached for $|\delta_{1\sigma} - \delta_{2\sigma}| = \pi/2$. We next argue that this is the case in the local moment regime, therefore retrieving the Kondo plateaus between two charge degeneracy points, as can be seen in the experimental data presented in Fig. 2.5.

2.6.5   Scattering phase shifts

For $\Gamma_{jL} = \lambda^2 \Gamma_{jR}$, the diagonalization of the scattering matrix, see Eq. (2.30) results in a real decoupling of the system into part 1 and 2, see Fig. 2.3 in Sec. 2.3. Depending on the relative sign $s_j = \text{sign}(V_{jL}V_{jR})$ of the hopping matrix elements, each level j couples only to channel 1 ($s_j = +$) *or* channel 2 ($s_j = -$), respectively. Therefore the phase shift for channel $1, 2$ can be related via the Friedel sum rule [21] to the occupation of the levels coupling to (only) channel $1, 2$,

$$\delta_{1\sigma}/\pi = n_1 \equiv \sum_{s_j = +} n_{j\sigma}, \qquad \delta_{2\sigma}/\pi = n_2 \equiv \sum_{s_j = -} n_{j\sigma}, \tag{2.33}$$

respectively. Thus, Eq. (2.31) and (2.32) can be expressed in terms of the occupations n_1 and n_2. For the one level Anderson model, the transformation u completely decouples one

---

[2] $\frac{df(\varepsilon - eV)}{dV} = -e\frac{df(\varepsilon)}{d\varepsilon}$

of the channels, say channel 2, therefore $\delta_{2\sigma} = 0$ always. The Kondo effect is fully developed deep in the local moment regime where local spin on the QD is maximal, i.e. $n_\sigma = 1/2$ (we do not count doubly occupied levels, since these contribute $\langle S_z \rangle = 0$). Therefore the phase shift of channel 1 is given by $|\delta_{1\sigma}| = \pi/2$ and the conductance reaches its maximum, see Eq. (2.32) The unitary limit (i.e. the maximal value of G) is reached if, additionally, the system possesses left-right symmetric coupling, $\Gamma_L = \Gamma_R$. Then,

$$G = \frac{2e^2}{h}. \tag{2.34}$$

Consequently, knowledge of the phase shifts or level occupations of the system is sufficient to obtain the transmission or linear conductance at zero temperature. Often these quantities can be calculated much easier than the local Green's function. The calculation of both the local Green's function and the occupation with NRG is subject of Sec. 3.5. The phase shifts can be also directly extracted from the eigenspectrum derived by this method [37], as explained in App. C.

Note that, actually, the Friedel sum rule relates the scattering phase shift not directly to the impurity occupation, but to the change in electron distribution in the *reservoir* near the impurity due to the screening of the local moment on the impurity, i.e. $\delta_\sigma = \delta N_\sigma / \pi$. Here N_σ is the total occupation of spin up electrons in a finite region around the impurity. For example, the complete screening of a local spin $1/2$ (e.g. in the Kondo case) requires $|\delta N_\uparrow - \delta N_\downarrow| = 1$, thus $|\delta_\uparrow - \delta_\downarrow| = \pi$. At zero magnetic field, particle-hole symmetry of the system implies $\delta_\uparrow = -\delta_\downarrow$, therefore the scattering phase shift is given by $|\delta_\sigma| = \pi/2$. Since the phase shifts are only defined modulo π, it does not make a difference whether to relate them to the occupation of the reservoir or to the occupation of the impurity, $|\delta N_\uparrow - \delta N_\downarrow| = n_\sigma \mathrm{mod}(1)$.

Chapter 3

Numerical Renormalization Group (NRG) after Wilson

In the preceding Chapter, we introduced perturbation theory and poor man's scaling to gain insight into the physics of strongly correlated impurity models, namely the Kondo problem. Both methods fail for energy scales smaller than the Kondo temperature. A method that is not restricted by the Kondo temperature is the numerical renormalization group method (NRG) [2]. In the 1970's, K.G. Wilson devised this ingenious scheme for solving the Kondo problem non-perturbatively. Since then the NRG was generalized to various impurity models, describing localized electronic states coupled to fermionic [38] or bosonic [39, 40] reservoirs. The NRG allows thermodynamic and dynamic properties of such strongly correlated systems to be calculated at zero as well as at finite temperature.

We explain the general concepts of NRG by means of the single impurity Anderson model. In a first step we sketch the derivation of the NRG Hamiltonian with its typical chain structure. The detailed derivations are nicely presented e.g. in the original article by Krishna-murthy *et al.* [38], or the review of Bulla *et al.* [41]. We then introduce the only recently developed concept of a complete basis set [42, 43], as well as the thereby improved [44, 45] calculation of correlation functions.

3.1   NRG transformations

We introduce the NRG method by means of the single-level Anderson model [20]. For convenience, we repeat the Hamiltonian. A multi-level and multi-channel version is given in Eq. (2.4). As most quantum impurity models, the Hamiltonian consists of three parts,

$$H = H_{\text{imp}} + H_{\text{res}} + H_{\text{imp−res}}, \tag{3.1a}$$

specifying the properties of the impurity, the reservoirs and the coupling between the two parts, respectively. For notation and discussion of the Anderson model, see Sec. 2.3. The

model describes a local impurity in a non-magnetic metal, implying

$$H_{\mathrm{imp}} = \sum_{\sigma} \varepsilon_d n_{d\sigma} + U n_{d\uparrow} n_{d\downarrow} \tag{3.1b}$$

$$H_{\mathrm{res}} = \sum_{\mathbf{k}\sigma} \varepsilon_{\mathbf{k}} c_{\mathbf{k}\sigma}^{\dagger} c_{\mathbf{k}\sigma} \tag{3.1c}$$

$$H_{\mathrm{imp-res}} = \sum_{\mathbf{k}\sigma} V_{\mathbf{k}} (c_{\mathbf{k}\sigma}^{\dagger} d_{\sigma} + d_{\sigma}^{\dagger} c_{\mathbf{k}\sigma}). \tag{3.1d}$$

Note that by basis transformation of the leads, the Hamiltonian also describes the situation where a left and right lead (as necessary for transport measurements) couple to a single impurity level, or a discrete energy level of a quantum dot, see Eq. (2.6).

In principle, NRG can be used for a variety of models where some impurity degrees of freedom are coupled to some reservoir degrees of freedom. Recent developments e.g. generalized the methods to bosonic reservoirs [39, 40]. The example of a superconducting bath will be treated in Chapter 5.

For simplicity, we restrict the current discussion to a model with $\mathbf{k}$-independent coupling V (for the case $V_{\mathbf{k}}$, see e.g. [41]). We further assume an isotropic and linearized dispersion $\varepsilon_{\vec{k}} = v_F |\vec{k}| = v_F k$, resulting in a constant density of states $\rho = 1/2D$, where the band ranges from $-D$ to D. Henceforth, $D = 1$ will serve as energy unit. Then the Hamiltonian of the Anderson model can be written as [38]

$$H = H_{imp} + \sum_{\sigma} \int_{-1}^{1} d\varepsilon\, \varepsilon a_{\varepsilon\sigma}^{\dagger} a_{\varepsilon\sigma} + \sqrt{\frac{\Gamma}{\pi}} \sum_{\sigma} \int_{-1}^{1} d\varepsilon (a_{\varepsilon\sigma}^{\dagger} d_{\sigma} + d_{\sigma}^{\dagger} a_{\varepsilon\sigma}), \tag{3.2}$$

where we transformed $\mathbf{k} \rightarrow \epsilon$ and as well as the fermionic operators $c_{\mathbf{k}\sigma} \rightarrow a_{\varepsilon\sigma}$. For details of this transformation, see [38]. The structure of the Hamiltonian (3.2) is depicted graphically in Fig. 3.1(a). The impurity, represented by a box, couples to a continuous bath with constant density of states.

For solving quantum impurity models one has to keep in mind that for such strongly correlated systems (i) all energy scales have to be taken into account and (ii) the properties of the system are governed by energy scales that can be much smaller than the bare energies of the initial Hamiltonian. For example, the energy scale of the Kondo effect, the Kondo temperature T_K, usually is orders of magnitudes smaller than the local Coulomb interaction U or the broadening Γ. Therefore the highest resolution is needed at the Fermi energy $E_F = 0$.

For solving this problem, K.G. Wilson invented the numerical renormalization group method. This non-perturbative method can be summarized as follows: The first step consists in a logarithmic discretization of the conduction band, as depicted in Fig. 3.1(b). The reservoir is divided into intervals $\pm[\Lambda^m, \Lambda^{m+1})$, with the discretization parameter $\Lambda > 1$ (typically $\Lambda \approx 1.5 - 3$) and $m = 0, 1, ...$.

In a second step, Fourier transformation of the lead operators on each of these intervals yields an infinite set of states for every interval. Each set of states can then be approximated
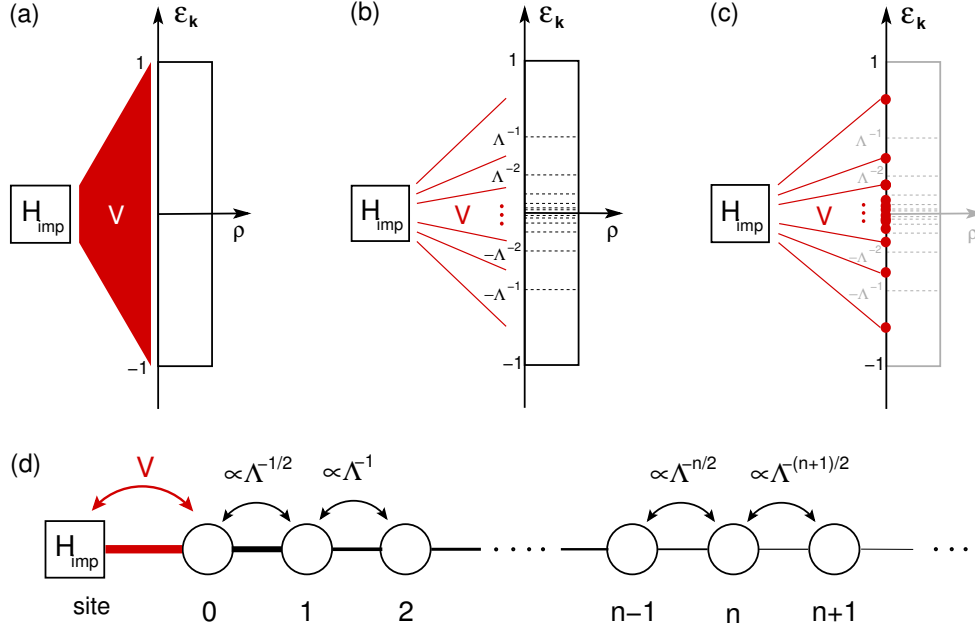
Figure 3.1: Sketch of the NRG steps. (a) Impurity (square) couples to *all* degrees of freedom of a continuous bath with constant density of states ρ. (b) Logarithmic discretization of the conduction band with discretization parameter $\Lambda > 1$. The impurity couples to infinitely many degrees of freedom of all energy scales. (c) The reservoir is approximated by one state per interval, coupling directly to the impurity. (d) Tridiagonalization leads to a chain Hamiltonian, the so-called Wilson chain. The impurity only couples to the zeroth site of the chain. The couplings between successive sites fall off exponentially like $\Lambda^{-n/2}$.

by the one state that directly couples to the impurity. The resulting situation with one state per interval is sketched in Fig. 3.1(c). The circles represent the reservoir states.

In a third step the system is mapped onto a semi-infinite chain, the so-called Wilson chain. A basis transformation of the leads combines all terms that directly couple to the impurity to yield one conduction electron site. By construction this is the only site that couples to the impurity. The remaining terms can be transformed by tridiagonalization to a chain Hamiltonian with only nearest neighbour hopping. Importantly, the couplings between the successive sites of that chain fall off exponentially with the site number. In this representation, the Hamiltonian (3.2) reads

$$H = H_{imp} + \sqrt{\frac{\Gamma}{\pi}} \sum_{\sigma} \left(f_{0\sigma}^{\dagger} d_{\sigma} + d^{\dagger} f_{0\sigma} \right) \tag{3.3}$$

$$+ \frac{1}{2} \left(1 + \Lambda^{-1} \right) \sum_{\sigma} \sum_{n=0}^{\infty} \Lambda^{-n/2} \xi_n \left(f_{n\sigma}^{\dagger} f_{n+1\sigma} + f_{n+1\sigma}^{\dagger} f_{n\sigma} \right). \tag{3.4}$$

Electrons on site n are created by $f_{n\sigma}^{\dagger}$ and $\xi_n = (1 - \Lambda^{-n-1})(1 - \Lambda^{-2n-1})^{-1/2}(1 - \Lambda^{-2n-3})^{-1/2}$, where $\xi_n \approx 1$ for large n. Due to the metallic reservoir, the chain part only consists

of nearest neighbour hopping terms, no on-site energy is present. The hopping matrix elements between the successive sites fall off exponentially with $\Lambda^{-n/2}$, as depicted in Fig. 3.1(d).

The resulting energy scale separation between the successive sites ensures that, in a fourth step, the problem can be solved iteratively. The recursion relation is found to be

$$
\begin{aligned}
\tilde{H}_0 &= 1/\sqrt{\Lambda}\,[H_{imp} + H_{hyb}] && (3.5)\\
\tilde{H}_{N+1} &= \sqrt{\Lambda}\,\tilde{H}_N + \frac{1}{2}\left(1 + \Lambda^{-1}\right)\sum_\sigma \xi_N \left(f_{N\sigma}^\dagger f_{N+1\sigma} + f_{N+1\sigma}^\dagger f_{N\sigma}\right).
\end{aligned}
$$

Where the initial Hamiltonian (3.2) of the system is related to the NRG Hamiltonian by $H_N \equiv \Lambda^{-(N-1)/2}\,\tilde{H}_N$, therefore

$$
H = \lim_{N \to \infty} H_N. \qquad (3.6)
$$

This mapping is exact in the limit $\Lambda \to 1$ and $N \to \infty$. The scaling is chosen such that at each iteration N the eigenenergies of $\tilde{H}_N$ are of the order 1.

Starting at the impurity, sites are added successively during the iterative procedure. At each iteration n the enlarged system gets diagonalized by an unitary transformation U_n. Since the couplings between the chain sites fall off exponentially with distance to the impurity, each added site can be understood as a perturbation of order $\Lambda^{-1/2}$ on the previous part of the chain, lifting the degeneracy of the old system. Consequently, the resolution of the eigenstates of H_N gets enhanced with increasing chain length, as sketched in Fig. 3.2(a). The typical energy resolution δ_n at iteration n is governed by $\delta_n \propto \Lambda^{-n/2}$, to be precise $\delta_n = \frac{1}{2}(1 + \Lambda^{-1})\Lambda^{-(n-1)/2}$. Conversely, the energy resolution δ_n is reached (approximately) at iteration

$$
N_{\delta_n} = \left[1 + 2\log_\Lambda[(1 + \Lambda^{-1})/2\delta_n]\right]. \qquad (3.7)
$$

Obviously, N_{δ_n} has to be rounded to an integer number. Thus, by choosing the length N of the chain large enough (so that $\Lambda^{-N/2}$ is much smaller than all other energies in the problem), all relevant energy scales can be resolved and treated properly. Typical chain lengths are of the order of $N \approx 60 - 80$.

When adding a site to the system, the dimension of the Hilbert space gets multiplied by the dimension of the state space $|\sigma\rangle$ of that site. For a single spinful fermionic lead, the local state space of a reservoir site consists of the states empty, singly occupied (either up or down) and doubly occupied, thus $dim = 4$ and $|\sigma\rangle = \{|0\rangle, |\uparrow\rangle, |\downarrow\rangle, |\uparrow\downarrow\rangle\}$. Therefore the dimension of the Hilbert space increases exponentially with the length of the chain. Wilson proposed a truncation scheme according to which only the lowest N_{kept} eigenstates are kept at each iteration, thereby ensuring that the dimension of the Hilbert space to treat stays manageable at each iteration. Consequently, the low energy part of the spectrum at a certain iteration gets resolved more accurately in the next iteration, therefore the energy resolution of NRG is highest at low energies. The truncation of the highest excited states at each iteration is indicated in Fig. 3.2(a) by the dashed red line, separating the kept and

discarded states. Usually one chooses N_{kept} such that no states are discarded during the first few n_0 iterations.

Accounting for the symmetries of the model, the dimensionality of the blocks that have to be diagonalized at each iteration (and therefore the numerical effort for a given N_{kept}) can be reduced significantly. As can be checked easily, the Hamiltonian Eq. (3.1a) conserves the z-component of the total spin, $S_{zN} = \frac{1}{2}\sum_{n=-1}^{N}(n_{n\uparrow} - n_{n\downarrow})$, as well as the particle number $Q_N = \sum_{n=-1,\sigma}^{N}(n_{n\sigma} - 1)$. Note that this definition yields $\tilde{Q} = 0$ for the Fermi sea together with a singly occupied dot at $\Gamma = 0$. Therefore the state space can be divided into subspaces according to the quantum numbers of the problem. Since the Hamiltonian does not couple the different subspaces, each block of the Hamiltonian can be diagonalized separately. In this work we use only Abelian symmetries like the z-component of the spin or the charge. Further improvement can be achieved by exploiting non-Abelian symmetries, as reported recently by Toth *et al.* [46].
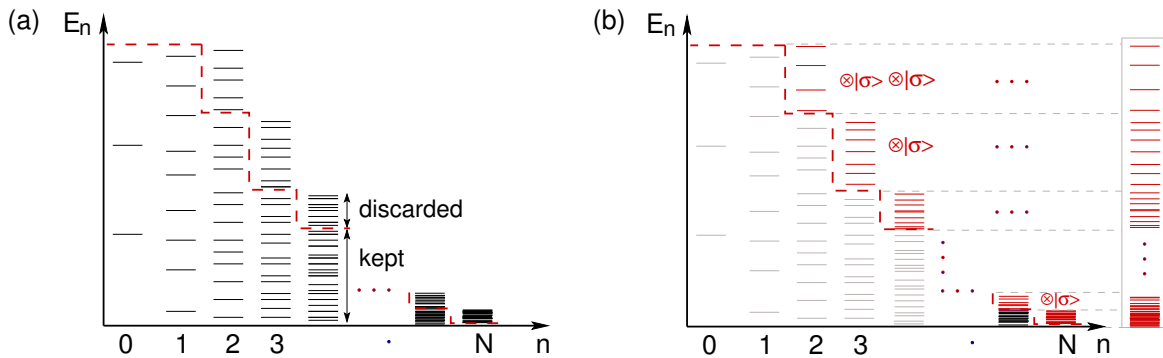
Figure 3.2: Sketch of the eigenenergies of H_n during the iterative procedure, where $H = \lim_{N\to\infty} H_N$. Added sites act as a perturbation of order $1/\sqrt{\Lambda}$ on the previous system, thus the resolution is increased exponentially with the iteration n. (a) To keep the dimension of the Hilbert state manageable, only the lowest N_{kept} eigenstates are used for later iterations, indicated by the dashed red line. Therefore the low energy properties of the system are resolved best (with resolution $\delta_N \propto \Lambda^{-(N/2)}$). (b) Anders-Schiller basis. The entirety of the discarded states form a complete (but approximate) basis [42, 43] of the d^{N+2} dimensional Fock space. The discarded states of all iterations $n < N$ are tracked to the last iteration N (where they are d^{N-n}-fold degenerate). The complete basis set is sketched inside the box on the right hand side.

In a fifth step, information gained about the system can be extracted. This can be done by analyzing the energy spectrum or by the calculation of operators or correlation functions, a problem covered in Sec. 3.5.

Before addressing these issues, we discuss the typical properties of NRG eigenspectra in more detail, including recent developments, such as the construction of a complete basis set.

3.2 NRG eigenstates

During the iterative process, the level spacing drops exponentially with every added site (see discussion above), leading to arbitrarily high resolution of the low energy physics, see Fig. 3.2(a). But NRG does not only provide a highly resolved spectrum at the end of the iterative process, instead information is gained at all iterations, i.e. energy scales. Thus, an appropriate way of visualizing the physics at different energy scales is achieved by rescaling of the energy spectrum. In these so-called energy flow diagrams, the eigenenergies for every chain length are plotted in units of $\Lambda^{-(n-1)/2} \propto \delta_n$, so that the average level spacing is constant. Said in a different way, these are the eigenenergies of $\tilde{H}_n$. As an example, the energy spectrum can be found in Fig. 3.3. The eigenenergies E_n of H_n (that fall off exponentially with n) are shown in subplot (a). In (b), the corresponding flow diagram is given. The flow of the energies is expected to change only at energy scales where the system changes its properties.

We are mainly interested in the lowest of these scales, the Kondo temperature $T_K = \sqrt{\frac{U\Gamma}{2}} \exp\left[\frac{\pi \varepsilon_d}{2\Gamma U}(U + \varepsilon_d)\right]$, indicated by a dashed arrow in the Figure. Below this temperature, i.e. for iterations with $\delta_n < T_K$, the system lowers its energy by means of the Kondo effect. The local spin (magnetic moment) on the dot gets screened by the conduction electrons, leading to a singlet ground state (Kondo singlet). The flow for $\delta_n < T_K$ is universal. For details of the various fixed points of the single-level Anderson model see e.g. [38].
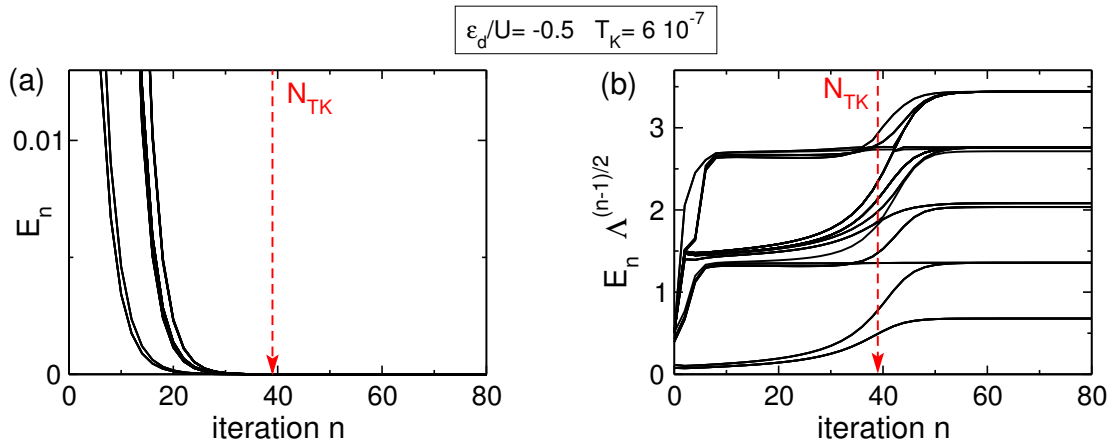
Figure 3.3: 50 lowest lying eigenenergies in the NRG procedure for a symmetric Anderson model with $U = -2\varepsilon_d = 0.6$ and $\Gamma = 0.02$. The Kondo temperature $T_K = 6 \cdot 10^{-7}$ (corresponding to $N_{T_K} = 39$ for the chosen $\Lambda = 2.1$) is indicated by the dashed arrow. (a) The eigenenergies $E^{(n)}$ of H_n fall off exponentially with the iteration number n. (b) Flow diagram. By rescaling the energies of (a) with $\Lambda^{(n-1)/2}$, the eigenenergies $\tilde{E}^{(n)}$ of $\tilde{H}_n$ are obtained. The flow changes at energy scales where the system changes its properties.

3.3 Complete basis of states

Recently, it was shown that by keeping track of the discarded states it is possible to construct complete, but approximate, sets of basis states [42, 43]. We first introduce this new concept and present its applications for the calculation of spectral properties in the remaining Sections of this Chapter.

Due to the truncation of states at every iteration, the state space of the last iteration of a NRG run obviously cannot be used as a complete basis for the whole system. It is then a natural choice to describe physics at some energy scale by the eigenstates of H_n corresponding to that scale. This implies the "NRG approximation"

$$H_N|j\sigma\rangle_n \approx H_n|j\rangle_n = E_n^j|j\rangle_n, \tag{3.8}$$

where $|j\sigma\rangle_n \equiv |j\rangle_n \otimes |\sigma\rangle^{\otimes(N-n)}$. The factor $|\sigma\rangle^{\otimes(N-n)}$ accounts for the $N - n$ sites (each having state space $|\sigma\rangle$) that will be added at iterations later than n. Eigenstates at some iteration $n < N$ are therefore "tracked back" to the N-th iteration, i.e. they are taken as d^{N-n}-fold degenerate eigenstates of the full chain, disregarding the fact that their degeneracy would have been lifted had the perturbation represented by the rest of the chain been taken into account.

Anders et al. [42, 43] where the first to see that by this tracking of the states to the last iteration, complete (but approximate) basis sets spanning the full d^{N+2}-dimensional Fock space can be constructed. This can be e.g. the entirety of the discarded states, some combination of discarded and kept states, or all kept states of iteration n_0, respectively. The identity can then be expressed in different ways, for example

$$\mathbb{1} = \sum_{n=n_o}^{N} \sum_j |j\sigma\rangle_n^D {}_n^D\langle j\sigma| \tag{3.9a}$$

$$= \sum_{n=n_o}^{k\leq N} \sum_j |j\sigma\rangle_n^D {}_n^D\langle j\sigma| + \sum_j |j\sigma\rangle_k^K {}_k^K\langle j\sigma| = \sum_j |j\sigma\rangle_{n_o}^K {}_{n_o}^K\langle j\sigma|, \tag{3.9b}$$

respectively. In the following, sums over $|\sigma\rangle$ are implied. The hyper index $X = D, K$ indicates whether a state is discarded ($X = D$) or kept ($X = K$) at some iteration. The states of the last iteration count as discarded. The basis set (3.9a) is visualized in Fig. 3.2(b). The second relation follows immediately, since all states that are discarded at some late iterations $n > k$ were kept at iteration k. Note that this also means that the subset of the basis related to the K-states is only resolved with an accuracy $\propto \delta_k$, even though NRG provides a better resolutions at later iterations.

For transformations between the different choices of basis sets the states are rotated according to the NRG iterations lying in between: All unitary transformations U_k applied to diagonalize the system at each iterative step between iteration n and iteration $m > n$ are now used to rotate states obtained at iteration n to the eigenstates obtained at iteration m, for example

$$|j\sigma\rangle_{m>n} = \sum_i (U_m \cdots U_{n+1})_{ji} |i\sigma\rangle_n^K \equiv \sum_i (u)_{ji}^{mn} |i\sigma\rangle_n^K. \tag{3.10}$$

Obviously, only states that were kept at a certain iteration may contribute to states of later iteration. Here one can see nicely that the eigenstates of NRG actually are matrix product states, as pointed out recently by Verstraete *et al.* [47].

3.4 Density matrix

It is convenient to write the density matrix such that the contribution of each iteration emerges clearly. This is achieved for the representation

$$\rho = \frac{1}{Z} \sum_n \sum_j e^{-\beta E_n^j} |j\sigma\rangle_n^D \, {}_n^D\langle j\sigma| = \sum_n w_n \rho_n, \tag{3.11}$$

where we use $\beta = 1/k_B T$ and summation over iterations $\sum_n \equiv \sum_{n=n_o}^N$ in the following. The density matrix ρ_n is composed of the discarded states of iteration n, and is weighted by the weight w_n that these states contribute to the total density matrix at a certain temperature T,

$$\rho_n = \frac{1}{Z_n} \sum_j e^{-\beta E_n^j} |j\rangle_n^D \, {}_n^D\langle j| \tag{3.12}$$

$$w_n = \frac{Z_n d^{N-n}}{Z}. \tag{3.13}$$

Clearly the density matrices fulfil $\text{Tr}[\rho] = \text{Tr}[\rho_n] = 1$, since we defined $Z_n \equiv \sum_{j \in D} e^{-\beta E_n^j}$. The partition function of the whole system reads $Z = \sum_n Z_n d^{N-n}$ and the weights sum up to one, $\sum_n w_n = 1$.

    One expects w_n to be peaked at some iteration $n \approx N_T$ where the energy resolution is of the order of the temperature. At earlier iterations temperature does not provide enough energy to drive excitations. At later iterations, states of energy $\gtrsim k_B T$ needed for thermal excitations are discarded already. The structure of w_n can be checked easily by approximating the energy of all states of iteration n by the typical energy scale $\delta_n \propto \Lambda^{-(n-1)/2}$ of that iteration. Then w_n first increases and then decreases exponentially with n. At $T = 0$ only the ground state of the system (i.e. the ground state of the last iteration N) contributes, thus $w_N = 1$ and $w_{n<N} = 0$.

3.5 Calculation of local correlators with NRG

The logical next step is the calculation of physical quantities, taking advantage of the complete basis set and density matrix derived above, as done recently [44, 45]. This can be (i) dynamic quantities like spectral functions, or (ii) thermodynamic quantities like the mean of some operator (occupation, magnetization, etc.). We will not discuss thermal quantities that can be calculated with the knowledge of the energy spectrum only, like the impurity specific heat.

At the end of the section we briefly comment on previous approaches for the calculation of physical quantities not based on a complete basis.

3.5.1   General Lehmann representation

The dynamics of the impurity can be characterized by spectral functions of the general form

$$\mathcal{A}_{BC}(\omega) = \int \frac{dt}{2\pi} e^{i\omega t} \langle B(t) C \rangle_T. \tag{3.14}$$

The thermal average is given in Lehmann representation by

$$\langle B(t) C \rangle_T \equiv \text{Tr}[\rho B(t) C] = \sum_{a,b} \frac{e^{-\beta E_a}}{Z} \langle a|B(t)|b\rangle \langle b|C|a\rangle, \tag{3.15}$$

where B and C are some local operators acting on the impurity (or the first n_o sites, respectively). With the time evolution defined by $B(t) = e^{iHt} B e^{-iHt}$, Fourier transformation yields

$$\mathcal{A}_{BC}(\omega) = \sum_{a,b} \frac{e^{-\beta E_a}}{Z} \langle a|B|b\rangle \langle b|C|a\rangle \, \delta(\omega - (E_b - E_a)). \tag{3.16}$$

3.5.2   Example of local density of states

In this thesis, we are mainly interested in transport properties. These often can be related to the local Green's functions (see Chapter 2.6) and accordingly the local density of states $A(\omega)$. The latter is defined via the Fourier-transform of the retarded Green's function $\mathcal{G}^R(t) = -i\theta(t)\langle [d(t), d^\dagger(0)]_+ \rangle_T$ as

$$A(\omega) \equiv -\frac{1}{\pi} \text{Im}[\mathcal{G}^R(\omega)]. \tag{3.17}$$

Consequently, the Lehmann representation of $A(\omega)$ reads

$$A(\omega) = \sum_{ij} \frac{e^{-\beta E_i} + e^{-\beta E_j}}{Z} |\langle i|d|j\rangle|^2 \, \delta(\omega - (E_j - E_i)). \tag{3.18}$$

The physical properties of the local density of states will be discussed in Sec.3.6.

In the following, we present how to calculate such expressions with NRG. In contrast to previous methods (see Sec. 3.5.6), the complete basis representations presented above (i) allows treat transitions between states resolved at different NRG iterations to be treated correctly and (ii) avoids over counting of transitions resolved at more than one iteration.

3.5.3 Local operators

NRG does not only provide the energy spectrum of an Hamiltonian, but matrix elements of local operators, needed to evaluate (3.16), can be calculated, too. For this purpose the operators have to be initialized in the local basis of the impurity, e.g.

$$
d_\uparrow = \begin{pmatrix} 0 & 1 & 0 & 0 \\ 0 & 0 & 0 & 1 \\ 0 & 0 & 0 & 0 \\ 0 & 0 & 0 & 0 \end{pmatrix}, \qquad d_\downarrow = \begin{pmatrix} 0 & 0 & 1 & 0 \\ 0 & 0 & 0 & 0 \\ 0 & 0 & 0 & -1 \\ 0 & 0 & 0 & 0 \end{pmatrix}, \tag{3.19}
$$

for the case of one spinful local level with state space $\{|0\rangle, |\uparrow\rangle, |\downarrow\rangle, |\uparrow\downarrow\rangle\}$. Similar to the Hamiltonian, the operators are updated at every iterative step. To be concrete, at iteration n the state space first gets inflated by the added site, followed by the unitary basis transformation U_n that diagonalizes the Hamiltonian H_n. Finally, for $n > n_0$, the state space gets truncated.

For each iteration, this only provides the matrix elements between the states resolved at that iteration. A representation involving *all* transitions can be obtained as follows. Starting from the complete basis at iteration n_o (see Eq. (3.9b) r.h.s.), all K-K transitions are successively expressed in terms of later iterations,

$$
B = \sum_{jj'} |j\sigma\rangle_{n_o}^{K} \, [B_{n_o}]_{jj'} \, {}_{n_o}^{K}\langle j'\sigma| = \sum_{n} \sum_{ii',X\bar{X}}^{\neq KK} |i\sigma\rangle_{n}^{X} \, [B_n]_{ii'} \, {}_{n}^{\bar{X}}\langle i'\sigma|. \tag{3.20}
$$

We defined $\sum_{jj'} |j\sigma\rangle_{n-1}^{K} \, [B_{n-1}]_{jj'} \, {}_{n-1}^{K}\langle j'\sigma| = [B_{n-1}^{KK}] = \sum_{XX'} U_n^\dagger [B_n^{XX'}] U_n$. The procedure is sketched in Fig. 3.4(a). This representation of B not only has the advantage that all necessary information is provided by NRG. It also accounts for the fact that transitions between K-states of a certain iteration are resolved with higher accuracy at later iterations.

Note that a time-dependent operator $B(t)$, when evaluated using the NRG approximation (3.8), only contains eigenenergies calculated at the same iteration, i.e. accuracy, $[B_n(t)]_{ij} \approx [B_n]_{ij} e^{it(E_n^i - E_n^j)}$.

3.5.4 Thermal averages

The proper representation of operators as derived in Eq. (3.20) together with the density matrix (3.11) leads to a NRG compatible expression of thermal averages,

$$
\langle B(t)C\rangle_T = \sum_{k} w_k \langle B(t)C\rangle_k, \tag{3.21}
$$

needed for the calculation of spectral functions. The thermal average for iteration k can be expressed as

$$
\begin{aligned}
\langle BC \rangle_k &= \mathrm{Tr}[\rho_k BC] \qquad\qquad\qquad\qquad\qquad\qquad\qquad\qquad\qquad\qquad (3.22) \\
&= \sum_{n,l} {}^{\bar{D}}_n\langle l| \left[\sum_{m \leq k} |j\rangle^{\bar{D}}_m \, [C_m] \, {}^{\bar{K}}_m\langle j'| \right] \left[\frac{e^{-\beta E^i_k}}{Z_k} |i\rangle^D_k \, {}^D_k\langle i| \right] \left[\sum_{m \leq k} |j\rangle^{\bar{K}}_m \, [B_m] \, {}^{\bar{D}}_m\langle j'| \right] |l\rangle^{\bar{D}}_n \\
&= \sum_{m \leq k} \sum_{lj} \sum_{i \in D} [C^{\bar{D}\bar{K}}_m]_{lj} \, |(u)^{mk}_{ji}|^2 \, \frac{e^{-\beta E^i_k}}{Z_k} \, [B^{\bar{K}\bar{D}}_m]_{jl} \, ,
\end{aligned}
$$

with implicit summation over i, j, j' inside the square brackets and $\bar{X} = X$ for $n < k$, $\bar{K} = K$ and $\bar{D} = K, D$ for $m = k$. The trace is calculated using the basis given in Eq. (3.9a), ρ_k using Eq. (3.12) and operators using the second Eq. of (3.20). For the second line we used the fact that only the K-states of the iterations $m < k$ have finite overlap with the states $|i\rangle^D_k$. To save space we use $|j\rangle = |j\sigma\rangle$. To go to the last line, the D-states of iteration k are rotated backwards to iteration m, equivalent to a change in basis (3.10).

We now can write the spectral function in an NRG compatible way, i.e.

$$
\mathcal{A}(\omega) = \sum_k w_k \mathcal{A}_k(\omega) \qquad\qquad\qquad\qquad\qquad (3.23)
$$

with

$$
\mathcal{A}_k(\omega) = \sum_{m < k} \sum_{lj} \sum_{i \in D} [C^{DK}_m]_{lj} \, |(u)^{mk}_{ji}|^2 \, \frac{e^{-\beta E^i_k}}{Z_k} \, [B^{KD}_m]_{jl} \, \delta(\omega - (E^l_m - E^j_m)). \qquad (3.24)
$$

An intuitive interpretation (that does not cover the details) of this formula is given in Fig. 3.4(b) for the case of the transition from the ground state ($k = N$) to an excited state already discarded at $m = 3$. The ground state is thereby expressed in terms of the K states of iteration m (or rotated back to iteration m).

Equation (3.23) yields a set of δ-peaks. Smoothening of the curve and improvement of the data is discussed in Appendix A. The smooth curve is obtained by broadening the δ-functions [48]. In this work we use the approach of [44]. For improvement of the curves, small widths σ of the broadening functions together with z-averaging [49] (where for fixed Λ the data is averaged for slightly shifted discretizations) can be used. For further improvement of the spectral function $A(\omega)$, the local Green's function may be expressed in terms of the self-energy $\Sigma \propto U\mathcal{G}^R$ [50] via the equation of motion. The resulting curves are almost independent of Λ as well as the broadening parameters the spectral function. For details, see App. A.

3.5.5 Sum rules and mean values

Integration of Eq. (3.14) immediately yields the relation $\int_{-\infty}^{\infty} d\omega \mathcal{A}_{BC} = \langle BC \rangle_T$ between a spectral function and the mean value of the corresponding operator product. Due to the
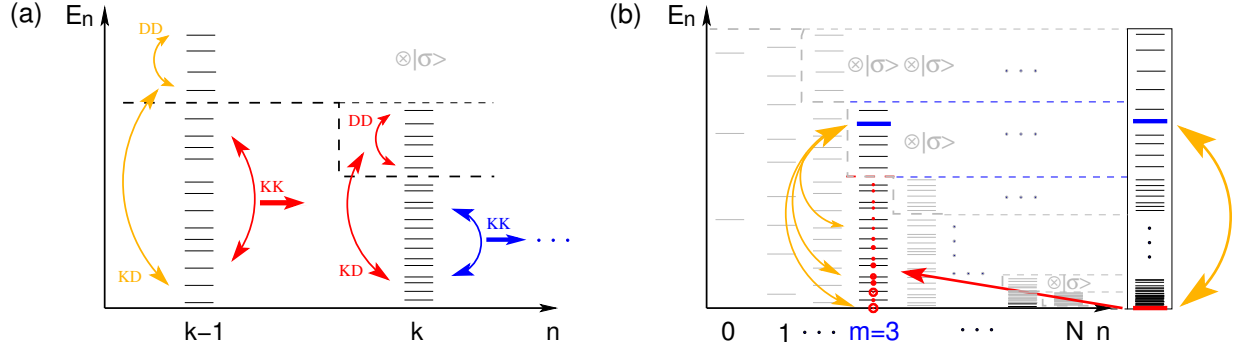
Figure 3.4: (a) Sketch of representation (3.20) for local operators. At each iteration, DD and KD transitions contribute; all KK transitions are successively expressed in terms of later iterations. (b) Intuitive interpretation of Eq. (3.24): Sketch of a transition (orange arrow(s)) between the ground state (red) and an excited state (blue) discarded in the $m = 3^{\text{rd}}$ iteration. Due to a change in basis representation (3.10), the state of a later iteration (here the ground state, $k = N$) is expressed as a linear superposition of the states of iteration n. The radius of the circles indicates that every K-state of iteration n contributes with a certain weight to the ground state. Thus, only matrix elements connecting K and D states of iteration m are needed to describe the transition properly.

complete basis we use, the presented NRG approach (3.23) for the calculation of spectral functions does fulfil this sum rule by construction for summation of the raw data (up to numerical precision for each data point), i.e. before broadening. This means that the overall spectral weight is calculated correctly. This is independent on the NRG parameter Λ or even the number of K-states N_{kept}. The error in the sum rule, if the integral is calculated using the broadened spectral function is usually of the order of $10^{-3} - 10^{-4}$.

   Note that the above sum rule implies that the mean of an operator of the structure $F = BC$ can be calculated by integration of either $\mathcal{A}_{BC}$, $\mathcal{A}_{F\mathbb{1}}$ or $\mathcal{A}_{\mathbb{1}F}$, respectively. $\mathbb{1}$ is the identity operator. Obviously, the mean of an operator F can be also calculated directly by evaluating the thermal average (3.21) w.r.t. F,

$$\langle F \rangle_T = \sum_k w_k \sum_{i \in D} \frac{e^{-\beta E_k^i}}{Z_k} [F_k^{DD}]_{ii} \,. \tag{3.25}$$

   For the calculation of transport properties (see Sec. 2.6) one is usually interested in the exact hight of the spectral function at $|\omega| \approx T$. Further, the Friedel sum rule [21] relates the occupation of the QD at $T = 0$ to the spectral function A at $\omega = 0$ via $A(0) = \frac{\sin^2(\delta_\sigma)}{\pi\Gamma}$, where $\delta_\sigma = n_\sigma/\pi$. For the symmetric case ($\varepsilon_d = -U/2$) the occupation is known to be $n_\sigma = 0.5$, therefore $A(0)\pi\Gamma = 1$.

3.5.6   Previous approaches

Before the concept of a complete NRG basis set was known, some property X (like mean value or spectral function) was calculated for each iteration separately, assuming that

$X(\omega) \approx X_n(\omega)$ for $\omega \approx \delta_n$ []. Though leading to qualitative good results, the strategy contains ambiguities. Transitions can be resolved at more than one X_n. Therefore data from subsequent iterations had to be combined using some patching scheme, see e.g. [51]. As a consequence, the above mentioned sum rule was fulfilled only within a few percent. The density matrix was represented by the contribution of iteration N_T only, i.e. $w_{N_T} = 1$, $w_{n \neq N_T} = 0$ [52]. The iterations have to be stopped at N_T, thus spectral information can only be provided for $\omega \gtrsim T$. In contrast to that, [44] report excellent agreement with exact Fermi-liquid relations even at $\omega \lesssim T$.

3.6   Spectral function of the Anderson model

We present data for the local density of states (as defined in Eq. (3.17)), also called spectral function $A(\omega)$, for $T = 0$ as well as finite temperature. We use $U = 0.3$, $\Gamma = 0.014$ and the NRG parameter $\Lambda = 2.1$ and $N_{\text{kept}} = 1024$ for the first 30 iterations, then $N_{\text{kept}} = 512$. Broadening is done as described in [44]. The results are improved by the self-energy trick [50]. Therefore they almost do not depend on the broadening parameter σ. We choose $\sigma = 0.6$. For details, see App. A.

The spectral function of the symmetric model is shown for $T = 0$ in Fig. 3.5. The three-peak structure, characteristic for the Kondo regime (where $n_\sigma \sim 0.5$, i.e. $\varepsilon_d \sim -U/2$), can be explained es follows. Due to the local level, two peaks separated by the Coulomb interaction U appear at ε_d and $\varepsilon_d + U$. Both peaks are of width Γ (half width half maximum), reflecting the coupling of the level to the leads. For temperatures below the Kondo temperature T_K the local spin on the QD gets screened by electrons of the reservoirs. This screening is due to virtual higher order spin-flip processes of electrons in a range of T_K near the Fermi energy with the local electron, giving raise to the third peak of the spectral function, a sharp resonance of width T_K. The net energy of the classically forbidden spin-flip processes is zero always. Therefore the Kondo resonance is pinned at the Fermi energy, independent of the exact energy ε_d of the local level.

The pinning of the resonance apart from half filling is visualized in Fig. 3.6(a). As expected from the Friedel sum rule [21], the hight of the resonance decreases like $A(0)/\pi\Gamma = \sin^2(n_\sigma \pi)$. The side peaks of $A(\omega)$ shift with ε_d. For both levels above/below E_F, most of the spectral weight accumulates at the level closest to the Fermi energy. Subplot (b) shows the occupation versus level position. Level energies used in (a) are indicated. Electrons enter the QD for $(\varepsilon_d, \varepsilon_d + U) \pm \Gamma \sim E_F$. The Kondo resonance does not affect the occupation (since only particle conserving higher order processes are involved).

The disappearance of the Kondo resonance for $T < T_K \rightarrow T > T_K$ is visualized in Fig. 3.7. The side-peaks remain unchanged for $T \ll U$.
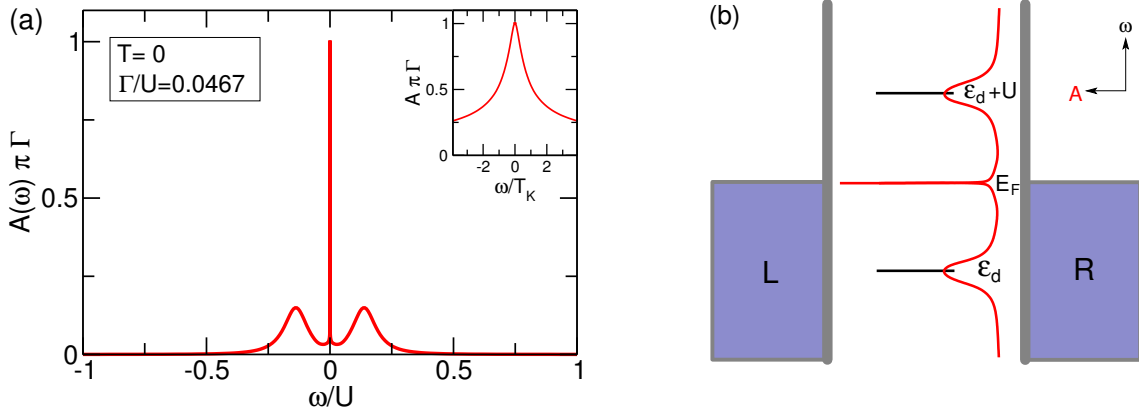
Figure 3.5: Spectral function $A(\omega)$ for the symmetric Anderson model at $T = 0$, $U = 0.3$, $\Gamma = 0.014$, i.e. $T_K = 10^{-5}$. (a) Two peaks of width Γ (half width half maximum) at $\varepsilon_d = -U/2$ and $U/2$ reflect the coupling of the local level to the leads as well as the Coulomb repulsion between electrons. The Kondo effect gives rise to a sharp resonance of width T_K at the Fermi energy, i.e. at $\omega = 0$. Inset: Zoom into the Kondo peak of hight $A(0)\pi\Gamma = 1$. (b) Sketch of the QD including the local density of states.
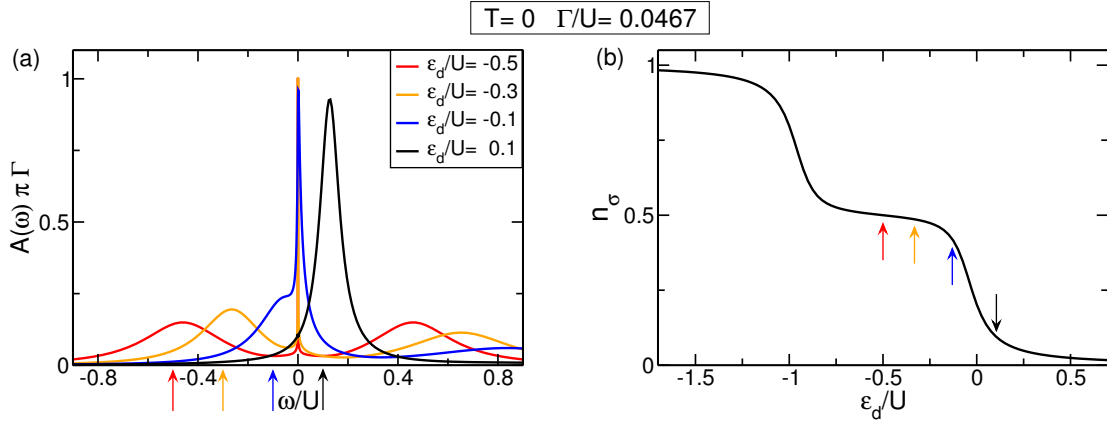
Figure 3.6: Asymmetric Anderson model for $T = 0$, $U = 0.3$ and $\Gamma = 0.014$. (a) Spectral function $A(\omega)$ for various values of ε_d. The hight of the resonance decreases according to the Friedel sum rule $A(\omega)/\pi\Gamma = \sin^2(n_\sigma\pi)$. The energy ε_d of the local level is indicated by arrows on the ω-axis. (b) Occupation versus ε_d. Level energies used in (a) are indicated. Electrons enter the QD for $(\varepsilon_d, \varepsilon_d + U) \pm \Gamma \sim E_F$. The Kondo resonance does not affect the occupation (since only particle conserving higher order processes are involved).

3.7   Recent developments

With the growth of computational power and improvements of the method, larger systems (e.g. multi-channel models, see Chapters 4 and 6) and different models (e.g. an impurity coupled to a superconducting reservoir, see Chapter 5) can be treated with higher and higher accuracy. But there are also new developments pushing the method to completely
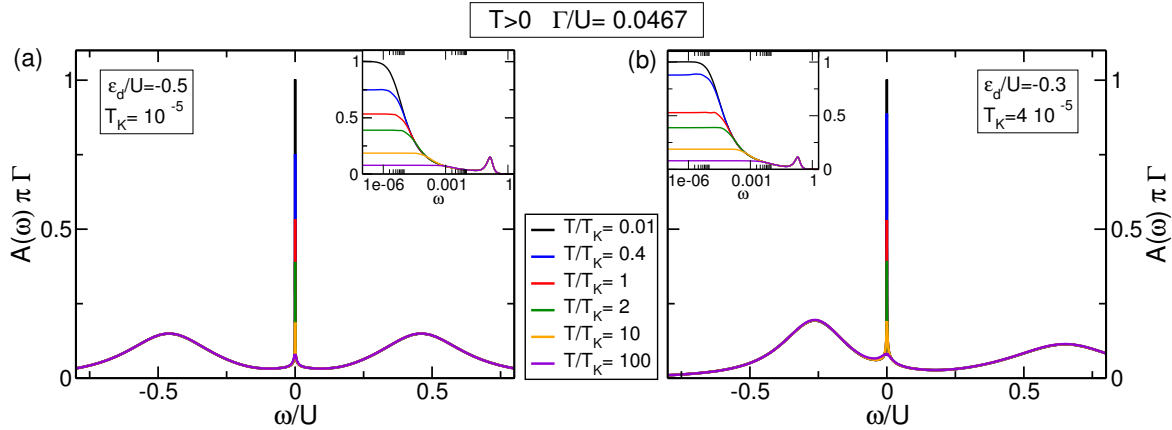
Figure 3.7: Temperature dependence of $A(\omega)$ for $U = 0.3$, $\Gamma = 0.014$ and (a) $\varepsilon_d/U = -0.5$, i.e. $T_K = 10^{-5}$ and (b) $\varepsilon_d/U = -0.3$, i.e. $T_K = 4 \, 10^{-5}$. Same in the insets on a log-scale. The side peaks remain unchanged for $T \ll U$.

new fields of application. The recent ideas of the concept of the complete basis as well as the matrix product state structure of the NRG eigenstates open up such new ways of thinking within the NRG method. Only recently, Anders *et al.* [42, 43] presented a time-dependent NRG approach as well as a non-equilibrium approach [23] based on the concept of the complete NRG basis. Further, the variational method of the density matrix renormalization group (DMRG) [53, 54] was applied to the Wilson chain - combining the clever mapping of NRG with the powerful variational tools of DMRG [55, 56]. This opens up the possibility of studying time-dependent quantum impurity models using time-dependent DMRG [57, 58], with possible applications to qubit-bath models. The thrilling question arises: What next!

3.8   Anderson-like impurity models studied in this work using NRG

In the second part of this thesis we analyze various Anderson-like impurity models within the NRG framework. For convenience, the different models are summarized with graphical depiction of the NRG Hamiltonians in Fig. 3.8.

The bare code used for the NRG calculations was generously provided by Andreas Weichselbaum.

(a) Concepts of NRG were discussed in the present Section at the example
     of the single–level single–channel Anderson model:
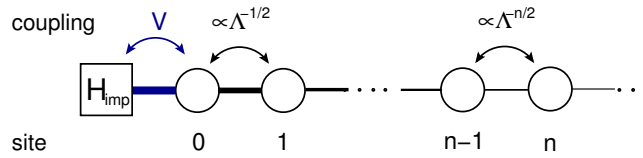
(b) Chapter 4: Amplitude and phase through a quantum dot is calculated for
     spinless and spinfull two, three and four level models with two channels
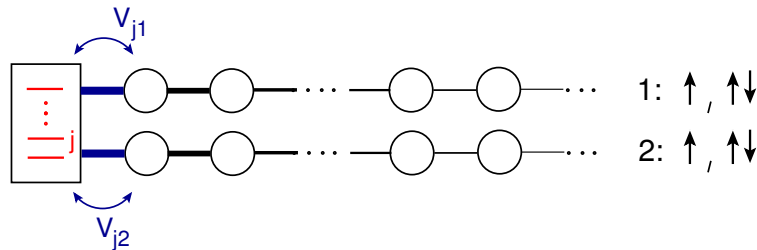
(c) Chapter 5: NRG is proven to work and the spectral function is calculated
     for a single impurity level coupled to a superconducting reservoir
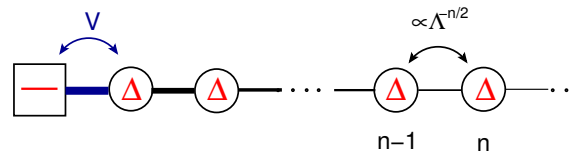
(d) Chapter 6: Two two–channel systems are analyzed concerning their
     two–channel Kondo properties
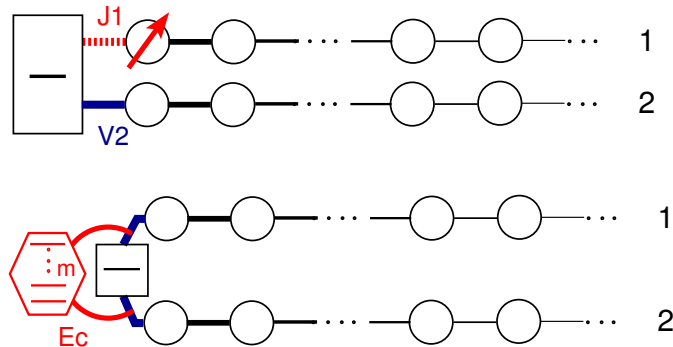
Figure 3.8: NRG representation of models analyzed within this thesis with NRG.

Part II

Results

Chapter 4

Universal and mesoscopic behaviour of transmission phase of multi-level quantum dots

Standard transport measurements only reveal information about the magnitude of the transmission amplitude, which does not distinguish between incoherent (like sequential tunnelling) or coherent (like resonant tunnelling) contributions to transport. In 1994, Yacoby et al. [3] were the first to prove directly that transport through a QD has a coherent component. In this novel kind of experiment, it was possible to measure not only the magnitude but also the phase of the transmission amplitude through the quantum dot. They showed that the signal oscillations of an Aharonov-Bohm interferometer still exist when a QD is embedded in one arm of the interferometer. Not only interference persists but also the oscillation period, strong indication of coherence. From the interference pattern, both magnitude and phase of the transmission amplitude can be extracted.

Since this first break-through, a series of experiments (all done in the Heiblum group) followed. In the Coulomb blockade regime, all experiments show a very striking behaviour of the phase for large QDs [3, 4, 12, 13, 5]. Lowering the level position of the QD, the transmission phase increases by π throughout each conductance peak. But between *any* two successive peaks, a phase-lapse by π occurs, i.e. the phase sharply jumps downwards by π. Contrary to intuitive expectations, this behaviour is independent of the dots shape, the parity of the wave functions or other parameters of the specific experimental setup, i.e. it is universal. New insight was gained in 2005 from an experiment that also explores the regime with only a few electrons in the QD [5]. For less than about 8 electrons in the QD, the universality of the phase is lost: The appearance of a phase lapse between successive conductance peaks depends on the parameters of the QD.

There has been a large amount of theoretical work on this topic [59, 60, 32, 61, 62, 63, 64, 65, 66] (for a review see [67]), with no full explanation of the observed universal occurrence of phase lapses. We explore the idea [5] that in large quantum dots, the level distance may become comparable to or smaller than the level broadening, causing levels to overlap.

In such a situation the transmission is not dominated by the properties of individual levels, thus making universal behaviour possible. In contrast, in the regime of only a few electrons (where the phase shows mesoscopic behaviour), the levels are well separated and transport is influenced by their specific properties. Varying the ratio of level spacing δ (assumed to be the same for all levels) to mean level broadening Γ, we find a crossover from an universal ($\delta/\Gamma \lesssim 1$) to a mesoscopic ($\delta/\Gamma \gg 1$) regime, independent on the exact parameters of the system, as observed experimentally [5]. This study is based not only on NRG calculations (performed by the author), but also on data obtained (by our collaborators C. Karrasch and V. Meden) using the functional renormalization group (fRG) method [15]. This is an approximation scheme to obtain the self-energy (and thus the one-particle Green's function) for many-body systems at zero temperature, allowing the study of the renormalized effective single-particle levels. Also higher order vertex functions can be obtained. We find that for decreasing ratio δ/Γ, one of the renormalized single-particle levels becomes wider than all others. Its energy hovers near the chemical potential of the leads, while the narrow ones are shifted with varying gate potential. Each time one of them crosses the chemical potential and therefore also the broad level, a Fano-type antiresonance causes a transmission zero and therefore a phase lapse, see Sec. 4.2.

In the Kondo regime, at zero temperature the typical Kondo plateaus form in the transmission amplitude for odd number of electrons in the dot. However, the phase is expected to raise by $\frac{\pi}{2}$ for each entering electron, with a plateau at $\frac{\pi}{2}$ in between. This is a direct result of the $\frac{\pi}{2}$ scattering phase shift off a Kondo impurity, as predicted by the Kondo model for the local spin completely screened yielding a zero-spin Kondo singlet [21, 68]. The $\frac{\pi}{2}$ phase shift was not observed in the first measurements of the transmission amplitude by Ji *et al.* [12, 13] claiming Kondo correlations. Only recently, Zaffalon *et al.* [14] measured the transmission amplitude through the first level of a quantum dot (starting from zero occupation). At temperature $T \ll T_K$ they do find the characteristic plateau, yielding experimental proof for the $\frac{\pi}{2}$ phase shift of the Kondo problem. At finite temperature, with the suppression of Kondo correlations, the monotonic phase evolution is lost and a smeared phase lapse of $\leq \pi$ forms. Our studies of a spinful Anderson model in the mesoscopic regime are in agreement with the results of [69, 70] where a single-level model is studied. We extend the discussion to the mutual influence of adjacent levels. We show numerical data for up to three levels. Then the second level can be assumed as any arbitrary level of a quantum dot, experiencing the influence of a lower and an upper level. Depending on the mesoscopic parameter and the relative couplings, the Kondo phase lapse of the middle level may be shifted in V_g direction. Therefore, the value of α where the phase lapse occurs is lowered or increased, possibly explaining the experimental data of Ji *et al.* [12, 13]. The regime of even number of local electrons is not affected by these spin effects; the evolution of the transmission amplitude is similar to the Coulomb blockade regime described above.

The Chapter is organized as follows: In the next Section, we briefly introduce the typical experimental setup and measurement procedure used by the Heiblum group. We

present experimental results characteristic for the universal and the mesoscopic regime. We further introduce the transmission formula and the model and summarize our arguments for the universal phase behaviour. In the second Section the crossover from the mesoscopic to universal phase behaviour in the Coulomb regime is analyzed with NRG and fRG. The third Section presents calculations for a two-level system for both a spinless and spinful model (using again NRG and fRG). In the last Section we present NRG results for the temperature dependence of a spinful model with up to three levels. In that Section also the transmission formula is derived.

4.1 Brief introduction to experiments and theory

4.1.1 Experimental setup

Figure 4.1 shows a top-view picture with a scanning electron microscope of the multi-terminal Aharonov-Bohm interferometer with a QD embedded in the left arm. A plunger gate allows the energy of the local levels of the QD to be swept, affecting transmission amplitude (magnitude and phase) as well as the occupation of the dot. The device is composed of three different regions: source (S), drain (D), and base (B). The source and drain are large 2-dimensional electron gas reservoirs that are coupled to the Aharonov-Bohm ring via two quantum point contacts (QPC). They support only one transverse mode, thus producing a planar electronic wavefront in the far field. The voltage drop occurs at the QPCs, therefore tunnelling processes through the QD can be described within linear response. Electrons that enter the interferometer can either directly reach the drain via one of the two interferometer arms or be scattered out of the interferometer to one of the base regions. This open geometry ensures that no loop paths traversing the loop multiple times are very rare and can be neglected. A four-terminal configuration [71] ensures that due to separation of current and voltage electrodes the measurement does not affect the result. Note that a special lithographic process, invoking a metallic air bridge, has been developed in order to contact the center metal gate (that depletes the ring's center).

4.1.2 Transmission

At low enough temperatures, both the elastic mean free path and the phase coherence length exceed the sample size, so that transport is expected coherent. Due to the open geometry, no loop paths are possible and the measured signal corresponds only to electrons that traverse the interferometer through one of the two arms directly. Generalizing [59], we derive in Appendix of Sec. 4.4 the Aharonov-Bohm contribution to the linear conductance through such a multi-terminal interferometer with open geometry and a multi-level quantum dot embedded in one arm. For convenience, we summarize the results. The linear conductance is given by

$$G^{AB} = \frac{e^2}{h} \int dE \left(-\frac{\partial f_0(E)}{\partial E} \right) |T_u| \, |T_d(E)| \, \cos(2\pi\Phi/\Phi_0 + \phi_0 + \phi_d(E)), \qquad (4.1)$$
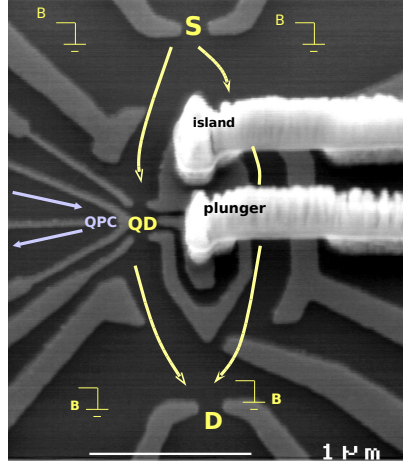
Figure 4.1: Scanning electron microscope picture of a multi-terminal Aharonov-Bohm interferometer with a QD embedded in the left arm (courtesy by Heiblum group). The two interfering paths are indicated by yellow arrows. A plunger gate enables to sweep the energy of the local levels of the QD, affecting transmission amplitude (magnitude and phase) as well as the occupation of the dot. The source (S) and drain (D) are large 2-dimensional electron gas reservoirs that are coupled to the Aharonov-Bohm ring via two quantum point contacts. The voltage drop occurs at the contacts, thus the QD remains in equilibrium. Electrons that enter the interferometer can either directly reach the drain via one of the two interferometer arms or be scattered out of the interferometer to one of the base regions (B). This open geometry ensures that no loop paths are possible.

where $T_u = |T_u|e^{i\phi_0}$ is the transmission amplitude through the reference arm which is assumed to be energy-, V_g- and temperature-independent. f_0 is the equilibrium Fermi function of the leads. A magnetic field penetrating the interferometer contributes an additional Aharonov-Bohm phase of $2\pi\Phi/\Phi_0$. It is added to one of the arms (here the reference arm). Here Φ is the magnetic flux enclosed by the two arms and $\Phi_o = h/e$ is the flux quantum [72, 19]. The magnetic field is assumed weak and the area of the QD small, therefore it does not influence transport through the QD.

The transmission amplitude T_d through the lower arm including the quantum dot is given by

$$T_d(E) = \sum_{jj'} \sum_{\sigma\sigma'} 2\pi\rho \ t_L^j t_R^{j'} \mathcal{G}_{j\sigma,j'\sigma'}^R(E) \equiv |T_d(E)| \ e^{i\phi_d(E)}, \qquad (4.2)$$

with the local retarded Green's function $\mathcal{G}_{j\sigma,j'\sigma'}^R$. Therefore, the temperature-dependent transmission amplitude through the quantum dot can be expressed as

$$t_d(T) = \int dE \left(-\frac{\partial f_0(E,T)}{\partial E}\right) T_d(E,T) \equiv |t_d(T)| \ e^{i\alpha(T)}, \qquad (4.3)$$

where only local properties and the Fermi function of the leads enter. The local Green's function is evaluated in equilibrium at temperature T. In the experiment, phase and mag-

nitude of this transmission amplitude can be extracted from the interference measurements, see below.

Note that for zero temperature and left-right symmetric coupling, $\Gamma_{jL} = \lambda\Gamma_{jR}$ for all levels j, the transmission amplitude can be expressed in terms of the scattering phase shift δ_E and δ_O of the even and odd combination of the leads, respectively. The phase shifts in turn can again be related via the Friedel sum rule [21] to the total occupation $n_{dE\sigma}$, $n_{dO\sigma}$, of the levels coupled to the even and odd lead, respectively. Then the transmission amplitude reads [73]

$$t_d = \sin(\pi(n_{dE\sigma} - n_{dO\sigma}))\, e^{i\pi(n_{dE\sigma}+n_{dO\sigma})}. \tag{4.4}$$

4.1.3 Measurement procedure

For fixed configuration of the QD, the phase dependent part of G^{AB} [Eq. (4.3)] oscillates as a function of the magnetic flux with period Φ_0. The maximum amplitude of the oscillation is proportional to $|t_{d\sigma}|$ and thus shows the same V_g dependence than $|t_{d\sigma}$. It can be extracted (by a fast Fourier transform) from the experimental data shown in Fig. 4.2 for various values of the gate voltage. Further, the shift of the Aharonov-Bohm oscillations for different choices of V_g can be identified via Eq. (4.3) with the voltage dependent phase $\alpha(V_g)$ of the transmission amplitude through the QD.
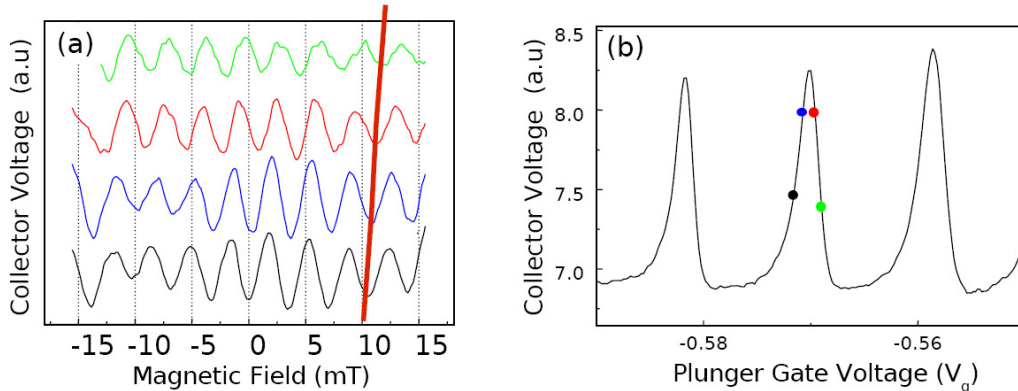
Figure 4.2: Phase measurement procedure (courtesy by Heiblum group). (a) Due to the Aharonov-Bohm effect, the collector voltage oscillates with changing magnetic field. The signal is shown for the values of gate voltage V_g indicated in (b). The shift of the oscillations with V_g (indicated by the solid red line) can be identified via Eq. (4.3) with the voltage-dependent transmission phase $\alpha(V_g)$. (b) Varying V_g, the collector voltage shows the typical conductance peaks. The values of V_g used for (a) are indicated.

4.1.4 Experimental results

Experiments done in the Coulomb blockade regime [3, 4, 5] showed a very striking behaviour of the phase. For large QDs occupied by many electrons the transmission phase increases

by π throughout each conductance peak. Between any two successive conductance peaks, the phase sharply jumps downwards by π, a phase-lapse occurs. This behaviour is found to be universal for large dots, independent of the dots shape, the parity of the wave functions, etc. Experimental data for this universal regime is shown (from the latest experiment) in Figure 4.3(a).

New insight into the phase-lapse problem was obtained in an experiment in 2005 [5], where also small QDs were probed. Measurements showed that for electron numbers up to 8 the phase is *not* universal but show mesoscopic behaviour. Whether a phase-lapse occurs in a Coulomb blockade valley or not depends on the specific specific sample they work with. Experimental data for this mesoscopic few-electron regime is shown in Figure 4.3(b). Increasing the number of electrons, they report a crossover of the transmission amplitude to the universal regime which is recovered for electron numbers above 14, see Fig. 4.3(a).
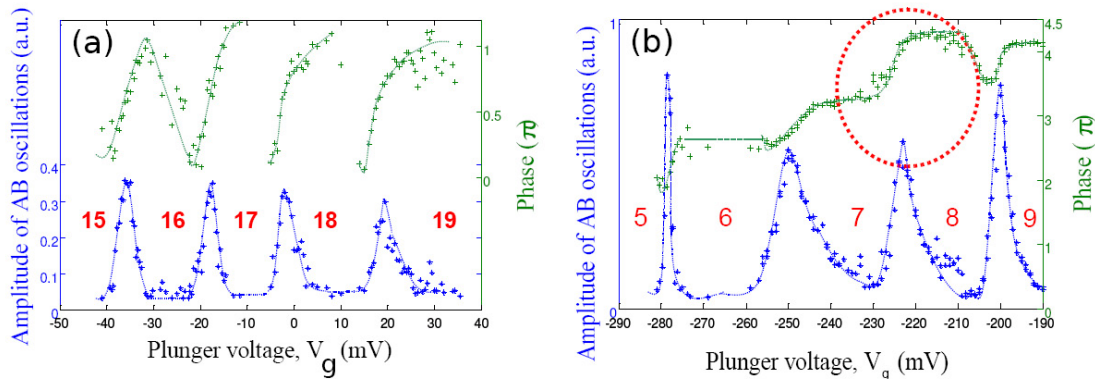
Figure 4.3: Transmission measurements in the universal and mesoscopic regime (courtesy by Heiblum group). The electrons occupying the QD is indicated in red. (a) For more than 14 electrons, the phase evolution is universal: Between any consecutive conductance peaks the phase sharply drops by π. (b) In the few-electron regime the occurence or not of a phase lapse depends on the mesoscopic parameters of the QD.

4.1.5 The model

We use a multi-level Anderson model with a left and right lead, as introduced in Sec. 2.3 in Eq. (2.4a). For the discussion of the system in Coulomb blockade regime (Sec. 4.2 and 4.3) spin effects are assumed to be negligible and a spinless model is studied. Note that notation in Sec. 4.3 is not consistent with Sec. 4.2 and 4.4: In Sec. 4.3 Γ denotes the total width of all levels, whereas it stands for the mean level width in the rest of the Chapter. $\gamma = \{\Gamma_{1L}, \Gamma_{1R}, ...\}/\Gamma$ changes accordingly. $s, \sigma = \mathrm{sgn}(t_{jL}t_{jR}t_{j+1L}t_{j+1R})$ indicates the relative signs of the matrix elements $t_{j\alpha}$ for successive levels. We assume equidistant level spacing δ and level-independent Coulomb interaction U.

4.2 Mesoscopic to universal crossover of transmission phase of multi-level quantum dots

We analyze the transmission amplitude through a spinless multi-level Anderson model. We find universal phase behaviour for the level spacing to be small compared to the mean level widths, as well as a crossover to mesoscopic behaviour for increasing ratio of level spacing to level width, in accordance with experiments. The universal character follows from Fano-type antiresonance between the renormalized single-particle levels. These are obtained by use of the functional renormalization group [15].

Mesoscopic to Universal Crossover of the Transmission Phase of Multilevel Quantum Dots

C. Karrasch,[1] T. Hecht,[2] A. Weichselbaum,[2] Y. Oreg,[3] J. von Delft,[2] and V. Meden[1]

[1]*Institut für Theoretische Physik, Universität Göttingen, 37077 Göttingen, Germany*
[2]*Physics Department, Arnold Sommerfeld Center for Theoretical Physics,*
and Center for NanoScience, Ludwig-Maximilians-Universität, 80333 Munich, Germany
[3]*Department of Condensed Matter Physics, The Weizmann Institute of Science, Rehovot 76100, Israel*
(Received 8 September 2006; published 1 May 2007)

Transmission phase α measurements of many-electron quantum dots (small mean level spacing δ) revealed universal phase lapses by π between consecutive resonances. In contrast, for dots with only a few electrons (large δ), the appearance or not of a phase lapse depends on the dot parameters. We show that a model of a multilevel quantum dot with local Coulomb interactions and arbitrary level-lead couplings reproduces the generic features of the observed behavior. The universal behavior of α for small δ follows from Fano-type antiresonances of the renormalized single-particle levels.

One of the longest-standing puzzles in mesoscopic physics is the intriguing phase-lapse behavior observed in a series of experiments [1–3] on Aharonov-Bohm rings containing a quantum dot in one arm. Under suitable conditions in linear response, both the phase and magnitude of the transmission amplitude $T = |T|e^{i\alpha}$ of the dot can be extracted from the Aharonov-Bohm oscillations of the current through the ring. If this is done as a function of a plunger gate voltage V_g that linearly shifts the dot's single-particle energy levels downward, $\varepsilon_j = \varepsilon_j^0 - V_g$ ($j = 1, 2, \ldots$ is a level index), a series of well-separated transmission resonances [peaks in $|T(V_g)|$, to be called "Coulomb blockade" (CB) peaks] of rather similar width and height was observed, across which $\alpha(V_g)$ continuously increased by π, as expected for Breit-Wigner–like resonances. In each CB valley between any two successive CB peaks, α always jumped sharply downward by π ["phase lapse" (PL)]. The PL behavior was observed to be "universal," occurring in a large succession of valleys for every many-electron dot studied in [1–3]. This universality is puzzling, since naively the behavior of $\alpha(V_g)$ is expected to be "mesoscopic," i.e., to show a PL in some CB valleys and none in others, depending on the dot's shape, the parity of its orbital wave functions, etc. Despite a large amount of theoretical work (reviewed in [4,5]), no fully satisfactory framework for understanding the universality of the PL behavior has been found yet.

A hint at the resolution of this puzzle is provided by the most recent experiment [3], which also probed the few-electron regime: as V_g was increased to successively fill up the dot with electrons, starting from electron number $N_e = 0$, $\alpha(V_g)$ was observed to behave mesoscopically in the few-electron regime, whereas the above-mentioned universal PL behavior emerged only in the many-electron regime ($N_e \gtrsim 15$). Now, one generic difference between few- and many-electron dots is that the latter have smaller level spacings $\delta_j = \varepsilon_{j+1}^0 - \varepsilon_j^0$ for the topmost filled levels. With increasing N_e, their δ_j's should eventually become

smaller than the respective level widths Γ_j stemming from hybridization with the leads. Thus, Ref. [3] suggested that a key element for understanding the universal PL behavior might be that several overlapping single-particle levels simultaneously contribute to transport. Because of the dot's Coulomb charging energy U, the transmission peaks remain well separated nevertheless.

Previous works have studied the transmission amplitude of multilevel, interacting dots [6–11]. However, no systematic study has yet been performed of the interplay of level spacing, level width, and charging energy that combines a wide range of parameter choices with an accurate treatment of the correlation effects induced by the Coulomb interaction. The present Letter aims to fill this gap by using two powerful methods, the numerical (NRG) [12,13] and functional (FRG) [14] renormalization group approaches, to study systems with up to 4 levels (for spinless electrons; see below). We find that if the ratio of average level spacing δ to average level width Γ is decreased into the regime $\delta \lesssim \Gamma$, one of the renormalized effective single-particle levels generically becomes wider than all others, and hovers in the vicinity of the chemical potential μ in the regime of V_g for which the PLs occur. Upon varying V_g, the narrow levels cross μ and the broad level, leading to Fano-type antiresonances accompanied by universal PLs. For $\delta \gtrsim \Gamma$, $\alpha(V_g)$ behaves mesoscopically [15] for all U. Decreasing δ thus causes the PL behavior to generically change from mesoscopic to universal, as observed experimentally [3].

Model.—The dot part of our model Hamiltonian is

$$H_{\text{dot}} = \sum_{j=1}^{N} \varepsilon_j n_j + \frac{1}{2} U \sum_{j \neq j'} \left(n_j - \frac{1}{2}\right)\left(n_{j'} - \frac{1}{2}\right),$$

with $n_j = d_j^\dagger d_j$ and dot creation operators $d_j^\dagger$ for spinless electrons, where $U > 0$ describes Coulomb repulsion. The semi-infinite leads are modeled by a tight-binding chain $H_l = -t \sum_{m=0}^{\infty} (c_{m,l}^\dagger c_{m+1,l} + \text{H.c.})$ and the level-lead couplings by $H_T = -\sum_{j,l}(t_j^l c_{0,l}^\dagger d_j + \text{H.c.})$, where $c_{m,l}$ annihi-

lates an electron on site m of lead $l = L$, R and t_j^l are real level-lead hopping matrix elements. Their relative signs for successive levels, $s_j = \mathrm{sgn}(t_j^L t_j^R t_{j+1}^L t_{j+1}^R)$, are sample-dependent random variables determined by the parity of the dot's orbital wave functions. The effective width of level j is given by $\Gamma_j = \Gamma_j^L + \Gamma_j^R$, with $\Gamma_j^l = \pi\rho|t_j^l|^2$. We take ρ, the local density of states at the end of the leads, to be energy independent, choose $\mu = 0$, and specify our choices of t_j^l using the notation $\sigma = \{s_1, s_2, \ldots\}$, $\gamma = \{\Gamma_1^L, \Gamma_1^R, \Gamma_2^L, \ldots\}$, $\Gamma = \frac{1}{N}\sum_{j,l}\Gamma_j^l$.

Methods.—We focus on linear response transport and, unless stated otherwise, on zero temperature ($\tau = 0$). Then the dot produces purely elastic, potential scattering between left and right lead, characterized by the transmission matrix $T_{ll'} = 2\pi\rho\sum_{ij}t_i^l \mathcal{G}_{ij}^R(0)t_j^{l'}$, where $\mathcal{G}_{ij}^R(\omega)$ is the retarded local Green function which we compute using NRG and FRG. The NRG is a numerically exact method that is known to produce very accurate results [12,13]. The FRG is a renormalization procedure for the self-energy Σ and higher order vertex functions (see [14] for details). We use a truncation scheme that keeps the flow equations for Σ and for the frequency independent part of the effective two-particle (Coulomb) interaction. Comparisons with NRG [14] have shown this approximation to be reliable provided that the number of (almost) degenerate levels and the interaction do not become too large. FRG is much cheaper computationally than NRG, enabling us to efficiently explore the vast parameter space relevant for multilevel dots.

At the end of the FRG flow, the full Green function at zero frequency takes the form $[\mathcal{G}^R(0)]_{ij}^{-1} = -h_{ij} + i\Delta_{ij}$, with an effective, noninteracting (but V_g and U-dependent) single-particle Hamiltonian $h_{ij} = (\varepsilon_j^0 - V_g)\delta_{ij} + \Sigma_{ij}$, whose level widths are governed by $\Delta_{ij} = \pi\rho\sum_l t_i^l t_j^l$. To interpret our results, we adopt the eigenbasis of $[\mathcal{G}^R(0)]_{ij}^{-1}$, with eigenvalues $-\tilde{\varepsilon}_j + i\tilde{\Gamma}_j$, and view $\tilde{\varepsilon}_j$ and $\tilde{\Gamma}_j$ as level positions and widths of a renormalized effective model (REM) describing the system.

For left-right (LR) symmetry, $\Gamma_j^L = \Gamma_j^R$, an NRG shortcut can be used, which is much less demanding than computing the full $G_{ij}^R(\omega)$: the S matrix is then diagonal in the even-odd basis of the leads and its eigenvalues depend on the total occupancies $n_\pm$ of all levels coupled to the even (odd) lead (Friedel sum rule), so that the transmission amplitude $T = T_{LR}$ takes the form $T = \sin[\pi(n_+ - n_-)]e^{i\pi(n_+ + n_-)}$. A transmission zero (TZ) and hence PL occurs when $n_+ = n_-$ mod 1 [Figs. 1(b), 1(e), and 1(h): $n_\pm$ in thin dashed (dash-dotted) line].

Results.—Our results are illustrated in Figs. 1–3. FRG and NRG data generally coincide rather well (compare black and orange lines in Figs. 1 and 2), except for $N = 4$ when both $U \gg \Gamma$, $\delta < \Gamma$, and correlations become very strong [Fig. 2(f)]. The figures show the following striking qualitative features, that we found to be generic by running the FRG for tens of thousands of parameter sets, which is
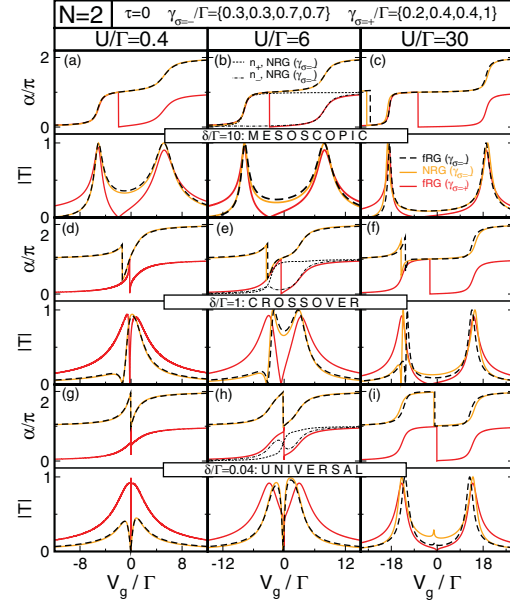
FIG. 1 (color). $|T(V_g)|$ and $\alpha(V_g)$ for $N = 2$, $\varepsilon_{2,1}^0 = \pm\delta/2$, and $\tau = 0$: decreasing δ/Γ produces a change from (a)–(c) mesoscopic via (d)–(f) crossover to (g)–(i) universal behavior; increasing U/Γ leads to increased transmission peak spacing. (b),(e),(h) Include the occupancies n_+ (thin dashed line) and n_- (thin dash-dotted line) of the levels coupled to the even (odd) lead in the case of LR symmetry. The condition $n_+ = n_-$ mod 1 produces a TZ and PL. For the blip and hidden TZ near $V_g = 0$ in (i), see [28].

possible as a complete $T(V_g)$ curve can be obtained within a few minutes on a standard PC.

Mesoscopic regime.—For $\delta \gtrsim \Gamma$ [Figs. 1(a)–1(c), 2(a)–2(c)], we recover behavior that is similar to the $U = 0$ case. Within the REM it can be understood as transport occurring through only one effective level at a time [see Figs. 3(a)–3(c)], with $\tilde{\Gamma}_j \simeq \Gamma_j$. Each $\tilde{\varepsilon}_j$ that crosses μ produces a Breit-Wigner–like transmission resonance of width $2\Gamma_j$ and height governed by Γ_j^L/Γ_j^R. At the crossing the other levels are shifted upward by U [charging effect; Fig. 3(a)] leading to renormalized peak separations ("level spacings") $\delta_j + U$. Between two peaks, $\alpha(V_g)$ behaves mesoscopically: depending on the sign s_j one either observes a PL ($s_j = +$) or continuous evolution of α ($s_j = -$) [15]. Additional PLs occur to the left or right, beyond the last transmission peak [Fig. 2(a)].

Mesoscopic to universal crossover.—As the ratio δ/Γ is reduced, the behavior changes dramatically: the TZs and PLs that used to be on the far outside move inward across CB resonances [see evolution in Figs. 1(b), 1(e), and 1(h)].

Universal regime.—A universal feature [16] emerges for $\delta \lesssim \Gamma \lesssim U$ (crossover scales are of order 1, but depend on the chosen parameters): for all choices of the signs σ and generic couplings γ, the N CB peaks over which α
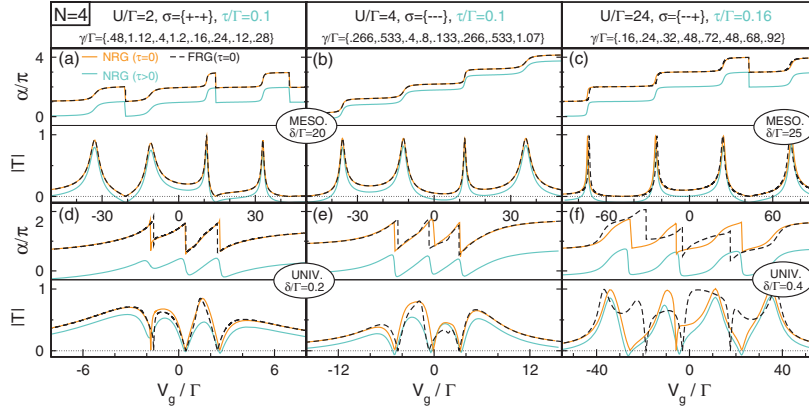
FIG. 2 (color). $|T(V_g)|$ and $\alpha(V_g)$ for $N = 4$, with equidistant levels, $\delta_j \equiv \delta$. The qualitative features do not change if this assumption is relaxed, or if U is assumed to be slightly level dependent, $U \to U_{jj'}$. Decreasing δ/Γ produces a crossover from (a)–(c) mesoscopic to (d)–(f) universal behavior; increasing U/Γ leads to increased spacing of the transmission peaks and PLs. For clarity the finite temperature ($\tau > 0$) curves were shifted downward (by 0.1 for $|T|$). (f) For $U/\Gamma \gg 1$ and $\tau/\Gamma = 0.16$, the CB peak and PL shapes are strikingly similar to those observed experimentally at comparable ratios of τ/Γ (see Fig. 3 of [2] and Fig. 6 of [3]). For small δ/Γ and $U/\Gamma \gg 1$ FRG becomes less reliable and the results begin to differ from those of NRG.

increases by π are separated by $N - 1$ PLs, each accompanied by a TZ [Figs. 1(g)–1(i), 2(d)–2(f)]. This is consistent with the experimentally observed trend. For small to intermediate values of U/Γ [Figs. 1(g) and 1(h), 2(d) and 2(e)], the transmission peaks are not well separated, and $\alpha(V_g)$ has a sawtooth shape. As U/Γ increases so does the peak separation and the corresponding phase rises take a more S-like form [Figs. 1(h) and 1(i), 2(e) and 2(f)]. At finite temperatures of order $\tau \gtrsim \delta$ [17] sharp features are smeared out (Fig. 2). For U/Γ as large as in Figs. 1(i) and 2(f), the behavior of $\alpha(V_g)$ (both the $S$-like rises and the universal occurrence of PLs in each valley) as well as the one of $|T(V_g)|$ (similar width and height of all CB peaks) is very reminiscent of that observed experimentally [Fig. 2(f)]. For $U/\Gamma \gg 1$ the full width of the CB peaks is of order $2N\Gamma$ (not $2\Gamma_j$ as in the mesoscopic regime), indicating that several bare single-particle levels simultaneously contribute to transport. The τ dependence of the width of the PLs is different from the behavior $\tau^2/(\delta + U)^2$ found in the mesoscopic regime [18] and will be discussed in an upcoming publication. Note that for the temperatures considered here the width of the PLs is still much smaller than the width of the CB peaks.

For certain fine-tuned parameters (γ and σ) the behavior at small δ/Γ deviates from the generic case. For $N = 2$ the nongeneric cases were classified in [9]. In Fig. 1 only generic parameters are shown. For $N \geq 3$ LR-symmetric couplings produce nongeneric features. However, these features are irrelevant to the experiments. They quickly disappear upon switching on LR asymmetry or $\tau > 0$.

Interpretation.—We can gain deeper insight into the appearance of the TZs and PLs in the universal regime from the properties of the REM obtained by FRG for moderate U/Γ [at which NRG and FRG agree well;

Figs. 2(b) and 2(e)]. For $N \geq 3$, $\delta \lesssim \Gamma$ and $U = 0$, two of the effective levels are much wider than the others, since Δ_{ij}, being a matrix of rank 2, has only two nonzero eigenvalues [19] (for the $N = 2$ case, see [16,18]). We found that this also holds at $U > 0$: for $N = 3, 4$ one effective level is typically a factor of 2 to 3 wider than the second widest, while the remaining 1 or 2 levels are very narrow [Fig. 3(f)]. At $\delta \lesssim \Gamma$ [Fig. 3(d)] the interaction leads to a highly nonmonotonic dependence of $\tilde{\varepsilon}_j$ on
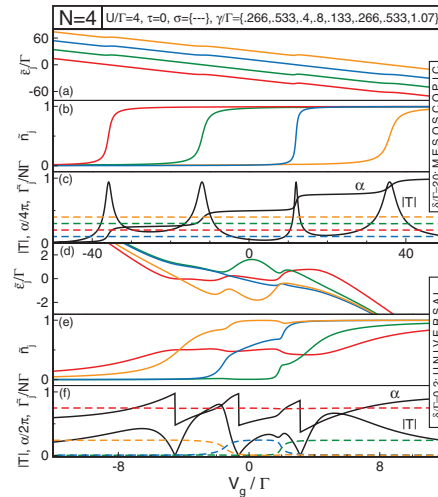

FIG. 3 (color). Renormalized single-particle energies $\tilde{\varepsilon}_j$, occupancies $\tilde{n}_j$, and level widths $\tilde{\Gamma}_j$ (dashed lines) of the REM, and the resulting $|T|$ and α (all as functions of V_g), for $N = 4$ and $\delta_j \equiv \delta$ at $\tau = 0$. The parameters are the same as in Figs. 2(b) and 2(e).

V_g which is essential for our universal PL scenario: As V_g is swept, the widest level hovers in the vicinity of μ over an extended range of V_g values, whereas the narrow ones cross μ—and therefore also the widest one—rather rapidly. This leads to a Fano-type effect [20–24] whose effective Fano parameter q is real, by time-reversal symmetry [21]. Thus, each TZ, and hence PL, can be understood as a Fano-type antiresonance arising (irrespective of the signs of t_i^l) from destructive interference between transmission through a wide and a narrow level. The crossings of the narrow levels and μ, and thus the PLs, are separated by U due to charging effects. In contrast, for $U = 0$, $\tilde{\varepsilon}_j \propto -V_g$ for all renormalized levels and no levels cross each other. Our FRG studies indicate that for the regime $\delta \lesssim \Gamma$, the Fano-antiresonance mechanism is generic for $U \gtrsim \Gamma$. We thus expect it to apply also for interactions $U \gg \Gamma$ for which FRG is no longer reliable.

The fact that the combination of a wide and several narrow levels leads to PLs was first emphasized in [8] (without reference to Fano physics). However, whereas in [8] a bare wide level was introduced as a model assumption (backed by numerical simulations for noninteracting dots of order 100 levels), in our case a renormalized wide level is generated for generic couplings if $\delta \lesssim \Gamma$. Also, whereas in [8] the wide level repeatedly empties into narrow ones as V_g is swept (because $\Gamma_{\text{wide}} \ll U$ was assumed), this strong occupation inversion [25] is not required in our scenario. In Fig. 3(e), e.g., the wide level remains roughly half-occupied for a large range of V_g, but TZs and PLs occur nevertheless. We thus view occupation inversion, if it occurs, as a side effect, instead of being the cause of PLs [26].

Conclusions.—The most striking feature of our results, based on exhaustive scans through parameter space for $N = 2, 3, 4$, is that for any given generic choice of couplings (γ and σ), the experimentally observed crossover [3] from mesoscopic to universal $\alpha(V_g)$ behavior can be achieved within our model by simply changing the ratio δ/Γ from $\gtrsim 1$ to $\lesssim 1$, provided that $U \gtrsim \Gamma$. The universal π PLs result from Fano-type antiresonances of effective, renormalized levels, which arise because interactions cause a broad level (occurring, if $\delta \lesssim \Gamma$, already for $U = 0$) to be repeatedly crossed by narrow levels. A quantitative description requires correlations to be treated accurately. We expect that the main features of this mechanism carry over to the case of spinful electrons, since for $\delta \lesssim \Gamma$ spin correlation physics (such as the Kondo effect) does not play a prominent role [27].

[1] Y. Yacoby *et al.*, Phys. Rev. Lett. **74**, 4047 (1995).

[2] R. Schuster *et al.*, Nature (London) **385**, 417 (1997).

[3] M. Avinun-Khalish *et al.*, Nature (London) **436**, 529 (2005).

[4] G. Hackenbroich, Phys. Rep. **343**, 463 (2001).

[5] Y. Gefen, in *Quantum Interferometry with Electrons: Outstanding Challenges*, edited by I. V. Lerner *et al.* (Kluwer, Dordrecht, 2002), p. 13.

[6] C. Bruder, R. Fazio, and H. Schoeller, Phys. Rev. Lett. **76**, 114 (1996).

[7] Y. Oreg and Y. Gefen, Phys. Rev. B **55**, 13726 (1997).

[8] P. G. Silvestrov and Y. Imry, Phys. Rev. Lett. **85**, 2565 (2000); Phys. Rev. B **65**, 035309 (2001).

[9] V. Meden and F. Marquardt, Phys. Rev. Lett. **96**, 146801 (2006).

[10] D. I. Golosov and Y. Gefen, Phys. Rev. B **74**, 205316 (2006).

[11] V. Kashcheyevs, A. Schiller, A. Aharony, and O. Entin-Wohlman, Phys. Rev. B **75**, 115313 (2007).

[12] H. R. Krishna-murthy, J. W. Wilkins, and K. G. Wilson, Phys. Rev. B **21**, 1003 (1980).

[13] A. Weichselbaum and J. von Delft, cond-mat/0607497.

[14] C. Karrasch, T. Enss, and V. Meden, Phys. Rev. B **73**, 235337 (2006).

[15] A. Silva, Y. Oreg, and Y. Gefen, Phys. Rev. B **66**, 195316 (2002); T.-S. Kim and S. Hershfield, *ibid.* **67**, 235330 (2003).

[16] For $\delta \lesssim \Gamma$, generic Γ_j^l and $N = 2$, the universal PL behavior (1 PL between the 2 CB peaks) already occurs at $U = 0$. For $N > 2$ and small U/Γ, universal behavior ($N - 1$ PL between N CB peaks) sets in only once U/Γ becomes large enough.

[17] For $\tau > 0$, we calculate $|T|e^{i\alpha} \equiv -\int d\varepsilon \partial_\varepsilon f(\varepsilon) T_{LR}^\tau(\varepsilon)$ [7,18], where the finite-temperature transmission matrix T^τ is obtained via the full density matrix NRG of [13].

[18] C. Karrasch *et al.*, cond-mat/0612490.

[19] R. Berkovits, F. von Oppen, and J. W. Kantelhardt, Europhys. Lett. **68**, 699 (2004). This paper shows that Coulomb blockade physics survives even in the limit $\delta < \Gamma$, in agreement with our findings.

[20] U. Fano, Phys. Rev. **124**, 1866 (1961).

[21] A. A. Clerk, X. Waintal, and P. W. Brouwer, Phys. Rev. Lett. **86**, 4636 (2001).

[22] O. Entin-Wohlman *et al.*, J. Low Temp. Phys. **126**, 1251 (2002).

[23] H. Aikawa *et al.*, J. Phys. Soc. Jpn. **73**, 3235 (2004).

[24] Y. Oreg (to be published).

[25] J. König and Y. Gefen, Phys. Rev. B **71**, 201308(R) (2005); M. Sindel, A. Silva, Y. Oreg, and J. von Delft, *ibid.* **72**, 125316 (2005).

[26] In a model with a weakly V_g-dependent, bare wide level and several narrow levels with $\delta > \Gamma$, Fano-like interference produces TZs and PLs even at $U = 0$, for which interaction-induced occupation inversions are absent [24].

[27] We have recently shown this explicitly for $N = 2$ [18].

[28] For $N = 2$, U larger than a critical value and in the limit $\delta \to 0$, two additional, sharp peaks appear on both sides of the TZ and exponentially close to it [peaks and TZ are visible only as a blip in Fig. 1(i), due to lack of resolution] [9]. Similar sharp features occur for $N > 2$; see Fig. 2(f). These features, which get smeared out with increasing temperature, are irrelevant for the PL puzzle.

4.2.1   Emergence of a broad level in the universal regime

In Sec. 4.2 we argue that the universal behaviour of the phase in the regime $\delta \ll \Gamma$ can be understood as a Fano-type antiresonance [74, 75, 76, 77] arising from destructive interference between transmission through a broad level hovering near the chemical potential and several narrow levels that successively cross the chemical potential (and the broad level) while the gate voltage is shifted. We shortly summarize the findings and provide supplementary data.

Contrary to [32, 61], we do *not* assume that one of the bare levels is much wider than the others. Actually, in the regime $\delta \ll \Gamma$, we find that this situation is realized automatically for the *renormalized* single-particle levels. Thereby the renormalized single-particle Hamiltonian $h_{ij} = (\varepsilon_{dj} - V_g)\delta_{ij} + \Sigma_{ij}$ with eigenvalues $-\tilde{\varepsilon}_j + i\tilde{\Gamma}$ can be obtained at the end of the fRG flow from the full Green's function at zero frequency,

$$\left[\mathcal{G}^R(0)\right]_{ij}^{-1} = -h_{ij} + i\Delta_{ij}, \tag{4.5}$$

where ε_{dj} are the bare level energies, Σ is the self-energy and $\Delta_{ij} = \sum_\beta \pi \rho t_j^\beta t_i^\beta$. For more detailed information, see [15] and "The fRG approach" in Sec. 4.3.

Extensive statistics of the renormalized level widths (starting from a Gaussian distribution for the relative bare level widths γ) show that one broad level emerges naturally once $\delta < \Gamma$, see Fig. 4.4. Interestingly, the renormalized level widths are essentially independent of U.
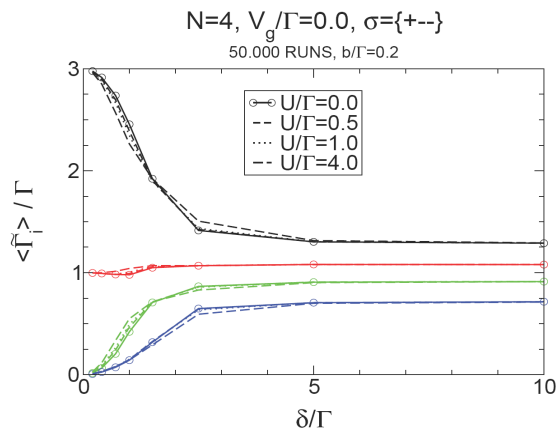
Figure 4.4: Statistics of renormalized level widths for a spinless four-level Anderson model at $V_g = 0$. The data is obtained with fRG. For $\delta < \Gamma$, one level is much wider than the others. Actually, due to the Dicke effect, two levels effectively decouple in the limit $\delta/\Gamma \to 0$. The level widths are essentially independent of U.

The emergence of effective sharp levels is due to the Dicke effect [78, 79], see [80]. For $\delta < \Gamma$, it is the second term that dominates the inverse of the Green's function given by Eq. (4.5). Therefore, the level widths are essentially the eigenvalues of Δ. Since the system has two independent reservoirs, this is a matrix of rank two - therefore possessing only two nonzero eigenvalues [80]. Thereby the larger dominates, see Fig. 4.4.

An (intuitive) picture is obtained when rearranging the tunnelling part of the Hamiltonian [Eq. (2.4d)],

$$H_{\text{imp}-\text{res}} = \sum_{\mathbf{k}\sigma} \left[c_{L\mathbf{k}\sigma}^\dagger \{\sum_{j=1}^{M} t_{jL} d_{j\sigma}\} + c_{R\mathbf{k}\sigma}^\dagger \{\sum_{j=1}^{M} t_{jR} d_{j\sigma}\} + \text{H.c.} \right]. \tag{4.6}$$

Therefore, there are *two* linear combination of dot levels that couple strongly to either the left or right lead (here in curly braces). Assuming that $\delta < \Gamma$, these two levels are close to the eigenlevels of the renormalized system.

4.2.2   Supplementary NRG data

We present some additional NRG data not included in the publication. They enlighten the crossover of mesoscopic to universal behaviour of the transmission phase of a four-level Anderson model with spinless electrons.

At $T \approx 0$, the crossover from mesoscopic to universal behaviour of the magnitude and phase of the transmission amplitude through a four-level quantum dot with spinless electrons is shown in Fig. 4.5. For the level spacing much larger than the coupling, $\delta/\Gamma \gg 1$ (a,b), the transmission amplitude shows mesoscopic behaviour, i.e. it depends on the relative sign σ. of the matrix elements of the successive levels, $\sigma = \text{sgn}(V_{iL} V_{iR} V_{i+1L} V_{i+1R})$: A phase lapse only occurs for $\sigma = +$. Decreasing δ/Γ, a crossover from mesoscopic to universal behaviour is observed: In one of the Coulomb blockade valleys, two additional phase lapses occur (c). One of them (indicated by an arrow) crosses the neighbouring Coulomb blockade peak for decreasing δ/Γ (d-f). Universal behaviour is reached for $\delta/\Gamma < 1$ (g). Then the properties of the system do not depend on the details of the parameters (like σ) any more; one phase lapse per Coulomb blockade valley always. For $\delta/\Gamma \ll 1$ (h) we find the correlation induced resonances (in accordance with [63]).

In the universal regime, finite temperature leads to universality not only of the phase (shown in Fig. 4.5 for $T \approx 0$) but also the magnitude of the transmission amplitude. The sharp features of the correlation induced resonances found for $\delta/\Gamma \ll 1$ smear and lead to the same structure than for moderate ratio δ/Γ. Fig. 4.6 compares the results of Fig. 4.5(g,h) for $T \approx 0$ to finite temperature calculations at $T/\Gamma \lesssim 1$. In the latter regime, the magnitude has a characteristic triangular form [4], therefore the transmission amplitude (phase *and* magnitude) capture the experimental trend qualitatively. Fig. 4.7 directly compares the NRG finite temperature curves. It is obvious that the universality of the curves not only holds w.r.t. the relative sign of the matrix elements σ, but also w.r.t. the ratio of level spacing to coupling strength as long as $\delta/\Gamma < 1$.
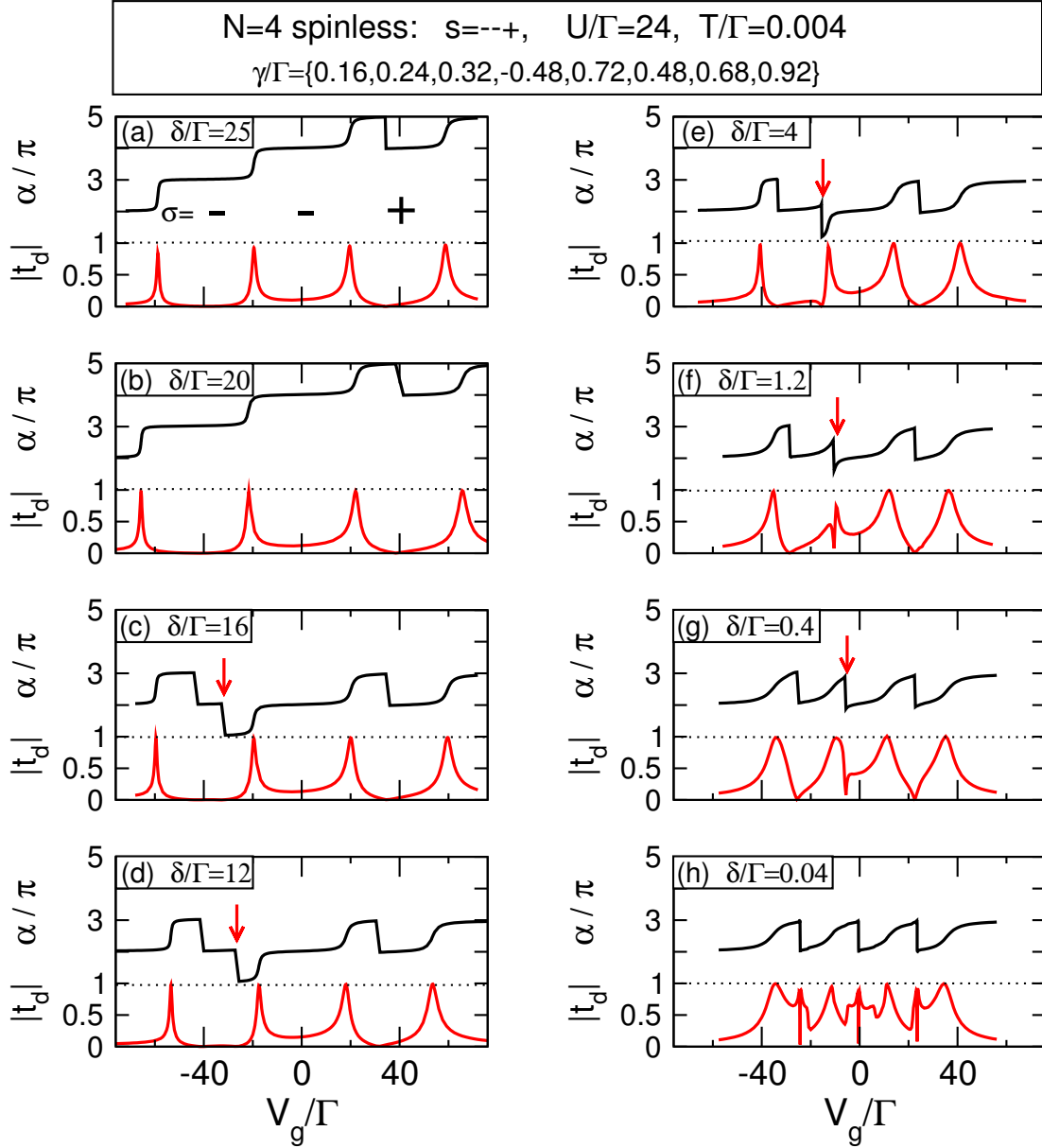
Figure 4.5: Crossover from mesoscopic to universal behaviour of magnitude and phase of the transmission amplitude t_d through a four-level quantum dot with spinless electrons. Parameters: $\sigma = --+$, $\Gamma = 0.2$, $U/\Gamma = 24$, $T/\Gamma = 0.04$ (corresponding to $T \approx 0$), $\Lambda = 2.2$ and $N_{\text{kept}} = 512$ for the first 6 iterations, then $N_{\text{kept}} = 256$. (a,b) Mesoscopic, $\delta/\Gamma \gg 1$: The phase depends on the relative sign σ of the matrix elements of the successive levels. In plot (a) σ is indicated; a phase lapse only occurs for $\sigma = +$. (c-f) Crossover: Decreasing δ/Γ, two additional phase lapses occur in one of the Coulomb blockade valleys. One of them (indicated by an arrow) crosses the neighbouring Coulomb blockade peak. (g) Universal: Therefore, for $\delta/\Gamma < 1$, the properties of the system do not depend on the details of the parameters (like σ) any more; each Coulomb blockade valley has its corresponding phase lapse. (h) For $\delta/\Gamma \ll 1$ we find correlation induced resonances (in accordance with [63]).
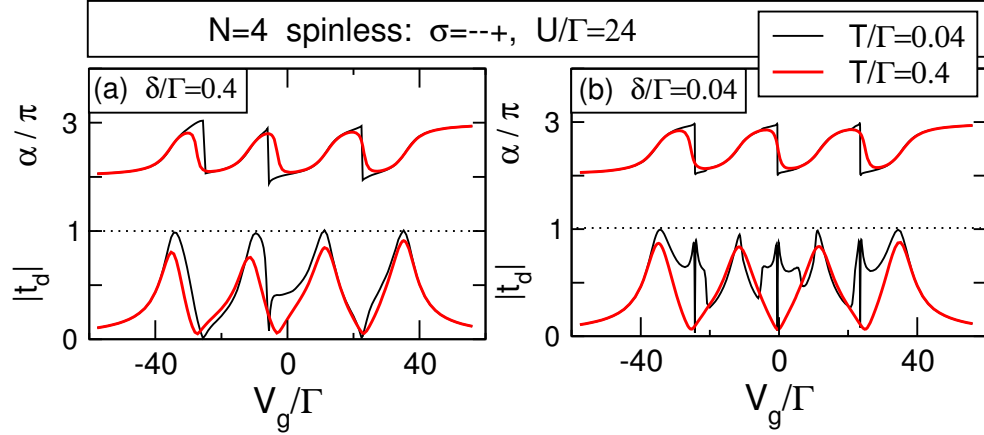
Figure 4.6: Universal regime: Comparison of zero and finite temperature ($T/\Gamma \lesssim 1$) results of the transmission amplitude through a spinless four-level quantum dot. Same parameters than Fig. 4.5(g,h). Sharp features in the magnitude of the transmission amplitude are smeared out at finite temperature; therefore also $|t_d|$ shows universal behaviour. (b) This even holds for the correlation induced resonances with its distinct structure.
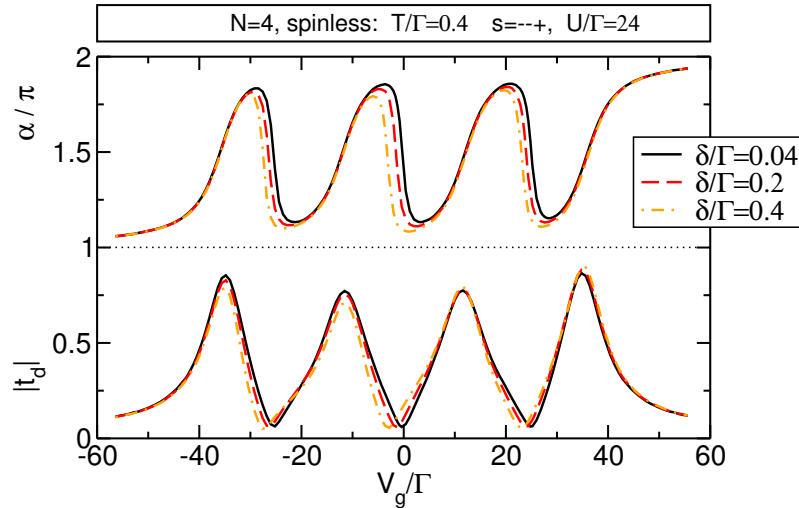
Figure 4.7: Universal regime, finite temperature: For $T/\Gamma \lesssim 1$, both magnitude *and* phase of the transmission amplitude show universal behaviour, independent not only of σ but also δ/Γ as long as $\delta/\Gamma < 1$. The magnitude is of triangular shape, therefore the experimental trend [4] is captured qualitatively.

4.3   Phase lapses in transmission through interacting two-level quantum dots

We study both spin-polarized as well as spin-degenerate two-level QDs in more detail. We therefore employ the NRG and fRG methods to a spinless and spinful two-level Anderson model, respectively. In accordance with the previous discussion, we find universal and mesoscopic behaviour, depending on the ratio of level distance to mean level width.

New Journal of Physics
The open—access journal for physics

Phase lapses in transmission through interacting two-level quantum dots

C Karrasch[1], T Hecht[2], A Weichselbaum[2], J von Delft[2], Y Oreg[3] and V Meden[1,4]

[1] Institut für Theoretische Physik, Universität Göttingen, 37077 Göttingen, Germany
[2] Physics Department, Arnold Sommerfeld Center for Theoretical Physics and Center for NanoScience, Ludwig-Maximilians-Universität, 80333 Munich, Germany
[3] Department of Condensed Matter Physics, The Weizmann Institute of Science, Rehovot 76100, Israel
E-mail: meden@theorie.physik.uni-goettingen.de

Abstract. We investigate the appearance of π lapses in the transmission phase θ of a two-level quantum dot with Coulomb interaction U. Using the numerical and functional renormalization group methods we study the entire parameter space for spin-polarized as well as spin-degenerate dots, modelled by spinless or spinful electrons, respectively. We investigate the effect of finite temperatures T. For small T and sufficiently small single-particle spacings δ of the dot levels we find π phase lapses between two transmission peaks in an overwhelming part of the parameter space of the level-lead couplings. For large δ the appearance or not of a phase lapse between resonances depends on the relative sign of the level-lead couplings in analogy to the $U = 0$ case. We show that this generic scenario is the same for spin-polarized and spin-degenerate dots. We emphasize that in contrast to dots with more levels, for a two-level dot with small δ and generic dot-lead couplings (that is up to cases with special symmetry) the 'universal' phase lapse behaviour is already established at $U = 0$. The most important effect of the Coulomb interaction is to increase the separation of the transmission resonances. The relation of the appearance of phase lapses to the inversion of the population of the dot levels is discussed. For the spin-polarized case and low temperatures we compare our results to recent mean-field studies. For small δ correlations are found to strongly alter the mean-field picture.

---

[4] Author to whom any correspondence should be addressed.

2   **IOP** Institute of Physics   Φ DEUTSCHE PHYSIKALISCHE GESELLSCHAFT

Contents

1. Introduction

The local Coulomb interaction $U > 0$ of electrons occupying quantum dots leads to a variety of effects. Many of them can conveniently be studied in transport through the dot within the linear regime. Theoretically as well as experimentally well-investigated examples are the Coulomb blockade (CB) peaks of the transmission (conductance) [1] as well as the plateaus of width U of the transmission (conductance) induced by the Kondo effect [2]. Additional features of interacting multi-level dots that have recently attracted considerable theoretical attention are the population inversions of the dot levels [3]–[6], the phase lapses of the transmission phase θ or, equivalently, the zeros of the transmission amplitude t (transmission zeros) [3], [7]–[12] and correlation-induced resonances of $|t|$ [13]. They appear in certain parts of the parameter space when the level occupancies and the transmission amplitude are investigated as functions of the level positions, which can be tuned via a nearby plunger gate voltage. Such effects were mostly studied in a minimal model involving only two levels. A very important step towards a unified understanding of population inversions, phase lapses and correlation-induced resonances in spin-polarized two-level dots was recently taken by a multi-stage mapping of the problem on a generalized Kondo model and a subsequent renormalization group and Bethe ansatz analysis of the effective Hamiltonian [14]–[16].

Theoretical studies of phase lapses (transmission zeros) are of primary interest in connection with a series of linear response transmission measurements by the Weizman group [17]–[19] on Aharonov–Bohm rings containing a quantum dot in one arm. Under suitable conditions both the phase θ and magnitude $|t|$ of the transmission amplitude $t = |t|e^{i\theta}$ of the dot can be extracted from the Aharonov–Bohm oscillations of the current through the ring [20]. When this is done as function of a plunger gate voltage V_g that linearly shifts the dot's single-particle energy levels downward, $\varepsilon_j = \varepsilon_j^0 - V_g$ ($j = 1, 2, \ldots$ is a level index), a series of well-separated CB peaks of rather similar width and height was observed in $|t(V_g)|$, across which $\theta(V_g)$ continuously increased by π, as expected for Breit–Wigner-like resonances. In each CB valley between any

two successive peaks, θ always jumped sharply downward by π. This phase lapse behaviour was found to be 'universal', occurring in a large succession of valleys for every *many*-electron dot studied in [17]–[19]. This universality is puzzling, since naively the behaviour of $\theta(V_g)$ is expected to be 'mesoscopic', i.e. to show a phase lapse in some CB valleys and none in others, depending on the dot's shape, the parity of its orbital wavefunctions, etc. Only recently [19], also the *few*-electron regime was probed experimentally: as V_g was increased to successively fill up the dot with electrons, starting from electron number $N_e = 0$, $\theta(V_g)$ was observed to behave mesoscopically in the *few*-electron regime, whereas the above-mentioned universal phase lapse behaviour emerged only in the *many*-electron regime ($N_e \gtrsim 15$).

It was suggested in [19] that a generic difference between the few- and many-electron dots may be that for the latter, transport might simultaneously occur through several partially filled single-particle levels in parallel. A possible reason could be that the mean (noninteracting) level spacing δ of the topmost filled levels decreases as the number of electrons increases, while the charging energy U still implies well-separated transmission resonances [21]. This scenario forms the basis of a recent systematic study by us of the interplay of level spacing, level width and charging energy on the phase lapses for up to four interacting levels and spin-polarized electrons [22]. We showed that the universal phase lapse and transmission zero behaviour appearing at small δ can be understood as resulting from a Fano-type interference effect [23] involving transport through two or more effective dot levels, whose positions and widths have been renormalized by the Coulomb interaction and coupling to the leads. The importance of several overlapping levels for phase lapses had earlier been pointed out by Silvestrov and Imry [3] in a rather specific model of a single wide and several narrow levels with strong interaction (see also [12]).

Here we supplement our earlier study [22] by discussing the relation between phase lapses and population inversions and by investigating the role of finite temperatures $T > 0$ as well as spin, focusing on $N = 2$ levels. When spin is included, the Kondo effect plays a role for an odd average occupation of the dot, but we will show that the phase lapse scenario is unaffected by this. Experimentally the behaviour of the phase in the presence of the Kondo effect was investigated in [24, 25]. As in [22] we are concerned with the *generic* behaviour and thus investigate the entire parameter space, going beyond subspaces of higher symmetry (such as left–right (l–r) or 1–2 symmetry of the couplings between the left and right leads and the two levels). For low temperatures and sufficiently small single-particle spacings δ of the dot levels, we find π phase lapses between two transmission peaks in an overwhelmingly large part of the parameter space of the level-lead couplings. We point out that the two level case is special compared to models with $N > 2$, as for generic level-lead couplings a transmission zero and phase lapse occurs between the two transmission peaks *even at $U = 0$*. The effect of the interaction is merely to increase the separation of the transmission peaks. For large δ the appearance or not of phase lapses between transmission peaks depends on the relative sign of the level-lead couplings in analogy to the noninteracting case [9].

For spin-polarized dots we in addition compare our $T = 0$ results with the ones of recent mean-field studies [10, 11]. In these works level-lead couplings beyond the subspaces with increased symmetry were studied, and a remarkably more complex behaviour was found once the symmetries were broken. The importance of considering such generic parameter sets was independently pointed out in [13]. We here elucidate how the phase lapse behaviour is affected by correlations, which are expected to be strong in low-dimensional systems. We find that upon including correlations, the part of the parameter space exhibiting universal π phase lapses between well-separated CB peaks becomes larger than suggested by the mean-field study. In particular,

we do not recover certain peculiar features of the mean-field results of [10, 11] namely the occurrence, in certain regimes of parameter space, of a phase lapse of less than π (instead of precisely π), accompanied by the disappearance of the corresponding transmission zero [6, 10]. These features thus turn out to be artefacts of the mean-field approximation, which misses the rather simple scenario for the phase lapse behaviour of a two-level dot at small δ: for generic level-lead couplings a phase lapse and transmission zero between two transmission peaks is already present at $U = 0$; increasing the Coulomb interaction the peaks become well-separated while the phase lapse and transmission zero remain in the valley between them.

In the model of a single wide and several narrow levels [3] a relation between phase lapses and population inversions was discussed. Therefore, in phase lapse studies quite often also the level occupancies n_j, $j = 1, 2$, are investigated. We emphasize that the generic appearance of a phase lapse and transmission zero even at $U = 0$ renders the two-level model unsuitable for establishing a general relation between phase lapses and population inversions, as the latter only appear at sufficiently large U. Furthermore, we show that discontinuities of the n_j as a function of V_g are an artefact of the mean-field solution (see [6, 10]). Within our approaches discontinuities are only found for l–r symmetric level-lead couplings with a relative plus sign of the underlying hopping matrix elements and degenerate levels, a case which was earlier identified as being nongeneric [13, 14], because the transmission shows only a single peak.

This paper is organized as follows. In section 2, we introduce our model for the spin-polarized and spin-degenerate two-level dot. We discuss the relation between the measured magnetic flux ϕ dependence of the interferometer's linear conductance and the magnitude and phase of the dot's transmission amplitude. The latter can be computed from the one-particle Green function of the dot. We present a brief account of our techniques to obtain the latter, the numerical renormalization group (NRG) [26] and functional renormalization group (fRG) methods. For an introduction to the use of the fRG to quantum dots see [27, 28]. We have implemented the full density matrix (FDM) NRG method of [29], which enables us to investigate dots with arbitrary level-lead state overlap matrix elements t_j^l (with $l = L, R$) as well as to study finite temperatures. In section 3–5 we present our results of the V_g dependence of $|t|$ and θ. First we briefly discuss the noninteracting two-level dot with generic level-lead couplings and point out that the phase lapse scenario differs from the one for more than two levels. We then investigate interacting, spin-polarized dots, study the relation between phase lapses and population inversions and compare to the mean-field results for the phase lapses. The issue of continuous versus discontinuous V_g dependence of the level occupancies n_1 and n_2 is commented on. Next we study the role of finite temperatures. Finally, we consider spin-degenerate levels at small T which implies the appearance of Kondo physics at odd average dot filling. Using NRG and fRG we show that the spin does not alter the universal phase lapse scenario. Our findings are summarized in section 6.

2. The model and methods

In this section, we introduce our model for the two-level dot. We argue that it is the energy dependent (effective) transmission amplitude $\tilde{t}(\omega)$ which one has to compute if one is interested in comparing to the measurements of [17]–[19] of the magnitude of the transmission amplitude and its phase. The amplitude $\tilde{t}(\omega)$ can be determined from the matrix elements of the dot's interacting one-particle Green function. We furthermore discuss aspects of the NRG and the fRG specific to our problem.

2.1. Two-level set-up and transmission amplitude

Our Hamiltonian consists of three parts

$$H = H_{\text{lead}} + H_{\text{dot}} + H_{\text{lead-dot}}. \tag{1}$$

The two semi-infinite leads are modelled as noninteracting one-dimensional tight-binding chains and for simplicity are assumed to be equal

$$H_{\text{lead}} = -\tau \sum_{l=L,R} \sum_{\sigma} \sum_{m=0}^{\infty} \left(c_{m,\sigma,l}^{\dagger} c_{m+1,\sigma,l} + \text{h.c.} \right). \tag{2}$$

The hopping strength in the leads is τ. We use standard second quantized notation with $l = L, R$ indicating the left and right leads, where the quantum numbers m and σ label Wannier states and spin, respectively. The dot is described by

$$H_{\text{dot}} = \sum_{\sigma} \sum_{j=1,2} \varepsilon_j d_{j,\sigma}^{\dagger} d_{j,\sigma} + \frac{1}{2} U \sum_{\sigma,\sigma'} \sum_{j,j'} \left(d_{j,\sigma}^{\dagger} d_{j,\sigma} - \tfrac{1}{2} \right) \left(d_{j',\sigma'}^{\dagger} d_{j',\sigma'} - \tfrac{1}{2} \right), \tag{3}$$

where the term with $j = j'$ and $\sigma = \sigma'$ is excluded from the sum in the interacting part. We define $\varepsilon_{1/2} = \mp \delta/2 - V_{\text{g}}$. In experimental systems the inter- and intra-level Coulomb repulsion can be expected to be comparable in size and to avoid a proliferation of parameters we assumed them to be equal. This assumption is not essential; by relaxing it we have checked that our results are robust against inter-level variations of the interaction strengths. Finally, the coupling between dot and lead states is given by

$$H_{\text{lead-dot}} = -\sum_{l=L,R} \sum_{\sigma} \sum_{j=1,2} \left(t_j^l c_{0,\sigma,l}^{\dagger} d_{j,\sigma} + \text{h.c.} \right) \tag{4}$$

with real overlap matrix elements t_j^l.

For simplicity, part of our studies will be performed on a model of spinless electrons, for which the spin index will be dropped. The resulting model may be regarded as a spin-polarized version of the spinful model obtained if the latter is put in a very large magnetic field.

The experimental two-path interferometer has the following structure (see figure 1(a) of [18]): an emitter and collector, are connected via two very narrow point contacts to a large, grounded base region between them. The layout of the base region has three important properties. (i) Electrons travelling from emitter to collector are guided by appropriately arranged gates through a ring-like structure in the base region, containing an upper and lower arm, the latter containing a quantum dot. (ii) The ring contains several additional wide exit channels (apart from collector and emitter) towards grounded leads; their presence strongly reduces the probability for an electron to traverse the upper or lower arm more than once along its journey from emitter to collector. Thus, multiple ring traversal trajectories can be assumed to make a negligible contribution to the measured conductance between collector and emitter. Moreover, in the resulting multi-terminal geometry, the transmission phase through the quantum dot is not fixed by Onsager relations (as it would be for a two-terminal device); instead, the phase evolves smoothly with system parameters such as gate voltage. (iii) Since all parts of the base regions are connected to ground, no voltage drops occur across the quantum dot, which thus is *in equilibrium with the Fermi seas* of the base regions to which it is connected on its right and left. Instead, voltage drops occur across the two point contacts between emitter and base region, and base region and collector, but these contacts are so narrow, and the conductance across them so small,

that the electrons traversing them do not drive the base region out of equilibrium. Thus, in this particular geometry, the emitter can be viewed as injecting electrons toward the base region (and quantum dot) at an energy set by the voltage difference between the two. The inelastic scattering length can be assumed to be longer than the total path length between emitter and collector, so that the Aharonov–Bohm interference signal is due solely to electrons reaching the collector with the same energy as that with which they were injected at the emitter. (Energy relaxation of these electrons can be assumed to occur only deep in the collector.) Moreover, we shall only be interested in the linear response regime, where the voltage drop across the emitter point contact is smaller than all other relevant energy scales.

Under these circumstances, the linear response conductance between source and drain is essentially given by the *equilibrium* transmission amplitude from emitter to collector, calculated at injection energy ω across the emitter point contact, and thermally averaged over all injection energies: $G_{\mathrm{EC}} = -\int_{-\infty}^{\infty} \mathrm{d}\omega f'(\omega)|t_{\mathrm{EC}}(\omega)|^2$, where f' is the derivative of the Fermi function. We may write $t_{\mathrm{EC}}(\omega) = t_{\mathrm{ref}}\mathrm{e}^{\mathrm{i}2\pi\phi/\phi_0} + t_{\mathrm{dot}}(\omega)$, where ϕ_0 is the flux quantum and $t_{\mathrm{ref}} = |t_{\mathrm{ref}}|\mathrm{e}^{\mathrm{i}\theta_{\mathrm{ref}}}$ and $t_{\mathrm{dot}} = |t_{\mathrm{dot}}|\mathrm{e}^{\mathrm{i}\theta_{\mathrm{dot}}}$ are the transmission amplitudes through the reference arm and the arm containing the dot, respectively. Thus, the flux-dependent part of G_{EC} takes the form [19, 20, 30]

$$G_{\mathrm{AB}} \propto -\int_{-\infty}^{\infty} \mathrm{d}\omega f'(\omega)|t_{\mathrm{dot}}(\omega)||t_{\mathrm{ref}}|\cos[2\pi\phi/\phi_0 + \theta_{\mathrm{ref}} + \theta_{\mathrm{dot}}(\omega)]. \tag{5}$$

The transmission t_{dot} is the product of the transmission $\tilde{t}$ through the dot and the transmission t_{rest} through the rest of the interferometer arm containing the dot. It is reasonable to assume that t_{rest} as well as t_{ref} are only weakly energy and gate voltage dependent and thus the V_{g}-dependence of the Aharonov–Bohm oscillations of the measured linear conductance of the interferometer is dominated by the V_{g} dependence of the magnitude and phase of the transmission amplitude through the dot. As usual [9], we compute the energy-averaged transmission phase θ and magnitude $|t|$ of the dot for a fixed spin direction as the phase and absolute value of

$$t(V_{\mathrm{g}}) = -\int_{-\infty}^{\infty} \mathrm{d}\omega f'(\omega)\tilde{t}(\omega), \tag{6}$$

where $\tilde{t}(\omega) = T_{LR}(\omega)$ is the LR-matrix element of the *equilibrium* transmission matrix of the dot, which gives the amplitude for an electron injected from the left towards the dot with energy ω and a given spin, to emerge with the same energy and spin on its right. In the limit $T \to 0, -f'$ reduces to a δ-function and $t(V_{\mathrm{g}})$ is equal to $\tilde{t}(\mu)$. We here take the chemical potential $\mu = 0$. Note that in contrast to the more common geometries where the voltage difference between emitter and collector causes voltages drops to arise across the quantum dot, so that the Meir–Wingreen formula [31] applies, so-called vertex contributions to the conductance are not needed in the present geometry.

Using scattering theory $\tilde{t}(\omega)$ (for fixed spin direction) can be related to the spin-independent matrix elements (in the $j = 1, 2$ indices of the Wannier states) of the dot's one-particle retarded Green function $\mathcal{G}$,

$$\tilde{t}(\omega) = 2\bigg(\sqrt{\Gamma_1^L\Gamma_1^R}\mathcal{G}_{1,1}(\omega + \mathrm{i}0) + \sqrt{\Gamma_2^L\Gamma_1^R}\mathcal{G}_{1,2}(\omega + \mathrm{i}0)$$

$$+s\sqrt{\Gamma_1^L\Gamma_2^R}\mathcal{G}_{2,1}(\omega + \mathrm{i}0) + s\sqrt{\Gamma_2^L\Gamma_2^R}\mathcal{G}_{2,2}(\omega + \mathrm{i}0)\bigg), \tag{7}$$

with (after taking the wide band limit; see below)

$$\Gamma_j^l = \pi |t_j^l|^2 \rho_{\text{lead}}(0) \geqslant 0, \tag{8}$$

where $\rho_{\text{lead}}(\omega)$ denotes the local density of states at the end of each semi-infinite lead. Without loss of generality we have assumed that $t_1^l \geqslant 0$, $t_2^L \geqslant 0$ and $t_2^R = s|t_2^R|$ with $s = \pm$. For later purposes we define $s = \text{sign}\,(t_1^L t_1^R t_2^L t_2^R)$ and $\gamma = \{\Gamma_1^L, \Gamma_1^R, \Gamma_2^L, \Gamma_2^R\}/\Gamma$. The spin-independent dot occupancies n_j (per spin direction), that we will also investigate, follow from the Green function $\mathcal{G}_{j,j}$ by integrating over frequency (or can be computed directly when using NRG). Here we will compute $\mathcal{G}$ in two ways, using both a truncated, that is approximate, fRG scheme, and a numerically exact method, the NRG. For l–r symmetry of the level-lead couplings the Friedel sum rule can be used and at temperature $T = 0$, $\tilde{t}(0)$ can also be expressed in terms of the spin independent occupancies [22]

$$\tilde{t}(0) = \sin\left([n_{\text{e}} - n_{\text{o}}]\pi\right) e^{i(n_{\text{e}} + n_{\text{o}})/\pi}, \tag{9}$$

where $n_{\text{e}} = n_1 + n_2$, $n_{\text{o}} = 0$ for $s = +$ and $n_{\text{e}} = n_1$, $n_{\text{o}} = n_2$ for $s = -$, respectively. A transmission zero occurs for gate voltages at which $n_{\text{e}} = n_{\text{o}} \bmod 1$. Assuming that $n_{\text{e}} - n_{\text{o}}$ is continuous close to these gate voltages at the same V_{g} a π phase lapse occurs.

2.2. The fRG approach

The truncated fRG is an approximation scheme to obtain the self-energy Σ (and thus the one-particle Green function) and higher order vertex functions for many-body problems [32]–[34]. As a first step in the application of this approach to quantum dots one integrates out the noninteracting leads within the functional integral representation of our many-body problem [35]. The leads provide a frequency dependent one-particle potential on the dot levels. On the imaginary frequency axis it is given by

$$V_{j,\sigma;j',\sigma'}^{\text{lead}}(i\omega) = \sum_l t_j^l t_{j'}^l g_{\text{lead}}(i\omega)\delta_{\sigma,\sigma'}, \tag{10}$$

where $g_{\text{lead}}(i\omega)$ denotes the spin-independent Green function of the isolated semi-infinite leads taken at the last lattice site

$$g_{\text{lead}}(i\omega) = \frac{i\omega + \mu}{2\,\tau^2}\left(1 - \sqrt{1 - \frac{4\,\tau^2}{(i\omega + \mu)^2}}\right). \tag{11}$$

As we are not interested in band effects we take the wide band limit. The potential then reduces to

$$V_{j,\sigma;j',\sigma'}^{\text{lead}}(i\omega) = -i\sum_l \sqrt{\Gamma_j^l \Gamma_{j'}^l}\,\text{sign}(\omega)\delta_{\sigma,\sigma'}. \tag{12}$$

After this step, instead of dealing with an infinite system we only have to consider the dot of two interacting levels.

In the computation of the interacting one-particle Green function projected on to the dot system the sum of the dot Hamiltonian with $U = 0$ and $V_{j,\sigma;j',\sigma'}^{\text{lead}}(i\omega)$ can be interpreted as a frequency dependent 'single-particle Hamiltonian' and in the following will be denoted by $h_0(i\omega)$.

For the spin-polarized case it is a 2×2 matrix in the quantum number $j = 1, 2$. Including spin, because of the additional quantum number $\sigma = \uparrow, \downarrow$, $h_0(i\omega)$ is a 4×4 matrix which is block-diagonal in σ (spin conservation). As we are here not interested in the role of a magnetic field lifting the spin-degeneracy of each level the $\sigma = \uparrow$ and $\sigma = \downarrow$ blocks are equivalent. The resolvent $\mathcal{G}_0(z) = [z - h_0(z)]^{-1}$ obtained from $h_0(z)$ is equivalent to the noninteracting propagator of our two-level many-body problem projected on the dot levels. In the generating functional of the one-particle irreducible vertex functions we replace $\mathcal{G}_0(i\omega)$ by

$$\mathcal{G}_0^\Lambda(i\omega) = \Theta(|\omega| - \Lambda)\mathcal{G}_0(i\omega) = \Theta(|\omega| - \Lambda)[i\omega - h_0(i\omega)]^{-1} \tag{13}$$

with Λ being an infrared cut-off running from ∞ down to 0. Taking the derivative with respect to Λ one can derive an exact, infinite hierarchy of coupled differential equations for vertex functions, such as the self-energy and the one-particle irreducible two-particle interaction. In particular, the flow of the self-energy Σ^Λ (one-particle vertex) is determined by Σ^Λ and the two-particle vertex W^Λ, while the flow of W^Λ is determined by Σ^Λ, W^Λ, and the flowing three-particle vertex. The latter could be computed from a flow equation involving the four-particle vertex, and so on. At the end of the fRG flow $\Sigma^{\Lambda=0}$ is the self-energy Σ of the original, cut-off-free problem we are interested in [32, 33] from which the Green function $\mathcal{G}$ can be computed using the Dyson equation. A detailed derivation of the fRG flow equations for a general quantum many-body problem that only requires a basic knowledge of the functional integral approach to many-particle physics [35] and the application of the method for a simple toy problem is presented in [34]. For an overview of the application to quantum dots see [27, 28].

We here truncate the infinite hierarchy of flow equations by only keeping the self-energy and the frequency-independent part of the two-particle vertex. Higher order terms can be neglected if the bare two-particle interaction is not too large. By comparison to NRG data this approximation scheme was earlier shown to provide excellent results for a variety of dot systems [13, 22, 27]. For further comparison see figure 7 below. The present scheme leads to a frequency-independent self-energy (see below). As finite frequency effects (inelastic processes) become important at temperatures $T > 0$, but these are not accurately treated by the level of approximation used here, in the present paper we shall show fRG results only for $T = 0$. It would be possible to extend our results to $T > 0$ by using a fRG truncation scheme in which the frequency dependence of the two-particle vertex is kept. Such a scheme was used in [33] to study the one-particle properties of the single-impurity Anderson model. The truncation leads to the coupled differential flow equations

$$\frac{\partial}{\partial \Lambda} \Sigma_{k',k}^\Lambda = -\frac{1}{2\pi} \sum_{\omega = \pm\Lambda} \sum_{l,l'} e^{i\omega 0^+} \mathcal{G}_{l,l'}^\Lambda(i\omega) W_{k',l';k,l}^\Lambda \tag{14}$$

and

$$\frac{\partial}{\partial \Lambda} W_{k',l';k,l}^\Lambda = \frac{1}{2\pi} \sum_{\omega = \pm\Lambda} \sum_{m,m'} \sum_{n,n'} \left\{ \tfrac{1}{2} \mathcal{G}_{m,m'}^\Lambda(i\omega) \mathcal{G}_{n,n'}^\Lambda(-i\omega) W_{k',l';m,n}^\Lambda W_{m',n';k,l}^\Lambda \right.$$
$$\left. + \mathcal{G}_{m,m'}^\Lambda(i\omega) \mathcal{G}_{n,n'}^\Lambda(i\omega) \left[- W_{k',n';k,l}^\Lambda W_{m',l';n,l}^\Lambda + W_{l',n';k,m}^\Lambda W_{m',k';n,l}^\Lambda \right] \right\}, \tag{15}$$

where k, l, etc. are multi-indices representing the quantum numbers j, σ and

$$\mathcal{G}^\Lambda(i\omega) = [\mathcal{G}_0^{-1}(i\omega) - \Sigma^\Lambda]^{-1}. \tag{16}$$

In the model with spin-degenerate levels each index k, l etc. can take four different values $j = 1, 2$ and $\sigma = \uparrow, \downarrow$ which gives 16 equations for Σ^Λ and 256 for the two-particle vertex. For a spin-polarized two-level dot the multi-indices take two values and one obtains 4 equations for Σ^Λ and 16 for the two-particle vertex. The number of independent equations can be significantly reduced (see below) taking into account the antisymmetry of the two-particle vertex and the spin symmetry (for spin-degenerate levels) both being preserved by equations (14) and (15). The initial conditions at $\Lambda = \Lambda_0 \to \infty$ are given by $\Sigma_{1,1'}^{\Lambda_0} = 0$ while $W_{1',2';1,2}^{\Lambda_0}$ is given by the bare antisymmetrized two-body interaction. In the spin-polarized case the only nonzero components of the two-particle vertex at $\Lambda = \Lambda_0 \to \infty$ are

$$W_{1,2;1,2}^{\Lambda_0} = W_{2,1;2,1}^{\Lambda_0} = U \quad \text{and} \quad W_{1,2;2,1}^{\Lambda_0} = W_{2,1;1,2}^{\Lambda_0} = -U. \tag{17}$$

In the model including spin the initial conditions take the form

$$W_{1\uparrow,1\downarrow;1\uparrow,1\downarrow}^{\Lambda_0} = U, \quad W_{1\uparrow,2\uparrow;1\uparrow,2\uparrow}^{\Lambda_0} = U, \quad W_{1\uparrow,2\downarrow;1\uparrow,2\downarrow}^{\Lambda_0} = U,$$
$$W_{2\uparrow,2\downarrow;2\uparrow,2\downarrow}^{\Lambda_0} = U, \quad W_{1\downarrow,2\downarrow;1\downarrow,2\downarrow}^{\Lambda_0} = U, \quad W_{1\downarrow,2\uparrow;1\downarrow,2\uparrow}^{\Lambda_0} = U. \tag{18}$$

All other components which do not arise out of these by permutations ($W_{1,2;1',2'}^{\Lambda_0} = W_{1',2';1,2}^{\Lambda_0}$ and $W_{1,2;1',2'}^{\Lambda_0} = -W_{1,2;2',1'}^{\Lambda_0}$) are zero. The self-energy matrix and thus the one-particle Green function is completely independent of the spin direction and in the following we suppress the spin indices.

As already mentioned the present approximation leads to a frequency-independent self-energy. This allows for a simple single-particle interpretation of its matrix elements. The sum of the $\Sigma_{j,j}^\Lambda$ and the bare level position correspond to the flowing effective level positions, $\varepsilon_j^\Lambda = \varepsilon_j + \Sigma_{j,j}^\Lambda$, while $t^\Lambda = -\Sigma_{1,2}^\Lambda = -\Sigma_{2,1}^\Lambda$ is a hopping between the levels 1 and 2 generated in the fRG flow. The fRG formalism then reduces to a set of coupled differential flow equations for $\varepsilon_j^\Lambda, t^\Lambda$ and a few (one in the spin-polarized case and seven for spin-degenerate levels) independent components of the two-particle vertex. These flow equations can easily be integrated numerically using standard routines. It is important to note that although we start out with intra- and inter-level Coulomb interactions of equal strengths they generically become different during the fRG flow (because of the different Γ_j^l). Furthermore, additional interaction terms which are initially zero will be generated in the flow. The set of equations significantly simplifies if the flow of the vertex is neglected while the results remain qualitatively the same. Within this additional approximation and for a spin-polarized dot the flow equations for ε_j^Λ and t^Λ are explicitly given in [13]. In certain limiting cases it is even possible to analytically solve the differential equations [13, 27]. However, in the present work, the flow of the vertex is retained which clearly improves the quality of the approximation [27].

At the end of the fRG flow, the full Green function takes the form $[\mathcal{G}(i\omega)]_{j,j'}^{-1} = i\omega\delta_{j,j'} - h_{j,j'}(i\omega)$ with an effective, *noninteracting* (but V_g-, U- and ω-dependent) 'Hamiltonian'

$$h_{j,j'}(i\omega) = h_{0;j,j'}(i\omega) - \Sigma_{j,j'} . \tag{19}$$

In a last step we have to perform the analytic continuation to the real frequency axis $i\omega \to \omega + i0$. This is straightforward, as the only frequency dependence of $h(i\omega)$ is the trivial one of the lead contribution equation (12). Then $\tilde{t}(\omega)$ can be computed using equation (7).

2.3. The NRG approach

The NRG was invented by K G Wilson in 1974 as a nonperturbative renormalization scheme for the Kondo model [36]. It was later extended to the fermionic [26, 37] Anderson model

which describes a localized electronic state coupled to a fermionic bath. The NRG allows thermodynamic and dynamic properties of such strongly correlated systems to be calculated at zero and finite temperature [29], [38]–[42].

The key idea of NRG is to discretize the conduction band of the bath logarithmically, leading to a tight-binding chain for which the hopping matrix elements between the successive sites fall off exponentially with $\Lambda_{\text{NRG}}^{-n/2}$, where $\Lambda_{\text{NRG}} > 1$ is the discretization parameter, typically $1 < \Lambda_{\text{NRG}} < 3$, and n is the site index. This energy scale separation ensures that the problem can be solved iteratively by adding one site at a time and diagonalizing the enlarged system at each step, thereby resolving successively smaller and smaller energy scales. Thus, by choosing the length N of the chain so large that the corresponding energy scale $\sim \Lambda_{\text{NRG}}^{-N/2}$ is smaller than all other energies in the problem, all relevant energy scales can be resolved and treated properly. Since the dimension of the Hilbert space of the chain increases exponentially with the length of the chain, a truncation scheme has to be adopted, according to which only the lowest N_{kept} eigenstates of the chain are retained at each iteration. Recently, it was shown that by also keeping track of discarded states a complete, but approximate, basis of states can be constructed [43]. This can be used to calculate spectral functions which rigorously satisfy relevant sum rules [29].

In order to obtain the transmission through the dot $\tilde{t}(\omega)$ equation (7) we follow [29, 39] to compute the imaginary part of the local Green functions at temperature T, using the Lehmann representation

$$
\begin{aligned}
\text{Im}\,\mathcal{G}_{j,j'}(\omega) = &-\pi \frac{\mathrm{e}^{-\omega_n/T}}{Z} \sum_{n,m} \langle n|d_{j,\sigma}|m\rangle \langle m|d_{j',\sigma}^\dagger|n\rangle \delta(\omega - [\omega_m - \omega_n]) \\
&-\pi \frac{\mathrm{e}^{-\omega_n/T}}{Z} \sum_{n,m} \langle n|d_{j',\sigma}^\dagger|m\rangle \langle m|d_{j,\sigma}|n\rangle \delta(\omega + [\omega_m - \omega_n]),
\end{aligned}
\tag{20}
$$

with $Z = \sum_n \mathrm{e}^{-\omega_n/T}$, the many-body eigenstates $|n\rangle$ and eigenenergies ω_n. Since these are causal functions, the real part can be accessed by performing a Kramers–Kronig transformation [44]. Using this method we obtain numerically exact results for the local Green function.

In the next three sections we present our results. In section 3 for the $U = 0$ case. In section 4 we present the generic phase lapse scenario for interacting spin-polarized dots, compare to the mean-field results and investigate the role of finite temperatures. Finally, in section 5 we study the spinful two-level dot.

3. Results: noninteracting dots

The large number of parameters makes it essential to analyse the transmission for the noninteracting case before considering the effect of two-particle interactions. We focus on $T = 0$. A closed expression for $|t(V_\mathrm{g})|$ and $\theta(V_\mathrm{g})$ (for a fixed spin direction) at $U = 0$ can be obtained from equations (6) and (7) by replacing $\mathcal{G}(0 + \mathrm{i}0)$ by $\mathcal{G}_0(0 + \mathrm{i}0)$,

$$
|t(V_\mathrm{g})| = \frac{2\left[\Gamma_1^L \Gamma_1^R \varepsilon_2^2 + \Gamma_2^L \Gamma_2^R \varepsilon_1^2 + 2s\sqrt{\Gamma_1^L \Gamma_1^R \Gamma_2^L \Gamma_2^R}\,\varepsilon_1 \varepsilon_2\right]^{1/2}}{\left[\left(\Gamma_1^L \Gamma_2^R + \Gamma_2^L \Gamma_1^R - 2s\sqrt{\Gamma_1^L \Gamma_1^R \Gamma_2^L \Gamma_2^R} - \varepsilon_1 \varepsilon_2\right)^2 + (\varepsilon_1 \Gamma_2 + \varepsilon_2 \Gamma_1)^2\right]^{1/2}},
\tag{21}
$$

IOP Institute of Physics $\quad \Phi$ DEUTSCHE PHYSIKALISCHE GESELLSCHAFT

$$\theta(V_{\mathrm{g}}) = \arctan \left[\frac{\varepsilon_1 \Gamma_2 + \varepsilon_2 \Gamma_1}{\varepsilon_1 \varepsilon_2 - \left(\sqrt{\Gamma_1^L \Gamma_2^R} - s \sqrt{\Gamma_1^R \Gamma_2^L} \right)^2} \right] \mod \pi, \tag{22}$$

with $\Gamma_j = \sum_l \Gamma_j^l$. For a fixed set of Γ_j^l the δ dependence of $|t(V_{\mathrm{g}})|$ and $\theta(V_{\mathrm{g}})$ is shown in the first columns of figures 1 and 2 for $U/\Gamma = 0.2$. The results are qualitatively the same as those obtained for $U = 0$. For generic level–lead couplings Γ_j^l the gate voltage dependence of equation (21) in the limit of small and large δ/Γ is dominated by two peaks (of height $\leqslant 1$) and a transmission zero. Associated with the transmission zero is a π phase lapse at the same gate voltage. The transmission zero (and phase lapse) follows from perfect destructive interference at a particular V_{g}. For a strong asymmetry in the couplings of the two levels to the leads, $\Gamma_1 \ll \Gamma_2$ or vice versa, this can be understood as follows: in this limit transport is simultaneous through a broad and a narrow level which for small δ are almost degenerate. This is the typical situation for the appearance of a Fano anti-resonance [23]. In the present set-up the Fano parameter q is real (due to time-reversal symmetry); this guarantees that, upon sweeping the gate voltage, the transmission amplitude must cross zero at some point or other, at which a phase lapse thus occurs. (In [22], we show that a similar mechanism of phase lapses due to Fano anti-resonances occurs in dots with more than two levels.) The Fano anti-resonance with vanishing transmission is robust if one goes away from this limit towards more symmetric level–lead couplings. Across each of the transmission resonances θ increases roughly by π as expected for a Breit–Wigner resonance. Further details of $|t(V_{\mathrm{g}})|$ and $\theta(V_{\mathrm{g}})$ depend on s. For $s = +$ the transmission zero (and phase lapse) is located between the two conductance peaks for all δ. For $\delta \to 0$ the resonance peak positions depend on the asymmetry of the Γ_j^l and the separation of the peaks is small if the Γ_j^l are close to l–r symmetry, that is close to $\Gamma_j^L = \Gamma_j^R$. For l–r symmetric dots and $\delta = 0$ the transmission zero (and phase lapse) disappears (not shown in the figures). This is an example of a submanifold in parameter space with nongeneric behaviour. A complete account of such cases (which also remain nongeneric for $U > 0$) is given in [13, 14]. As they require fine tuning these parameter sets are presumably irrelevant in connection with the experiments and we will here only briefly mention results obtained in such cases.

For $s = -$ and fixed Γ_j^l the position of the transmission zeros and phase lapses with respect to the CB peaks is different for small or large δ/Γ (see figure 2). At small δ/Γ it is located between the two conductance peaks, whereas for large δ/Γ it lies on one of the outer sides of these peaks [9]. In the crossover regime between these limiting cases the height of one of the peaks decreases, while the other becomes broader and splits up into two resonances separated by a minimum with nonvanishing conductance (see figures 2(g) and (j)). The crossover scale δ_{c} depends on the choice of Γ_j^l. For large δ/Γ, $|t|$ has three local maxima, although the height of one of the maxima is significantly smaller than the height of the other two (not shown in figure 2). For fixed, asymmetric Γ_j^l and $\delta \to 0$ the separation of the two conductance peaks for $s = -$ is significantly larger than for $s = +$ (compare figures 1(a) and 2(a)).

It is important to note that for small δ/Γ essential features of the universal phase lapse regime established in the experiments are already found at $U = 0$: regardless of the sign s for generic Γ_j^l (that is with the exception of a few cases with increased symmetry) two transmission resonances are separated by a transmission zero and π phase lapse. At $U = 0$ the peak separation is too small and the shape of the V_{g} dependence of the transmission and phase close to the
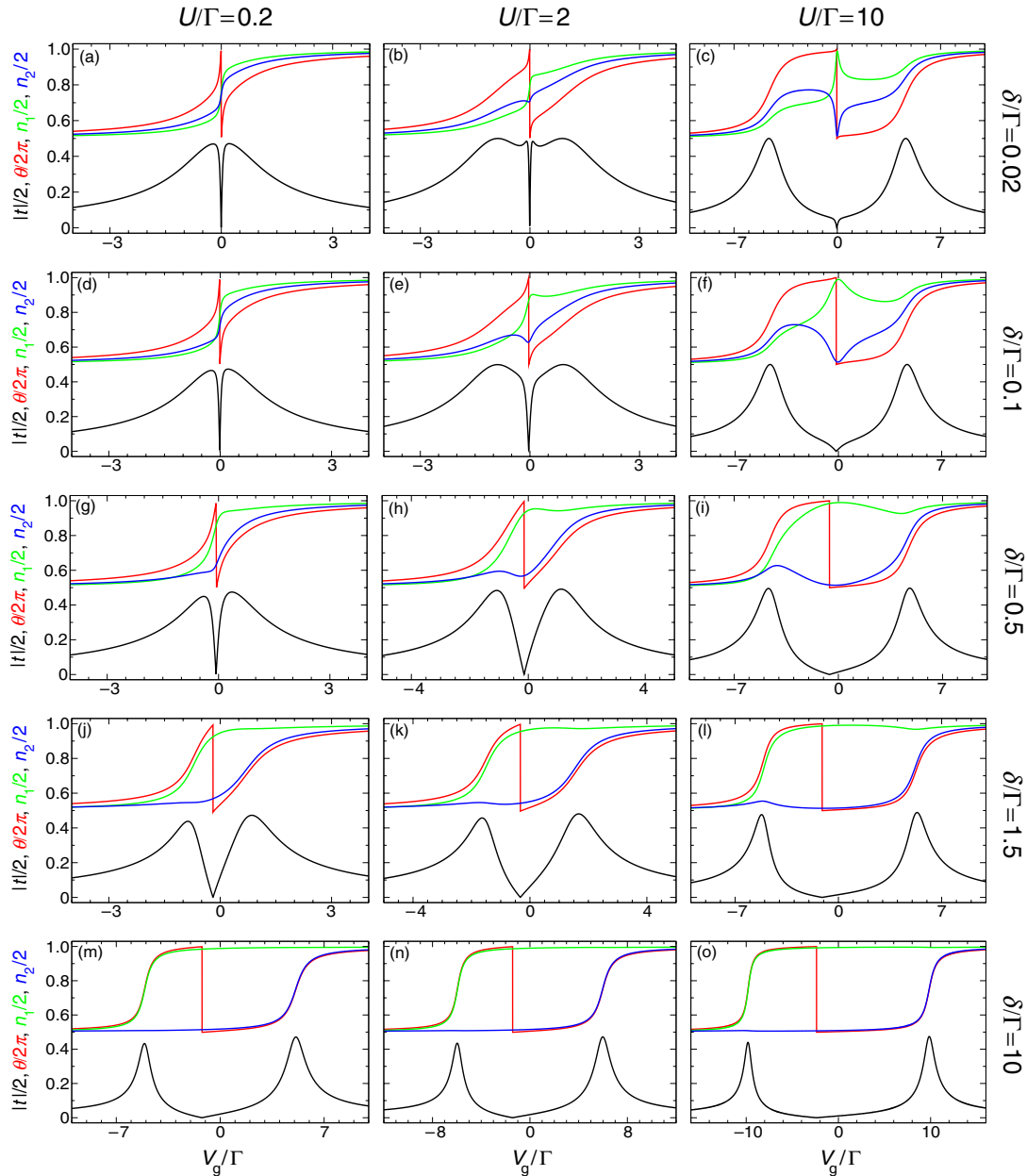
Figure 1. Systematic account of the energy scales U/Γ and δ/Γ that govern the gate voltage V_g dependence of the magnitude of the transmission $|t|$ (black), the transmission phase θ (red) and the level occupancies (green and blue) of a spin-polarized two-level dot at $T = 0$. The parameters are $\gamma = \{0.1, 0.3, 0.4, 0.2\}$ and $s = +$. For better visibility $n_{1/2}$ were shifted by 1. The depicted behaviour is the generic one and in particular qualitatively independent of the actual choice of γ (up to certain cases of increased symmetry; for examples see the text). The behaviour at $U/\Gamma = 0.2$ is qualitatively the same as the one at $U = 0$. The results were obtained using the truncated fRG.
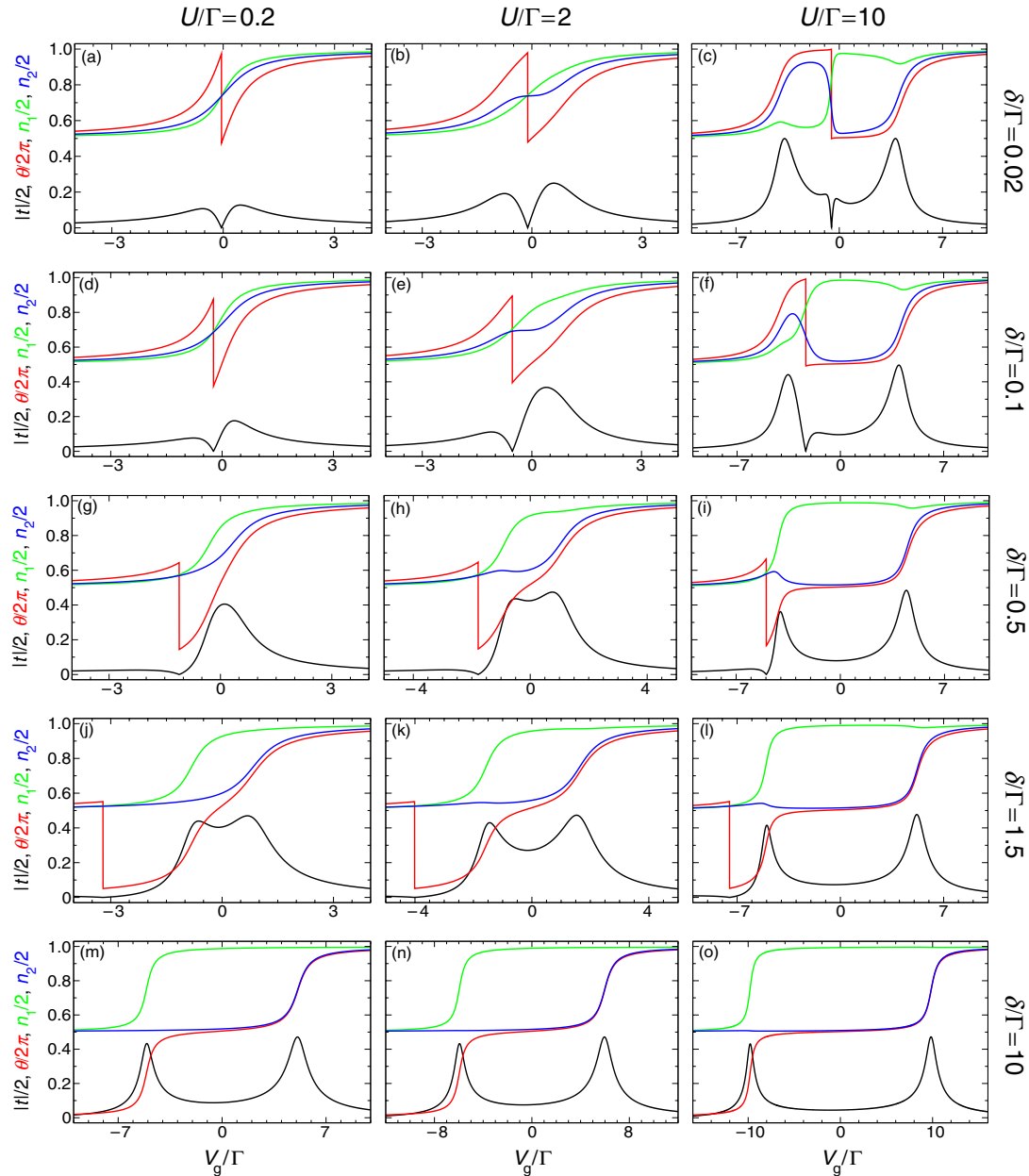
Figure 2. The same as in figure 1, but for $s = -$.

peaks is qualitatively different from those observed experimentally (namely Lorentzian-like for the magnitude of the transmission, S-shaped for the phase). As we show next the latter problems do not arise for sufficiently large interaction U, which in particular leads to an increased separation $U + \delta$ of the transmission peaks.

4. Results: spin-polarized dots

4.1. The generic phase lapse scenario

In [22] it was shown that fRG and NRG results for $|t(V_g)|$ and $\theta(V_g)$ agree quantitatively up to fairly large U. For a generic set of couplings γ we present fRG data for $\theta(V_g)$ and $|t(V_g)|$ together with the occupancies of the levels n_j for different U and δ in figures 1 ($s = +$) and 2 ($s = -$). Increasing U/Γ the separation of the transmission peaks in the limit of small and large δ/Γ increases and is eventually given by $U + \delta$. Even though this charging effect appears to be straightforward it is important to note that in particular the groundstate at small δ/Γ is highly correlated. This becomes explicit from the mapping of the present problem on a generalized single impurity Anderson and Kondo model as discussed in [14]–[16]. An indication of strong correlation effects are the correlation-induced resonances of the transmission found in [13], which we briefly mention below. With increasing U, even at small δ/Γ the gate voltage dependence of $\theta(V_g)$ across the transmission resonances becomes S-shaped and the resonances more Lorentzian-like (see third columns of figures 1 and 2). Obviously, for $s = +$ the transmission zero and phase lapse remain between the two transmission peaks for all δ and U (see figure 1). For $s = -$ this only holds for sufficiently small level spacings as, similar to the $U = 0$ case, with increasing δ/Γ a crossover sets into a regime in which the transmission zero and phase lapse are no longer between the peaks. Analogously to the $U = 0$ case, the crossover scale δ_c depends on the particular choice of Γ_j^l. As can be seen from the second row of figure 2 (the CB peaks at large U have still almost equal height), with increasing U/Γ, δ_c is pushed towards larger values. The Coulomb interaction thus stabilizes the parameter regime of universal phase lapses. This shows that the effect of the Coulomb interaction leading to universal π phase lapses between separated CB peaks in a two-level dot is rather straightforward: for small δ/Γ the phase lapse and transmission zero are already present at $U = 0$, and the effect of finite U is simply that the CB peaks become well-separated because of charging effects. They also lead to a Lorentzian-like lineshape of the peaks and an S-like variation of θ across them. The present scenario has to be contrasted to the one obtained for $N > 2$ levels discussed in [22]. The generic appearance of $N - 1$ transmission zeros and phase lapses separating the transmission peaks at small δ/Γ and $U = 0$ is specific to the case with $N = 2$ levels. For $N > 2$ the number of transmission zeros and phase lapses at $U = 0$ strongly depends on the parameters and the mechanism leading to universal π phase lapses at sufficiently large U (at small δ/Γ) is much more involved [22]. This shows that although important insights can be gained from studying two-levels, to achieve a *complete* understanding of the phase lapse scenario it is essential to study dots with Coulomb interaction and more than two levels [22].

The lineshape of $|t|$ shows characteristic differences in the limits of small and large δ/Γ. In the universal regime at small δ/Γ and for sufficiently large U/Γ the two CB peaks have equal width of order Γ (not Γ_j) and equal height which is consistent with the expectation that at each peak the transport occurs through both bare levels simultaneously. A similar behaviour is observed in the experiments. In the mesoscopic regime ($\delta/\Gamma \gg 1$) the width of the jth peak is given by Γ_j and the relative height h_j governed by Γ_j^L/Γ_j^R, independent of the value of U. This effectively noninteracting lineshape can be understood from the gate voltage dependence of the effective level positions $\varepsilon_j^{\Lambda=0}$ at the end of the fRG flow. When one level is charged the effective level position of the other level is pushed downwards by U. Besides this, the gate voltage dependence of the $\varepsilon_j^{\Lambda=0}$ remains linear, leading to two transmission peaks at gate voltages $\varepsilon_j^{\Lambda=0}(V_g) = 0$ with

IOP Institute of Physics $\bigoplus$ DEUTSCHE PHYSIKALISCHE GESELLSCHAFT

separation $U + \delta$, but with the same width and height as for $U = 0$. The hopping between the two effective levels generated in the fRG flow is small and can be neglected.

Apart from the CB peaks, for sufficiently large U/Γ the transmission shows additional features at small V_g/Γ (see figures 1(b), (c), (e) and 2(c)). These are the correlation-induced resonances mentioned in the Introduction section, which have been found to be most pronounced at $\delta = 0$ and in this case occur for interactions larger than a critical U_c which depends on the Γ_j^l and s [13, 14]. Their appearance indicates that the groundstate at small δ/Γ is strongly correlated (as mentioned in [13] the correlation-induced resonances are not captured by a mean-field analysis; see below). Associated with the correlation-induced resonances is a sharp increase of θ (see figures 1(b) and (e)). At large U/Γ the correlation-induced resonances are exponentially (in U/Γ) sharp features that vanish quickly with increasing T (see below), which might be one of the reasons why up to now they have not been observed in experiments. The correlation-induced resonances are not directly linked to the universal phase lapse scenario.

For increasing U/Γ at fixed δ/Γ and decreasing δ/Γ at fixed U/Γ we observe an increased tendency towards population inversion of the n_j. We define that a population inversion occurs if (i) $n_1(V_g^{PI}) = n_2(V_g^{PI})$ at a certain V_g^{PI} and (ii) one n_j has positive and one negative slope at V_g^{PI} so that the filling of one level causes a tendency for the other to empty. For large U/Γ and small δ/Γ it is mainly the more strongly coupled level (in figures 1 and 2, this is the level 2 shown in blue) whose population increases across both CB peaks while it is depopulated in between. This behaviour is reminiscent of the one discussed in the model with a broad and several narrow levels [3], where a relation between population inversion and phase lapse behaviour was proposed. Remarkably, for sufficiently large U/Γ, we find population inversion even for small asymmetries Γ_2/Γ_1 (which is only 1.5 in the example of figures 1 and 2). We emphasize that despite this resemblance to the observation of [3], the $N = 2$ model is not appropriate to establish a general relation between the appearance of population inversions and π phase lapses at small δ/Γ [6, 10]. While the latter are already present at $U = 0$, the former only develop with increasing U (compare figures 1(a), (d) or 2(a), (d) to figures 1(c), (f) or 2(c), (f)). Note that the gate voltage V_g^{PI} at which the population inversion occurs is generically *not* identical to the position of the phase lapse and transmission zero (see figures 1(b), (c), (f) and 2(c), (f)) [14]. However, for l–r symmetric Γ_j^l equation (9) ensures that if a population inversion occurs its position is identical to the one of the phase lapse and transmission zero.

As can be seen in figures 1(c), (f) and 2(c), (f) for small δ/Γ and large U/Γ the n_j show a rather strong gate voltage dependence between the CB peaks. Nevertheless the total dot occupancy $n_1 + n_2$ is only weakly V_g dependent and close to 1 within the entire CB valley. This is reminiscent of the plateau-like occupancy in the local moment regime of the single impurity Anderson model showing the Kondo effect. As discussed in [14]–[16] a relation to this model can indeed be established.

We note in passing that with the exception of the nongeneric case of l–r symmetric Γ_j^l, $s = +$ and $\delta = 0$, the n_j are continuous functions of V_g.

4.2. Comparison with mean-field theory

In [10, 11] Golosov and Gefen (GG) analyse the phase lapse scenario of the spin-polarized interacting two-level dot within the mean-field approximation. However, they anticipated themselves that correlations not captured in the mean-field approach could be important. Examples of this had been pointed out already in [5, 13]. Thus, GG emphasized that the effects of

such correlations on their results need to be studied in subsequent work. The present subsection is devoted to this task.

GG consider the subspace of level-lead couplings defined by $\Gamma_1^L - \Gamma_1^R = \Gamma_2^R - \Gamma_2^L$. Performing a unitary transformation on the dot states the part of the Hamiltonian equation (1) containing dot operators can be transformed to (see [10, 11])

$$
\begin{aligned}
H_{\text{dot}} + H_{\text{lead-dot}} = & \sum_{j=1,2} \hat{\varepsilon}_j \hat{d}_{j,\sigma}^\dagger \hat{d}_{j,\sigma} + U \hat{d}_1^\dagger \hat{d}_1 \hat{d}_2^\dagger \hat{d}_2 - \hat{t}(\hat{d}_1^\dagger d_2 + \text{h.c.}) \\
& - \left[c_{0,L} \left(\hat{t}_1 \hat{d}_1^\dagger + \hat{t}_2 \hat{d}_2^\dagger \right) + c_{0,R} \left(\hat{t}_1 \hat{d}_1^\dagger - \hat{t}_2 \hat{d}_2^\dagger \right) + \text{h.c.} \right],
\end{aligned}
\tag{23}
$$

with the transformed operators and parameters indicated by a hat. The change of basis leads to a direct hopping $\hat{t}$ between the transformed levels. We here focus on the relative sign $\hat{s} = -$. GG then introduce the two new dimensionless parameters κ and α as $\hat{t} = -\kappa\hat{\delta}/(2\sqrt{1-\kappa^2})$ and $\alpha = (|\hat{t}_1| - |\hat{t}_2|)/\sqrt{\hat{t}_1^2 + \hat{t}_2^2}$. Varying κ and α GG investigate the phase lapse behaviour for fixed level spacing (in the new basis) $\hat{\varepsilon}_2 - \hat{\varepsilon}_1 = \hat{\delta} = 0.256\hat{\Gamma}$ and interaction $U/\hat{\Gamma} = 6.4$. As the parameters in the new basis are rather complicated combinations of the original ones, the variation of α and κ corresponds to the variation of the Γ_j^l (within the above specified subspace), δ and even s. Our simple picture that increasing the level spacing δ of the untransformed model leads from the universal to the mesoscopic regime cannot easily made explicit using the parameters of GG. To make the comparison of our results to the mean-field study definite we nevertheless follow the steps of GG.

Varying $\alpha, \kappa \in [0, 1[$ at $\hat{s} = -$ we move around in the right part of what is called the 'phase diagram' by GG (figure 4 of [11]). In figure 3, we show the behaviour of $|t|$ and θ varying α at fixed κ (figures 3(a)–(d)) and κ at fixed α (figures 3(e)–(h)), respectively. In the first case, upon increasing α at constant $\kappa = 0.5$, we move from GGs 'phase 2', (red in figure 4 of [11]), with the transmission zero and phase lapse outside the two CB peaks, into 'phase 1' (blue in figure 4 of [11]), with the transmission zero and phase lapse between the peaks. The mean-field approximation correctly captures the presence of these two regimes. We find a smooth crossover between them (which is why we prefer the notion of different 'regimes' rather than 'phases'): the V_g value at which the transmission zero and phase lapse occur *smoothly* crosses from lying outside the right CB peak to lying between the two CB peaks. This is similar to the smooth crossover we observe in the $s = -$ case of the untransformed model when moving from the mesoscopic to the universal regime (see columns of figure 2).

For fixed $\alpha = 0.6$ and increasing κ we move from 'phase 3' (green in figure 4 of [11]) into 'phase 1'. In contrast to the mean-field approximation where an abrupt transition from 'phase 3' to 'phase 1' occurs, figures 3(e)–(h) show a rather smooth evolution. The mean-field 'phase 3' is characterized by discontinuous population switching and a phase lapse between the CB peaks which, surprisingly, is smaller than π [6, 10]. Furthermore, in this parameter regime the mean-field results show no transmission zero, as discussed in [6]. However, from figures 3(e)–(h) it is apparent that 'phase 3', is an artefact of the mean-field approximation: upon taking correlations into account via fRG, the π phase lapse and the transmission zero are found to remain in the CB valley. The evolution with increasing κ is similar to the $s = +$ case of the untransformed model when the level spacing is increased at fixed Γ_j^l (see the second and third columns of figure 1). 'Phase 3' then corresponds to the parameter regime with small level spacing and a sizeable U/Γ in which correlations are of particular importance leading e.g. to the correlation-induced resonances (see figures 3(e)–(h)). That the mean-field approximation fails to properly describe
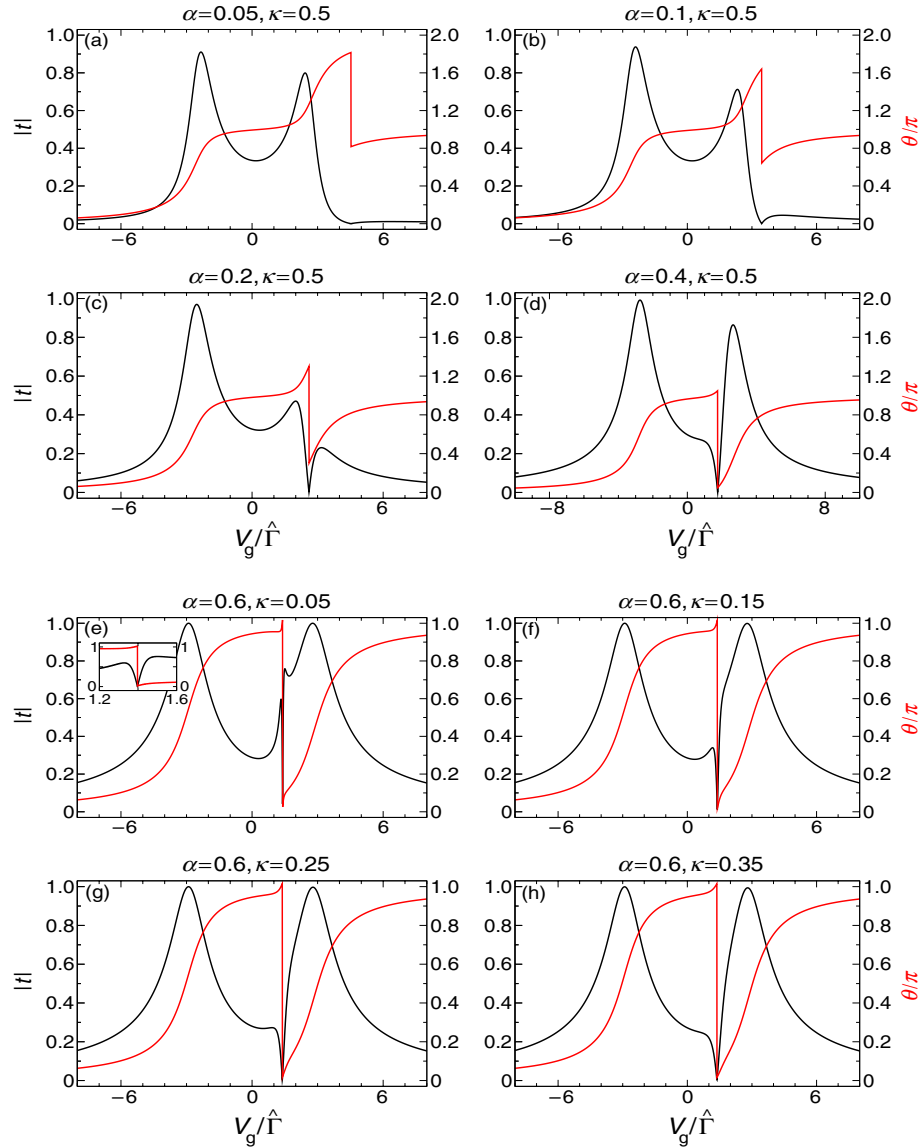
Figure 3. Two traces through the mean-field 'phase diagram' of GG. Panels (a)–(d) are for constant κ and different α moving from GGs 'phase' 2 into 'phase' 1. Panels (e)–(h) are for constant α and different κ moving from GGs 'phase 3' into 'phase 1'. The inset in panel (e) shows a zoom in of the gate voltage region around the phase lapse. For a detailed comparison to the mean-field results see the text. The results were obtained at $T = 0$ using the truncated fRG.
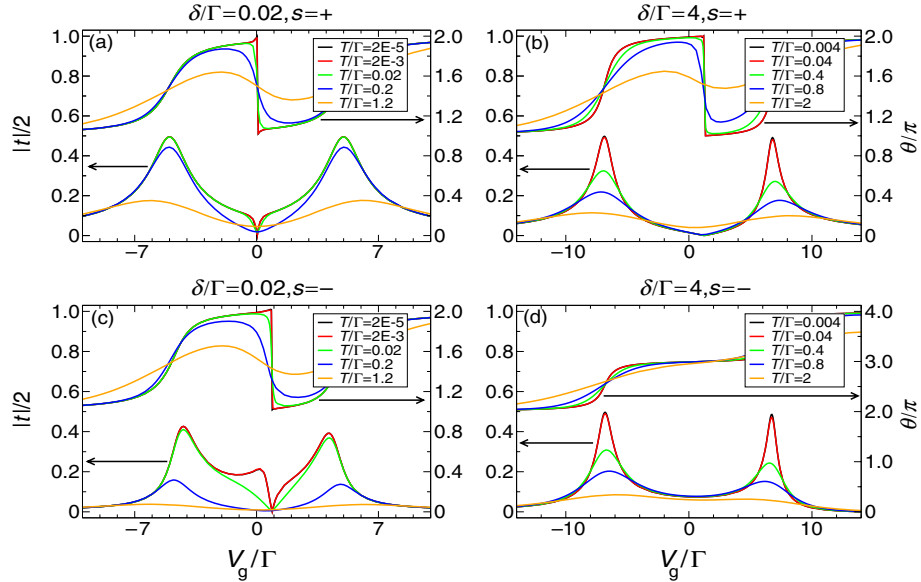
Figure 4. Temperature dependence of $|t(V_g)|$ and $\theta(V_g)$ obtained by NRG for $\gamma = \{0.27, 0.33, 0.16, 0.24\}$, $U/\Gamma = 10$ for $s = \pm$ and in the universal ($\delta/\Gamma = 0.02$) and the mesoscopic ($\delta/\Gamma = 4$) regime. We used the NRG parameters $\Lambda_{\mathrm{NRG}} = 2.3$ and $N_{\mathrm{kept}} \sim 512$.

this strongly correlated regime is not surprising and has been recognized earlier [13]. In [14]–[16] a connection between the small δ regime of the present model and the local moment (Kondo) regime of the single-impurity Anderson model was established. Thus, the artefacts of the mean-field approximation for the spinless two-level dot are reincarnations of the well-known artefacts it produces when applied to the Anderson model in the local moment regime.

Upon taking correlations into account, the discontinuities of the $n_{1/2}$ in 'phase 3' are washed out. The only choice of parameters for which we find discontinuous behaviour is the one with l–r symmetric Γ_j^l, $s = +$ and $\delta = 0$, a case which was already identified as being nongeneric [13]. Any arbitrarily small deviation from these conditions leads to a continuous gate voltage dependence of $n_{1/2}$. For parameters close to the nongeneric point the change in n_j at first sight appears to be rather sharp and an extremely high resolution in V_g is required to identify the behaviour as continuous.

The fact that the mean-field treatment at $U > 0$ and small level spacings incorrectly causes the transmission zero to disappear and the corresponding phase lapse to become smaller than π is its most consequential problem. By generating such features, the mean-field treatment masks the very simple scenario that emerges upon properly including fluctuations: for increasing U, the π phase lapse and transmission zero found for small δ/Γ at $U = 0$ remain in the CB valley, while the transmission peaks become well-separated, Lorentzian-like and the phase acquires an S-shape across the resonances.

4.3. Finite temperatures

We next investigate how the phase and magnitude of the transmission are affected by finite temperatures. To this end, we use the new FDM-NRG algorithm recently proposed in [29]. In figure 4 we show NRG data for $|t(V_g)|$ and $\theta(V_g)$ at different T. We consider generic level-lead couplings $\gamma = \{0.27, 0.33, 0.16, 0.24\}$, $U/\Gamma = 10$, $s = \pm$ and $\delta/\Gamma = 0.02$ (universal regime) as well as $\delta/\Gamma = 4$ (mesoscopic regime). As expected, with increasing temperature the sharp π phase lapses are gradually smeared out, the transmission zero vanishes and the change of θ at the phase lapse becomes smaller than π. Furthermore, the CB peaks decrease and broaden. For $\delta/\Gamma = 4$ and $s = -$ (figure 4(d)) the phase lapse lies outside the CB peaks and outside the window of gate voltages shown.

In the mesoscopic regime (figures 4(b) and (d)) the explicit temperature dependence of the Green function entering equation (6) via equation (7) is rather weak and the temperature dependence of the CB peaks and the phase lapse can be understood from the behaviour in the noninteracting model, but with level spacing $U + \delta$. For small T the height $h_j(T)$ of the jth CB peak scales as $1 - h_j(T)/h_j(0) \sim T^2/\Gamma_j^2$ and the width w of the phase lapse as $w \sim T^2/(\delta + U)^2$ [9]. The relevant scale for sizeable temperature effects in the peak height is thus Γ_j while it is $U + \delta$ in the smearing of the phase lapses. Since we have chosen $\Gamma_j \ll \delta + U$ a reduction of h_j is visible for temperatures at which the phase lapse is still fairly sharp (see figure 4(b)).

Due to the importance of correlation effects at small δ/Γ, the T dependence of $|t(V_g)|$ and $\theta(V_g)$ in the universal regime is different from the noninteracting case. Here the explicit temperature dependence of $\mathcal{G}$ is much stronger and cannot be neglected. The resulting T dependence of $|t(V_g)|$ and $\theta(V_g)$ is shown in figures 4(a) and (c). A comparison to figure 4(b) shows that in the universal regime the smearing of the phase lapse sets in at a lower energy scale than in the mesoscopic regime. This scale depends on the relative sign s of the level-lead hopping matrix elements (compare figures 4 (a) and (c)). Furthermore, in contrast to the mesoscopic regime the scales on which the CB peaks and the phase lapse are affected by temperature are comparable. A more detailed investigation of the temperature dependence in the universal regime, which also discusses the fate of the correlation-induced resonances, is beyond the scope of the present work and is left as subject for future studies.

5. Results: spin-degenerate dots

We finally investigate the effect of the spin degree of freedom on the discussed phase lapse scenario, at $T = 0$. In figures 5 ($s = +$, $U/\Gamma = 3$) and 6 ($s = -$, $U/\Gamma = 4$) we show fRG data for the evolution of $|t(V_g)|$, $\theta(V_g)$ and $n_j(V_g)$ (for a fixed spin direction) with increasing δ for a generic $\gamma = \{0.1, 0.2, 0.5, 0.2\}$. The overall dependence of $\theta(V_g)$ on δ is similar to the one observed in the spinless case (compare figures 1 and 2). In particular, the behaviour at small δ/Γ appears to be almost unaffected by the presence of the spin degree of freedom (figures 5(a), (b) and 6(a), (b)). For large δ/Γ (figures 5(d) and 6(d)) the transmission resonances are located at odd average total filling of the two-level dot indicated by shoulders in the n_j. At these fillings and for sufficiently large U/Γ the Kondo effect is active and the resonances cannot be regarded as Lorentzian-like CB peaks. Instead they show a plateau-like shape known from the spinful single-level dot (see [30] and references therein). Across the Kondo plateaux of $|t|$ the S-shaped increase of the phase is interrupted by a shoulder at $\theta \approx \pi/2$ as expected for the Kondo effect
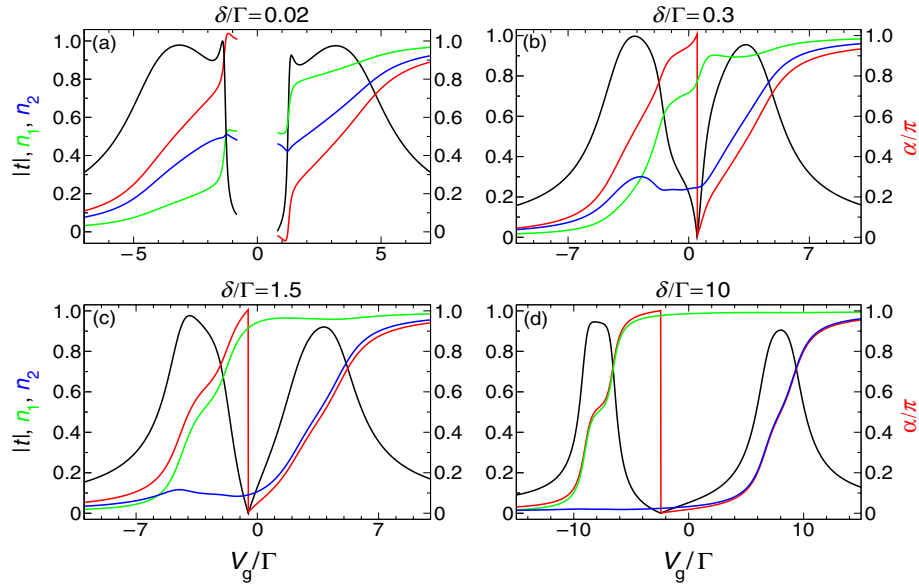
Figure 5. Gate voltage V_g dependence of $|t|$ (black), θ (red) and the level occupancies per spin direction (green and blue) of a spinful two-level dot at $T = 0$ for different δ obtained by fRG. The parameters are $U/\Gamma = 3$, $\gamma = \{0.1, 0.2, 0.5, 0.2\}$ and $s = +$. In (a), no data are shown around $V_g = 0$ for reasons explained in the text.

[30]. It would be very interesting to study how each of the Kondo plateaus of $|t|$ with increasing temperature crosses over to two CB peaks and how the phase behaves in the generated CB valley. This question is left for future investigations.

The behaviour of the phase in the presence of the Kondo effect was experimentally investigated at temperatures comparable to the Kondo temperature [24], and much below the Kondo temperature [25]. As we study the zero temperature case it is proper to compare our calculations to the measurements at low temperatures. Indeed figure 6(c) for intermediate δ/Γ qualitatively reproduces the experimental results at low temperature as shown in figure 3 (c) of [25]. In particular the increase of the phase by more then π and the absence of clearly developed Kondo plateaus are reproduced.

In figure 5(a) we left out the fRG data around $V_g = 0$ as for these gate voltages some of the components of the flowing two-particle vertex become large. This indicates the breakdown of our present truncation scheme [27, 28] and the results for $|t|$, θ and n_j become unreliable. For an explicit comparison to NRG data of $|t|$ see figure 7(a). We note in passing that for $s = +$ correlation-induced resonances occur also in the model with spin (figure 5(a)]) [27].

In figure 7 we compare fRG and NRG results for l–r symmetric level-lead couplings. The computational resources required to obtain NRG data away from l–r symmetry become large and such data are not required for the aim of the present paper. We can then use equation (9) and must only compute the occupancies n_j, which is numerically less demanding. For $\delta > 0$ (as exclusively shown) it is only the absence of the correlation-induced resonances for $s = +$ (compare figures 5(a) and 7(a)) which is different from the results of the generic γ shown in
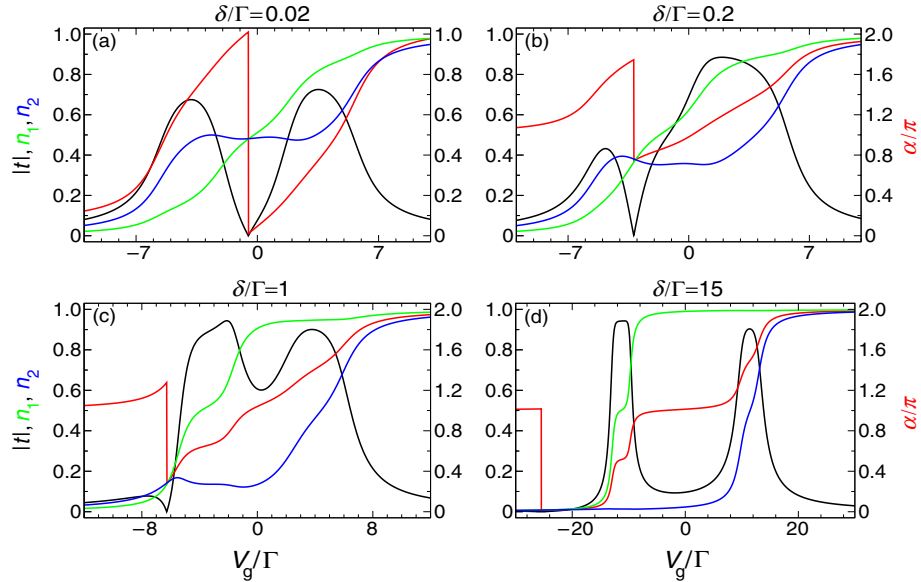
Figure 6. The same as in figure 5, but for $U/\Gamma = 4$ and $s = -$.

figures 5 and 6. With the exception of the $V_g \approx 0$ regime in the case of small δ and $s = +$ the fRG and NRG data compare quite well. In this case we only show the fRG data for $|t|$ as the results for the phase and occupancies become rather erratic. The reason for the breakdown of the currently used truncated fRG is explained in [27, 28] and is related to the fact that at small δ and small V_g the correlations in effect become extremely large.

6. Summary

In the present paper, we studied the appearance of phase lapses in an interacting two-level quantum dot considering the entire parameter space using NRG and a truncated fRG scheme.

As a starting point we briefly discussed the noninteracting case at temperature $T = 0$ and pointed out that for generic level-lead couplings, that is up to cases with increased symmetry, essential features of the universal phase lapse scenario are already established at $U = 0$. For single-particle level spacings δ small compared to the level broadenings Γ_j the transmission is characterized by two transmission peaks of equal width with a transmission zero and an associated π phase lapse between them (universal regime). For a large asymmetry of the level-lead couplings, $\Gamma_1 \ll \Gamma_2$ or vice versa this can be understood as resulting from a Fano anti-resonance. The Fano effect is robust for more symmetric couplings as well as for $U > 0$. For large δ/Γ at $U = 0$ the appearance or not of a transmission zero and phase lapse between the two transmission peaks depends on the relative sign s of the level-lead couplings (mesoscopic regime). Within a spinless model we have shown that the separation of the two transmission peaks increases linearly with the interaction U while the π phase lapse and transmission zero remain in the valley between them. Furthermore, with increasing U the increase of the phase across the peaks takes an S-shape and the peaks become Lorentzian-like, thus assuming shapes resembling those
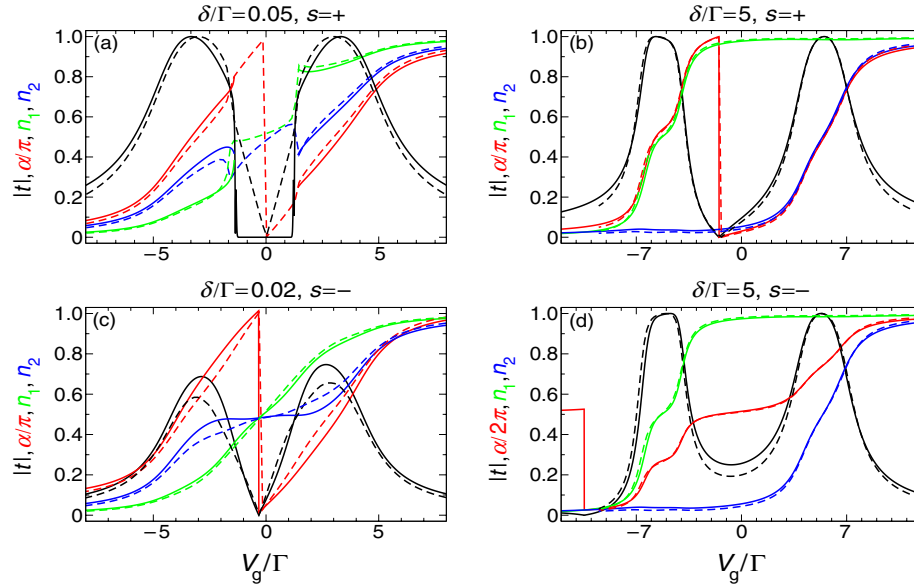
Figure 7. Comparison of fRG (solid) and NRG (dashed) data for $|t(V_g)|$, $\theta(V_g)$ and $n_j(V_g)$ (per spin direction) in the universal (small δ/Γ) and mesoscopic regime (large δ/Γ) of a spinful two-level dot at $T = 0$. The parameters are $U/\Gamma = 3$ and $\gamma = \{0.15, 0.15, 0.35, 0.35\}$. In (a) the fRG data for $\theta(V_g)$ and $n_j(V_g)$ around $V_g = 0$ are not shown. Already the unsatisfactory comparison between fRG and NRG for $|t|$ indicate that the fRG becomes unreliable in this regime. For more details on this, see the text. For the NRG parameters we used $\Lambda_{NRG} = 2.5$, $N_{kept} = 1024$ for $s = +$ and $N_{kept} = 2048$ for $s = -$.

observed experimentally [17]–[19]. For $s = -$ and increasing δ, a crossover occurs to a regime in which the π phase lapse and transmission zero lies outside the two CB peaks. The crossover scale δ_c increases with increasing interaction and thus the Coulomb repulsion stabilizes the universal phase lapse behaviour. We have investigated the relation between phase lapses and population inversions of the level occupancies n_j.

Experimentally the universal phase lapse behaviour was found for every many-electron dot measured [17]–[19]. In contrast, for dots with only a few electrons the phase behaves mesoscopically, that is it shows a $-\pi$ jump in certain transmission valleys while it increases continuously in others, depending on the dot measured [19]. One generic difference between few- and many-electron dots is the noninteracting single-particle level spacing of the topmost filled levels. It is expected to decrease as the number of electrons increases. Consistent with this we find a crossover from mesoscopic to universal phase lapse behaviour when δ was decreased in our model.

We have shown that a mean-field treatment of the present problem correctly reproduces certain features of the behaviour discussed above, but is not able to produce the universal phase lapse scenario at small δ/Γ due to artefacts of the approximation such as a phase lapse by less than π [10, 11] and a vanishing of the transmission zero [6]. Furthermore, the discontinuous gate voltage dependence of the n_j found in the mean-field approximation turned out to be an artefact.

Next, we studied how the phase lapse behaviour is affected by temperatures $T > 0$. The universal phase lapse (at small δ/Γ) is smeared out but remains visible for not too large T. In the mesoscopic regime with $\delta/\Gamma \gg 1$ the smearing of the phase lapse and the decrease of the CB peaks can be understood in detail in analogy to the noninteracting case. For $\delta/\Gamma \ll 1$ correlations are more important and a detailed understanding of the temperature dependence of the transmission $t(V_g)$ requires further studies.

The phase lapse behaviour in both the universal and mesoscopic regimes is also stable if the spin degree of freedom is included. For sufficiently large U/Γ in this case the Kondo effect is active at odd average dot filling, leading to minor modifications of the scenario discussed above. In particular, at large δ/Γ the $T = 0$ transmission peaks are Kondo plateaus rather than Lorentzian-like CB peaks. Across these Kondo plateaus the phase shows a shoulder at $\theta \approx \pi/2$. In contrast, the behaviour at small δ/Γ appears to be almost unaffected by the spin degree. A study of the combined effect of finite temperature and spin is left for future work.

Acknowledgments

References

[1] Sohn L L, Kouwenhoven L P and Schön G (ed) 1997 *Mesoscopic Electron Transport* (Dordrecht: Kluwer)
[2] Kouwenhoven L P and Glazman L 2001 *Phys. World* **14** 33
[3] Silvestrov P G and Imry Y 2000 *Phys. Rev. Lett.* **85** 2565
      Silvestrov P G and Imry Y 2001 *Phys. Rev.* B **65** 035309
[4] König J and Gefen Y 2005 *Phys. Rev.* B **71** 201308(R)
[5] Sindel M, Silva A, Oreg Y and von Delft J 2005 *Phys. Rev.* B **72** 125316
[6] Goldstein M and Berkovits R 2006 *Preprint* cond-mat/0610810
[7] Hackenbroich G 2001 *Phys. Rep.* **343** 463
[8] Gefen Y 2002 *Quantum Interferometry with Electrons: Outstanding Challenges* ed I V Lerner *et al* (Dordrecht: Kluwer) p 13
[9] Silva A, Oreg Y and Gefen Y 2002 *Phys. Rev.* B **66** 195316
[10] Golosov D I and Gefen Y 2006 *Phys. Rev.* B **74** 205316
[11] Golosov D I and Gefen Y 2007 *New J. Phys.* **9** 120
[12] Kim S and Lee H-W 2006 *Phys. Rev.* B **73** 205319
[13] Meden V and Marquardt F 2006 *Phys. Rev. Lett.* **96** 146801
[14] Kashcheyevs V, Schiller A, Aharony A and Entin-Wohlman O 2007 *Phys. Rev.* B **75** 115313
[15] Lee H-W and Kim S 2006 *Preprint* cond-mat/0610496
[16] Silvestrov P G and Imry Y 2007 *Phys. Rev.* B **75** 115335
[17] Yacoby Y, Heiblum M, Mahalu D and Shtrikman H 1995 *Phys. Rev. Lett.* **74** 4047
[18] Schuster R, Buks E, Heiblum M, Mahalu D, Umansky V and Shtrikman H 1997 *Nature* **385** 417
[19] Avinun-Khalish M, Heiblum M, Zarchin O, Mahalu D and Umansky V 2005 *Nature* **436** 529
[20] Aharony A, Entin-Wohlman O, Halperin B and Imry Y 2002 *Phys. Rev.* B **66** 115311

[21] Berkovits R, von Oppen F and Kantelhardt J W 2004 *Euro. Phys. Lett.* **68** 699
[22] Karrasch C, Hecht T, Weichselbaum A, Oreg Y, von Delft J and Meden V 2006 *Phys. Rev. Lett.* at press
     (*Preprint* cond-mat/0609191)
[23] Fano U 1961 *Phys. Rev.* **124** 1866
[24] Ji Y, Heiblum M, Sprinzak D, Mahalu D and Shtrikman H 2000 *Science* **290** 779
[25] Ji Y, Heiblum M and Shtrikman H 2002 *Phys. Rev. Lett.* **88** 076601
[26] Krishna-murthy H R, Wilkins J W and Wilson K G 1980 *Phys. Rev.* B **21** 1003
[27] Karrasch C, Enss T and Meden V 2006 *Phys. Rev.* B **73** 235337
[28] Karrasch C 2006 *Diploma-thesis* Universität Göttingen (*Preprint* cond-mat/0612329)
[29] Weichselbaum A and von Delft J 2006 *Preprint* cond-mat/0607497
[30] Gerland U, von Delft J, Costi T A and Oreg Y 2000 *Phys. Rev. Lett.* **84** 3710
[31] Meir Y and Wingreen N S 1992 *Phys. Rev. Lett.* **68** 2512
[32] Salmhofer M and Honerkamp C 2001 *Prog. Theor. Phys.* **105** 1
[33] Hedden R, Meden V, Pruschke Th and Schönhammer K 2004 *J. Phys.: Condens. Matter* **16** 5279
[34] Meden V, *Lecture notes on the 'Functional renormalization group'* online at http: //www.theorie.physik.uni-
     goettingen.de/∼meden/funRG/
[35] Negele J W and Orland H 1988 *Quantum Many-Particle Physics* (Reading, MA: Addison-Wesley)
[36] Wilson K G and Kogut J 1974 *Phys. Rep.* **12** 75
[37] Krishna-murthy H R, Wilkins J W and Wilson K G 1980 *Phys. Rev.* B **21** 1044
[38] Costi T A, Hewson A C and Zlatic V 1994 *J. Phys.: Condens. Matter* **6** 2519
[39] Bulla R, Hewson A C and Pruschke Th 1998 *J. Phys.: Condens. Matter* **10** 8365
[40] Bulla R, Costi T A and Vollhardt D 2001 *Phys. Rev.* B **64** 45103
[41] Hofstetter W 2000 *Phys. Rev. Lett.* **85** 1508
[42] Verstraete F, Weichselbaum A, Schollwöck U, Cirac J I and von Delft J 2005 *Preprint* cond-mat/0504305
[43] Anders F B and Schiller A 2005 *Phys. Rev. Lett.* **95** 196801
[44] Pines D and Noziéresp 1966 *The Theory of Quantum Liquids* Vol 1 (New York: Benjamin)

4.4   Interplay of mesoscopic and Kondo effects for transmission amplitude of few-level quantum dots

We present numerical calculations of the magnitude and phase of the transmission amplitude of a multi-level quantum dot in the mesoscopic regime. We discuss the T- and Γ-dependence of the transmission amplitude with focus on the influence on Kondo correlations. The influence of the neighbouring levels is discussed for the different choices of the mesoscopic paramter s. We give a derivation of a formula for the Aharonov-Bohm contribution to the linear conductance through a multi-terminal interferometer with open geometry, as used in the Heiblum group. This formula has already been used in the previous Sections.

Interplay of mesoscopic and Kondo effects for transmission amplitude of few-level quantum dots

T. Hecht,[1] A. Weichselbaum,[1] Y. Oreg,[2] and J. von Delft[1]

[1]*Physics Department, Arnold Sommerfeld Center for Theoretical Physics and Center for NanoScience,*
Ludwig-Maximilians-Universität München, Germany
[2]*Department of Condensed Matter Physics, The Weizmann Institute of Science, Rehovot 76100, Israel*
(Dated: May 20, 2008)

The magnitude and phase of the transmission amplitude of a multi-level quantum dot is calculated for the mesoscopic regime of level spacing large compared to level width. The interplay between Kondo correlations and the influence by neighboring levels is discussed. As in the single-level case, the Kondo plateaus of magnitude and phase disappear with increasing temperature. At certain gate voltages, "stationary" points are found at which the transmission phase is independent of temperature. Depending on the mesoscopic parameters of the adjacent levels (like relative sign and magnitude of tunneling matrix elements), the stationary points are shifted to or repelled by the neighboring level.

PACS numbers: 73.23.Hk, 73.23.-b, 73.63.Kv, 73.40.Gk

I. INTRODUCTION

In a remarkable series of experiments,[1,2,3,4,5,6] the Heiblum group has analyzed the complex transmission amplitude, $t_d = |t_d|e^{i\alpha}$, of a quantum dot embedded in an Aharonov-Bohm ring. In particular, by analyzing the Aharonov-Bohm oscillations of the conductance of such a ring, the dependence of both the magnitude and phase of the transmission amplitude, $|t_d|$ and α, were measured as a function of various parameters such as gate voltage V_g applied to the dot, temperature T, mean coupling strength to the leads Γ, etc.

The first two experiments in this series,[1,2] dealt with large dots containing many (> 100) electrons. The experiment by Yacoby et al.[1] showed that coherent transport through a quantum dot is possible despite the presence of strong interactions. The next experiments by Schuster et al.[2] generated tremendous interest because the behavior of the transmission phase showed a surprisingly "universal" behavior as function of gate voltage: the phase experienced a series of sudden jumps by $-\pi$ (phase lapses) between each pair of Coulomb blockade peaks in the conductance through the dot. This contradicted a naive expectation that the behavior of the transmission phase should depend on microscopic details of the dot, such as the signs of the matrix elements coupling a given level to the left or right lead.

Subsequent experiments by Ji et al.,[3,4] performed on smaller dots containing tens of electrons, analyzed how the occurrence of the Kondo effect influences the transmission amplitude, and in particular its phase. For transmission at zero temperature through a *single* level, the Kondo effect causes the magnitude of the transmission amplitude to exhibit (as function of gate voltage) a plateau at the unitary limit ($|t_d| = 1$). For this regime it had been predicted by Gerland et al.[7] that the phase should show a plateau at $\alpha = \pi/2$, a result very different from the universal behavior mentioned above. While the

experiments of Ji et al. did yield deviations from the universal phase behavior, they did not verify the prediction of a $\pi/2$ Kondo plateau in the phase. With hindsight, the reason probably was that the experiments did not realize the conditions assumed in the calculations of Gerland et al.,[7] namely transport through only a *single* level.

Truly "mesoscopic" behavior for the phase was observed only rather recently by Avinun-Kalish et al.,[5] in even smaller dots containing only a small (< 10) number of electrons. For these, the mean level spacing δ was significantly larger than the average level width Γ, so that for any given gate voltage, transport through the dot is typically governed by the properties of only a single level, namely that closest to the Fermi energies of the leads. When the number of electrons was increased beyond about 14, universal behavior for the phase was recovered. Consequently, it was proposed[5,8,9,10,11,12,13] that the universal behavior occurs whenever a quantum dot is large enough for that the ratio δ/Γ is sufficiently small ($\simeq 1$) that for any given gate voltage, typically more than one level contributes to transport.

The latest paper in this series, by Zaffalon et al.,[6] studied the transmission phase through a quantum dot in the "deep mesoscopic" regime $\delta/\Gamma \gg 1$, containing only one or two electrons. When this system was tuned into the Kondo regime, the transmission phase indeed did show the $\pi/2$ Kondo plateau predicted by Gerland et al.[7].

The experiments of Avinun-Kalish et al.,[5] which observed mesoscopic effects for the transmission phase through a small number of levels, and those of Zaffalon et al.,[6] which found characteristic signatures of the Kondo effect in the transmission phase through a single level, raise the following question: what type of phase behavior can arise in the deep mesoscopic regime from the interplay of (i) *random signs* for tunneling amplitudes of neighboring levels and (ii) the *Kondo effect* for individual levels? In the present paper, we address this question by studying spin-degenerate models of dots with 2 or 3 levels in the deep mesoscopic regime of $\delta/\Gamma \gg 1$. This is the

regime relevant for the experiments of Zaffalon *et al.*[6] (for those of Ji *et al.*,[3,4] the ratio δ/Γ was presumably smaller than used here). Our goal is to provide a catalogue of the types of behavior that can occur in this regime, and to illustrate how the characteristic transmission amplitude (magnitude and phase) depends on temperate as well as on the strength of the coupling to the leads.

This paper is organized as follows. In Sec. II we introduce our many-level model for the quantum dot system. We discuss the relation between the Aharonov-Bohm contribution to the linear conductance and the transmission amplitude through the quantum dot. The latter can be expressed in terms of the local Green's function of the dot. We briefly present the technique used to calculate the latter, the numerical renormalization group method. In Sec. III we present our numerical results of both the phase and the magnitude of the transmission amplitude through a two- and three-level model in the regime $\delta/\Gamma \gg 1$. We discuss the T- and Γ-dependence of the transmission amplitude with focus on the influence on Kondo correlations. We study all relevant choices of the mesoscopic parameters given by the relative signs of the tunneling amplitudes of adjacent levels. The influence of neighboring levels is studied. It results not only in a phase lapse in Coulomb blockade valleys but also introduces a V_g-asymmetry in the finite temperature modulations of the Kondo plateaus. "Stationary" points of T- and Γ-independence are discussed. In the Appendix, we give a derivation of a formula for the Aharonov-Bohm contribution to the linear conductance through a multiterminal interferometer with open geometry, as used in the Heiblum group. This formula has been used in several publications including some of the present authors,[7,11,12] but its derivation had not been published before.

II.   THE MODEL AND THE METHOD

In the experiments,[2,3,4,5,6] the temperature-dependent transmission amplitude through the quantum dot is extracted from the Aharonov-Bohm oscillations of the conductance in a multi-lead ring geometry. In the Appendix we show that this transmission amplitude can be expressed in terms of the equilibrium local Green's function of the dot tunnel-coupled only to *two* leads on its left and right side, without explicitly incorporating the other leads of the ring geometry in the calculation.

In this Section we introduce a "reduced model" describing the latter situation of a spinful multi-level quantum dot coupled to two reservoirs and present the transmission formula derived in the Appendix. Further, we comment on NRG, the method used to calculate the local Green's function.

1.   The model Hamiltonian

The model Hamiltonian can be split into three parts,

$$H = H_{\rm d} + H_{\rm l} + H_{\rm t}, \tag{1a}$$

specifying the properties of the bare dot, the leads and the coupling between the two systems, respectively. For N spinful levels coupled to a left (emitter) and right (collector) lead, these terms are given by

$$H_{\rm d} = \sum_{j=1..N} \sum_{\sigma} \varepsilon_{dj} n_{dj\sigma} + \sum_{\{j\sigma\}\neq\{j'\sigma'\}} U n_{dj\sigma} n_{dj'\sigma'} \tag{1b}$$

$$H_{\rm l} = \sum_{\alpha=L,R} \sum_{k\sigma} \varepsilon_k c^{\dagger}_{\alpha k\sigma} c_{\alpha k\sigma} \tag{1c}$$

$$H_{\rm t} = \sum_{j} \sum_{\alpha=L,R} \sum_{k\sigma} (t^j_{\alpha} c^{\dagger}_{\alpha k\sigma} d_{j\sigma} + \text{H.c.}) . \tag{1d}$$

Dot creation operators for level j and spin $\sigma = \{\uparrow, \downarrow\}$ are denoted by $d^{\dagger}_{j\sigma}$, with $n_{dj\sigma} = d^{\dagger}_{j\sigma} d_{j\sigma}$, where $j = 1 \cdots N$ labels the levels in order of increasing energy ($\varepsilon_{dj} < \varepsilon_{dj+1}$). We use an inter- and intra-level independent Coulomb energy $U > 0$. The leads are assumed to be identical and non-interacting with constant density of states $\rho = 1/2D$, where the half-bandwidth $D = 1$ serves as energy unit. Electrons in lead α are created by $c^{\dagger}_{\alpha k\sigma}$. The local levels are tunnel-coupled to the leads, with real overlap matrix elements t^j_{α} that for simplicity we assume to be energy- and spin-independent. The resulting broadening of each level is given by $\Gamma_j = \Gamma_{jL} + \Gamma_{jR}$, with $\Gamma_{j\alpha} = \pi\rho(t^j_{\alpha})^2$. Notation: We define $s_i = \text{sgn}(t^i_L t^i_R t^{i+1}_L t^{i+1}_R) = \pm$. For example, matrix elements of same sign result in $s_i = +$, whereas one different sign yields $s_i = -$. We further define $s \equiv \{s_1 \cdots s_{N-1}\}$, and use $\gamma = \{\Gamma_{1L}, \Gamma_{1R}, \cdots, \Gamma_{NL}, \Gamma_{NR}\}/\Gamma$, with the mean level broadening $\Gamma = 1/N \sum_j \Gamma_j$. We assume constant level spacing $\delta = \varepsilon_{di+1} - \varepsilon_{di}$. The local levels can be shifted in energy by a plunger gate voltage V_g, with $\varepsilon_{dj} = j\delta - (V_g + V_{g0})$, where $V_{g0} = \frac{N-1}{2}\delta + \frac{2N-1}{2}U$. This convention ensures that in case of maximal symmetry ($t^j_{\alpha} = const.$ for all j, α), the system possesses particle-hole symmetry at $V_g = 0$.

2.   Transmission

In the Appendix we generalize a result of Bruder, Fazio and Schoeller[14] to show that the Aharonov-Bohm contribution to the linear conductance through the multiterminal interferometer with open geometry with a multilevel quantum dot embedded in one arm (see Fig. 4 in the Appendix) can be expressed as

$$G^{AB}(T) = \frac{e^2}{h} |T_u||t_d(T)| \cos(2\pi\Phi/\Phi_0 + \phi_0 + \alpha(T)). \tag{2}$$

Here $T_u = |T_u| e^{i\phi_0 + i2\pi\Phi/\Phi_0}$ is the energy- and temperature-independent transmission amplitude

through the upper reference arm including the Aharonov-Bohm contribution $2\pi\Phi/\Phi_0$ to the phase, where Φ is the magnetic flux enclosed by the interferometer arms and $\Phi_0 = h/e$ is the flux quantum. The equilibrium Fermi function of the leads are denoted by f_0. The effective, temperature-dependent transmission amplitude $t_d(T)$ through the lower arm including the quantum dot is given by

$$t_d(T) = \int dE \left(-\frac{\partial f_0(E,T)}{\partial E} \right) T_d(E,T) \equiv |t_d|\ e^{i\alpha}, \quad (3)$$

where

$$T_d(E,T) = \sum_{jj'} \sum_{\sigma\sigma'} 2\pi\rho\ t_L^j t_R^{j'} \mathcal{G}_{j\sigma,j'\sigma'}^R(E,T). \quad (4)$$

Therefore, only local properties like the local retarded Green's function $\mathcal{G}_{j\sigma,j'\sigma'}^R$ and the Fermi function of the leads enter in the transmission amplitude through the quantum dot t_d [Eq. (3)]. Thereby the local Green's function is evaluated for the model given in Eqs. (1) in equilibrium at temperature T.

In the zero temperature limit and in linear response, the dot produces purely elastic potential scattering between left and right leads, which can be fully characterized[15] by the eigenvalues $e^{i2\delta_\nu}$ ($\nu=a,b$) per spin of the S-matrix, and the transformation $\begin{pmatrix} \cos\theta & \sin\theta \\ -\sin\theta & \cos\theta \end{pmatrix}$, that maps the left-right basis of lead operators onto the a-b eigenbasis of S. The transmission amplitude through the dot then reads

$$t_d = -iS_{LR} = \sin(2\theta)\sin(\delta_a - \delta_b)e^{i(\delta_a+\delta_b)}, \quad (5)$$

where in general θ and δ_ν are all V_g-dependent. The phase δ_ν is related by the Friedel sum rule[16] to the charge (per spin) $n_\nu = \delta_\nu/\pi$ extracted by the dot from effective lead ν. As V_g is swept, the transmission amplitude goes through zero whenever $n_a = n_b \bmod 1$, and a phase lapse by π occurs. Equation (5) is useful for the special case of "proportional couplings", $t_L^j = \pm\lambda t_R^j$ with λ independent of j, in which the occupations $n_{a,b}$ take a simple form. Then the two effective leads a and b are the even and odd combinations of the left and right leads, respectively, with $\tan\theta = 1/\lambda$ independent of V_g. Then each level either couples to the even *or* the odd lead, and the occupations extracted from the leads are given by $n_{E,O} = \sum_{j\in E,O} n_{dj\sigma}$. Note that if all levels are coupled to the same effective lead (which is the case for $s = \{+\cdots+\}$), the other effective lead decouples, thereby reducing the computational complexity significantly.

3.   The method

We calculate the local Green's function $\mathcal{G}^R$ needed for the transmission amplitude (Eqs. (3) and (4), respectively) using the numerical renormalization group method[17] (NRG), a well-established method for the study of strongly correlated impurity systems. For a review, see Ref. 18. The key idea of NRG is the logarithmic discretization of the conduction band with a discretization parameter $\Lambda > 1$. As a result, H_l is represented as a semi-infinite chain, where only the first site couples to the local level. The hopping matrix elements along the chain fall off exponentially like $\Lambda^{-(n-1)/2}$ with the site number n (energy scale separation). The NRG Hamiltonian can be solved iteratively by successively adding sites and solving the enlarged system, thereby increasing the energy resolution with each added site by a factor of $\Lambda^{1/2}$. The corresponding increase in Hilbert space is dealt with by a truncation strategy that keeps only the lowest $N_{\rm keep}$ states for the next iteration.

For the calculation of $\mathrm{Im}\mathcal{G}^R$ we use the full density matrix NRG[19,20], based on the only recently developed concept of a complete basis set within NRG[21]. The real part of $\mathcal{G}^R$ is obtained by Kramers-Kronig transformation. Improvement of the results is obtained by the self-energy representation, where the U-dependent part of the impurity self-energy $\Sigma(\omega) = U\frac{F^R(\omega)}{G^R(\omega)}$ is expressed by two correlation function[22], which both are calculated with the full density matrix NRG.

III.   RESULTS

In this Section we present our results for the phase and magnitude of the transmission amplitude t_d through the quantum dot. The gate voltage V_g is swept over a range sufficiently large that the full occupation spectrum of the quantum dot is covered ranging from 0 to $2N$. The exact distribution of the couplings seems to play only minor role for the transmission amplitude. Therefore we choose left-right symmetric coupling in the cases where all $s_j = +$, reducing the computational effort significantly, since then the odd channel decouples.

In the regime of interest, the deep mesoscopic regime, the mean level spacing δ is much larger than the typical level widths Γ_j, $\delta/\Gamma \gg 1$. Therefore electrons enter the dot one by one when increasing the gate voltage. Transport thus occurs mainly through one level at a time; more precisely, it occurs through a linear combination of all levels, where in the mesoscopic regime the level closest to the Fermi energy dominates.[11]

The Section is organized as follows: We first elucidate the basic properties of the transmission amplitude for the example of a two-level system. Varying temperature T (at fixed coupling Γ), or average coupling Γ (at fixed T), we study both possible choices $s = +$ and $s = -$, respectively. In order to analyze the interplay of $s = +$ and $s = -$, we then present data for a three-level system for all four possible combinations of s_1, s_2. Additionally, this has the advantage that for the middle level "boundary effects" (effecting the outermost levels) can be assumed to be eliminated, thus the behavior of the middle level can
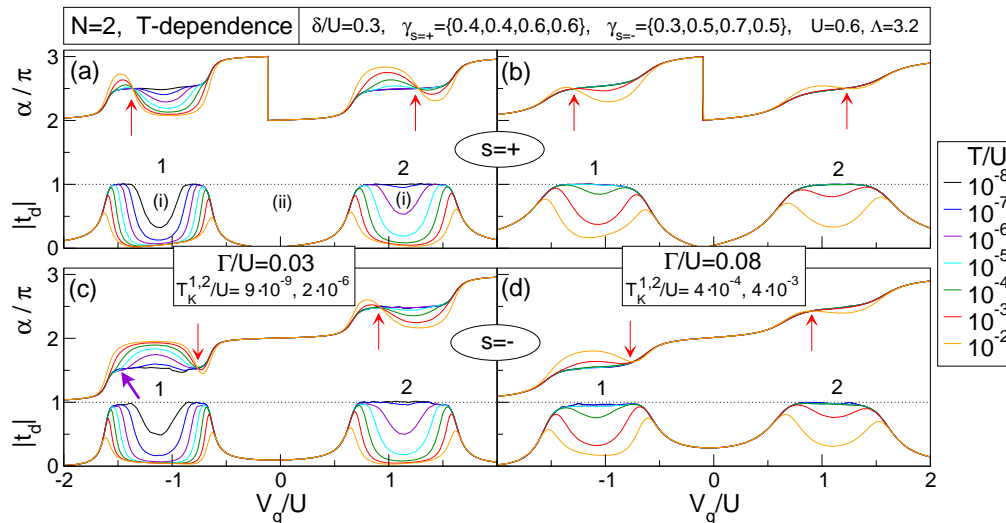
FIG. 1: Transmission $t_d = |t_d|e^{i\alpha}$ through a spinful two-level quantum dot for various temperatures and constant couplings. Regimes (i), (ii), indicated in panel (a) only, refer to Kondo valleys or Coulomb blockade valleys, respectively (see text). The levels involved are indicated by their level number $1, 2$. Level 2 is coupled more strongly to the leads than level 1, resulting in different bare Kondo temperatures, e.g. $T_K^{j=1} > T_K^{j=2}$. We use $\Gamma/U = 0.03$ (a,c) and $\Gamma/U = 0.08$ (b,d), thus $T_K^{(a,c)} < T_K^{(b,d)}$. The minimum value of the T_K^j (in the center of the Kondo valleys) are indicated in the legends. In accordance with Ref. 23, we find shoulders in the phase (see e.g. the fat purple arrow and the purple curve ($T/U = 10^{-6}$) in (c) for level 1) and an enhanced sensitivity of the phase to Kondo correlations compared to the magnitude, see e.g. the green ($T/U = 10^{-4}$) curves in (d) for level 1 or the purple curve ($T/U = 10^{-6}$) for level 2 in (a). There, the typical $\frac{\pi}{2}$-Kondo plateau in the phase is present, whereas the Kondo plateau in amplitude is not fully developed yet. At certain points in gate voltage, say $V_g^{c_j}$ (as indicated by red arrows), we find stationary points where the curves for α for all temperatures intersect. The position of $V_g^{c_j}$ is shifted by the presence of a neighboring level, being repelled by or shifted towards the latter for $s = +$ or $-$, compare (a,c) or (b,d), respectively. Depending on the mesoscopic parameter $s = \pm$, the phase either exhibits a sharp drop of π, accompanied by a zero in the amplitude $|t_d|$ ($s = +$, see (a,b)), or increases monotonically ($s = -$, see (c,d)) in the Coulomb blockade valleys.

be viewed as representative of a generic level in a multi-level quantum dot in the deep mesoscopic regime.

Unless otherwise noted, we use $U = 0.6$. In order to cover all relevant energy scales with reasonable computational effort, we usually use $\Lambda = 3.2$ for the two-level model and $\Lambda = 3.5$ in case of three levels. We checked that already by keeping ~ 1000 states at each iteration, also for the two-channel calculations (that involve at least one $s_i = -$) the physical trends are captured qualitatively. Note that since the eigenvalues of the scattering matrix are given by $e^{i2\delta_\nu}$, the transmission phase α is defined modulo π. For clarity of the Figures, curves showing α are shifted by multiples of π as convenient.

A.   Two-level model

1.   Temperature dependence

Figure 1 shows the transmission amplitude for both $s = +$ (a,b) and $s = -$ (c,d), for fixed dot parameters and various different temperatures. The mean level broadening is chosen to be $\Gamma/U = 0.03$ in panels (a,c), and $\Gamma/U = 0.08$ in panels (b,d). Therefore the (V_g-

dependent) bare Kondo temperatures

$$T_K^j = \sqrt{\frac{\Gamma_j U}{2}} \exp\left[-\pi \frac{\varepsilon_{dj}}{2U} \frac{(\varepsilon_{dj} + U)}{\Gamma_j}\right] \qquad (6)$$

vary in a lower-lying range of energies for panels (a,c) than for panels (b,d). In all panels the relative coupling of the first and the second levels are chosen to be $\gamma = \{0.8, 1.2\}$. Therefore, the bare Kondo temperature for level 1 is lower than for level 2, $T_K^{j=1} < T_K^{j=2}$, as indicated in the legends. The resulting difference in the temperature dependence can be nicely observed in the Figure. We first describe those general properties of the transmission amplitude that qualitatively agree with those that one would obtain for just a single level, then discuss the effect of the presence of a second level.

General properties: In the mesoscopic regime, where transport mainly occurs through one level at a time, two different regimes of transmission can be distinguished as V_g is varied, as indicated in Fig. 1(a): (ii) In the regime between the Kondo valleys, to be called "Coulomb blockade valleys", the transmission amplitude is mainly determined by the mesoscopic parameter s, showing a phase lapse only in case $s = +$, similar for both spinful and

spinless models[11,12].

In the zero temperature limit, $T \ll T_K^{(j)}$, the transmission amplitude exhibits the typical Kondo behavior: in the local-moment regime a typical Kondo plateau forms, with $|t_d|$ approaching the unitary limit, $|t_d| \to 1$. In the mixed valence regime the magnitude changes rapidly as a function of V_g. In the Coulomb blockade valleys, transmission is suppressed by Coulomb interaction. The transmission phase increases by $\sim \pi/2$ for each entering electron (see black curves for α in Fig. 1), increasing only slightly in between. In the Kondo valleys this results in a plateau at $\alpha \mathrm{mod}\pi = \frac{\pi}{2}$, as direct consequence of the $\frac{\pi}{2}$ phase shift due to the formation of the Kondo singlet.

With increasing temperature, the Kondo effect is suppressed, thus the behavior in the middle of the Kondo valleys changes dramatically. The Kondo plateaus in t_d and α disappear: The magnitude tends towards Coulomb blockade behavior, with a resonance of width $\sim \Gamma_j$ for each entering electron. The phase develops a S-like shape in the Kondo valleys with increasing temperature. As in the single-level case, all finite-temperature curves of the phase intersect the zero-temperature at the *same* gate voltage, say $V_g^{c_j}$ (see red arrows). We shall refer to this gate voltage as a "stationary" point (w.r.t. temperature).

As observed in the experiments of Ji *et al.*[3] and emphasized by Silvestrov and Imry,[23] the transmission phase reacts more sensitively to the buildup of Kondo correlations with decreasing temperature than the transmission magnitude: α approaches its $T = 0$ behavior already at temperatures $T \simeq T_K$ (the $\frac{\pi}{2}$-plateau develops), whereas $|t_d|$ develops its plateau for T significantly less than T_K (see, the green curve ($T/U = 10^{-4}$) for level 1 in Fig. 1(b) or the purple curve ($T/U = 10^{-6}$) for level 2 in Fig. 1(a)). Similar to the predictions of Silvestrov and Imry,[23] we find shoulders in the evolution of the phase, see for example the fat purple arrow and the purple curve ($T/U = 10^{-6}$) in Fig. 1(c). This indicates that the temperature is large enough to suppress Kondo correlations in the deep local-moment regime (in the middle of the Kondo valley), where T_K is very small. Towards the borders of the local-moment regime the crossover temperature for the onset of phase sensitivity increases (as does the Kondo temperature, see Eq. (6)), eventually exceeding the temperature. Then the phase tends towards its zero-temperature behavior, thus producing shoulders.

Properties special to the multi-level model: The most obvious difference between the transmission amplitude of the many-level model in the mesoscopic regime compared to the single-level model is the phase behavior in the Coulomb blockade valleys between the levels. Depending on s, i.e. on the relative sign of the tunnelling matrix elements of the two adjacent levels, the phase either exhibits a sharp drop (phase lapse) by π in the $s = +$ case (accompanied by a transmission zero, $|t_d| = 0$), or evolves continuously for $s = -$.[11,12,14,24,25,26] Contrary to the non-monotonic phase evolution discussed above, this ef-fect occurs already at zero temperature and also exists for spinless models.[11,12] Therefore, the relevant energy scale for the temperature dependence of this phase lapse is not related to the Kondo temperature but to the level distance and width of the effective transport levels.[23] It is therefore not a relevant energy scale in the temperature range studied in this work.

A further peculiarity for models with more than one level is the *asymmetry* (w.r.t. the center of the Kondo valleys) of the transmission amplitude in the local-moment regime at finite temperature, introduced by the mixing of neighboring levels. The asymmetry in phase can be characterized by the position of the stationary points, $V_g^{c_j}$ (indicted by red arrows in Fig. 1). In case $s = +$, these points are repelled by the neighboring level, whereas they are shifted to the latter for $s = -$, compare for example Fig. 1(a) and (c) or (b) and (d). For $\Gamma_1/\Gamma_2 \neq 1$, the repulsion and attraction is enhanced or reduced compared to $\Gamma_1 = \Gamma_2$ for the level that is coupled less or more strongly to the leads, respectively. Clearly, in the limit of one decoupled level (effective one-level system), the stationary point of the other level is symmetric w.r.t. the corresponding Kondo plateau. The dips that form in the plateaus of the amplitude with increasing temperature develop a distinct asymmetry only for $T \gg T_K^{(j)}$, for which they tend to shift towards the corresponding $V_g^{c_j}$. This is consistent with the fact that as the phase drop in the Kondo valley gets sharper with increasing temperature and approaches a quasi-phase lapse, the magnitude experiences a minimum, as for every complex function. Interestingly, the asymmetry in phase is the same for all temperatures, thus already at temperature $T \lesssim T_K$ the phase "knows" in which direction (of V_g) the dip in magnitude will shift at higher temperatures.

B. Dependence on the coupling strength

In experiments, it is more convenient (and easier to control) to change the coupling strength between the quantum dot and the reservoirs than the temperature. Accordingly, Fig. 2 presents the transmission amplitude for various values of Γ, keeping the temperature constant. With decreasing Γ, the decrease of T_K together with the suppression of Kondo correlations is nicely illustrated. At fixed temperature $T > T_K$, the S-like shape of the phase evolution gets more pronounced and sharper with decreasing Γ.

In the single-level problem, in addition to stationary points w.r.t. temperature, we also find stationary points w.r.t. Γ for t_d, i.e. for magnitude and phase of the transmission amplitude. These occur at the outer flanks of the Kondo plateaus. Varying the mean coupling strength Γ at fixed γ, δ and T in the two-level model, as shown in Fig. 2, these points can still be recognized (indicated by green arrows in (d)), even though the Γ-independence
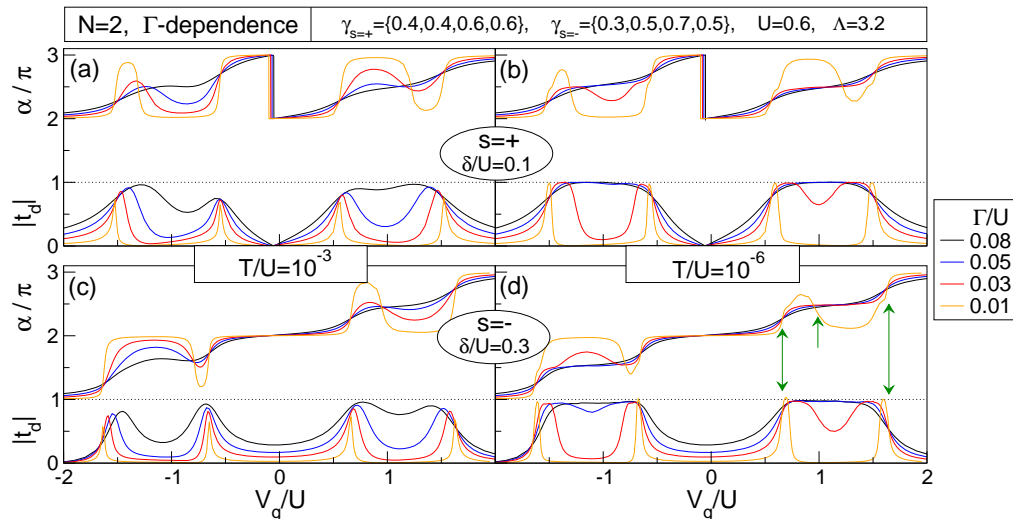
FIG. 2: Transmission through a spinful two-level quantum dot for both choices of $s = \pm$ and various values of mean couplings Γ at fixed temperature T, level spacing δ and relative couplings γ. Due to the mixing of the levels, no stationary points w.r.t. Γ exist, Γ-independence exist, see text and the green arrows in (d).

is not perfect (within our numerical accuracy). We expect that due to the mixing of the levels, also the level distance δ has to be taken into account to recover these stationary points. Between the levels, near $V_g/U \approx 0$, another stationary point seems to occur.

C. Three-level model

Naturally, the question arises about the effects of several levels, with different choices of $s_i = \pm$, which is present only for models with more than two levels. Assuming that in the mesoscopic regime only neighboring levels mix significantly, i.e. simultaneously influence transport, any local level of a quantum dot (except the lowest or highest one) can be represented adequately by the middle level of a three-level model.

In Fig. 3 we present numerical data of a three-level model for all four possible combinations of $s = s_1, s_2$ and various temperatures. The second level is influenced by the effect of both s_1 and s_2, resulting in an effective enhancement or compensation of the asymmetry of the stationary point $V_g^{c_2}$ of level 2, as discussed in Section III A 1. Also the relative strength of the level-couplings (given by γ) has to be considered. In Fig. 3(a), both s and γ symmetrize the transmission curves of the middle level, whereas in panel 3(b) γ shifts $V_g^{c_2}$ to positive V_g. In panels 3(c) and 3(d) both s and γ tend to increase the asymmetry.

Therefore, the transmission phase through a spinful quantum dot with Kondo correlations present has S-like shape in the local-moment regimes at $T \gg T_K$. Analogously to experiments, we find an asymmetry of this S-

like shape. It is determined by both the relative strength γ and the sign s of the level couplings.

IV.   CONCLUSION

In this paper we present temperature-dependent NRG calculations of the magnitude and phase of the transmission amplitude through a multi-level quantum dot in the regime $\delta/\Gamma \ll 1$. Clearly, the Kondo correlations are suppressed with increasing temperature. The presence of neighboring levels results in a V_g-asymmetry in the finite temperature modulation of the Kondo valleys. The asymmetry depends on the relative signs of the tunneling matrix elements as well as on the relative couplings of the adjacent levels. Further, sharp phase lapses may occur between the levels. Studying a three-level model, the middle level can be understood as a representative of a generic level in a multi-level quantum dot.

Throughout the paper, we deliberately focussed only on the deep mesoscopic regime, for which the results can be understood rather straightforwardly. The crossover into the regime $\delta/\Gamma \simeq 1$, which is certainly of interest too in order to understand the fate of Kondo physics in the universal regime, and which we believe to be the regime relevant for the experiments of Ji et al.,[3,4] will be left as a subject for future studies.
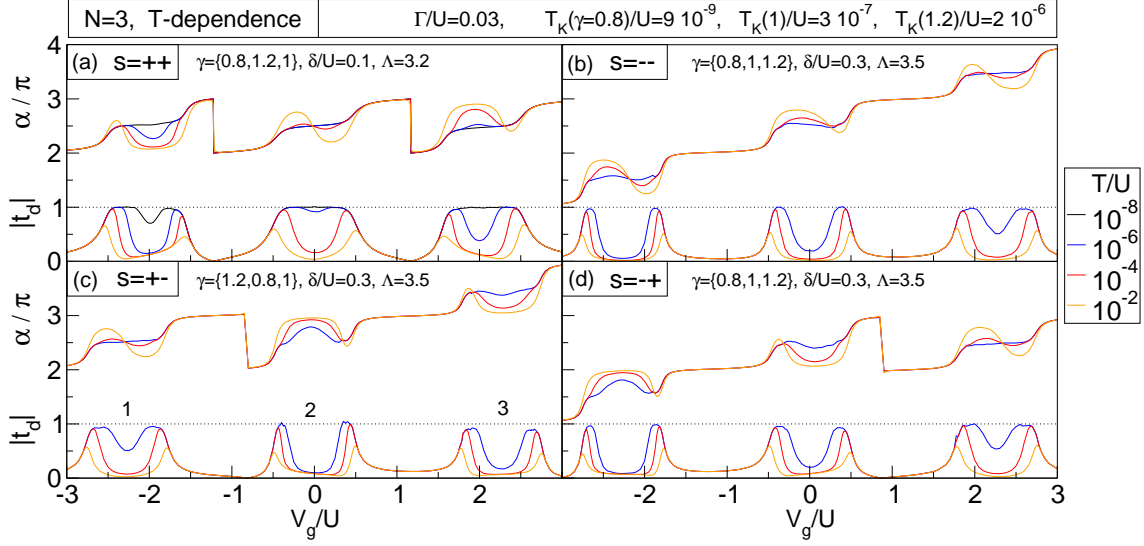
V.   ACKNOWLEDGEMENT

FIG. 3: Transmission through a three-level model for all four possible combinations of $s = s_1, s_2$ and various temperatures, for fixed $\Gamma/U = 0.03$. The two-channel calculations for (b,c,d) qualitatively capture the physical trends. The asymmetry in the Kondo valleys is determined by both s and γ. For convenience the figure legends for γ display only the total relative coupling of each level. The minimal bare Kondo temperatures are indicated. (a) $s = ++$: $\gamma = \{0.6, 0.6, 0.4, 0.4, 0.5, 0.5\}$. The case $T/U = 10^{-8}$ is included only for this panel. (b) $s = --$: $\gamma = \{0.5, 0.3, 0.4, 0.6, 0.5, 0.7\}$. (c) $s = +-$: $\gamma = \{0.4, 0.8, 0.4, 0.4, 0.3, 0.7\}$. (d) $s = -+$: $\gamma = \{0.5, 0.3, 0.3, 0.7, 0.7, 0.5\}$.

APPENDIX A: CONDUCTANCE FORMULA FOR MULTI-TERMINAL GEOMETRY

1. General case

We generalize the current formula derived in by Bruder, Fazio and Schoeller[14] for a single-level quantum dot embedded into one arm of an Aharonov-Bohm interferometer with two-terminal geometry to a multi-terminal geometry with a multi-level dot (as used in the Heiblum group[2,3,4,5,6]).

Consider a N-level quantum dot described by H_d [Eq. (1b)] embedded in one arm of an Aharonov-Bohm interferometer connected to M leads, as depicted in Fig. 4. Each lead, and each arm connecting them, is assumed to support only a mode. The tunnelling between the local levels $j = 1 \cdots N$ on the quantum dot and the leads $\alpha = 1 \cdots M$ is described by

$$H_t = \sum_{j\sigma} \sum_{\alpha k} t^j_{\varepsilon\alpha\sigma} c^\dagger_{\alpha\varepsilon\sigma} d_{j\sigma} + \text{H.c.} \qquad (A1)$$

Here $t^j_{\varepsilon\alpha\sigma} = \sum_{i=L,R} t^j_{i\sigma} A^i_{\varepsilon\alpha\sigma}$ (indicated in green in Fig.

4) is chosen real, where $t^j_{i\sigma} = \langle x_i | j\sigma \rangle$ (blue) is the amplitude to get from dot state $|j\sigma\rangle$ of level j and spin σ to point x_i on side $i = L, R$ of the dot, and $A^i_{\varepsilon\alpha\sigma} = \langle \varepsilon\alpha\sigma | x_i \rangle$ (red) is the amplitude to get from point x_i to lead state $|\varepsilon\alpha\sigma\rangle$ in lead α with energy ε and spin σ, see Fig. 4.
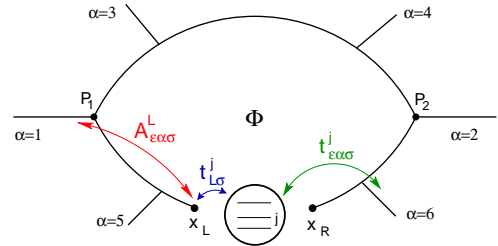
FIG. 4: Geometry of the multi-terminal Aharonov-Bohm interferometer with a multi-level quantum dot embedded in the lower arm. The different tunnelling amplitudes used in the text are indicated. Φ is the magnetic flux penetrating the interferometer.

Following Büttiker,[27] the current operator in reservoir α is given by

$$\hat{I}_\alpha(t) = \frac{e}{h} \sum_{\varepsilon\varepsilon'} \sum_{\sigma\sigma'} \frac{1}{\rho} \left[c^\dagger_{\varepsilon'\alpha\sigma'}(t) c_{\varepsilon\alpha\sigma}(t) - b^\dagger_{\varepsilon'\alpha\sigma'}(t) b_{\varepsilon\alpha\sigma}(t) \right],$$
$$(A2)$$

where ρ, the density of states, is assumed to be constant and equal for each reservoir. The first term inside the bracket stands for the incident, the second term for the

reflected current in reservoir α, thus $b_{\varepsilon\alpha\sigma} = \sum_\beta S^\varepsilon_{\alpha\beta} c_{\varepsilon\beta\sigma}$, with $S^\varepsilon_{\alpha\beta}$ the scattering amplitude to get from lead β to lead α with energy ε. Defining the lesser, retarded and advanced correlation functions

$$\mathcal{G}^<_{\mu,\mu'}(t-t') \equiv \frac{i}{\hbar}\langle a^\dagger_{\mu'}(t') a_\mu(t)\rangle$$
$$= \int \frac{dE}{2\pi\hbar} e^{-iE(t-t')/\hbar}\, \mathcal{G}^<_{\mu,\mu'}(E), \quad \text{(A3)}$$

$$\mathcal{G}^{R,A}_{\mu,\mu'}(t-t') \equiv -\frac{i}{\hbar}\theta(\pm(t-t'))\langle\left[a^\dagger_{\mu'}(t'), a_\mu(t)\right]_+\rangle$$
$$= \int \frac{dE}{2\pi\hbar} e^{-iE(t-t')/\hbar}\, \mathcal{G}^{R,A}_{\mu,\mu'}(E), \quad \text{(A4)}$$

where a_μ denotes a fermionic operator with composite index μ, the expectation value of the current operator (A2) can be expressed as

$$\langle \hat{I}_\alpha(t)\rangle = \frac{e}{h}\sum_{\varepsilon\varepsilon'}\sum_{\beta\beta'}\sum_{\sigma\sigma'} \frac{1}{\rho}\left[\delta_{\alpha\beta'}\delta_{\alpha\beta} - S^{\star\varepsilon'}_{\alpha\beta'} S^\varepsilon_{\alpha\beta}\right]$$
$$\times (-i)\int \frac{dE}{2\pi}\, \mathcal{G}^<_{\varepsilon\beta\sigma,\varepsilon'\beta'\sigma'}(E). \quad \text{(A5)}$$

To calculate $\mathcal{G}^<(E)$ in Eq. (A5), we use the standard Dyson equation for the Keldysh 2×2 matrix Green's function[28] $\hat{\mathcal{G}}(E)$,

$$\hat{\mathcal{G}}_{\varepsilon\alpha\sigma,\varepsilon'\alpha'\sigma'}(E) = \delta_{\varepsilon\varepsilon'}\delta_{\alpha\alpha'}\delta_{\sigma\sigma'}\hat{\mathcal{G}}^0_{\varepsilon\alpha\sigma}(E) \quad \text{(A6)}$$
$$+ \sum_{jj'}\hat{\mathcal{G}}^0_{\varepsilon\alpha\sigma}(E) t^j_{\varepsilon\alpha\sigma}\hat{\mathcal{G}}^d_{j\sigma,j'\sigma'}(E) t^{\star j'}_{\varepsilon'\alpha'\sigma'}\hat{\mathcal{G}}^0_{\varepsilon'\alpha'\sigma'}(E),$$

which yields

$$\mathcal{G}^<_{\varepsilon\alpha\sigma,\varepsilon'\alpha'\sigma'}(E) = \delta_{\varepsilon\varepsilon'}\delta_{\alpha\alpha'}\delta_{\sigma\sigma'}\mathcal{G}^{0<}_{\varepsilon\alpha\sigma}(E) \quad \text{(A7)}$$
$$+ \sum_{jj'} t^j_{\varepsilon\alpha\sigma}\left[A+B+C\right] t^{\star j'}_{\varepsilon'\alpha'\sigma'},$$

where terms in square brackets are given by

$$A = \mathcal{G}^{0R}_{\varepsilon\alpha\sigma}(E)\, \mathcal{G}^R_{j\sigma,j'\sigma'}(E)\, \mathcal{G}^{0<}_{\varepsilon'\alpha'\sigma'}(E)\,,$$
$$B = \mathcal{G}^{0R}_{\varepsilon\alpha\sigma}(E)\, \mathcal{G}^<_{j\sigma,j'\sigma'}(E)\, \mathcal{G}^{0A}_{\varepsilon'\alpha'\sigma'}(E)\,,$$
$$C = \mathcal{G}^{0<}_{\varepsilon\alpha\sigma}(E)\, \mathcal{G}^A_{j\sigma,j'\sigma'}(E)\, \mathcal{G}^{0A}_{\varepsilon'\alpha'\sigma'}(E)\,,$$

where the free Green's functions for the leads have the form

$$\mathcal{G}^{0R,A}_{\varepsilon\alpha\sigma}(E) = \frac{1}{E - \varepsilon \pm io^+}, \quad \text{(A8)}$$
$$\mathcal{G}^{0<}_{\varepsilon\alpha\sigma}(E) = 2\pi i f_\alpha(E)\delta(\varepsilon - E), \quad \text{(A9)}$$

with $f_\alpha(E)$ the Fermi function of lead α. Inserting $\mathcal{G}^<$ [Eq. (A7)] into Eq. (A5), the current can be written as

$$\langle \hat{I}_\alpha\rangle = I^0_\alpha + \delta I_\alpha. \quad \text{(A10)}$$

I^0_α arises from the first term of Eq. (A7). It describes the situation when the dot is completely decoupled ($t^j_{\varepsilon\alpha\sigma} = 0$), thus does not contribute to Aharonov-Bohm

oscillations. The influence of the quantum dot on the Aharonov-Bohm oscillations is caused by δI_α, arising from the second expression of Eq. (A7). Performing the energy sums $\sum_{\varepsilon\varepsilon'}$ in Eq. (A10) or (A5), respectively, the two contributions to the current read

$$I^0_\alpha = \frac{e}{h}\int dE \sum_\sigma \sum_\beta \left[\delta_{\alpha\beta} - |S^E_{\alpha\beta}|^2\right] f_\beta(E)\,, \quad \text{(A11a)}$$

$$\delta I_\alpha = \frac{e}{h}\mathrm{Re}\Bigg\{\int dE \sum_{\beta\beta'}\sum_{jj'}\sum_{\sigma\sigma'}\left[\delta_{\alpha\beta'}\delta_{\alpha\beta} - S^{\star E}_{\alpha\beta'} S^E_{\alpha\beta}\right]$$
$$\times \pi\rho\, t^j_{E\beta\sigma} t^{\star j'}_{E\beta'\sigma'}(-i) \quad \text{(A11b)}$$
$$\times \left[2\mathcal{G}^R_{j\sigma,j'\sigma'}(E) f_{\beta'}(E) + \mathcal{G}^<_{j\sigma,j'\sigma'}(E)\right]\Bigg\}.$$

2.   Simplification to effective 2-lead geometry

For the experimental setup used by Schuster et al.[2] (and equivalently for the ensuing papers[3,4,5,6]) to measure transmission phase shifts, two simplifying assumptions can be made. The first allows us to neglect non equilibrium effects, the second to perform NRG calculations for a simplified geometry, in which the dot is coupled only to two leads.

(i) Neglect of non equilibrium effects: In the experimental setup used by Schuster et al.,[2] the leads $\alpha = 3, 4, 5$ and 6 serve as draining reservoirs (to prevent multiple traversals of the ring, see below), and are all kept at chemical potential $\mu_\alpha = 0$. This also fixes the chemical potential of the ring, referred to as "base region" in Ref. 2, to equal zero. Lead 1 and 2 serve as emitter and collector, respectively, with chemical potentials μ_1 and μ_2, and Fermi functions $f_{1,2}(E) = f_0(E - \mu_{1,2})$. Now, the point contacts between emitter or collector and the base region (marked P_1 and P_2 in Fig. 4) are so small that the voltage drops occur directly at these point contacts, and *not* at the tunnel barriers coupling the dot to the ring. Thus, while the emitter or collector inject or extract electrons into or from the base region, respectively, this is assumed to happen at a sufficiently small rate that the base region is not disturbed. In other words, *we may assume that the dot, ring, and electrodes 3, 4, 5, 6 are all in equilibrium with each other,* and that the dot Green's functions $\mathcal{G}^{R,A,<}_{j\sigma,j'\sigma'}(E)$ do not depend on μ_1 and μ_2 at all. Thus, the lesser function can be expressed in terms of the retarded and advanced ones using the following standard equilibrium relation:

$$\mathcal{G}^<_{j\sigma,j'\sigma'}(E) = -f_0(E)\left[\mathcal{G}^R_{j\sigma,j'\sigma'}(E) - \mathcal{G}^A_{j\sigma,j'\sigma'}(E)\right]\,. \quad \text{(A12)}$$

The conductance in the linear response regime can be obtained by taking $\mu_1 - \mu_2 = eV$, where $e = |e|$, e.g. by setting

$$\mu_1 = 0, \qquad \mu_2 = -eV, \quad \text{(A13)}$$

and calculating $G = \partial I_1/\partial V$, with I_1 given by Eq. (A11).

(ii) Reduction to two-lead geometry: The reason why a multi-lead geometry was used in experiment is to avoid phase-rigidity: in an Aharonov-Bohm ring connected to only two leads, the transmission phase of the dot does not vary smoothly with gate voltage, but can assume only two distinct values, differing by π. A multi-lead geometry avoids this by strongly reducing the probability amplitudes for paths from emitter to collector to traverse the ring multiple times, since with each traversal of the ring the probability increases that electrons travelling in the ring are "siphoned off" into the side arms. We shall exploit this fact by making the assumption that *the probability amplitudes for multiple traversals of the ring are negligibly small.* This assumption allows us to replace the multi-lead geometry with one where the Aharonov-Bohm ring is coupled to only two leads, i.e. α is restricted to the values 1 and 2 (corresponding to emitter and collector), while multiple traversals of the ring are eliminated (by hand) by the following specification: The amplitude $t^j_{\varepsilon\alpha\sigma}$ to get from state $|j\sigma\rangle$ on the dot to state $|\varepsilon\alpha\sigma\rangle$ in lead α is taken to be nonzero only for the *short, direct* path from the dot to lead α, *without* traversing the upper arm (more correctly: we take $A^L_{\varepsilon\alpha\sigma} = 0$ for $\alpha = 2, 4, 6$ and $A^R_{\varepsilon\alpha\sigma} = 0$ for $\alpha = 1, 3, 5$). When calculating the current we do allow for direct paths from lead 1 to 2 via the upper arm, and lump all flux-dependence into the corresponding scattering amplitude, taking $S^E_{12} \sim e^{i2\pi\Phi/\Phi_0}$. However, the upper arm is *ignored* for the calculation of the equilibrium local retarded or advanced Green functions $\mathcal{G}^{R,A}_{j\sigma,j'\sigma'}(E)$ using NRG. For the latter purpose, we thus use a model of a multi-level dot coupled to two independent leads, say L and R, with *equal* chemical potentials $\mu_L = \mu_R$, representing the two segments of the ring to the left and right of the ring, coupled to it by tunnelling contacts. (These two segments should be treated as independent leads, due to the assumption of no multiple traversals made above.) With the assumptions (i) and

(ii) just described, let us now obtain an expression for that part of the conductance showing Aharonov-Bohm oscillations with applied flux, $G^{AB} = \frac{\partial I_1^{AB}}{\partial V}$, where I_1^{AB} is that part of the current in lead 1 depending on $e^{i2\pi\Phi/\Phi_0}$. For the chemical potentials given by Eq. (A13), this corresponds to evaluate Eq. (A11b) with $\alpha = 1$, $\beta' = 2$ and $\beta = 1$, and we readily obtain

$$G^{AB}(T) = \frac{e^2}{h} \int dE \text{ Re } [T^\star_u(E)T_d(E)] \left(-\frac{\partial f_0(E)}{\partial E}\right),$$
$$(A14)$$

where

$$T_d(E) = \sum_{jj'}\sum_{\sigma\sigma'} 2\pi\rho \; t^j_{E1\sigma}\mathcal{G}^R_{j\sigma,j'\sigma'}(E)t^{\star j'}_{E2\sigma'} \quad (A15)$$

$$T^\star_u(E) = iS^{\star E}_{12}S^E_{11} = |T_u(E)|e^{i(2\pi\Phi/\Phi_0+\phi_0(E))} \; (A16)$$

may be interpreted as the transmission amplitudes through the lower and upper arms, respectively.

Assuming the transmission amplitude T_u through the upper arm to be energy- and temperature-independent, the Aharonov-Bohm contribution to the conductance is given by

$$G^{AB}(T) = \frac{e^2}{h}|T_u||t_d(T)|\cos(2\pi\Phi/\Phi_0+\phi_0+\alpha(T)).(A17)$$

Then, the temperature-dependent *magnitude and phase* of the transmission amplitude through the quantum dot,

$$t_d(T) = \int dE \left(-\frac{\partial f_0(E,T)}{\partial E}\right) T_d(E,T) \equiv |t_d(T)|e^{i\alpha(T)},$$
$$(A18)$$

can be (i) extracted via Eq. (A17) from the experimental results as well as (ii) calculated with NRG using Eq. (A15).

---

[1] A. Yacoby, M. Heiblum, D. Mahalu and H. Shtrikman, Phys. Rev. Lett. **74**, 4047 (1995).

[2] R. Schuster, E. Buks, M. Heiblum, D. Mahalu, V. Umansky and H. Shtrikman, Nature **385**, 417 (1997).

[3] Y. Ji, M. Heiblum, D. Sprinzak, D. Mahalu and H. Shtrikman, Science **290**, 779 (2000).

[4] Y. Ji, M. Heiblum and H. Shtrikman, Phys. Rev. Lett. **88**, 076601 (2002).

[5] M. Avinun-Kalish, M. Heiblum, O. Zarchin, D. Mahalu and V. Umansky, Nature **436**, 529 (2005).

[6] M. Zaffalon, B. Aveek, M. Heiblum, D. Mahalu and V. Umansky, cond-mat/0711.1172 (2007).

[7] U. Gerland, J. von Delft, T. A. Costi and Y. Oreg, Phys. Rev. Lett. **84**, 3710 (2000).

[8] P. G. Silvestrov and Y. Imry, Phys. Rev. Lett. **85**, 2565 (2000).

[9] P. G. Silvestrov and Y. Imry, Phys. Rev. B **65**, 035309 (2001).

[10] D. I. Golosov and Y. Gefen, Phys. Rev. B **74**, 205316 (2006).

[11] C. Karrasch, T. Hecht, A. Weichselbaum, Y. Oreg, J. von Delft and V. Meden, Phys. Rev. Lett. **98**, 186802 (2007).

[12] C. Karrasch, T. Hecht, A. Weichselbaum, J. von Delft, Y. Oreg and V. Meden, New J. Phys. **9**, 123 (2007).

[13] Y. Oreg, New J. Phys. **9**, 122 (2007).

[14] C. Bruder, R. Fazio and H. Schoeller, Phys. Rev. Lett. **76**, 114 (1996).

[15] M. Pustilnik and L. I. Glazman, Phys. Rev. Lett. **87**, 216601 (2001).

[16] D. C. Langreth, Phys. Rev. **150**, 516 (1966).

[17] H. R. Krishna-murthy, J. W. Wilkins and K. G. Wilson, Phys. Rev. B **21**, 1003 (1980).

[18] R. Bulla, T. A. Costi and T. Pruschke, Rev. Mod. Phys. **80**, 395 (2008).

[19] R. Peters, T. Pruschke and F. B. Anders, Phys. Rev. B **74**, 245114 (2006).

[20] A. Weichselbaum and J. von Delft, Phys. Rev. Lett. **99**, 076402 (2007).

[21] F. B. Anders and A. Schiller, Phys. Rev. Lett. **95**, 196801 (2005).

[22] R. Bulla, A. C. Hewson and T. Pruschke, J. Phys.: Condens. Matter **10**, 8365 (1998).

[23] P. G. Silvestrov and Y. Imry, Phys. Rev. Lett. **90**, 106602 (2003).

[24] Y. Oreg and Y. Gefen, Phys. Rev. B **55**, 13726 (1997).

[25] A. L. Yeyati and M. Büttiker, Phys. Rev. B **52**, R14360 (1995).

[26] G. Hackenbroich, Phys. Rep. **343**, 463 (2001).

[27] M. Büttiker, Phys. Rev. B **46**, 12485 (1992).

[28] J. Rammer and H. Smith, Rev. Mod. Phys. **58**, 323 (1986).

Chapter 5

NRG calculation for the Anderson model with superconducting leads

In Chapter 3 we introduced the NRG method for the single level Anderson model. Generalization to a multi-level and multi-band Anderson model is straightforward , "only" limited by the increase of the Hilbert space and for this reason by the computational resources.

For conceptual change of the system, e.g. when replacing the fermionic reservoirs by bosonic baths [39, 40], one has to check carefully that the concepts of NRG (like energy scale separation due to the logarithmic discretization of the conduction band) still apply to the new model.

Such an issue is addressed in this Chapter. Imagine a magnetic moment coupled to a superconducting reservoir. In principle, the system is well known in terms of a magnetic impurity in a superconducting host. In the low temperature limit, the two many-body effects involved, i.e. Cooper pair formation and the Kondo effect, compete with each other. For a system dominated by the superconducting gap Δ ($T_K \ll \Delta$), all reservoir electrons within the gap around the Fermi energy are paired to effective spin-0 bosons (Cooper pairs). Therefore, no electrons are available at the Fermi energy to screen the local moment on the QD. This unscreened moment leads to spin doublet as ground state. For $T_K \gg \Delta$, electrons clearly do exist within a range of T_K around the Fermi energy. The local spin gets screened and the ground state is the Kondo singlet.

But new questions arise with the possibility of well-controlled measurements of transport through a quantum dot coupled to a left and a right superconducting lead, similar to a Josephson contact. But in this setup the Josephson effect is not only determined by the phase difference of the superconducting order parameter of left and right reservoir, but it also depends on the properties of the quantum dot.

Reliable impurity solvers are needed to tackle this system. Already in the early 1990's use the numerical renormalization group method (NRG) to determine the ground state of the system [81, 82, 83, 84]. But also dynamic quantities like the spectral function [85] or the Josephson current can be calculated with NRG, as was done recently [86, 87].

It is, however, not at all obvious whether NRG still works for energy resolutions well below the gap. One aspect of this work is to show that, indeed, NRG is a reliable method

for solving this system, even at *resolutions well below the gap.*

Why does this question arise? In order to describe the pairing property of the leads, the term H_Δ

$$H_\Delta = -\sum_{\mathbf{k}} \Delta(c_{\mathbf{k}\uparrow}^\dagger c_{-\mathbf{k}\downarrow}^\dagger + c_{-\mathbf{k}\downarrow}c_{\mathbf{k}\uparrow}) \tag{5.1}$$

is added to the Anderson model given by Eq. (3.1). For simplicity we assume only a single-channel system with real superconducting order parameter Δ. Applying the standard NRG transformations (see Chapter 3.1) to the additional term H_Δ, it gives a *constant* on-site contribution of magnitude Δ for each site of the Wilson chain, contrary to the exponentially decaying couplings between neighbouring sites. The situation is depicted in Fig. 5.1. At iterations where the coupling of the Wilson chain reaches Δ, it is not obvious whether the then added sites still can be understood as a perturbation in the iterative process or not, that is whether NRG still works or not.

In the next Section we find that NRG is able to solve the impurity-superconductor problem without restriction of the energy resolution by the gap. We further calculate the local spectral function. We focus on the near-gap behaviour and find (and are able to resolve) very sharp peaks near the gap edge in the regime $\Delta \ll T_K$. For illustration of the effect of the competition between the Kondo effect and Cooper pair formation, we study the ground state of the system as a function Γ/Δ, see the last Section of this Chapter.
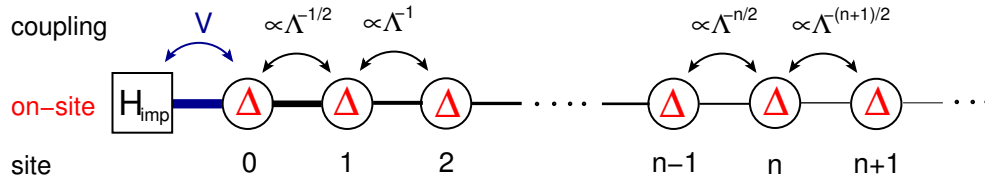

Figure 5.1: Sketch of the Wilson chain for a local level coupled to a superconducting reservoir. The superconducting property of the lead contributes a constant on-site term of magnitude Δ for each site, additional to the exponentially decaying couplings of the standard Anderson model.

Numerical renormalization group calculation of near-gap peaks in spectral functions of the Anderson model with superconducting leads

T Hecht[1], A Weichselbaum[1], J von Delft[1] and R Bulla[2,3]

[1] Physics Department, Arnold Sommerfeld Center for Theoretical Physics and Center for NanoScience, Ludwig-Maximilians-Universität München, Germany
[2] Theoretische Physik III, Elektronische Korrelationen und Magnetismus, Universität Augsburg, Germany
[3] Institut für Theoretische Physik, Universität zu Köln, Germany

E-mail: `Theresa.Hecht@physik.uni-muenchen.de`

Abstract. We use the numerical renormalization group method (NRG) to investigate a single-impurity Anderson model with a coupling of the impurity to a superconducting host. Analysis of the energy flow shows, in contrast to previous belief, that NRG iterations can be performed up to a large number of sites, corresponding to energy differences far below the superconducting gap Δ. This allows us to calculate the impurity spectral function $A(\omega)$ very accurately for frequencies $|\omega| \sim \Delta$, and to resolve, in a certain parameter regime, sharp peaks in $A(\omega)$ close to the gap edge.

1. Introduction

The vast progress in nanofabrication during the last decades made it possible to study basic physical effects in a very controlled manner. One example of such highly controllable devices are quantum dots [1], which are used, amongst various applications, for a detailed and very controlled study of the Kondo effect [2, 3, 4, 5], which is one of the prime examples of many-body phenomena. Below a critical temperature (Kondo temperature T_K) a local moment, provided by the spin of an electron occupying the quantum dot, gets screened by reservoir electrons within an energy window T_K around the Fermi energy.

These seminal experimental works on the Kondo effect, together with the possibility to engineer reservoir properties, raise the following intriguing question: What interesting effects may arise if the local moment in the quantum dot is coupled to superconducting leads while parameters like the Kondo temperature or the superconducting gap can be adjusted arbitrarily? In a superconductor as described by Bardeen, Cooper and Schrieffer (BCS) [6], electrons with opposite spin and momentum form Cooper pairs, thereby expelling the lead density of states around the Fermi energy. An energy

gap occurs. Obviously, when combining a Kondo quantum dot with superconducting reservoirs both effects compete: Screening of the local moment by electrons around the Fermi energy against pair formation of the latter.

This competition has attracted a lot of interest and various methods were used to analyze the properties of the system in the above-mentioned limits, see for example the references in [7] or [8, 9, 10, 11]. In the early 1990's Satori *et al.* [12] proposed to apply the numerical renormalization group method (NRG) [13, 14] to the problem. Since then NRG was used to calculate the ground state and subgap bound state properties like position and degeneracy [12, 15, 16] as well as their spectral weight [17, 18]. Also dynamic quantities like the spectral function [18] or the Josephson current [19, 20] can be calculated with NRG, as was done recently.

The first main goal of the present paper is to gain insight into the way NRG works when applied to a system of one local level coupled to a superconducting lead. NRG is a well established method for solving strongly correlated impurity problems. Actually, it was invented to solve the Kondo problem [13] and since then has been generalized to various schemes involving localized states coupled to fermionic [21] or bosonic [22, 23] baths. For a review, see [14]. The key idea of NRG is to discretize the conduction band logarithmically. This leads to a chain Hamiltonian with exponentially decreasing couplings, the so called Wilson chain. It can be solved iteratively by enlarging the system site by site: Due to the decreasing couplings every new site can be treated as a perturbation of the old system, thus increasing the resolution with every step.

It is, however, not at all obvious whether NRG still works for superconducting leads at energy resolutions well below the gap. This is because the pairing energy Δ is the same at all energy scales, thus remains a constant on-site contribution also in the above-mentioned chain structure. At iterations where the coupling of the Wilson chain reaches Δ, it is not obvious whether added sites still can be understood as a perturbation in the iterative process or not, that is whether NRG still works or not.

In order to address this problem, we analyze in detail the flow of the eigenenergies during the NRG procedure. We show that NRG is indeed capable to resolve the continuum close to the gap without any restriction on the energy scale of the superconducting gap.

The second goal of this work consists in the calculation of the impurity spectral function close to the gap edge at zero temperature. As in the Anderson model (with normal leads) a Kondo resonance may form. However, due to the superconducting property of the leads a gap opens up around the Fermi energy, cutting the resonance. Our main interest lies in the study of the continuum contribution to the spectral function close to the gap edge, implying the need of high resolution in that regime. Our calculations cover not only the regime $\Delta \gtrsim T_K$, for which the continuum part of the spectral function was studied in [18], but also $\Delta \ll T_K$. In the latter regime we find a sharp peak at the gap edge, vastly exceeding the Kondo resonance contribution. We expect this to lead to an enhanced linear conductance, as observed in a recent experiment [24] with carbon nanotube quantum dots coupled to superconducting leads. They report

dramatic enhancement of the linear conductance (only) in the regime $\Delta \ll T_K$.

We find similar behaviour of the spectral function in the non-interacting case where an analytical solution exists. We analyze this solution and compare our NRG results against it. We find excellent agreement especially at energies close to the gap, as expected from our study of the energy spectrum.

The paper is organized as follows: In section 2 we introduce the superconducting-lead Anderson model (SC-AM) and the NRG method. In section 3 the flow of the energy spectrum of the SC-AM is analyzed. NRG is shown to work at resolutions well below the energy scale of the superconducting gap. Section 4 discusses the calculation of the spectral function. In the last part we conclude and summarize our results.

2. The model and the method

In this section we introduce our model for the quantum dot coupled to a left and right superconducting reservoir, as well as the method we use, the numerical renormalization group method [13, 21]. We perform a Bogoliubov as well as a particle-hole transformation. We derive the formulas in a general form. For convenience, the discussions in the later sections will be restricted to a real order parameter of the superconductors, equivalent to only one lead. In the non-interacting limit the system can be understood in terms of a simple single-particle picture. The latter can be solved exactly and will serve as a guideline for gaining a deeper understanding of the problem.

2.1. Superconducting-lead Anderson model (SC-AM)

To describe a quantum state coupled to two superconducting reservoirs, we consider the standard Anderson model (AM) for a local level coupled to two metallic, non-interacting reservoirs [25], and add a BCS-type term H_Δ, describing pair formation in the leads. This SC-lead Anderson model, to be called SC-AM, is then described by

$$H = H_{dot} + H_{hyb} + H_{lead} + H_\Delta, \tag{1}$$

with

$$H_{dot} \;=\; \sum_\sigma \varepsilon_d n_{d\sigma} + U n_{d\uparrow} n_{d\downarrow} \tag{2}$$

$$H_{hyb} \;=\; \sum_{l=L,R} \sum_{\mathbf{k}\sigma} V_l(c_{l\mathbf{k}\sigma}^\dagger d_\sigma + d_\sigma^\dagger c_{l\mathbf{k}\sigma}) \tag{3}$$

$$H_{lead} \;=\; \sum_{l=L,R} \sum_{\mathbf{k}\sigma} \varepsilon_\mathbf{k} c_{l\mathbf{k}\sigma}^\dagger c_{l\mathbf{k}\sigma} \tag{4}$$

$$H_\Delta \;=\; -\sum_{l=L,R} \sum_{\mathbf{k}} \Delta_l(e^{i\phi_l} c_{l\mathbf{k}\uparrow}^\dagger c_{l-\mathbf{k}\downarrow}^\dagger + e^{-i\phi_l} c_{l-\mathbf{k}\downarrow} c_{l\mathbf{k}\uparrow}). \tag{5}$$

Electrons on the dot with spin $\sigma = \{\uparrow, \downarrow\}$ are created by $d_\sigma^\dagger$ and interact via the Coulomb repulsion U with each other, $n_{d\sigma} = d_\sigma^\dagger d_\sigma$ being the charge operator for spin σ. In

the hybridization term H_{hyb}, the coupling strength V_l between dot and lead states is assumed to be real and independent of the wave vector $\mathbf{k}$. $c_{l\mathbf{k}\sigma}^\dagger$ creates an electron in lead $l = L, R$, respectively. H_{lead} describes the conduction band of metallic leads. We assume an isotropic and linearized dispersion. The density of states is then constant, $\rho_0 = 1/2D$, where the band ranges from $-D$ to D. In the following $D = 1$ will serve as energy unit. The pairing of electrons with opposite spin and momentum (Cooper-pairs) is described by H_Δ. Δ_l is the magnitude (later on often called the gap), ϕ_l the phase of the order parameter of the superconductor. For simplicity, we assume left-right symmetry, i.e. $\Delta_l = \Delta$, $\phi_l = \pm\phi/2$ and $V_l = V$, where $l = L, R$, respectively. Then the unitary rotation

$$\begin{pmatrix} c_{e\mathbf{k}\sigma} \\ c_{o\mathbf{k}\sigma} \end{pmatrix} = \frac{1}{\sqrt{2}} \begin{pmatrix} e^{-i\phi/4} & e^{i\phi/4} \\ -ie^{-i\phi/4} & ie^{-i\phi/4} \end{pmatrix} \begin{pmatrix} c_{L\mathbf{k}\sigma} \\ c_{R\mathbf{k}\sigma} \end{pmatrix}$$

of the reservoir operators yields a real Hamiltonian.

It is well known [26, 27] that the Hamiltonian of a bulk superconductor [equations (4) and (5)] can be diagonalized by a Bogoliubov transformation. Note, though, that the SC-AM cannot be understood as an AM with a superconducting lead density of states ($\rho_\Delta = |\varepsilon_k|/\sqrt{\varepsilon_k^2 + \Delta^2}$). This is because the Bogoliubov transformation explicitly depends on $\mathbf{k}$. The hybridization term $c_{l\mathbf{k}\sigma}^\dagger d_\sigma + d_\sigma^\dagger c_{l\mathbf{k}\sigma}$ would transform to a complicated object that cannot be simplified by rotating the d operators of the local dot space.

2.2. The numerical renormalization group method (NRG)

In the 1970's, K.G. Wilson came up with a scheme for solving the Kondo problem nonperturbatively: the numerical renormalization group (NRG) [13]. Since then it was generalized to various schemes, describing localized electronic states coupled to fermionic [21] or bosonic [22, 23] baths. The NRG allows thermodynamic and dynamic properties of such strongly correlated systems to be calculated at zero as well as at finite temperature. We first discuss the method for the AM ($\Delta = 0$), then for $\Delta \neq 0$. For brevity we apply all NRG transformations to the full SC-AM already in the discussion of the AM.

The key idea of NRG is to discretize the conduction band of the reservoir logarithmically. The Hamiltonian can then be transformed to a chain Hamiltonian. In this representation, equations (3) to (5) are mapped onto

$$H_{hyb} = \sqrt{\frac{2\Gamma}{\pi}} \sum_\sigma \left[\cos\frac{\phi}{4}(f_{e0\sigma}^\dagger d_\sigma + h.c.) - \sin\frac{\phi}{4}(f_{o0\sigma}^\dagger d_\sigma + h.c.) \right] \tag{6}$$

$$H_{lead} = \frac{1}{2}\left(1 + \Lambda^{-1}\right) \sum_{l=e,o} \sum_\sigma \sum_{n=0}^\infty \Lambda^{-n/2} \xi_n \left(f_{ln\sigma}^\dagger f_{ln+1\sigma} + f_{ln+1\sigma}^\dagger f_{ln\sigma}\right) \tag{7}$$

$$H_\Delta = -\Delta \sum_n \left[(f_{en\uparrow}^\dagger f_{en\downarrow}^\dagger + h.c.) - (f_{on\uparrow}^\dagger f_{on\downarrow}^\dagger + h.c.) \right]. \tag{8}$$

Electrons on site n in lead $l = e, o$ are created by $f_{nl\sigma}^\dagger$. The dot level only couples to the zeroth site of the so-called Wilson chain H_{lead}, where the hybridization is given by

$\Gamma = \pi\rho 2V^2$ (the factor 2 stems from the two leads). $\Lambda > 1$ is the discretization parameter of the conduction band. $\xi_n = (1 - \Lambda^{-n-1})(1 - \Lambda^{-2n-1})^{-1/2}(1 - \Lambda^{-2n-3})^{-1/2} \approx 1$ for large n. The hopping matrix elements between successive sites of H_{lead} fall off exponentially with $\Lambda^{-n/2}$. The resulting energy scale separation ensures that the AM can be solved iteratively. The recursion relation reads

$$H_0 = 1/\sqrt{\Lambda}\left[H_{dot} + H_{hyb} - \Delta\sum_{l=e,o}\sum_{\sigma}s_l\left(f_{l0\uparrow}^\dagger f_{l0\downarrow}^\dagger + h.c.\right)\right]$$

$$H_{N+1} = \sqrt{\Lambda}\,H_N + \frac{1}{2}\left(1 + \Lambda^{-1}\right)\sum_{l=e,o}\sum_{\sigma}\xi_N\left(f_{lN\sigma}^\dagger f_{lN+1\sigma} + h.c.\right) \quad (9)$$

$$- \Delta\,\Lambda^{N/2}\sum_{l=e,o}\sum_{\sigma}s_l\left(f_{lN+1\uparrow}^\dagger f_{lN+1\downarrow}^\dagger + h.c.\right),$$

ere $s_l = \pm 1$ for $l = e, o$, respectively. The initial Hamiltonian of the system is related to the NRG Hamiltonian by $H = \lim_{N\to\infty}\Lambda^{-(N-1)/2}\,H_N$. This relation is exact in the limit $\Lambda \to 1$ and $N \to \infty$.

Sites are added successively and at each step the enlarged system is diagonalized. Each added site then acts as a perturbation of order $\Lambda^{-1/2}$ on the previous part of the chain. Consequently, the typical energy resolution δ_n of the AM at iteration n is given by $\delta_n^{AM} \propto \Lambda^{-n/2}$. Thus, by choosing the length N of the chain large enough (so that $\Lambda^{-N/2}$ is much smaller than all other energies in the problem), all relevant energy scales can be resolved and treated properly. When adding a site to the system, the dimension of the Hilbert space gets multiplied by the dimension d of the state space of that site, yielding $d = 4$ for a single fermionic lead (empty, singly occupied (either up or down), doubly occupied). Therefore the dimension of the Hilbert space increases exponentially with the length of the chain. Wilson proposed a truncation scheme according to which only the lowest N_{kept} eigenstates are kept at each iteration, thereby ensuring that the dimension of the truncated Hilbert space stays manageable. Recently, it was shown that by keeping track of the discarded states a complete, but approximate, basis of states can be constructed [28, 29]. This can be used to calculate dynamic properties like the spectral function $\mathcal{A}$ (see equation (20) below) which rigorously satisfy relevant sum rules [30, 31], like $\int d\omega\mathcal{A}(\omega) = 1$.

Applying the NRG mapping also to the pairing term of the SC-AM (as already done above), an on-site contribution appears, see equation (8), constant in magnitude for each site. In the limit $\Lambda^{-n/2} \gg \Delta$, this additional term hardly affects the properties of the system. But, when $\Lambda^{-n/2} \sim \Delta$, it is not obvious whether the added sites still act as a perturbation in the iterative process (9) or not, that is whether the energy scale separation still works or not. In section 3 we will show that the separation of energy scales does work also at resolutions much smaller than the gap.

2.3. Bogoliubov and particle-hole transformations

Satori *et al.* [12] have shown that a computationally more convenient representation of the Hamiltonian can be obtained by performing a Bogoliubov-Valatin transformation $[b_{ln,\sigma} = 1/\sqrt{2}(\sigma f_{ln,\sigma} + f_{ln,-\sigma}^{\dagger})]$ as well as a particle-hole transformation $[\tilde{c}_{l,2n,\sigma} = b_{l,2n,\sigma}, -\sigma\tilde{c}_{l,2n-1,-\sigma} = b_{l,2n-1,\sigma}^{\dagger}]$. $n = -1$ represents the dot, thus $\tilde{d}_{\sigma} = \tilde{c}_{-1,\sigma}$. Applying these transformations to (9), the Hamiltonian reads

$$\tilde{H}_{dot} = \frac{U}{2}(1 - \tilde{n}_d + 2\tilde{n}_{d\uparrow}\tilde{n}_{d\downarrow}) - (\varepsilon_d + \frac{U}{2})(\tilde{d}_{\uparrow}^{\dagger}\tilde{d}_{\downarrow}^{\dagger} + \tilde{d}_{\downarrow}\tilde{d}_{\uparrow}) \tag{10}$$

$$\tilde{H}_{hyb} = \sqrt{\frac{2\Gamma}{\pi}} \sum_{\sigma} \left[\cos\frac{\phi}{4} \ (\tilde{c}_{e0\sigma}^{\dagger}\tilde{d}_{\sigma} + h.c.) - \sin\frac{\phi}{4} \ (\tilde{c}_{o0\sigma}^{\dagger}\tilde{d}_{\sigma} + h.c.) \right] \tag{11}$$

$$\tilde{H}_{lead} = \frac{1}{2}(1 + \Lambda^{-1}) \sum_{l=eo} \sum_{\sigma,n=0}^{\infty} \Lambda^{-n/2} \, \xi_n \, (\tilde{c}_{ln\sigma}^{\dagger}\tilde{c}_{ln+1\sigma} + \tilde{c}_{ln+1\sigma}^{\dagger}\tilde{c}_{ln\sigma}) \tag{12}$$

$$\tilde{H}_{\Delta} = -\sum_{n=0,\sigma}^{\infty} (-1)^n \Delta \, (\tilde{n}_{en\sigma} - \tilde{n}_{on\sigma}). \tag{13}$$

Operators in the new basis will always be denoted by a tilde, e.g. $\tilde{n}_{d\sigma} = \tilde{d}_{\sigma}^{\dagger}\tilde{d}_{\sigma}$ or $\tilde{n}_{ln\sigma} = \tilde{c}_{ln\sigma}^{\dagger}\tilde{c}_{ln\sigma}$. The $\tilde{Q}$ nonconserving property of H_{Δ} has been transferred to $\tilde{H}_{dot}$. This has two useful effects: (i) For the *symmetric model* not only the z-component of the total spin (per iteration), $\tilde{S}_{zN} = \frac{1}{2}\sum_{l,n=-1}^{N}(\tilde{n}_{ln\uparrow} - \tilde{n}_{ln\downarrow})$, but also the particle number $\tilde{Q}_N = \sum_{l,n=-1,\sigma}^{N}(\tilde{n}_{ln\sigma} - 1)$ is a conserved quantum number (note that this definition yields $\tilde{Q} = 0$ for the Fermi sea together with a singly occupied dot at $\Gamma = 0$). Therefore the dimensions of the matrices to be diagonalized at each iteration (and therefore the numerical effort) is reduced significantly. (ii) Additionally, in the non-interacting symmetric case $(U, \varepsilon_d = 0)$ the Hamiltonian takes a very simple quadratic form. We will focus on its exact solution in the next section. In section 3 the resulting single-particle picture will serve as a tool to gain a deeper understanding of reasons why NRG does work for the SC-AM.

For simplicity, we use $\phi = 0$ in the following. Then, the odd channel decouples and the problem reduces to an effective one-lead system. The resulting model is equivalent to that describing an impurity embedded in a bulk superconductor.

2.4. Single-particle picture

Some properties of the system show up already in the non-interacting case, $U = 0$. The Hamiltonian is then of quadratic form and we only have to solve a single-particle problem. The NRG Hamiltonian [(10)-(13)] can be diagonalized up to a large number of iterations exactly - that is without truncating the Hilbert space. One can use the resulting exact solution as benchmark for the NRG result. We obtain very good agreement in the energy spectrum, thus confirming that NRG is capable of accurately treating superconducting leads. In section 3 the single-particle picture will also serve as a tool to gain a deeper understanding of reasons why NRG does work for the SC-AM.

Without lack of generality we restrict the discussion to the symmetric case, $\varepsilon_d = 0$. Then the NRG Hamiltonian only contains quadratic terms of the form $a_i^\dagger a_{i'}$, with a_i some fermionic operator. For every iteration N the single-particle Hamiltonian can be diagonalized by some unitary transformation T to $H_N = \sum_{j=-1}^{N} \varepsilon_j \alpha_j^\dagger \alpha_j$. Here $\alpha_j = T_{ji}^\dagger a_i$ and the eigenstates $|n_j\rangle = \alpha_j^\dagger |\text{vac}\rangle$ satisfy $\alpha_j^\dagger \alpha_j |n_j\rangle = n_j |n_j\rangle$. The many-body eigenstates and the energy spectrum follow from the Schrödinger equation

$$H|m\rangle = E_m|m\rangle, \quad E_m = \left(\sum_{\{n_j\}_m} \varepsilon_j n_j\right) - E_0, \tag{14}$$

with the many-body eigenstates $|m\rangle = |n_1 \dots n_N\rangle$ and eigenenergies E_m which are calculated w.r.t. the ground state energy E_0. In the ground state $|0\rangle$ all single-particle levels with energy below the Fermi energy $\varepsilon_F = 0$ are occupied, thus $E_0 = \sum_{l(\varepsilon_l < 0)} \varepsilon_l$. Expectation values of local operators are evaluated easily, e.g. $\langle 0|a_{-1} a_{-1}^\dagger |0\rangle = \sum_l U_{-1,l}^\dagger \langle 0|\alpha_l \alpha_l^\dagger |0\rangle U_{l,-1} = \sum_{l(\varepsilon_l < 0)} |U_{l,-1}|^2$.

The construction of the many-body spectrum from the single-particle energy levels using (14) is illustrated in figure 1 for the SC-AM. Figure 1(a) shows a sketch of a typical single-particle spectrum. The single-particle level spectrum consists of a continuum above and below the gap, $|\varepsilon_l| > \Delta$ (represented by a discrete set of closely-spaced levels), as well as one subgap level with energy $0 \leq \varepsilon_0 < \Delta$, the so-called Andreev level. Note that because of the discretized conduction band, we also have a discretized continuum.

The sketch also demonstrates the construction of the lowest lying many-body eigenenergies using (14). For $\Gamma > 0$, no single-particle level exists at the Fermi energy and the many-body ground state is a singlet ($\tilde{S}_z = 0$, $\tilde{Q} = 0$). The first excitation is a degenerate doublet ($E_{1,2} = \varepsilon_0$, $\tilde{S}_z = \pm 1/2$, $\tilde{Q} = 1$), corresponding to the bound single-particle level, occupied by either a spin up or down. If $\varepsilon_0 < \Delta/2$, an additional subgap state forms ($E_3 = 2\varepsilon_0 < \Delta$, $\tilde{S}_z = 0$, $\tilde{Q} = 2$), corresponding to spin up *and* down occupying the subgap single-particle level. Otherwise $E_3 > \Delta$ is part of the continuum energies. A concrete example of the many-body as well as the single-particle eigenenergies is shown in figure 1(b). Both the single-particle levels (stars, crosses) as well as the resulting many-body eigenenergies are shown. On the vertical axis the energies of the many-body eigenstates constructed in figure 1(a) are specified.

3. Energy spectrum

In this section we analyze the many-body energy spectrum generated during the iterative NRG procedure. As already mentioned in the last section, the spectrum consists of a continuum above and subgap bound states below the gap Δ. The competition between the Kondo effect and Cooper pair formation is reflected in the ground state properties of the system. A detailed analysis of the structure of the continuum with the help of the single-particle picture reveals that, interestingly, energy scale separation is even more efficient at energy scales smaller than the gap (compared to the AM).
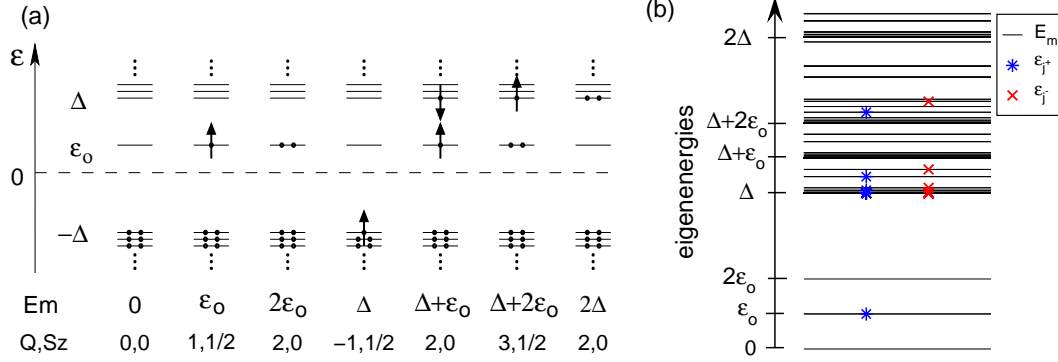
Figure 1. Single-particle and many-body eigenenergies for the SC-AM ($U = \varepsilon_d = 0$). (a) Schematic sketch of a typical single-particle level spectrum of the SC-AM. The continuum is represented by a discrete set of closely-spaced levels. The construction of the lowest lying many-body eigenstates in terms of single-particle states according to (14) is illustrated. The corresponding energies E_m (w.r.t. the ground state energy) and quantum numbers of the many-body states are also given. Two dots stand for a doubly occupied level. (b) Single-particle energies ε_j ($\varepsilon_j^+ > 0$: stars, $\varepsilon_j^- < 0$: crosses), as well as the corresponding many-body eigenenergies E_m (lines) for $\Delta = 10^{-4}$ and $\Gamma/\Delta = 0.3$ at a late NRG iteration ($\delta_n \ll \Delta$). The many-body eigenenergies depicted in (a) are specified on the right hand side. The single-particle continuum energies go like $\varepsilon_j^\pm - \Delta \propto \Lambda^{2j}$, see section 3.2. Due to many-particle excitations, this dense profile repeats as substructures in the many-body spectrum at $m\Delta + r\varepsilon_0$ ($m = 1, 2, \ldots$, $r = 0, 1, 2$).

Figure 2 shows the 280 lowest lying many-body eigenstates for the even NRG iterations of a SC-AM in different regimes of T_K/Δ. We first discuss the case $\Delta = 0$ (AM, figure 2(a),(d)), then $\Delta \neq 0$. For the AM the effective level spacing of the Wilson chain drops exponentially with every added site (see discussion above). The energy resolution of the kept states is enhanced exponentially with increasing iteration n, see figure 2(a). Thus, an appropriate way of visualizing the physics at different energy scales is given by the rescaled energy spectrum. In these "energy flow diagrams", the eigenenergies are plotted in units of $\Lambda^{-n/2} \propto \delta_n^{\mathrm{AM}}$, see figure 2(d). Only at energy scales where the system changes its properties, the flow of the eigenenergies changes. For the AM we are interested in the lowest of these scales, the Kondo scale $T_K = \sqrt{\frac{U\Gamma}{2}} \exp\left[\frac{\pi\varepsilon_d}{2\Gamma U}(U + \varepsilon_d)\right]$, indicated by dashed arrows in the figure. For details of the various fixed points of the AM see e.g. [21].

In contrast to the exponential decaying couplings of the Wilson chain (7), the on-site contribution Δ of the pairing term (8) is constant in magnitude for each site. Consequently, for $\delta_n < \Delta$, the BCS contribution is a relevant perturbation and determines the physics of the system. Typical energy spectra (or energy flow diagrams, respectively) for finite Δ are shown in figure 2(b,c) (or 2(e,f)). At energy scale Δ, the exponential reduction of the eigenenergies crosses over to a saturation towards Δ. The characteristic gap as well as the subgap Andreev bound states form.

NRG calculation of the spectral function of the SC-AM 9

The structure of the continuum energies near the gap will be discussed in section 3.2. We show there that even though the on-site terms of H_Δ do not fall off exponentially like the couplings of the Wilson chain, the energy scale separation (the heart of NRG) still works.
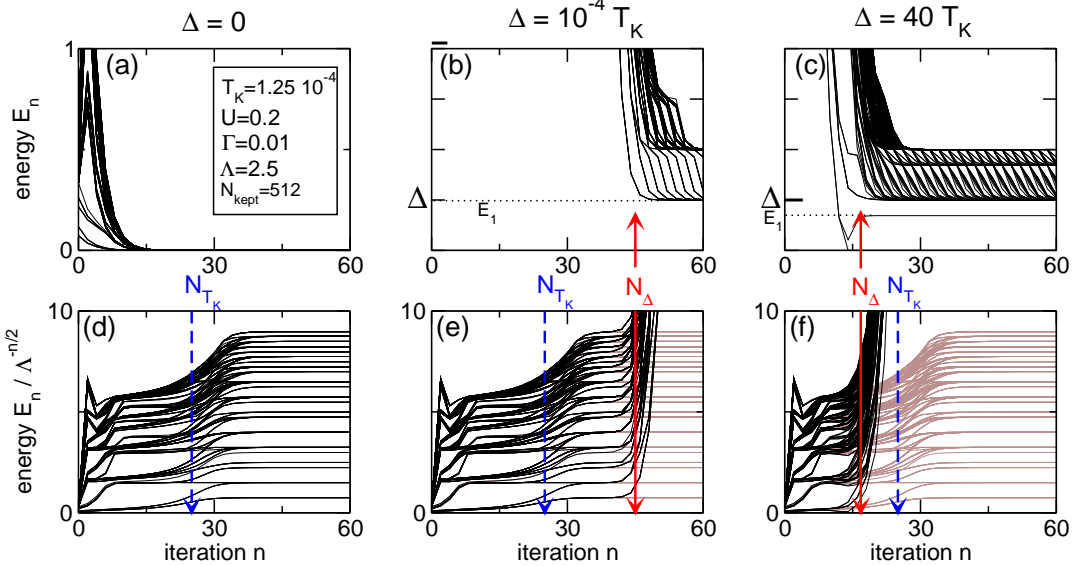

Figure 2. Energy spectra (a,b,c) and the corresponding energy flow diagrams (d,e,f) for the lowest 280 eigenenergies of the even NRG iterations of a SC-AM. $U = 0.2$, $\Gamma = 0.01$, $T_K = 1.25 \cdot 10^{-5}$, $\Lambda = 2.5$ and $N_{\text{kept}} = 512$ in all plots. The iteration numbers N_{T_K} or N_Δ, where $\delta_n^{\text{AM}} \approx T_K$ or Δ, respectively, are indicated by dashed or solid arrows. (a,d): $\Delta = 0$, AM. Since $\delta_n^{\text{AM}} \propto \Lambda^{-n/2}$, the eigenenergies (a) fall off exponentially with n and the energy flow diagram (d) converges. At energy scale T_K the localized spin gets screened by the conduction electrons and the Kondo singlet (ground state) forms. (b,c,e,f): $\Delta > 0$. At energy scale Δ the exponential decrease crosses over to a saturation towards Δ. The characteristic gap as well as the Andreev bound states form. Consequently, the flow diagram energies grow with $\Delta\Lambda^{n/2}$ due to rescaling. For comparison, the result for the AM is indicated (brown), too. For $\Delta \ll T_K$ (b,e) it is energetically favorable to break Cooper pairs and lower the energy by T_K by screening the local spin, thus the ground state is a singlet. For $\Delta \gg T_K$ (c,f) Cooper pair formation dominates the low energy properties and the ground state is a doublet.

3.1. Competition between Kondo effect and Cooper pair formation

The system possesses two energy scales determining the characteristics of the system, T_K and Δ. The resulting competition between Kondo effect and Cooper pair formation is reflected in the ground state properties of the system: For $T_K \ll \Delta$, H_Δ is the dominant term of the Hamiltonian. The system lowers its energy by Δ by the formation of Cooper pairs leading to effective spin zero bosons (singlets) in the reservoir. The lead density of states gets depleted, a gap from $-\Delta$ to Δ forms. Therefore no electrons are available

to screen the localized spin. Consequently, the ground state is a spin doublet with $S_z = \pm 1/2$. In case when the Kondo effect is dominant ($T_K \gg \Delta$), it is energetically favorable to break Cooper pairs so that the localized spin on the quantum dot gets screened by the non-paired electrons near the Fermi energy. The energy is lowered by T_K and as ground state the typical Kondo singlet forms ($S_z = 0$). The influences of the different scales is also apparent in the NRG energy flow diagrams, see figure 2(e),(f). For example, for $T_K \gg \Delta$, the effect of H_Δ sets in at iterations after the Kondo fixed point is reached (i.e. at lower energies). A phase diagram for the singlet and doublet ground state including the spectral weight of the bound states was recently derived by [18] (also using NRG) for the whole regime of Δ, Γ.

3.2. Analysis of the continuum

The key feature of NRG is the energy scale separation: The couplings between successive sites of the Wilson chain describing a normal lead fall off exponentially, therefore each added site can be treated as a perturbation of the previous system. However, when generalizing the AM to superconducting leads, a *constant* on-site energy Δ is added at each site (see (9)). In order to understand why NRG works even at resolutions well below Δ, we now take a closer look at the structure of the continuum produced during the iterative NRG procedure.

We therefore analyze the (positive) continuum of the single-particle problem. Figure 3 shows an example of a single-particle spectrum for three different scalings of the vertical axis: In (a) the (unscaled) spectrum is plotted versus the iteration number. The NRG eigenenergies decrease with iteration number n and tend towards Δ. However, the decrease of the continuum eigenenergies depends on whether n is smaller or larger than N_Δ, the iteration number for which $\delta_n^{\mathrm{AM}} \approx \Delta$. We find the following asymptotic behaviour:

$$\varepsilon_{jn}: \quad \begin{cases} \varepsilon_{jn} & \propto & \Lambda^{j-n/2} & \text{for} & n < N_\Delta, \\ \varepsilon'_{jn} = \varepsilon_{jn} - \Delta & \propto & \Lambda^{2j-n} & \text{for} & n > N_\Delta. \end{cases} \tag{15}$$

Primed energies will henceforth always be understood to be measured relative to Δ. Both relations of (15) are illustrated in figures 3(b) and 3(c), by plotting the eigenenergies ε_{jn} and ε'_{jn} in units of $\Lambda^{-n/2}$ and Λ^{-n}, respectively.

These results can already be understood by further reducing the problem to only the superconducting reservoir ($H_l + H_\Delta$): For fixed iteration n, the j-dependence of (15) reflects the standard logarithmic discretization of the continuous conduction band, according to which the single-particle energies of the Wilson chain grow in powers of Λ, i.e. $\varepsilon_k \propto \Lambda^j$ [21]. Inserting this into the single-particle dispersion relation of BCS quasiparticles, the effective discretization of the isolated superconducting reservoir is obtained, as sketched in figure 4. The limits yield

$$\xi_k = \sqrt{\varepsilon_k^2 + \Delta^2}: \quad \begin{cases} \xi_k \approx & \varepsilon_k & \rightarrow & \Lambda^j & \text{for} & \varepsilon_k \gg \Delta & (n < N_\Delta), \\ \xi'_k \approx & \frac{\varepsilon_k^2}{2\Delta} & \rightarrow & \Lambda^{2j} & \text{for} & \varepsilon_k \ll \Delta & (n > N_\Delta). \end{cases} \tag{16}$$

The n-dependence of (15) follows heuristically from considering the coupling of two neighbouring sites $n-1$ and n, with hopping matrix element $t_n \sim \delta_n^{\mathrm{AM}}$ and on-site energy $\pm\Delta$ (see (12) and (13), respectively). Since $t_n \sim \Lambda^{-n/2}$, the eigenstates $\lambda_\pm$ of this two-state problem show the asymptotic behaviour

$$\lambda_{n\pm} = \pm\sqrt{\Delta^2 + t_n^2} : \quad \begin{cases} \lambda_{n+} \approx & t_n & \propto & \Lambda^{-n/2} & \text{for} & n < N_\Delta, \\ \lambda'_{n+} \approx & \frac{t_n^2}{2\Delta} & \propto & \Lambda^{-n} & \text{for} & n > N_\Delta. \end{cases} \quad (17)$$

Note that the $\Lambda^{-n/2}$ versus Λ^{-n} scaling of the two limits of (15) implies that the energy scale separation is actually *more* efficient in the second limit, when the gap dominates the spectral features. *This establishes one of the central results of the present paper:* The energy scale separation, being the heart of the NRG approach, is not impaired but rather enhanced (w.r.t. Δ) by the presence of the energy gap in the superconducting leads. Increasing the chain length leads to an exponential enhancement of the resolution at the continuum edge at Δ.

The many-body spectrum is constructed according to equation (14). For $n < N_\Delta$, as in the AM, the mean level spacing (at fixed iteration) does not depend on energy, as can be seen in figure 2(d-f). For $n > N_\Delta$ the gap forms, and every many-body state with energy $E_m < \Delta + \varepsilon_0$ can only stem from adding one electron (or hole) to the Fermi sea. ε_0 is the energy of the single-particle subgap level. Therefore in this regime $E_{j\sigma n} = \varepsilon_{jn}$. Due to many-particle excitations, this dense profile repeats as substructures in the many-body spectrum at $m\Delta + r\varepsilon_0$ ($m = 1, 2, \ldots$; $r = 0, 1, 2$), as can be found in figure 1(b), which was calculated for some late iteration with $n \gg N_\Delta$.

4. Spectral function

In this section we study basic properties of the spectral function that are special for the SC-AM. We therefore begin by analyzing the analytic solution of the non-interacting case and find not only a continuum for energies $|\omega| > \Delta$ together with subgap resonances (as expected from the energy spectrum), but also a sharp peak at the gap edge for $\Delta < \Gamma$. The agreement between NRG results and the analytic solution is excellent, especially when resolving that sharp feature, again confirming that NRG is valid also at resolutions well below the gap. Subsequently, we consider spectral functions at finite U, which show some of the same feature as found for the non-interacting case.

Knowledge of the energy spectrum suffices to calculate thermodynamic quantities, such as the impurity specific heat. We focus here instead on the more complex calculation of the local spectral function $A_\sigma(\omega)$. As this is a dynamic quantity, all energy scales have to be taken into account even at temperature zero. The spectral function is defined as

$$\mathcal{A}_\sigma(\omega) = -\frac{1}{\pi} \mathrm{Im}\, G_\sigma^R(\omega), \quad (18)$$

where $G_\sigma^R(\omega)$ is the Fourier-transformed of the retarded Green's function $G_\sigma^R(t) \equiv -i\theta(t)\langle [d_\sigma(t), d_\sigma^\dagger(0)]_+ \rangle$. Motivated by the structure of the eigenspectrum we distinguish
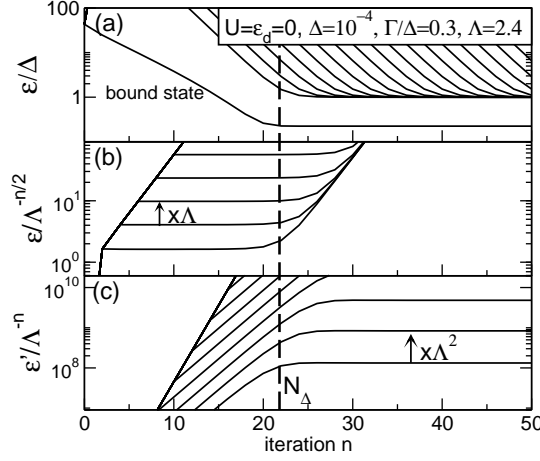
Figure 3. Positive single-particle energies plotted for three different scalings of the vertical axis for even iterations. The vertical dashed line indicates the iteration N_Δ for which $\delta_n^{\mathrm{AM}} \approx \Delta$. (a) Energy versus iteration number. The single-particle levels flow towards the gap and form a continuum. The bound state can be also seen. (b) The eigenenergies ε representing the continuum in units of $\Lambda^{-n/2}$, corresponding to the customary scaling for energy flow diagrams of the (normal) AM. For $n < N_\Delta$, the single-particle energies run horizontally, since they obey $\varepsilon_{jn} \propto \Lambda^{j-n/2}$, see text and [21]. (c) ε' in units of Λ^{-n}. The single-particle energies run horizontally for $n > N_\Delta$, since here they scale as $\varepsilon'_{jn} \propto \Lambda^{2j-n}$. The line sloping upwards at the left of figures (b) and (c) is due to the fact that at every iteration a degeneracy is split and hence an extra eigenenergy is generated.
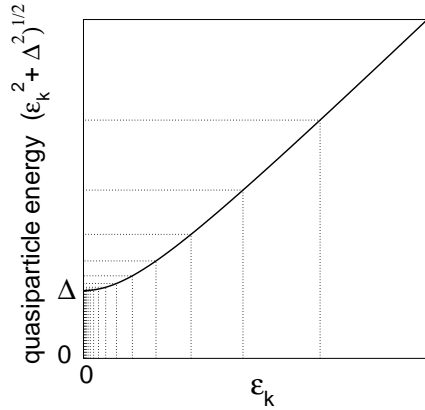

Figure 4. Logarithmic discretization of ε_k leads to high resolution at the band edge of the BCS quasiparticle eigenenergies.

two contributions to the spectral function,

$$\mathcal{A}_\sigma(\omega) = \sum_{|E_m| < \Delta} w_m \delta(\omega - E_m) + A_\sigma(\omega)\, \theta(|\omega| - \Delta). \tag{19}$$

w_m denotes the weight of excitations to the Andreev bound states, which contribute as δ-peaks within the gap between $-\Delta$ and Δ. $A_\sigma(\omega)$ represents the continuum contribution,

with $|\omega| > \Delta$. In the following we present results for the continuum part of the spectral function. We focus on the behaviour of the continuum contribution of the spectral function close to the gap.

4.1. NRG

NRG calculations of the spectral function are based on the Lehmann representation:

$$\mathcal{A}_\sigma(\omega) = \frac{1}{Z} \sum_{mm'} (e^{-\frac{E_m}{k_B T}} + e^{-\frac{E_{m'}}{k_B T}}) \, |\langle m|d_\sigma^\dagger|m'\rangle|^2 \, \delta(\omega - (E_m - E_{m'})). \quad (20)$$

Here $Z = \sum_m e^{-E_m/k_B T}$ is the partition function at temperature T, and $|m\rangle$ denotes an exact eigenstate of the Hamiltonian with eigenenergy E_m. The matrix elements of these operators as well as the eigenenergies can be calculated with NRG at all energy scales. The δ-peaks of the continuum contribution are broadened as described by [32, 31]. As expected from the findings about the spectra, broadening w.r.t. Δ (i.e. using $\omega' = |\omega| - \Delta$ in [31]) leads to good results, see below. We use the full density matrix NRG [31, 30] at effective temperature zero, i.e. at temperature much smaller than any other energy scale of the problem. Only matrix elements connecting the ground state(s) with excited states then contribute.

As NRG parameters we choose $\Lambda = 1.8$ and use z-averaging [33] (where for fixed Λ data is averaged for different discretizations) with an interval spacing of $\delta z = 0.05$ to impoove the results. We keep $N_{\text{kept}} = 1024$ at the first 6 to 10 iterations, and use $N_{\text{kept}} = 512$ for the rest of the iterations. We test NRG against the analytic solution at $U = 0$ and find excellent agreement, implying that the broadening procedure as well as the choice of N_{kept} are adequate for the present problem.

4.2. Spectral function for $U = 0$

For analyzing the basic properties of $A(\omega)$, we first review the non-interacting problem. There, the local (retarded) Green's function is known exactly [18]. The continuum contribution to G^0 then reads

$$G_\Delta^0(\omega) = \frac{1}{D(\omega)} \{(\omega + \varepsilon_d) + i \, \Gamma \rho_\Delta\}, \quad (21)$$

with $D(\omega) = (\omega^2 - \Gamma^2 - \varepsilon_d^2) + i \, 2\Gamma\omega\rho_\Delta$, and ρ_Δ the density of states of a bulk superconductor. At temperature $T = 0$, the latter has the limits

$$\rho_\Delta(\omega) = \frac{\theta(|\omega| - \Delta) \, |\omega|}{\sqrt{\omega^2 - \Delta^2}} \approx \begin{cases} \sqrt{\frac{\Delta}{2|\omega'|}} \, \theta(\omega'), & \text{for} \quad \omega' \ll \Delta, \\ 1, & \text{for} \quad \Delta \ll |\omega|. \end{cases} \quad (22)$$

For $\Delta = 0$, equation (21) simplifies to the well known formula for the AM, $G_{\Delta=0}^0(\omega) = (\omega - \varepsilon_d - i\Gamma)^{-1}$. For the spectral function we obtain from equations (21) and (18),

$$A(\omega) = \frac{(\omega + \varepsilon_d)^2 + \Gamma^2}{(\omega^2 - \varepsilon_d^2 - \Gamma^2)^2 + (2\Gamma^2\omega\rho_\Delta)^2} \, \Gamma \, \rho_\Delta/\pi. \quad (23)$$

This function is shown for various parameter combinations in figure 5. The common features are (i) the atomic resonance of width (half width half maximum) $\sim \Gamma$ centered
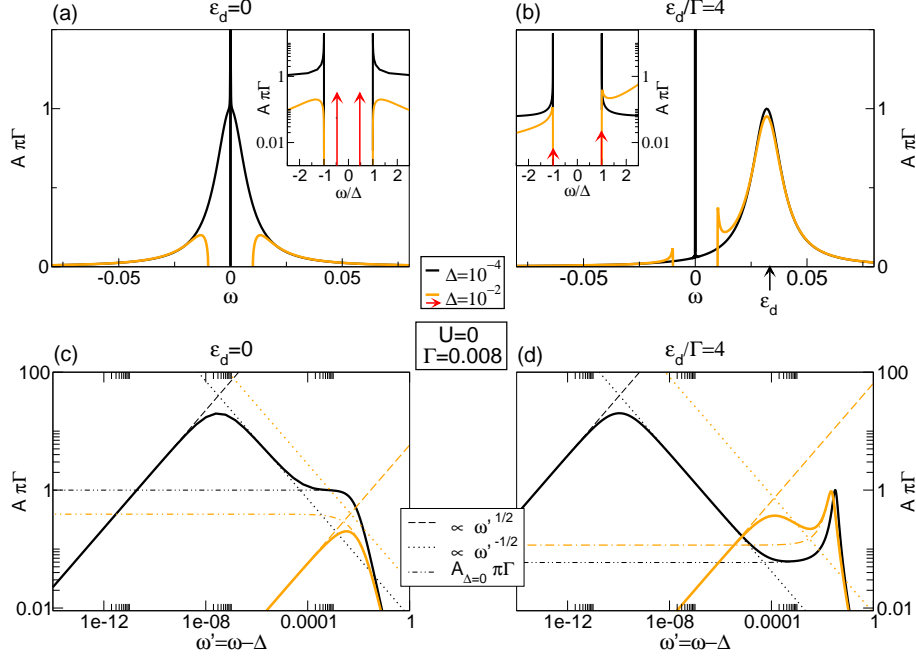
Figure 5. Continuum contribution $A(\omega)$ to the spectral function for $U = 0$, $\Gamma = 0.008$ and $\Delta = 10^{-4}$ as well as $\Delta = 10^{-2}$ obtained from equation (23). (a,c) show a symmetric and (b,d) an asymmetric SC-AM. In (a,b), a linear scale is used revealing sharp peaks near the gap if $\omega_c' \ll \Delta$. The insets, which zoom in the region of the gap edge, show the full height of the near-gap peaks. They also indicate, using position and length of arrows, the energy and weight of the subgap contribution for the case $\Delta = 10^{-2}$ (calculated with NRG). In (c,d), for the same data a log-log scale is used to elucidate the asymptotic behaviour of (25) (dashed and dotted lines) and (26) (dashed-dotted lines).

at ε_d, reflecting the level broadening due to the level-lead coupling and (ii) a gap from $-\Delta$ to Δ, with (iii) bound states at some energy $\pm\omega_B$ inside the gap. The energy and weight of the subgap contribution is indicated for $\Delta = 10^{-2}$ by position and length of the red arrows in the insets of figure 5(a,b). Here they are calculated with NRG, but can be also obtained analytically, see equation (7) of [18]. Note that for finite Γ bound states exist also for $\varepsilon_d \gg \Delta$, see figure 5(b). They asymptotically approach the gap edge for $|\varepsilon_d| \to \infty$, in accordance with equation (7) of [18].

Additionally, the continuum part of the spectral function may feature near-gap sharp peaks, point of interest in the following discussion. The behaviour near the gap edge can be approximated (using equation (22) and writing $s = \text{sign}(\omega)$) by

$$A(\omega) \approx \frac{(s\Delta + \varepsilon_d)^2 + \Gamma^2}{(\Delta^2 - \Gamma^2 - \varepsilon_d^2)^2 + 4\Gamma^2\Delta^2 + 2\Gamma^2\Delta^3/\omega'} \, \Gamma\rho_\Delta/\pi \qquad (24)$$

$$\approx \begin{cases} \frac{(s\Delta+\varepsilon_d)^2+\Gamma^2}{2\Gamma^2\Delta^3} \, \Gamma\rho_\Delta\omega'/\pi & \propto \sqrt{\omega'}, \quad \text{for} \quad \omega' \ll \omega_c', \\ \frac{(s\Delta+\varepsilon_d)^2+\Gamma^2}{(\Delta^2-\Gamma^2-\varepsilon_d^2)^2+4\Gamma^2\Delta^2} \, \Gamma\rho_\Delta/\pi & \propto \frac{1}{\sqrt{\omega'}}, \quad \text{for} \quad \omega_c' \ll \omega' \ll \Delta. \end{cases} \qquad (25)$$
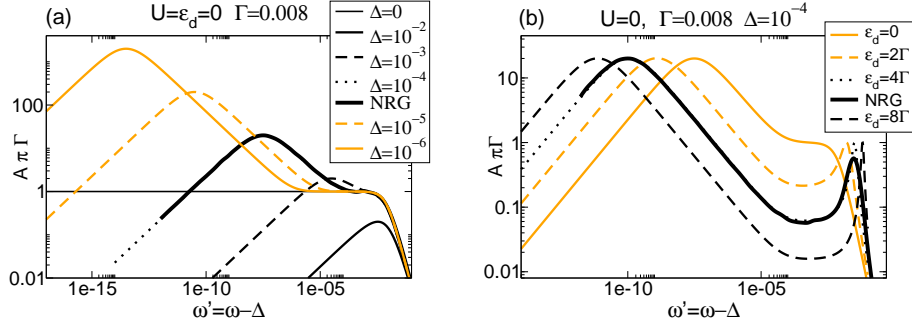
Figure 6. Continuum contribution $A(\omega')$ to the spectral function for $U = 0$, $\Gamma = 0.008$, as obtained from (23), for (a) various values of Δ and $\varepsilon_d = 0$ (symmetric model) and (b) $\Delta = 10^{-4}$ and various values of ε_d (asymmetric model). For $\omega'_c \ll \Delta$ a sharp peak forms at the gap edge. The increase (decrease) of $A(\omega')$ goes as $\omega'^{\frac{1}{2}}$ ($\omega'^{-\frac{1}{2}}$). NRG results, shown for $\Delta = 10^{-4}$ only (thick black lines), are in excellent agreement with the exact analytical results for $\omega' \ll \Delta$. Note in (b) that the height of the near-gap peak at the gap edge does not depend on ε_d.

The limits given in (25) are indicated by the thin lines in figure 5(c,d): $A(\omega)$ increases as $\sqrt{\omega'}$ when ω' is increased from 0 (dashed lines), decreasing again for $\omega' > \omega'_c = \frac{2\Gamma^2\Delta^3}{(\Delta^2 - \Gamma^2 - \varepsilon_d^2)^2 + 4\Gamma^2\Delta^2}$ (which is the zero of derivative of equation (24)). If $\omega'_c \ll \Delta, \Gamma$, this leads to a very sharp near-gap peak which decreases as ρ_Δ (dotted lines). Then the near-gap spectral function is greatly enhanced compared to the AM (where the symmetric case yields $A(0)\pi\Gamma = 1$).

The solution of the AM (dash-dotted lines) describes the high-energy limit of the SC-AM:

$$A(\omega) \approx \frac{\Gamma/\pi}{(\omega - \varepsilon_d)^2 + \Gamma^2} = -\frac{1}{\pi}\text{Im}\, G_0^0 \quad \text{for} \quad \Delta < |\omega|. \tag{26}$$

The emergence of the near-gap peak is depicted in figure 6(a) for the symmetric model, where the gap Δ is varied over four orders of magnitude, starting from $\Delta = 0$. For $\Delta = 10^{-4}$, we also show numerical NRG results (fat solid line). Their agreement with the analytical results is excellent. The height of the near-gap peak does not depend on ε_d, see figure 6(b), where ε_d is increased up to 8Γ for fixed $\Delta = 10^{-4}$.

4.3. Spectral function for finite U

Figure 7 shows spectral functions of the SC-AM for finite U and $-U < \varepsilon_d < 0$. The two atomic resonances of width Γ are now separated by the Coulomb repulsion, thereby they are centered near ε_d and $\varepsilon_d + U$. The Coulomb repulsion also drives the Kondo effect, yielding a sharp resonance of width T_K pinned at the Fermi energy. This resonance is cut by a gap reaching from $-\Delta$ to Δ, reflecting the influence of the superconducting lead. Depending on the ratio T_K/Δ, the Kondo resonance can be cut completely ($T_K/\Delta \ll 1$) or emerge clearly ($T_K/\Delta \gg 1$).
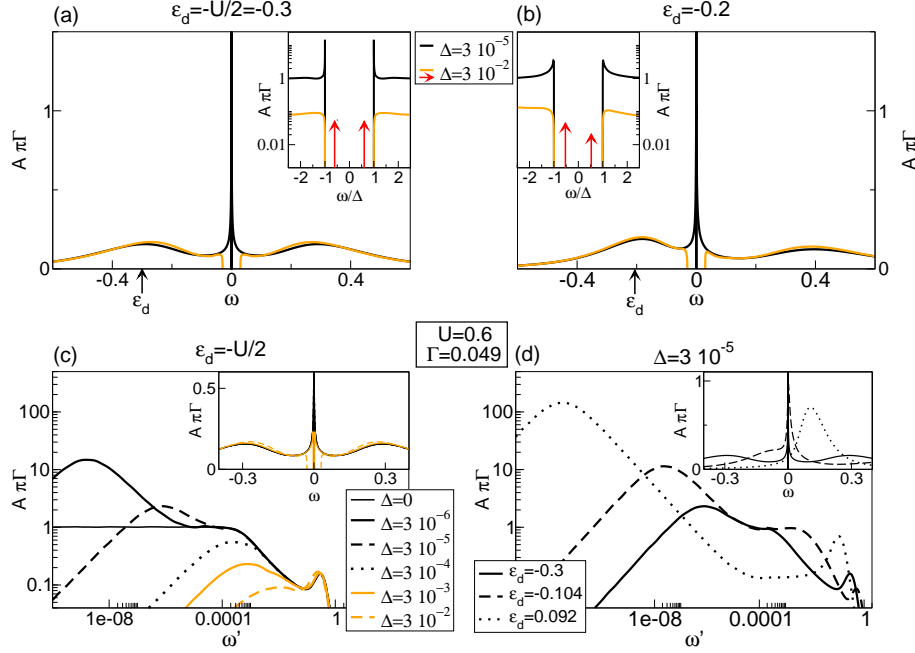
Figure 7. Continuum contribution $A(\omega)$ to the spectral function for $U = 0.6$, $\Gamma = 0.049$, calculated using NRG. (a,c) show a symmetric and (b,d) an asymmetric SC-AM. In (a,b), a linear scale is used revealing the sharp near-gap peaks appearing for $\Delta \ll T_K$. The position ε_d of the local level is indicated by an arrow. The insets zoom into the gap edge and show the sharp peaks as well as the subgap resonances (for $\Delta = 3 \cdot 10^{-2}$, indicated by red arrows). In (c,d), $A(\omega')$ is plotted on a log-log scale for various parameters. The asymptotic behaviour of the near-gap peaks is in agreement with that given in (25) and (26). In particular, for $\omega' \to 0$, the continuum edge decreases as $\sqrt{\omega'}$. (c) $\varepsilon_d = -U/2$, $T_K = 10^{-3}$, various Δ. The singlet-doublet transition occurs between $\Delta/T_K = 0.3$ and 3 (orange: ground state is doublet, black: singlet). (d) $\Delta = 3 \cdot 10^{-5}$, various ε_d, $\Delta \ll T_K$ always.

Additionally, a similar near-gap feature as found for the non-interacting case may emerge. For $T_K/\Delta \gg 1$, a sharp resonance forms at the gap edge, highly exceeding the Kondo resonance, see figure 7 for the symmetric case (where the height of the Kondo resonance is given by $1/\pi\Gamma$) as well as the antisymmetric case. The asymptotic behaviour of the near-gap peak is in agreement with that given in equations (25) and (26). In particular, for $\omega' \to 0$, the continuum edge decreases as $\sqrt{\omega'}$.

5. Conclusion

The NRG is a well established method for a variety of quantum impurity models. It is usually applicable in the whole parameter range and allows to calculate physical quantities for a wide range of temperatures and frequencies. In this paper we showed that in the presence of a superconducting reservoir, NRG provides information for resolutions far below the energy scale of the gap Δ. Moreover, Wilsonian energy scale

separation, being the heart of the success of the NRG approach, is not impaired but rather enhanced by the presence of the energy gap of the superconducting leads. This allows sharp features of spectral functions at the continuum gap edge to be resolved. Our calculations of the impurity spectral function cover the whole region from $\Delta \gg T_K$ to $\Delta \ll T_K$. In the latter case, we find a sharp peak at the continuum gap edge, vastly exceeding the Kondo resonance contribution. We expect this to result in an enhanced linear conductance, as recently reported for experiments with carbon nanotube quantum dots coupled to superconducting leads [24].

The ability of the NRG to resolve spectral functions at energy resolutions well below the gap should be useful for other problems as well. As discussed in detail in [34], the problem of an impurity in a superconducting host can be mapped (under certain conditions) to a model in which the superconductor couples to a normal metal, with a modified density of states. For the problem studied in this paper we have performed such a mapping; the resulting Hamiltonian is given in Equation (8). In this case, the oscillating on-site energies, $(-1)^n \Delta$, generate a hard gap of width 2Δ.

This connection allows us, in principle, to calculate the dynamic quantities for impurity models with arbitrary gapped bath spectral function (but for this one still has to develop an algorithm which produces directly the chain parameters from the hybridization function). Such calculations might also help to improve the resolution of the NRG in DMFT calculations for the Hubbard model where the standard implementation of the NRG does not describe the shape of the Hubbard bands properly (for dynamic DMRG calculations for this problem, see [35]).

Acknowledgments

References

[1] Kouwenhoven L and Marcus C 1998 *Physics World* **11**, 35–39
[2] Kondo J 1964 *Prog. Theor. Phys.* **32** 37–49
[3] Glazman L I and Raikh M E 1988 *JETP Lett.* **47** 452–455
[4] Ng T K and Lee P A 1988 *Phys. Rev. Lett.* **61** 1768–1771
[5] Goldhaber-Gordon D, Shtrikman H, Mahalu D, Abusch-Magder D Meirav U and Kastner M A 1998 *Nature* **391** 156–159
[6] Bardeen J, Cooper L N, and Schrieffer J R 1957 *Phys. Rev.* **108** 1175–1204
[7] Balatsky A V, Vekhter I, and Zhu J-X 2006 *Rev. Mod. Phys.* **78** 373
[8] Glazman L I and Matveev K A 1989 *JETP Lett.* **49** 659
[9] Shiba H 1973 *Prog. Theo. Phys.* **50** 50–73
[10] Clerk A A and Ambegaokar V 2000 *Phys. Rev. B* **61(13)** 9109–9112
[11] Avishai Y, Golub A, and Zaikin D 2003 *Phys. Rev. B* **67** 041301
[12] Satori K, Shiba H, Sakai O, and Shimizu Y 1992 *JPSJ* **61** 3239–3254

NRG calculation of the spectral function of the SC-AM   18

[13] Wilson K G 1975 *Rev. Mod. Phys.* **47** 773–840
[14] Bulla R, Costi T, and Pruschke T 2008 *Rev. Mod. Phys.* **80** 395
[15] Yoshioka T and Ohashi Y 2000 *JPSJ* **69** 1812–1823
[16] Tanaka Y, Oguri A, and Hewson A C 2007 *New Journal of Physics* **9** 115
[17] Lim J S and Choi M-S 2006 *cond-mat/0609333*
[18] Bauer J, Oguri A, and Hewson A C 2007
[19] Oguri A, Tanaka Y, and Hewson A C 2004 *JPSJ* **73** 494–2504
[20] Karrasch C, Oguri A, and Meden V 2008 *Phys. Rev. B* **77** 024517
[21] Krishna-murthy H R, Wilkins J W, and Wilson K G 1980 *Phys. Rev. B* **21** 1003–1043
[22] Bulla R, Tong N-H, and Vojta M 2003 *Phys. Rev. Lett.* **91** 170601
[23] Bulla R, Lee H-J, Tong N-H, and Vojta M 2005 *Phys. Rev. B* **71** 045122
[24] Buitelaar M R, Nussbaumer T, and Schönenberger C 2002 *Phys. Rev. Lett.* **89** 256801
[25] Anderson P W 1961 *Phys. Rev.* **124** 41–53
[26] Bogoliubov N N 1958 *Sov. Phys.-JETP* **7** 41
[27] Valatin J G 1958 *Nuovo Cimento* **7**843
[28] Anders F B and Schiller A 2005 *Phys. Rev. Lett.* **95** 196801
[29] Anders F B and Schiller A 2006 *Phys. Rev. B* **74** 245113
[30] Peters R, Pruschke T and Anders F B 2006 *Phys. Rev. B* **74** 245114
[31] Weichselbaum A and von Delft J 2007 *Phys. Rev. Lett.* **99** 076402
[32] Bulla R, Costi T A, and Vollhardt D 2001 *Phys. Rev. B* **64** 045103
[33] Oliveira W C and Oliveira L N 1994 *Phys. Rev. B* **49** 11986–11994
[34] Fritz L and Vojta M 2005 *Phys. Rev. B* **72** 212510
[35] Karski M, Raas C and Uhrig G S 2005 *Phys. Rev. B* **72** 113110

5.1   Ground and bound states

Due to the coupling of a superconductor to a local level, Andreev bound states form below the gap. Figure 5.2(a) shows the energy of these bound states as well as the nature of the ground state. If the ground state is a (Kondo) singlet, the first two bound states are degenerate and form a doublet, similar to the $U = 0$ case. If the ground state is a degenerate doublet, the first bound state is a singlet. Varying the ratio Γ/Δ, a level crossing of the lowest bound states with the ground state occurs when $T_K/\Delta \sim O(1)$. At this point (where $E_{singlet} - E_{doublet} = 0$), the ground state (and therefore the properties of the system) changes its nature. A phase diagram for the singlet and doublet ground state scanning the whole parameter regime was derived recently by [85] (also using NRG).

Figure 5.2(a) also shows higher excited bound states (thin lines). For $U = 0$, the relation $E_3 = 2E_{doublet}$, obtained in the preceding Section, is recovered.

The limit $\Gamma/\Delta \to 0$ corresponds to the decoupling of the local level from the superconducting reservoir. Therefore the energy spectrum is composed of the continuum of the superconducting reservoir together with the eigenenergies of a bare quantum dot described by H_{imp} in Eq. (3.1b). As illustrated in figure 5.2(b), these are 0, ε_d and $2\varepsilon_d + U$ for the states $|0\rangle$, $|\uparrow\rangle$, $|\downarrow\rangle$ and $|\uparrow\downarrow\rangle$, respectively. The nature of the ground state (thick dashed line) and the excited states can be read off. These appear as Andreev bound states in the full energy spectrum if they lie within the superconducting gap. It follows immediately that in this limit, a doublet ground state only exists for $\varepsilon_d \in (-U, 0)$, including the symmetric case (indicated by the vertical dotted line). Note that for $U = 0$, all four eigenstates of H_{imp} are degenerate at energy zero.
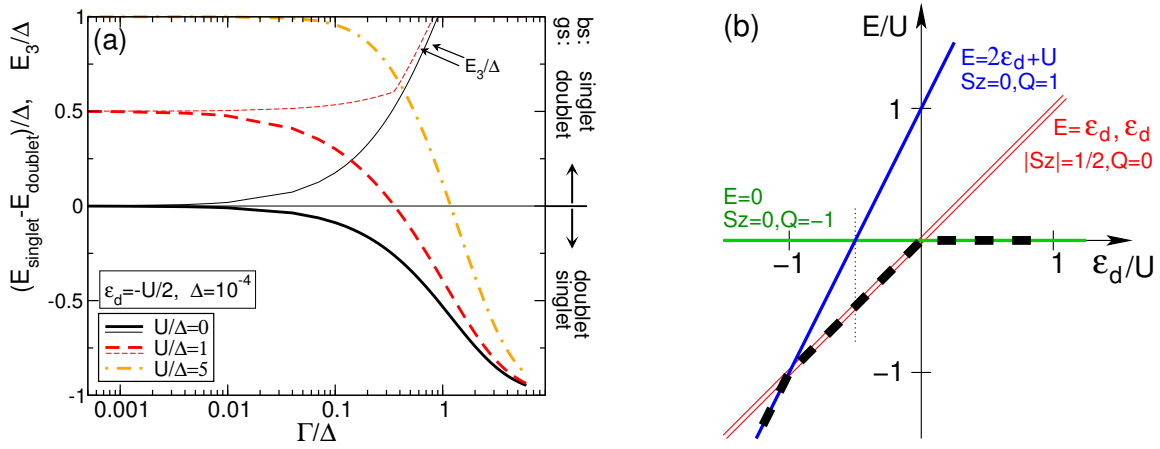
Figure 5.2: (a) Subgap bound state energies for the symmetric model at fixed $\Delta = 10^{-4}$ as functions of Γ/Δ, for three values of U/Δ. The lowest bound state (bs) is either a doublet or a singlet, depending on whether the ground state (gs) is a singlet or a doublet, respectively. Thus, a level crossing occurs when $E_{singlet} - E_{doublet}$ (thick lines) changes sign. Additional bound states (of energy E_3, thin lines) may occur. (b) Eigenenergies of an isolated level described by H_{imp} (3.1b) as a function of ε_d/U. These energies determine the subgap energy spectrum of the superconductor-Anderson model in the limit $\Gamma/\Delta \to 0$. The ground state (thick dashed line) is a doublet only for $\varepsilon_d \in (-U, 0)$, what includes the symmetric case (vertical dotted line). Otherwise it is a singlet.

Chapter 6

Two-channel Kondo effect in two different models

In 1998, Goldhaber-Gordon *et al.* [9] where the first to observe the Kondo effect in quantum dot devices. Electrons confined within a small region (quantum dot, modelled by a local level) provide a local net spin, say $S = \frac{1}{2}$. Below a critical temperature T_K the spin gets completely screened by the reservoir electrons and the ground state is a spin singlet. Therefore, at $T = 0$, the electrons exhibit only potential scattering and the system is a Fermi liquid (FL) [68]. The number of channels is irrelevant, as long as they are connected by tunnelling via the impurity. As shown in Section 2.3, they then can be combined to one effective reservoir that couples exclusively to the impurity. The other effective channels decouple and the system is reduced to a single-channel problem, exhibiting the standard Kondo effect.

The situation changes if two (or more) *independent* electronic channels couple to the quantum dot, in such a way that no channel mixing occurs. For equal coupling strengths each channel tends to screen the local spin, resulting in an overscreening, called "two-channel Kondo effect". The ground state is a twofold degenerate spin-1/2 singlet. The system then cannot be described by (potential) scattering theory and the FL description does not apply, the system exhibits non-Fermi liquid (NFL) behaviour [88].

The experimental challenge consists in realizing two channels that have to be disconnected from each other in the low-temperature limit, so that no mixing of electrons from different channels is possible. A possible scenario was proposed by Oreg and Goldhaber-Gordon (OG) [16]. They suggest to prevent mixing of the channels by a Coulomb interaction on one of the reservoirs that suppresses occupation non-preserving tunnelling processes. Experimental success of the proposed setup was reported only recently [17], again in the group of Goldhaber-Gordon.

In this Chapter we study two theoretical models that cover not only the particle-hole symmetric point (as in [16] or the two-channel Kondo model, see below) but allow for a tuning of the energy of the local level into the mixed-valence regime. We are interested in studying for how long NFL behaviour survives when emptying the local level. The models are motivated by the proposal of OG. Their key idea is that mixing between the channels

can be suppressed if the number of particles of at least one reservoir is kept constant; this can be achieved by realizing one of the reservoirs by a large quantum dot exhibiting Coulomb interaction. We generalize the idea that processes that result in channel mixing have to be energetically unfavourable.

In the following, we first introduce the standard two-channel model and comment on the idea of an ending NFL line for a energy-dependent local level more precisely. Then we introduce two different two-channel models both exhibiting NFL behaviour. We analyze the models at $T = 0$ and find a non-vanishing NFL line in the first case, whereas the NFL line of the second model stops at some critical gate voltage. Note that the work presented in this Chapter was done in collaboration with M. Pustilnik. It is still in process, so that several open questions remain.

6.1   Introductory remarks

6.1.1   Brief introduction to the standard two-channel Kondo model

For the local occupation fixed to $n_{d\sigma} = \frac{1}{2}$, the standard impurity model with two disconnected channels is the two-channel Kondo model [89, 90],

$$H_{2CK} = 2J_1 \mathbf{S} \cdot \mathbf{s_1} + 2J_2 \mathbf{S} \cdot \mathbf{s_2} + H_{\text{res1}} + H_{\text{res2}}. \tag{6.1}$$

It is derived analogously to the one-channel Kondo model introduced in Eq. (2.14). For equal coupling of the reservoirs, $J_1 = J_2$, *both* channels screen the impurity spin, resulting in an overscreening of the local magnetic moment. Therefore the ground state has spin $1/2$. It is degenerate so that the system is a NFL that cannot be described by scattering formalism.

If $J_1 \neq J_2$, one of the channels dominates and "wins" the screening competition. The other channel effectively decouples at low energies (the competition and the decoupling can be seen in the NRG flow diagrams, see Fig. 6.3) and the system is reduced to an effective one-channel Kondo problem [89]. Therefore the system is a FL and the scattering phases can be extracted from the NRG flow diagram, see App. C.

In the two-channel Kondo model the occupation of the local level is fixed to $n_{d\sigma} = 1/2$. At $T = 0$, the two-channel Kondo effect can be only destroyed by an asymmetry in the couplings. In this Chapter we are interested in systems exhibiting two-channel Kondo effect where the occupation is not fixed but can be varied by shifting the energy of the local level. We study whether and how the NFL behaviour breaks down when, for symmetric effective coupling of the two channels, the system is driven from the local-moment regime with $n_{d\sigma} \approx 1/2$ (NFL) to the empty-orbital regime with $n_{d\sigma} \approx 0$. In the latter regime no local spin is left to be screened, thus no (two-channel) Kondo effect is possible and the system is a FL for all couplings. Thus, as the level position is swept, we expect a transition

to occur from a NFL to a FL.

Within our convention, the gate voltage is related to the position of the local level via $V_g = -\varepsilon_d + U/2$. Therefore $V_g/U = 0$ corresponds to the symmetric model, $V_g/U = -0.5$ to $\varepsilon_d = 0$. Obviously, for $V_g \to -V_g$ one gets $n_{d\sigma} \to |1 - n_{d\sigma}|$, thus we restrict our studies to $|V_g|$ and only discuss the case $n_{d\sigma} \leq 1/2$.

6.1.2 Expected phase diagram for two-channel models symmetric in the coupling mechanisms

When the system does not exhibit two-channel Kondo correlations, one of the channels "wins", i.e. completely screens the local spin while the other channel decouples. Then, at zero temperature, the FL description applies and only potential scattering occurs. The system can be characterized by two scattering phase shifts $\delta_{1,2}$. Since the two channels are disconnected, each phase describes the scattering properties of one of the channels. For spin asymmetry (e.g. induced by a magnetic field), four phase shifts have to be considered. The scattering phase shifts can be extracted from the NRG-flow diagrams, see App. C. In case of NFL behaviour, the system (and therefore the NRG flow diagrams) cannot be expressed in terms of phase shifts.

In this introductory Section, we qualitatively discuss the phase behaviour expected at $T = 0$ for a system where two-channel Kondo behaviour is possible. From simple considerations, one expects (i) the NFL-line to end at some V_g^c when the system is driven out of the local-moment regime, and (ii) a rapid change of continuous to discontinuous phase evolution near the end of the NFL line.

Assume a local level coupled to two disconnected channels by the same coupling mechanism. The coupling constants are denoted by J_1 and J_2, respectively. Figure 6.1 depicts the scattering phases one intuitively expects of such a system as a function of the local occupation and the couplings. Later we will see, that for the models we study this picture is oversimplified, i.e. it is influenced too much by our understanding of the standard Anderson model.

In the local moment regime, the two-channel system exhibits NFL behaviour at $J_1 = J_2$, indicated by the yellow line. Apart from that line, the system is a FL. We distinguish different regimes: In the local moment regime, where the local level provides enough spin for Kondo correlations, the channel coupled strongest completely screens the spin, the other channel is decoupled and the system is a FL. We denote these regions by FL1 ($J_1 > J_2$) and FL2 ($J_1 < J_2$), respectively. They are separated by the NFL line, as indicated in the Figure. In the empty orbital regime, $n_{d\sigma} \approx 0$, no Kondo screening and therefore no competition between the two channels is possible. This FL regime (called FL0) connects FL1 and FL2.

By definition, the system is either a FL or a NFL, thus the NFL abruptly ends at some point in the mixed valence regime when emptying the local level for $J_1 = J_2$ fixed. We

are interested in gaining a deeper understanding of the NFL-FL transition and the system properties nearby. Let us illustrate the problem by discussing the phase evolution along the three different paths indicated by arrows (green) in Fig. 6.1. The paths connect two points in FL1 and FL2 (indicated by rounded boxes) of known scattering phase configuration: For asymmetric coupling (say $J_i > J_{i'}$) and $n_{d\sigma} = S_z = 1/2$, the phases are given by $\delta_i = \pi/2$ (fully evolved Kondo effect) and $\delta_{i'} = 0$ (decoupled channel).

Path 1: Crossing the NFL line at fixed occupation, the phases jump by $|\Delta\delta_i| = \pi/2$. Hereby the phase decreases if the channel decouples. Actually, the jump of $\pi/2$ is independent of $n_{d\sigma}$.

Path 2 is chosen such that the phase evolution is continuous: Physically decoupling channel 2 by $J_2 \to 0$, the phases do not change but δ_1 can now be related to the occupation, $\delta_1 = n_{d\sigma}\pi$ (Friedel sum rule, see Sec. 2.6.5). Depopulating the local level continuously such that $\delta_1 \sim 0$, the system is brought into the FL0 regime where no Kondo-correlations are present. Increasing the coupling J_2, the point where $J_1 = J_2$, i.e. $\delta_1 = \delta_2 = n_{d\sigma}/2 \sim 0$, is reached without any discontinuity in the scattering phases. The phase evolution along the remaining path is analog, but with interchanged indices.

The question of interest arises for path 3. It passes along the NFL-line. Assuming that this line ends at some point, the path can either cross the line slightly before its end (accompanied by phase jumps of $|\Delta\delta_i| = \pi/2$) or pass via the FL0, yielding a continuous phase evolution, since it is topological equivalent to path 2. It is the interest about this transition from continuous to discontinuous behaviour that triggered our interest in that problem. In the following two Sections, we shall explore this question in the context of two different models.

6.2   Two-channel Kondo-Anderson model

We study the possibility of NFL behaviour in a two-channel impurity model exhibiting both Kondo- and Anderson-like coupling. By analyzing the scattering phases obtained from the NRG flow diagrams, we find that the NFL-line divides the parameter space into two disconnected regions. Therefore, in this model, the NFL-line does not stop at some critical gate voltage, contrary to the simple considerations sketched in Fig. 6.1. This is because large enough Kondo-like coupling forces the local occupation to stay near $n_{d\sigma} = \frac{1}{2}$, therefore extending the local moment regime allowing for Kondo physics to $|V_g/U| \to \infty$.

6.2.1   The model

The model is motivated by the proposal of OG [16]. They suggest to mimic one of the reservoirs by a large quantum dot. Neglecting the discreteness of the level spectrum in the large dot but retaining Coulomb repulsion, the number of electrons on the large dot is fixed for the dot in Coulomb blockade at zero temperature. Therefore, only occupation-preserving higher-order tunnelling processes between the large dot and the local impurity level are allowed energetically. Consequently, the two reservoirs are not connected to each
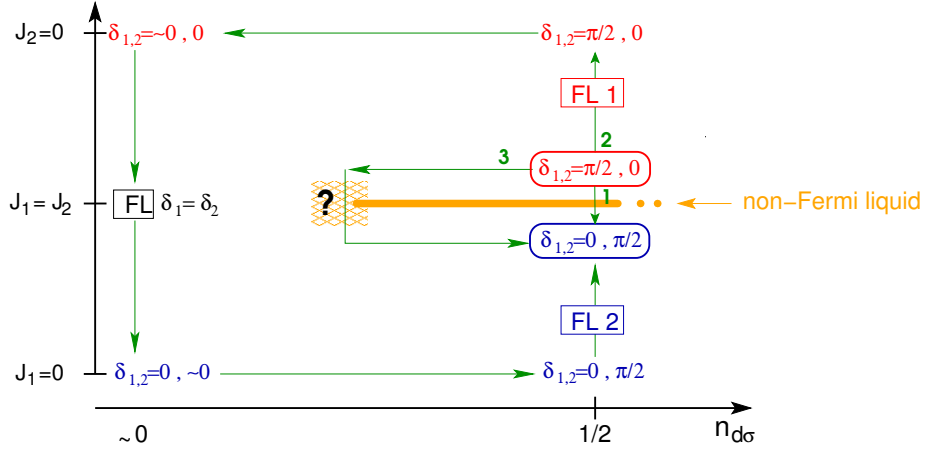
Figure 6.1: Sketch of the expected scattering phases $\delta_{1,2}$ of an impurity system coupled to two disconnected channels. In the local-moment regime, the system exhibits non-Fermi liquid (NFL) behaviour for equally coupled channels, $J_1 = J_2$ (yellow line). For $J_i > J_{i'}$, channel i' effectively decouples and only channel i screens the local spin (FLi) and the system is a Fermi liquid. For $n_{d\sigma} \approx 0$, the local level does not provide enough spin for Kondo screening and the system is a FL (FL0), independent on the couplings. Therefore, the NFL-line is expected to stop at some critical occupation. In the text, we discuss three different paths to go from the FL1 to FL2, indicated by the green arrows.

other and independently screen the impurity, resulting in two-channel Kondo physics for equal effective coupling of the two reservoirs.

In the proposal they focus on the particle-hole symmetric point with one electron on the local level. Therefore they perform a Schrieffer-Wolff transformation, eliminating charge fluctuations on the small dot. In the low-temperature limit where also charge fluctuations on the large dot are frozen, they obtain the standard two-channel Kondo model [88] given by Eq. (6.1).

In this work we want to analyze the dependence of the NFL behaviour on the local occupation. We therefore assume that at low energies, the coupling between the large dot and the local level is dominated by a spin-spin exchange interaction, but tunnelling is possible between the local level and reservoir 2, resulting in the following toy model:

$$H = H_{\text{imp}} + (H_{\text{res1}} + H_{\text{J}}) + (H_{\text{res2}} + H_{\text{V}}), \tag{6.2a}$$

with

$$H_{\text{imp}} = \sum_{\sigma} \varepsilon_d n_{d\sigma} + U n_{d\uparrow} n_{d\downarrow}, \tag{6.2b}$$

$$H_{\text{res }\alpha} = \sum_{\mathbf{k}\sigma} \varepsilon_{\mathbf{k}} c^{\dagger}_{\alpha\mathbf{k}\sigma} c_{\alpha\mathbf{k}\sigma}, \tag{6.2c}$$

$$H_J = 2J_1 \, \mathbf{S} \cdot \mathbf{s_1}, \tag{6.2d}$$

$$H_V = \sum_{\mathbf{k}\sigma} V_2 (c^{\dagger}_{2\mathbf{k}\sigma} d_{\sigma} + d^{\dagger}_{\sigma} c_{2\mathbf{k}\sigma}). \tag{6.2e}$$

The impurity level (small dot, index d) with energy ε_d and Coulomb repulsion U is coupled by Kondo-like (spin-spin) interaction to reservoir 1 (large dot), whereas the coupling to reservoir 2 is described by an Anderson-like tunnelling term, allowing for change of the local occupation. Therefore the model is not restricted to the local moment regime, contrary to the standard two-channel model given by Eq. (6.1). As usual we define $\Gamma_2 = \pi\rho V_2^2$ with $\rho = 1/(2D)$ the density of states per spin near the Fermi energy and $D = 1$ the half-bandwidth. The spin of the local level is given by $\mathbf{S} = 1/2\sum_{\sigma\sigma'} d_\sigma^\dagger \vec{\sigma}_{\sigma\sigma'} d_{\sigma'}$, the spin of the large dot reads $\mathbf{s_1} = 1/2\sum_{\mathbf{kk'},\sigma\sigma'} c_{\mathbf{1k},\sigma}^\dagger \vec{\sigma}_{\sigma\sigma'} c_{\mathbf{1k'},\sigma'}$. Due to the structure of this toy-model we refer to it as the *Kondo-Anderson model.*

Note that this model truly has the status of a toy model, since it cannot be derived by a Schrieffer-Wolff transformation with fixed occupation of the large dot. We perform the according transformation in Appendix B. It results in a variety of terms with prefactors that non-trivially depend on the bare parameters of the system.

Applying the NRG transformations described in Sec. 3.1 to the Kondo-Anderson model [Eq. (6.2)], the NRG chain Hamiltonian reads

$$H_{\text{imp}} \;\; = \;\; \sum_\sigma \varepsilon_d n_{d\sigma} + U n_{d\uparrow} n_{d\downarrow}, \tag{6.3a}$$

$$H_{\text{res } \alpha} \;\; = \;\; D\frac{1}{2}(1+\Lambda^{-1}) \sum_\sigma \sum_{n=0}^\infty \Lambda^{-n/2}\xi_n (f_{\alpha n\sigma}^\dagger f_{\alpha n+1\sigma} + f_{\alpha n+1\sigma}^\dagger f_{\alpha n\sigma}), \tag{6.3b}$$

$$H_J \;\; = \;\; 2\rho D\, 2J_1\, \mathbf{S} \cdot \mathbf{s_1} = 2J_1\, \mathbf{S} \cdot \mathbf{s_1}, \tag{6.3c}$$

$$H_V \;\; = \;\; \sqrt{\frac{2\Gamma_2 D}{\pi}} \sum_\sigma f_{20\sigma}^\dagger d_\sigma + h.c., \tag{6.3d}$$

which can be solved iteratively analogous to the Anderson model, see Sec. 3. $f_{\alpha n\sigma}^\dagger$ creates an electron on site n of the Wilson chain, and $\mathbf{s_1} = \sum_{\sigma\sigma'} 1/2 f_{10\sigma}^\dagger \vec{\sigma}_{\sigma\sigma'} f_{10\sigma}$ is the spin operator of the zeroth reservoir site.

In the following, we study the NFL-line as a function of the gate voltage and the occupation. The line is characterized by a jump $\Delta\delta_i = \pm\frac{\pi}{2}$ of the scattering phases of channel $i = 1,2$ when changing the relative couplings at fixed gate voltage. Contrary to expectations, we do *not* find a critical value V_g^c where the NFL-line ends.

In order to be able to compare the strength of the Kondo-like and Anderson-like coupling in same units, we define a parameter $J_2(\Gamma_2)$, having the same units as J_1. For simplicity we use the relation connecting the standard Kondo and Anderson model in the particle-hole symmetric point,

$$J_2 = \frac{4\Gamma_2}{\pi\rho U}, \tag{6.4}$$

independent of ε_d [1]. Therefore, at fixed U, we get $J_2 \propto \Gamma_2$. For scanning the parameter

---

[1]The ε_d-dependent analogon, see Eq. (B.15) would complicate things since J_2 is negative for $\varepsilon_d > 0$.

space, we keep J_2 fixed and vary the parameter

$$j \equiv \frac{J_1}{J_2}, \tag{6.5}$$

i.e. the coupling strength J_1, see below. We use $U = 0.2$ and $\Lambda = 2.5$.

6.2.2 Related single-channel models

For a detailed understanding of the impact of each of the two different types of coupling we first study the scattering phase of the corresponding single-channel models in which we set either $J_1 = 0$ or $J_2 = 0$. At zero temperature, both models exhibit Fermi liquid behaviour, therefore the scattering phases can be related to the occupation of the local level using the Friedel sum rule [21], $\delta' = n_{d\sigma}\pi$. The single-channel models are labelled by a prime.

Kondo-like model

We first discuss a system representing the large dot coupled via Kondo-like spin-spin coupling to the local level, which is described by H_{imp} (6.2b). Contrary to the standard Kondo model, the occupation of the local level is *not* fixed. The Hamiltonian of the system then reads

$$H'_{KM} = H_{\text{imp}}(\varepsilon_d, U) + 2J'_1 \mathbf{S} \cdot \mathbf{s}_1 + H_{res1}. \tag{6.6}$$

From the FL relation and the absence of a hopping term it is clear that the scattering phase δ'_1 (or occupation) can have either the value $\frac{\pi}{2}$ ($\frac{1}{2}$) - resulting in a Kondo effect - or 0 (0), where no Kondo effect is possible.

The border between these two regions (as a function of V_g) is indicated in Fig. 6.2(a) by the dashed red line. Let us start at $J'_1 = 0$, where the model simply consists of a localized level at energy ε_d and a decoupled reservoir. Clearly, for $|V_g/U| \leq 0.5$, one electron occupies the dot, thus $\delta'_1 = \frac{\pi}{2}$, whereas for $|V_g/U| > 0.5$, either both or no levels are below the chemical potential, thus $\delta'_1 = 0$. For finite J_1 the system can lower its energy by spin-spin coupling and accordingly by the Kondo effect. Obviously, this is only possible for finite spin on the dot. Therefore, the regime with $\delta'_1 = \frac{\pi}{2}$ and $n_{d\sigma} = \frac{1}{2}$ is extended with increasing coupling strength. Consequently, we conclude that in the Kondo-like model given by Eq. (6.6), the Kondo effect tends to maximize the local spin. Obviously, for this model, the width of the transition region from $\delta'_1 = \frac{\pi}{2}$ to $\delta'_1 = 0$ is zero for all J'_1.

Anderson model

The second single-channel model, obtained from the Kondo-Anderson model by setting $J_1 = 0$, is the standard Anderson model,

$$H'_{AM} = H_{\text{imp}} + H_{res2} + \sum_{\mathbf{k}\sigma} J'_2(\Gamma_2) \left(c^\dagger_{2\mathbf{k}\sigma} d_\sigma + d^\dagger_\sigma c_{2\mathbf{k}\sigma} \right). \tag{6.7}$$
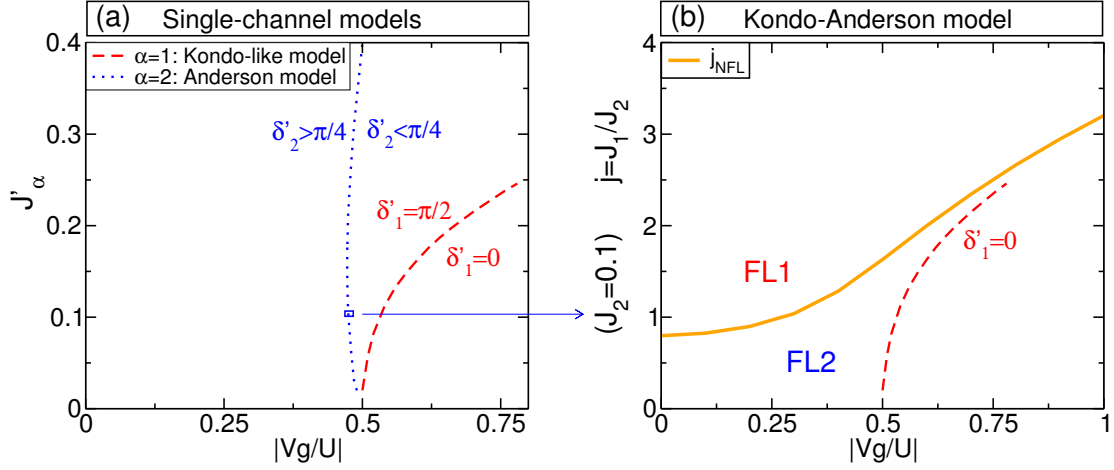
Figure 6.2: Phase diagram: The single-channel models are labelled by a prime. (a) Phase diagram of the single-channel models in $(V_g\text{-}J'_\alpha)$-space. In the Kondo-like model given by Eq. (6.6), the phase is either $\delta'_1 = 0$ or $\delta'_1 = \frac{\pi}{2}$. Only for the latter case the system can lower its energy by the spin-spin coupling term (Kondo effect). Therefore this region is extended for large coupling. The dashed red line separates the two regions. For the single-channel Anderson model (6.7), the phase evolution of δ'_2 is continuous due to the hopping term. We indicate the border between Kondo possible/not possible by the dotted blue line defined by $\delta'_2(V_g, J_2) = \frac{\pi}{4}$. (b) The yellow solid line $j_{NFL}(V_g, j)$ is the value of j separating the region where (i) the Kondo-like coupling wins (FL1) and (ii) the Anderson-like coupled channel wins (FL2), thus it is the line of NFL behaviour. Dashed red line: same as in (a) but in $(V_g\text{-}j)$ space, $j = J_1/J_2$. Note that in order to have a constant width Δ_{AM}, we fix the Anderson coupling to $J_2 = 0.1$. Note that j_{NFL} lies within the region where Kondo is possible for the single-channel Kondo-like model. For details, see text.

The tunnelling term allows the phase to change *continuously* from $\frac{\pi}{2}$ (at $V_g/U = 0$) to ≈ 0 (for $|V_g/U| >> 0.5$). In order to compare the coupling-dependence of the phase with the results of the Kondo-like model, we define the border between Kondo possible / not possible as the line where the phase obeys $\delta'_2(V_g, J'_2) = \frac{\pi}{4}$. The border is indicated by the blue dotted line in Fig. 6.2(a). Obviously, as in the Kondo-like model, for zero coupling the line starts at $|V_g/U| = 0.5$. The width of the phase change (at constant J'_2) scales with the coupling strength J'_2.

6.2.3   Two-channel Kondo-Anderson model

When combining the two single-channel models to the two-channel Kondo-Anderson model given by the Hamiltonian (6.2), we fix the coupling strength J_2 of the tunnel coupling. Therefore, for both (individual) channels the scale on which the system changes from Kondo possible / not possible is constant for all j. Scanning the parameter space, we vary V_g and J_1. For the presented data we fix the Anderson coupling to $J_2 = 0.1$ and the Coulomb interaction to $U = 0.2$.

The NFL-line $j_{\mathrm{NFL}}(V_g)$ of the Kondo-Anderson model is shown in Fig. 6.2(b) (yellow solid line). It separates the region where (i) the Kondo-like channel 1 ($j > j_{\mathrm{NFL}}$, FL1) or (ii) the Anderson-like coupled channel 2 ($j < j_{\mathrm{NFL}}$, FL2) completely screens the local spin. The line starts at $V_g = 0$ at $j \approx 0.8$, where the effective couplings (and Kondo temperatures) of the two channels equal. The NFL-line increases with increasing spin-spin coupling J_1, we find that there is *no* critical V_g^c where the line stops.

How can we understand this result contradicting the intuitive picture of Fig. 6.1? For clarity, Fig. 6.2(b) also shows the border line of the Kondo-like model. As in that model, the spin-spin coupling of the Kondo-Anderson model tends to maximize the local spin. Upon increasing the coupling strength J_1, the system prefers to keep the local occupation can be kept close to $n_{d\sigma} = \frac{1}{2}$ even in the limit $|V_g/U| \to \infty$. Therefore, at all values of V_g the dot can provide enough local spin for screening, i.e. for a screening-competition between the two channels which results in NFL behaviour. Consequently, due to the spin-spin coupling, the dot does not necessarily enter the regime $n_{d\sigma} \approx 0$ when increasing $|V_g|$, and therefore the NFL-line does *not* stop at some V_g^c in the Kondo-Anderson model.

NRG flow diagrams

The transition between FL1 to FL2 when crossing the NFL line manifests itself in the NRG flow diagrams. The energy flow for fixed V_g/U and different couplings is given in Fig. 6.3. From top to bottom the system starts in FL2 (a,b), exhibits NFL behaviour for $j = j_{\mathrm{NFL}}$ in (c) and finally ends in FL1 (d,e). Not only the (non-)FL character and the scattering phases (if existent) can be extracted, as explained in App. C, but also the competition between the two-channels becomes apparent. At high energy scales (low iteration number n), an initially small difference in the couplings of the two channels is not resolved, thus all flow diagrams start similarly to the NFL. During the renormalization flow, with increasing iteration number (i) the energy resolution gets enhanced and (ii) the couplings renormalize such that one channel effectively decouples and the other one completely screens the impurity spin.

At the iteration where the difference in the renormalized couplings is resolved, the flow diagram changes from NFL-like to FL behaviour, and the scattering phases can be extracted, see App. C. Obviously, this change in energy flow is shifted to smaller energy scales (larger iterations) when approaching the NFL line. Note that in the Figure $|V_g/U| \neq 0.5$, therefore the degeneracy of the energy levels shown in Fig. 6.1 for a symmetric Anderson and two-channel Kondo model is lifted.

More details about the scattering phases and the occupation

Let us take a closer look at the scattering phases and the local occupation near the NFL-line. The two scattering phases describing the two-channel system (except at the NFL-line) are directly related to the Kondo channel ($\delta_1 = \frac{\pi}{2}$ or 0) and the Anderson channel (continuously varying phase δ_2).
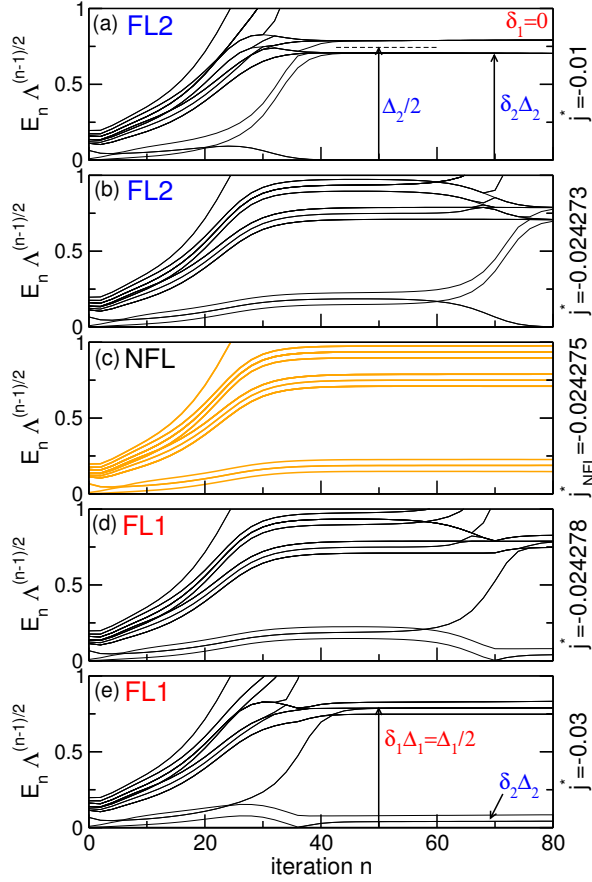
Figure 6.3: NRG flow diagrams for the Kondo-Anderson model at $V_g/U = 0.3$ and various couplings j^*. Here $j^* \equiv (J_2 - J_1)/J$, with varying $J_{1,2}$ but $J = J_1 + J_2 = 0.2$. $U = 0.2$ and $\Lambda = 2.5$. The transition from (a,b) FL2 to (d,e) FL1 when crossing (c) the NFL line manifests itself in the characteristics of the energy flow. Only when the energy resolution is large enough to resolve the difference in the renormalized couplings, the energy flow changes from NFL-like to FL behaviour, see e.g. $n \approx 60$ in (d). In the FL regime the scattering phases can be extracted, see (a,e). For details, see App. C.

They are shown in Fig. 6.4 as a function of j and V_g. For clarity of Fig. (b) the phase δ_2 in FL1 is shifted upwards by π. The two regions separated by the NFL-line are characterized as follows: (i) FL1 ($j > j_{\text{NFL}}$). Channel 1 screens the local spin, thus $\delta_1 = \frac{\pi}{2}$, channel 2 decouples. (ii) FL2 ($j < j_{\text{NFL}}$). Channel 1 decouples, $\delta_1 = 0$, and the local spin is either screened by channel 2 or, for $j \ll j_{\text{NFL}}$, the local spin $\to 0$ and no screening is possible. Crossing the NFL-line at fixed V_g, both phases jump by $\pm\frac{\pi}{2}$, respectively. Approaching the NFL-line from FL2, δ_2 is given by $\frac{\pi}{2}$ for $V_g/U = 0$. Increasing $|V_g/U|$, it decreases and saturates at $\frac{\pi}{4}$, see below.

The local occupation is shown in Fig. 6.5. In the limit $j = J_1 = 0$ (remember that $J_2 = 0.1$ always), the standard Anderson model is recovered and the occupation changes rapidly at $|V_g/U| \approx 0.5$. For finite J_1, the influence of the spin-spin coupling on the

occupation can be nicely seen for $|V_g/U| > 0.5$. $n_{d\sigma}$ increases abruptly with j and saturates at $n_{d\sigma} = 0.5$.
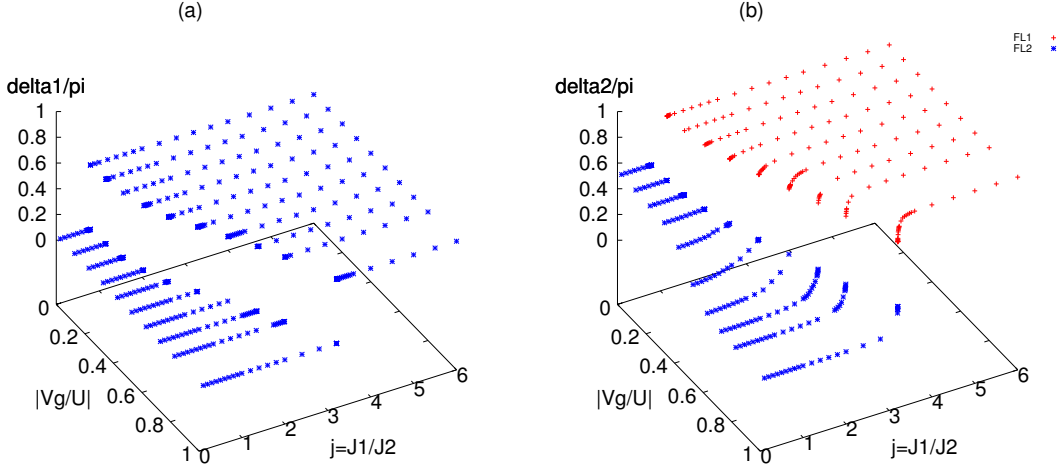

Figure 6.4: $(V_g\text{-}j)$-dependence of the scattering phases of the Kondo-Anderson model. Crossing the NFL-line at fixed V_g, they jump by exactly $\pm\frac{\pi}{2}$. (a) Due to the Kondo-like coupling of channel 1, δ_1 can take either the values 0 or $\frac{\pi}{2}$. (b) The scattering phase δ_2 varies continuously, except at the NFL-line, where it jumps by $-\frac{\pi}{2}$ when crossing from the FL2 (blue) to FL1 (red). Note that for better visibility we shifted the phase by $+\pi$ in the FL1.
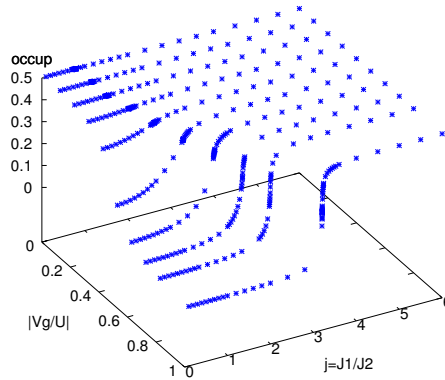

Figure 6.5: $(V_g\text{-}j)$-dependence of the local occupation $n_{d,\sigma}$. For $J_1, j \to \infty$ the spin-spin coupling dominates the system and the occupation saturates at $n_{d\sigma} = 0.5$.

Properties at the NFL-line in the limit $|V_g/U| \to \infty$

Next we summarize the properties of the system at the NFL-line and extend the regime of the gate voltage to $|V_g/U| \to \infty$.

The NFL-line separates the regimes in parameter space where channel 1 screens the spin and channel 2 decouples (FL1) and vice versa (FL2). In $(V_g\text{-}j)$ space, the NFL line $j_{NFL}(V_g)$ increases with $|V_g|$, see Fig. 6.6. It does *not* stop at some critical point.

Large enough spin-spin coupling between channel 1 and the local level forces the occupation to remain close to $n_{d\sigma} = 0.5$. The occupation at the NFL line saturates at $n_{d\sigma} = 0.25$ as $|V_g/U|$ increases to ∞, see Fig. 6.7(a). The scattering phases jump by $\pm\frac{\pi}{2}$ when crossing the NFL-line at fixed V_g. Due to the spin-spin coupling, the scattering phase δ_1 of channel 1 is either $\frac{\pi}{2}$ (FL1) or zero (FL2). In contrast, the scattering phase δ_2 of the tunnel-coupled channel 2 changes continuously, except at the NFL-line. The behaviour at the NFL-line is shown in Fig. 6.7(b). For $j \to j_{\text{NFL}}$ from the FL2 (or FL1)-side, the phase is given by $\delta_{2,NFL2} = \frac{\pi}{2}$ (or $\delta_{2,NFL1} = 0$) at $V_g = 0$, saturating at $\delta_{2,NFL2} = \frac{\pi}{4}$ (or $\delta_{2,NFL1} = -\frac{1\pi}{4}$) for $|V_g/U| \to \infty$.
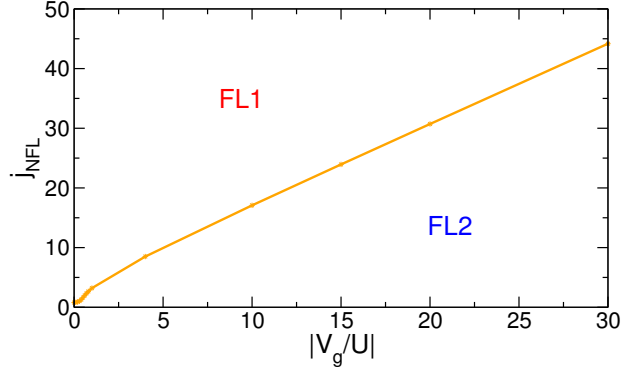

Figure 6.6: Phasediagram in $(V_g\text{-}j)$-space. The NFL-line separates the regime where channel 1 screens the local spin and channel 2 is decoupled (FL1) and vice versa (FL2). j_{NFL} increases linearly in the limit $|V_g/U| \to \infty$. For the limit $|V_g/U| \approx 0$, see Fig. 6.2.

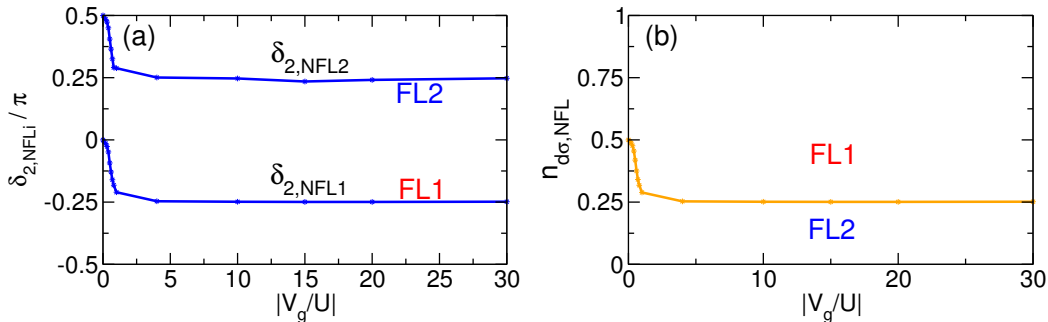**Figure 6.7:** Properties at the NFL-line. (a) The jump of the scattering phase at the NFL-line is always $\frac{\pi}{2}$. For $j \to j_{\text{NFL}}$ from the FL2 side, δ_2 is given by $\delta_{2,NFL2} = \frac{\pi}{2}$ for $V_g = 0$, saturating at $\delta_{2,NFL2} = \frac{\pi}{4}$ for increasing $|V_g/U|$. (b) The occupation at the NFL-line is given by $n_{d\sigma} = \frac{1}{2}$ for $V_g = 0$ and saturates at $n_{d\sigma} = 0.25$ ($V_g > 0$) and 0.75 ($V_g < 0$) for increasing $|V_g/U|$.

The experimentally accessible quantity to observe the NFL-line is the differential conductance. Due to the related jump in phase when crossing the NFL line, also the conductance exhibits a jump which can be observed. Let us assume that the conductance is probed via reservoir 2 (which could be the even combination of a left and right channel coupled with matrix elements t_L, t_R, respectively). The conductance then reads (see Eq. (2.32) or [73]).

$$G/G_0 = \frac{1}{2} \sum_\sigma \sin^2 \delta_{2\sigma} = \sin^2 \delta_2, \qquad (6.8)$$

where $G_0 = \frac{2e^2}{h} \sin 2\theta$ with $\tan \theta = |t_L/t_R|$. Therefore, the jump of the conductance crossing the NFL-line is given by

$$\Delta G/G_0 = \left[\sin^2 \delta_{2,FL2} - \sin^2 \delta_{2,FL1}\right] = 2\sin^2 \delta_{2,FL2} - 1, \qquad (6.9)$$

since the phase jump of δ_2 is always $\frac{\pi}{2}$. The evolution of ΔG as a function of the gate voltage is shown in Fig. 6.8. At $V_g = 0$, $\delta_{2,FL2} = \frac{\pi}{2}$, thus $\Delta G/G_0 = 1$. In the limit $|V_g/U| \to \infty$, the phase approaches $\frac{\pi}{4}$, therefore $\Delta G/G_0$ asymptotically goes to zero. The inset shows the conductance for $j \to j_{\mathrm{NFL}}$ from the FL1 and FL2, respectively. The dependence of G and ΔG on channel asymmetry, temperature and magnetic field for the two-channel Kondo model is studied in [25].
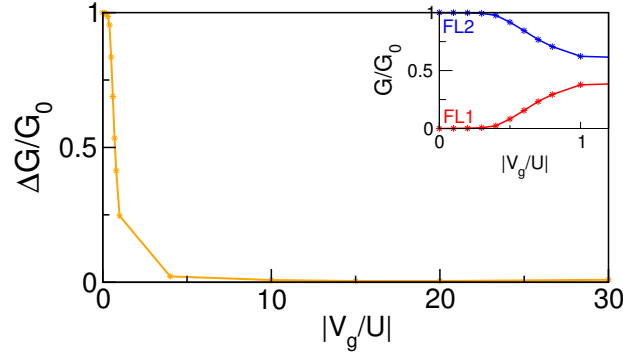

Figure 6.8: Differential conductance G (probed at channel 2) at the NFL line. The jump in phase and therefore the NFL line manifest in a jump in G which can be observed experimentally. In the limit $|V_g/U| \to 0$ this jump vanishes. In the inset a zoom of G approaching the NFL line from FL1 or FL2, respectively, is shown.

To visualize the difference of the Kondo-Anderson model to the scenario of Fig. 6.1, we show for conclusion the NFL-line in $(n_{d\sigma}\text{-}j)$-space in Fig. 6.9. There one can see that, actually, below $n_{d\sigma}^c = \frac{1}{4}$ no NFL-behaviour does occur. However, the NFL-line does not stop at $n_{d\sigma}^c$ but approaches infinity asymptotically with increasing spin-spin coupling. Therefore, in the Kondo-Anderson model, it is *not possible to connect the two Fermi liquid regions FL1 and FL2 without crossing the NFL-line*. This qualitatively coincides with a result of Anders *et al.* [91] where they study a related model for $|V_g/U| < 0.5$.
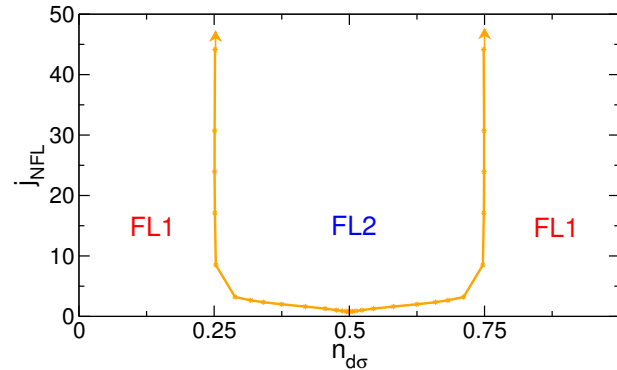
Figure 6.9: Phase diagram in $(n_{d\sigma}$-$j)$-space for the Kondo-Anderson model. High enough **Ss**-coupling between channel 1 and the local level forces the occupation to remain finite. On the NFL-line, the occupation saturates at $n_{d\sigma} = 0.25$ and 0.75, respectively. Therefore, in the Kondo-Anderson model, the two Fermi liquids FL1 and FL2 are *not* connected, contrary to the considerations sketched in Fig. 6.2.

The two main conceptual differences between the considerations that lead to Fig. 6.1 and the Kondo-Anderson model are, that (i) in the Kondo-Anderson model large enough spin-spin coupling always favours the occupation to stay between $\frac{1}{4}$ and $\frac{3}{4}$, therefore extending the local moment regime allowing for Kondo physics to $|V_g/U| \to \infty$, and that (ii) the effective couplings of the two channels do not scale equally with V_g, resulting in the asymmetry in j of Fig. 6.9. In the next Section we analyze a model where both channels are tunnel-coupled to the local level in the same way, to ensure that point (ii) is eliminated.

6.3 Two-channel Pustilnik model

The second model that we analyze, proposed by M. Pustilnik (private communication), is symmetric w.r.t. channel 1 and channel 2, therefore the effective couplings evolve equally when sweeping the gate voltage. We find a NFL-line for $J_1 = J_2$ in the regime where $n_{d\sigma} \approx 0.5$. The NFL-line ends at some critical gate voltage, similar to Fig. 6.1. Contrary to the simple considerations that motivated that Figure, we find a non-monotonic behaviour of the occupation. The non-monotonicity occurs at a critical gate voltage V_g^c for $J_1 = J_2$, but it also exists for arbitrary asymmetry.

We first introduce the model, then present NRG energy-flow diagrams that clarify the FL or NFL-character of the system. In a third part the jump in occupation is analyzed.

6.3.1 The model

The Hamiltonian of the Pustilnik model consists of four parts,

$$H = H_{\text{imp}} + H_{\text{res}} + H_{\text{imp-res}} + H_M, \tag{6.10a}$$

describing the local level, the non-interacting reservoirs, the tunnel coupling between the reservoirs and the local level and a fourth term that suppresses inter-channel particle exchange, respectively. The four contributions are given by

$$H_{\text{imp}} = \sum_{\sigma} \varepsilon_d n_{d\sigma} + U n_{d\uparrow} n_{d\downarrow}, \tag{6.10b}$$

$$H_{\text{res}} = \sum_{\alpha=1,2} \sum_{\mathbf{k}\sigma} \varepsilon_{\mathbf{k}} c_{\alpha\mathbf{k}\sigma}^{\dagger} c_{\alpha\mathbf{k}\sigma}, \tag{6.10c}$$

$$H_{\text{imp}-\text{res}} = \sum_{\alpha=1,2} \sum_{\mathbf{k}\sigma} V_l (c_{\alpha\mathbf{k}\sigma}^{\dagger} d_{\sigma} + d_{\sigma}^{\dagger} c_{\alpha\mathbf{k}\sigma}), \tag{6.10d}$$

$$H_M = E_c (n_1 - n_2)^2. \tag{6.10e}$$

For $E_c > 0$, the last term can be interpreted as a Coulomb-like potential that favours the reservoirs to be equally occupied ($n_{\alpha=1,2} = \sum_{\mathbf{k}\sigma} c_{\alpha\mathbf{k}\sigma}^{\dagger} c_{\alpha\mathbf{k}\sigma}$), thus suppressing all tunnelling processes that contribute to a mixing of the channels. Note, that this term also disfavours a change in the local occupation. The term H_M cannot be treated within the NRG formalism. It combines operators with arbitrary $\mathbf{k}$, thus cannot be transformed to a Wilson chain-like Hamiltonian.

Following the idea of [92, 91], H_M can be mapped to yield a local term that is treatable with standard NRG. This is done by introducing the pseudo spin operator $\hat{M}$, where

$$M_z \equiv n_1 - n_2 = \sum_{m=-\infty}^{\infty} m|m\rangle\langle m| \tag{6.11}$$

labels the occupation difference between the channels. m is lowered or increased by the operators

$$M^{\pm} = |m \pm 1\rangle\langle m|. \tag{6.12}$$

According to the tunnelling processes between reservoirs and local level, $H_{\text{imp}-\text{res}}$ (6.10d) is replaced by

$$H_{\text{imp}-\text{res}} = \sum_{\mathbf{k}\sigma} V_1 (M^+ c_{1\mathbf{k}\sigma}^{\dagger} d_{\sigma} + h.c.) + V_2 (M^- c_{2\mathbf{k}\sigma}^{\dagger} d_{\sigma} + h.c.). \tag{6.13}$$

For consistency in notation (compared to Fig. 6.1), the level broadening is henceforth denoted by $J_i = \pi \rho V_i^2$ (usually called Γ_i). At temperature $T \ll E_c$, asymmetric occupation is strongly suppressed, thus one can restrict the discussion to a finite-size local subspace, $M_z = \sum_{m=-\tilde{m}}^{\tilde{m}} m|m\rangle\langle m|$. Then, the Coulomb-like potential term H_M (6.10e) reads

$$H_M = E_c (M_z)^2. \tag{6.14}$$

The resulting Hamiltonian can be treated with NRG: the Hilbert space of the first iteration is built not only of the state space of the local level (dimension 4) and the first sites of the Wilson chain (dimension 4 for each site and channel), but also of the

$2\tilde{m} + 1-$dimensional state space of the pseudo spin, as indicated in the second model illustrated in Fig. 3.8(d).

We use $E_c/U = 0.4$ and fix the total coupling to $J/U = 0.1$, where $J = J_1 + J_2$ and $U = 1$. An asymmetry parameter α is defined by

$$\alpha = \frac{J_1 - J_2}{J}, \tag{6.15}$$

yielding $\alpha = 0$ for symmetric coupling and $\alpha = \pm 1$ if one of the channels is decoupled.

In our calculations we use $\tilde{m} = 1, 2$; checks with up to $\tilde{m} = 4$ qualitatively lead to the same results. In order to keep enough states as well as to cover all relevant energy scales with reasonable computational cost, we keep about 6000 states for the first $4 - 10$ iterations and choose the NRG discretization parameter to be $\Lambda \geq 3$. Checks for up to 9000 kept states during the first 20 iterations qualitatively lead to the same results.

6.3.2   Energy flow diagrams

Information about the FL or NFL character of the system can be obtained by analyzing the NRG flow diagrams, see App. C. Typical examples of flow diagrams of the Pustilnik model are shown in Fig. 6.10. For $\alpha = 0$ (symmetric coupling) the energy flow is shown in Fig. 6.10(a-c). In the particle-hole symmetric point, see (a), the lowest energy levels are given by 1, 4, 5 and 8 (in units of the lowest excited level), typical for the two-channel Kondo effect. For increasing $|V_g|$, the degeneracy of the levels is lifted but the NFL structure is still apparent, see (b). At the critical gate voltage $V_g^c/U \approx 0.4799$, the structure of the energy flow changes abruptly to a FL spectrum, as shown in (c) for $|V_g| \gtrsim V_g$. V_g^c/U depends on E_c/U. We find $V_g^c < 0.5$ always.

A small asymmetry in the couplings, $\alpha \neq 0$, results in a FL spectrum for all V_g. Fig. 6.10(d-f) show flow diagrams for the same gate voltages than (a-c), but at $\alpha = 0.05$. As for $\alpha = 0$, an abrupt change in the flow diagrams is observed at $\sim V_g^c$. As explained in App. C, in (d,e) the flow starts similar to $\alpha = 0$, but changes to FL behaviour at iterations where the asymmetry in the couplings is resolved. For $|V_g| > V_g^c$, the system is a FL for all couplings, thus the energy spectra in (c) and (f) are similar.

6.3.3   Occupation

We calculate the mean value of the local occupation of the Pustilnik model with NRG, as explained in Chapter 3.5. The local occupation $n_{d\sigma}$ is shown in Fig. 6.11(a) as a function of gate voltage. We find for *all* values of α a sharp jump (within our resolution) from $n_{d\sigma} \lesssim \frac{1}{2}$ to $n_{d\sigma} \gtrsim 0$ at some critical gate voltage. The Figure visualizes the two extreme cases of (i) symmetric coupling, $\alpha = 0$, where the position of the jump coincides with the border between NFL and FL, and (ii) $\alpha = 1$, where channel 2 is physically decoupled, i.e. $J_2 = 0$ and $J_1 = J$, since $J_1 + J_2 = J$ is kept constant. The results qualitatively agree with the phase shifts extracted from the flow diagrams in the FL regions (here $\delta_1 + \delta_2 = \pi n_{d\sigma}$).
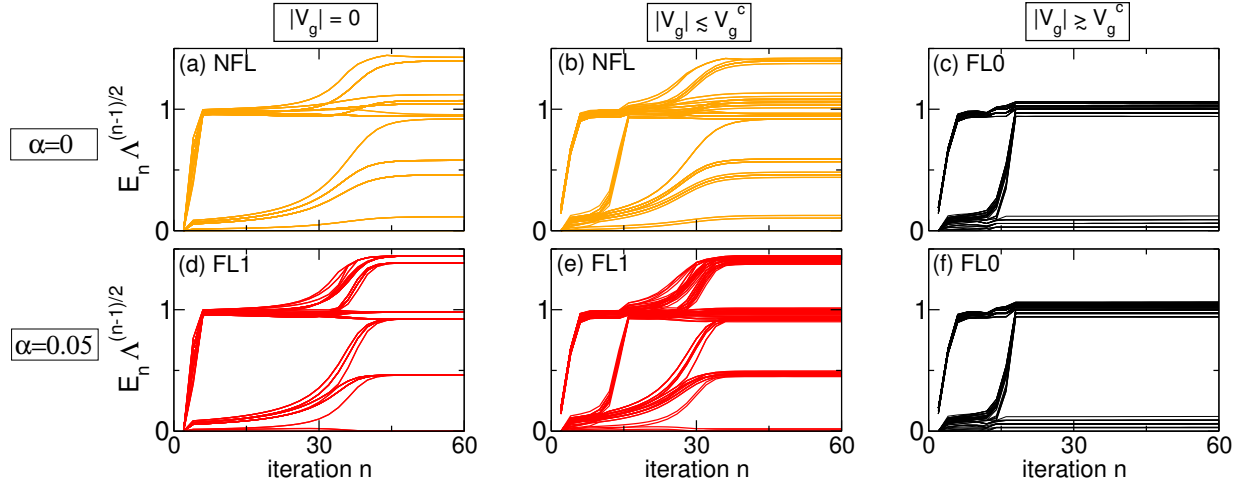
Figure 6.10: NRG flow diagrams of the Pustilnik model. $\Lambda = 3$, $\tilde{m} = 1$. (a-c) $\alpha = 0$: At $V_g^c/U \approx 0.4799$, the flow diagram changes abruptly from NFL [(a), $|V_g| = 0$, (b) $|V_g/U| = 0.478$] to FL [(c) $|V_g/U| = 0.48$] characteristics. (d-f) $\alpha = 0.05$: Same V_g than in (a-c). For asymmetric couplings, the system is a FL for all V_g. Still an abrupt change in the flow diagrams is observed at $|V_g| \sim V_g^c$.

The α-dependence of the critical gate voltage is shown in Fig. 6.11(b). For $J =$const. it seems to obey a quadratic rule, $V_g^c(\alpha) \approx (0.067\alpha)^2 + V_g^c(0)$.

The jump can be understood as follows: Independent of any initial asymmetry in the couplings, the Coulomb-like term H_M suppresses a change in occupation of the reservoirs. Consequently, this term also counteracts a change in local occupation $n_{d\sigma}$. This is similar to an impurity system that exhibits Kondo-like coupling (favouring $n_{d\sigma} = 0, \frac{1}{2}$), together with a small tunnelling term. Therefore, both the local-moment regime with $n_{d\sigma} \approx \frac{1}{2}$, as well as the empty-orbital regime, where $n_{d\sigma} \sim 0$, are extended maximally. Consequently, the mixed-valence regime usually connecting the two regimes does not exist and the occupation jumps abruptly as a function of V_g. Whether there is some critical value E_c for the jump to occur is left for further studies. In the limit $E_c \to \infty$ the tunnelling contribution is expected to vanish and the difference in occupation at the jump approaches $\frac{1}{2}$.

The results for the Pustilnik model are very encouraging, in that they suggest that an abrupt transition between NFL and FL regimes as functions of V_g does indeed occur. It would be very interesting to follow up this study with a detailed investigation of the properties of this critical point, but that lies beyond the scope of this thesis.
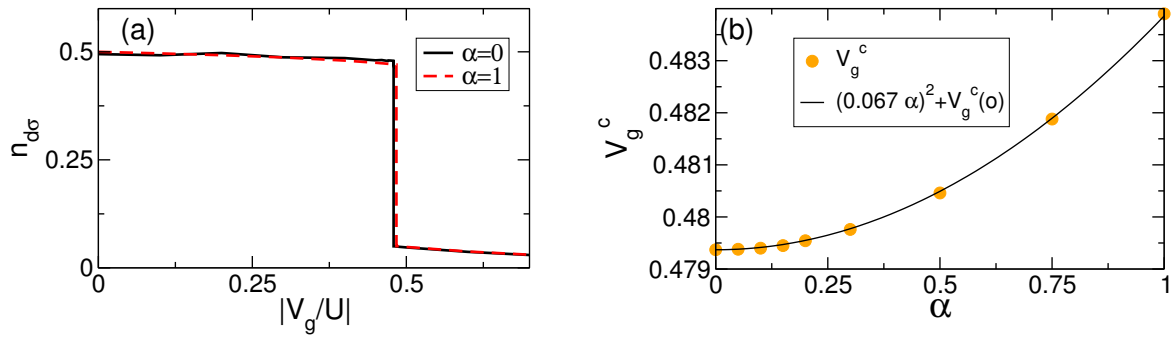
Figure 6.11: Local occupation $n_{d\sigma}$ of the Pustilnik model. $\Lambda = 4$, $\tilde{m} = 2$. (a) Occupation for both extremal cases $\alpha = 0$ $(J_1 = J_2)$ and $\alpha = 1$ $(J_1 = J, \ J_2 = 0)$. For any α we find a jump in the occupation at some critical gate voltage $V_g^c(\alpha)$. This agrees with the abrupt change in flow diagrams, see Fig. 6.10(e,f). (b) For $J =$const. V_g^c seems to depend quadratically on α. For $E_c/U = 0.4$, we find $V_g^c(\alpha) \approx (0.067\alpha)^2 + V_g^c(0)$.

Part III

Appendix

Appendix A

Spectral function

A.1 Smoothening discrete data

A NRG calculation of a spectral function via the Lehmann sum (3.23) yields a discrete set of data points (ω_j, a_j),

$$A_{\text{raw}}(\omega_i) = \sum_j a_j \, \delta(\omega_i - \omega_j). \tag{A.1}$$

In this Appendix, we explain the basics about the typical structure of (ω_j, a_j), show the effects of the broadening of the raw data to a smooth function and explain some tricks to improve the results.

Without loss of generality, the discussion is done for positive frequencies of a symmetric single-level Anderson model (where $A(\omega) = A(-\omega)$ anyway). As in Chapter 3.5, we use $U = 0.3$, $\Gamma = 0.014$ and the NRG parameters $\Lambda = 2.1$ and $N_{kept} \approx 1024$ for the first 30 iterations, then $N_{kept} \approx 512$.

A.1.1 Discrete data

Figure A.1(a) shows typical NRG raw data (ω_j, a_j) in the Kondo regime. Due to the logarithmic discretization, the density of data points increases exponentially with $\omega \to 0$. For $\omega \ll T_K$, no new physics is expected. Remember that also the flow diagram is constant in that regime, see Fig. 3.3(a). Therefore, the structure of the data does not change any more. It can be modelled by

$$\omega_l \propto \frac{1}{2}(1 + \Lambda^{-1}) \, \Lambda^{-(l-1)/2}, \quad a_l \propto \frac{1}{2}(1 + \Lambda^{-1}) \, \Lambda^{-(l-1)/2}, \tag{A.2}$$

thus $a_l/\omega_l = const.$, and the spectral weight is constant in that regime. $l = 1, 2, \ldots$.

"z-averaging" [49]: The density and therefore the quality and resolution of the raw data can be increased by combining several (say N_z) data sets obtained for slightly shifted logarithmic discretizations ($\Lambda^{-n} \to \Lambda^{-n-z}$). In order to obtain a regular data grid, the values of z are chosen to lie at equidistant intervals (of range Δz) between -0.5 and 0.5.

To ensure normalization, $A(\omega) = 1/N_z \sum_z A^z_{\mathrm{raw}}(\omega)$. The raw data shown in Fig. A.1(b) consists of 5 data sets (each indicated by different colour), thus $\Delta z = 0.2$. For each choice of z, the tridiagonalization leading to the Wilson chain has to be done separately. Note that z-averaging does not cure NRG intrinsic errors due to the logarithmic discretization.
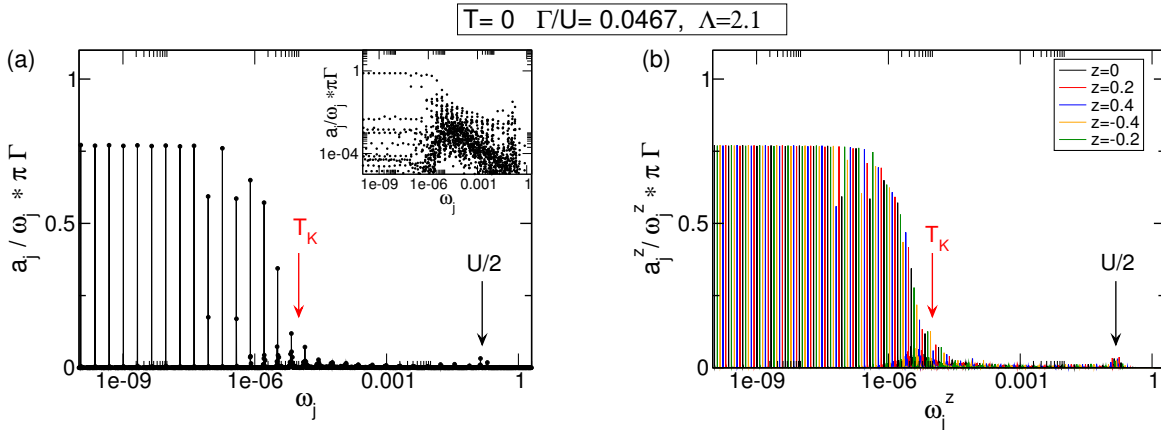

Figure A.1: Raw data for the spectral function $A(\omega)$ of the symmetric single-level Anderson model at $T = 0$ for $\Lambda = 2.1$, $U = 0.3$ and $\Gamma = 0.014$. The Kondo temperature $T_K = 10^{-5}$ and U are indicated by arrows. (a) For $\omega \ll T_K$, clearly $a_j/\omega_j = const.$, as in the model data (A.2). Inset: Same data on a log-log scale. (b) 5 data sets (ω^z_j, a^z_j) obtained for slightly shifted discretization grids ($\Delta z = 0.2$) are combined to one (dense) data set [49].

A.1.2   Smooth curves

Equation (A.1) yields a set of discrete δ peaks. A smooth curve can be obtained by broadening of the δ functions [48]. This is done by folding of the raw data with a properly chosen kernel $K(\omega, \omega')$,

$$A(\omega) \equiv \int d\omega' K(\omega, \omega') A_{\mathrm{raw}}(\omega'). \tag{A.3}$$

A common choice for the kernel K is a log-Gaussian for $\omega \gtrsim \omega_0$ and a Lorenzian [51] or regular Gaussian [44] for connecting the regimes $\pm\omega \lesssim \omega_0$, where $\omega_0 \approx T$. In this work, we follow the approach of [44] and use $\omega_0 = T/2$. Then, at $T = 0$, the kernel is given by the log-Gaussian

$$L(\omega, \omega') = \frac{\theta(\omega\omega')}{\sqrt{\pi}\sigma|\omega|} e^{-\left(\frac{\log|\omega/\omega'|}{\sigma} - \frac{\sigma}{4}\right)^2}. \tag{A.4}$$

On a logarithmic scale, where the raw data is almost uniformly distributed, this is a Gaussian of width $\propto \sigma$ always. Therefore this kernel allows to treat high and low energy data in the same way. Since $\int d\omega L(\omega, \omega') = 1$, it conserves the overall spectral weight, $\int d\omega A(\omega) = \int d\omega A_{\mathrm{raw}}(\omega)$. The influence on the broadening parameter σ is presented in Fig. A.2(a). Usually, $\sigma \approx 1/\sqrt{\Lambda}$ leads to a nicely smoothened curve without suppressing

details. For small choices of σ, the underlying discretization gets visible. $A(\omega)$ is not constant for $\omega \ll T_K$ (due to broadening). This can be cured with z-averaging. Then also small values of σ are allowed, see Fig. A.2(b), so that sharp features can be resolved.
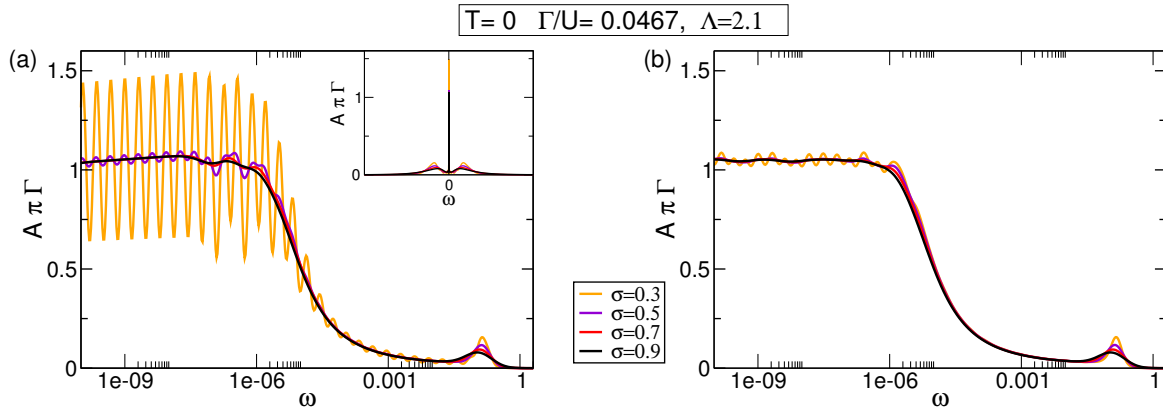

Figure A.2: Smoothened spectral function $A(\omega)$ of the symmetric model at $T = 0$ for $\Lambda = 2.1$, $U = 0.3$, $\Gamma = 0.014$. Various widths σ of the log-Gaussian kernel are used. Same raw data as shown in Fig. A.1 is used. (a) For small values of σ, the underlying discreteness of the raw data is resolved. Inset: Same data on a linear ω-scale. Often, a good choice of σ is given by $\sigma = 1/\sqrt{\Lambda}$ (here: ≈ 0.7). (b) With z-averaging, much smaller values of σ can be used.

Further improvement of the spectral function (e.g. $A(\omega = 0)\pi\Gamma = 1$) is obtained by the self-energy representation, presented in the next Section.

A.2   Self-energy representation

In the Heisenberg picture, the time evolution of an operator $B(t) = e^{iHt}Be^{-iHt}$ can be expressed as a linear differential equation,

$$\dot{B} = -\frac{i}{\hbar}\left[B, H\right]. \tag{A.5}$$

We use $\hbar = 1$ in the following. Bulla *et al.* [50] showed that applying this equation of motion to local correlation functions, the quality of spectral functions obtained with NRG can be improved significantly. The local correlator is written in terms of the self-energy which in turn is a ratio of two correlators that both can be calculated with NRG. Dependencies of each correlator on the discretization parameter Λ or on broadening parameters cancel to a high degree, leading to high quality curves. Additionally, the exact solution for $T = 0$ and $U = 0$ can be obtained - useful to test the accuracy of the results (e.g. in dependence of N_{kept}, Λ, etc.). A comparison of the spectral function at finite U calculated with and without the self-energy representation is given in Fig. A.3.

For keeping notation simple, we write (where convenient) the retarded correlation function between two operators D and B as

$$\mathcal{G}_{DB}^R(t) = \langle D||B\rangle_t = -i\theta(t)\langle [D(t), B]_+\rangle, \tag{A.6}$$

with the Fourier transform $\langle D||B\rangle_\omega$. For convenience, we usually drop the index ω and R. Square brackets with index $+$ correspond to anti-commutation, without index to commutation.

With Eq. (A.5), the equation of motion of a correlation function $\mathcal{G}_{DB}(t)$ reads

$$\frac{d}{dt}\mathcal{G}_{DB}(t) = -i\theta(t)\langle [-i[D, H], B]_+\rangle - i\delta(t)\langle [D, B]_+\rangle. \tag{A.7}$$

Fourier transformation together with analytic continuation $\omega \to \omega_1 + i\omega_2 \equiv z$ leads to

$$z\mathcal{G}_{DB}(z) = \mathcal{G}_{[D,H]B}(z) - \mathrm{tr}\left(\rho[D, B]_+\right). \tag{A.8}$$

A.2.1 Example: Single-level Anderson model coupled to super-conducting leads

As an example, we derive the self-energy representation of the local Green's function for a single level coupled to a superconducting reservoir, a model studied in Chapter 5. The Hamiltonian is given by

$$\begin{aligned}
H &= \sum_\sigma \varepsilon_d n_\sigma + U n_\uparrow n_\downarrow + \sum_{\mathbf{k}\sigma} V(c_{\mathbf{k}\sigma}^\dagger d_\sigma + d_\sigma^\dagger c_{\mathbf{k}\sigma}) \\
&\quad + \sum_{\mathbf{k}\sigma} \varepsilon_\mathbf{k} c_{\mathbf{k}\sigma}^\dagger c_{\mathbf{k}\sigma} - \sum_\mathbf{k} \Delta\left(c_{\mathbf{k}\uparrow}^\dagger c_{-\mathbf{k}\downarrow}^\dagger + c_{-\mathbf{k}\downarrow} c_{\mathbf{k}\uparrow}\right).
\end{aligned} \tag{A.9}$$

For the calculation of the Green's function of this system it is convenient to work in Nambu space, where the operators are combined to the spinors

$$\mathbf{D}^\dagger \equiv \begin{pmatrix} d_\uparrow^\dagger \\ d_\downarrow \end{pmatrix}, \quad \mathbf{C}_\mathbf{k}^\dagger \equiv \begin{pmatrix} c_{\mathbf{k}\uparrow}^\dagger \\ c_{-\mathbf{k}\downarrow} \end{pmatrix}, \tag{A.10}$$

which obviously fulfil the standard fermionic anti-commutation relations by components, $[\mathbf{C}_{\mathbf{k}\mu}, \mathbf{C}_{\mathbf{k}'\mu'}^\dagger]_+ = \delta_{\mathbf{k}\mathbf{k}'}\delta_{\mu\mu'}$ and $[\mathbf{C}_{\mathbf{k}\mu}, \mathbf{C}_{\mathbf{k}'\mu'}]_+ = 0$, analogously for $\mathbf{D}_\mu$. Thereby $\mu = 1, 2$ denotes the first and second component of the spinors. In this representation, the Hamiltonian (A.9) reads

$$H = (\varepsilon_d + \frac{U}{2}) N_d + \frac{U}{2}(N_d)^2 + \sum_\mathbf{k} V\left(\mathbf{C}_\mathbf{k}^\dagger \sigma_z \mathbf{D} + H.c.\right) + \sum_\mathbf{k} \mathbf{C}_\mathbf{k}^\dagger A_\mathbf{k} \mathbf{C}_\mathbf{k}, \tag{A.11}$$

where we use $N_d = \mathbf{D}^\dagger \sigma_z \mathbf{D}$, $A_\mathbf{k} = \varepsilon_\mathbf{k}\sigma_z - \Delta\sigma_x$, and the Pauli matrices σ_z and σ_x. The local Green's function

$$\mathcal{G}_\Delta(\omega) = \langle \mathbf{D}||\mathbf{D}^\dagger\rangle = \begin{pmatrix} \langle d_\uparrow||d_\uparrow^\dagger\rangle & \langle d_\uparrow||d_\downarrow\rangle \\ \langle d_\downarrow^\dagger||d_\uparrow^\dagger\rangle & \langle d_\downarrow^\dagger||d_\downarrow\rangle \end{pmatrix} \tag{A.12}$$

can then be calculated componentwise by evaluation of the equation of motion (A.8). The commutator $[\mathbf{D}_\mu, H]$ yields

$$[\mathbf{D}_\mu, H] = \varepsilon_d s_\mu \mathbf{D}_\mu + U \mathbf{D}_\mu N_d + \sum_{\mathbf{k}} V s_\mu \mathbf{C}_{\mathbf{k}\mu}, \tag{A.13}$$

where for simplicity of notation we define $s_\mu = \sigma_{z,\mu\mu}$. The resulting equation of motion reads

$$(z - s_\mu \varepsilon_d) \, \langle \mathbf{D}_\mu || \mathbf{D}_{\mu'}^\dagger \rangle = U \langle \mathbf{D}_\mu N_d || \mathbf{D}_{\mu'}^\dagger \rangle + \sum_{\mathbf{k}} \, s_\mu V \langle \mathbf{C}_{\mathbf{k}\mu} || \mathbf{D}_{\mu'}^\dagger \rangle - \delta_{\mu\mu'}. \tag{A.14}$$

The correlators $\langle \mathbf{C}_{\mathbf{k}\mu} || \mathbf{D}_{\mu'}^\dagger \rangle$ still need to be expressed in terms of local operators. For this we apply Eq. (A.8) to $\langle \mathbf{C}_{\mathbf{k}\mu} || \mathbf{D}_{\mu'}^\dagger \rangle$,

$$z \langle \mathbf{C}_{\mathbf{k}\mu} || \mathbf{D}_{\mu'}^\dagger \rangle = s_\mu V \langle \mathbf{D}_\mu || \mathbf{D}_{\mu'}^\dagger \rangle + s_\mu \varepsilon_{\mathbf{k}} \langle \mathbf{C}_{\mathbf{k}\mu} || \mathbf{D}_{\mu'}^\dagger \rangle - \Delta \langle \mathbf{C}_{\mathbf{k}\bar{\mu}} || \mathbf{D}_{\mu'}^\dagger \rangle, \tag{A.15}$$

where $\bar{\mu} \neq \mu$. Replacing the last term by the analogous expression with interchanged μ and $\bar{\mu}$, we arrive at

$$\langle \mathbf{C}_{\mathbf{k}\mu} || \mathbf{D}_{\mu'}^\dagger \rangle = \left[z - s_\mu \varepsilon_{\mathbf{k}} + \frac{\Delta}{z + s_\mu \varepsilon_{\mathbf{k}}} \right]^{-1} V s_\mu \left(\langle \mathbf{D}_\mu || \mathbf{D}_{\mu'}^\dagger \rangle + \frac{\Delta}{z + s_\mu \varepsilon_{\mathbf{k}}} \langle \mathbf{D}_{\bar{\mu}} || \mathbf{D}_{\mu'}^\dagger \rangle \right). \tag{A.16}$$

Inserting this result into Eq. (A.15), we obtain an expression where only local operators contribute,

$$\sum_\beta \left(z \delta_{\mu\beta} - \varepsilon_d \sigma_{z\mu\beta} - \sum_{\mathbf{k}} V^2 \frac{z \delta_{\mu\beta} + \varepsilon_{\mathbf{k}} \sigma_{z\mu\beta} - \Delta \sigma_{x\mu\beta}}{z^2 - (\varepsilon_{\mathbf{k}}^2 - \Delta^2)} \right) \langle \mathbf{D}_\beta || \mathbf{D}_{\mu'}^\dagger \rangle = U \langle \mathbf{D}_\mu N || \mathbf{D}_{\mu'}^\dagger \rangle - \delta_{\mu\mu'}. \tag{A.17}$$

In the wide band limit where we assume a constant density of states in the leads ρ, the summation over $\mathbf{k}$ leads to the hybridization term [85]

$$\mathbf{\Pi}(z) = -\Gamma \frac{z \mathbb{1}_2 - \Delta \sigma_x}{E(z)}, \tag{A.18}$$

with $\Gamma = \pi \rho V^2$. Note that Π is usually referred to as $\mathbf{\Delta}$, which is already in use for the superconducting gap in this Appendix. After analytic continuation, $E(z)$ reads

$$E(\omega) = \begin{cases} -i \, \mathrm{sgn}(\omega) \sqrt{\omega^2 - \Delta^2} & \text{for } |\omega| > \Delta, \\ \sqrt{\Delta^2 - \omega^2} & \text{for } |\omega| < \Delta. \end{cases} \tag{A.19}$$

In matrix notation, the Green's function is then defined by the equation

$$\left(\omega \mathbb{1}_2 - \varepsilon_d \sigma_z + \Gamma \frac{\omega \mathbb{1}_2 - \Delta \sigma_x}{E(\omega)} \right) \mathcal{G}_\Delta(\omega) = U F(\omega) - \mathbb{1}_2, \tag{A.20}$$

where the local correlator F is given by $F(\omega) = \langle \mathbf{D}_\mu N || \mathbf{D}_{\mu'}^\dagger \rangle$. For the non-interacting Green's function the analytic expression follows to be

$$\mathcal{G}_{0\Delta}(\omega)^{-1} = \omega \mathbb{1}_2 - \varepsilon_d \sigma_z + \Gamma \frac{\omega \mathbb{1}_2 - \Delta \sigma_x}{E(\omega)}. \qquad (A.21)$$

For each of the components of $\mathcal{G}_{0\Delta}$, this leads to an analytic expression for the corresponding spectral function $(A(\omega) = -\frac{1}{\pi} \mathrm{Im} \mathcal{G}(\omega))$, which can be very useful for checking the NRG results. As an example we give the formulas for the continuum contribution $(|\omega| > \Delta)$ of the $1 - 1$ component (as used in Chapter 5 mainly to check the broadening procedure for the special case of superconducting leads at $T = 0$). Matrix inversion immediately yields

$$\mathcal{G}_{0\Delta,11}(\omega) = \frac{1}{D(\omega)} \left\{ (\omega + \varepsilon_d) + i\,\Gamma\rho_\Delta \right\}, \qquad (A.22)$$

with the determinant $D(\omega) = (\omega^2 - \Gamma^2 - \varepsilon_d^2) + i\,2\Gamma\omega\rho_\Delta$, where $\rho_\Delta(\omega) = \frac{\theta(|\omega|-\Delta)\,|\omega|}{\sqrt{\omega^2-\Delta^2}}$ is the density of states of a bulk superconductor. Therefore the spectral function for $U = 0$, $T = 0$ and $|\omega| > \Delta$ is given by

$$A(\omega) = \frac{(\omega + \varepsilon_d)^2 + \Gamma^2}{(\omega^2 - \varepsilon_d^2 - \Gamma^2)^2 + (2\Gamma^2\omega\rho_\Delta)^2} \,\Gamma\rho_\Delta/\pi. \qquad (A.23)$$

A.2.2 General self-energy representation

Equation (A.20) can be rewritten in terms of the Dyson equation,

$$\mathcal{G}^{-1}(\omega) = \mathcal{G}_0^{-1} - \mathbf{\Sigma}(\omega), \qquad (A.24)$$

which is a general way to express impurity Green's functions. Comparison with Eq. (A.20) leads to the (also general) expression for the self-energy

$$\mathbf{\Sigma}(\omega) = U\mathbf{F}(\omega)\mathcal{G}^{-1}(\omega). \qquad (A.25)$$

Therefore the self-energy can be obtained with NRG by the calculation of the two correlation functions $\mathcal{G}$ and $\mathbf{F}$ [50]. To be precise, the imaginary part of the correlation functions is calculated with NRG. The real part of $\mathcal{G}^R$ is obtained by Kramers-Kronig transformation. Moreover, Bulla *et al.* [50] point out that the full Green's function can be obtained with higher accuracy when employing Eq. (A.24) compared to the direct evaluation of $\mathcal{G}(\omega)$. NRG-intrinsic errors as due to the Λ-discretization or the broadening procedure are the same for $\mathcal{G}$ and F, therefore "cancel" up to some point in the self-energy $\Sigma \propto F/\mathcal{G}$. Figure A.3 shows the example of the spectral function of the single-level Anderson model calculated with and without this self-energy representation. The formulas for this case are given below. Clearly, the oscillations due to the Λ-discretization reduce considerably and the Friedel sum rule [21] stating $A(0)\pi\Gamma = 1$ is fulfilled to high extent.

A.2.3 Example: M-level, N-lead Anderson model

As a further example we give the results for the M-level N-lead Anderson model (as used in Chapter 4), which can be obtained via the equation of motion in a similar way. The non-interacting Green's function matrix then reads

$$\mathcal{G}_0(\omega) = [\omega \mathbb{1} - \mathbf{h_0} - \Pi(\omega)]^{-1}, \tag{A.26}$$

with the local term $(h_0)_{i\mu,i'\mu'} = \varepsilon_{d,i\mu}\delta_{ii'}\delta_{\mu\mu'}$, the hybridization

$$\boldsymbol{\Pi}_{i\mu,i'\mu'}(z) = \sum_{\mu\mathbf{k}} \frac{V_{i\mu\mathbf{k}\mu}V^*_{i'\mu\mathbf{k}\mu'}}{z - \varepsilon_{\mathbf{k}}}\delta_{\mu\mu'} = (-i\pi + \log\{|(z-1)/(z+1)|\})\rho V_{i\mu}V^*_{i'\mu} \tag{A.27}$$

and the $\mathbf{F}$-correlation matrix $F_{i\mu,i'\mu'} = \langle d_{i\mu}\sum_{j\mu''}n_{d,j\mu''}||d^\dagger_{i'\mu'}\rangle$.
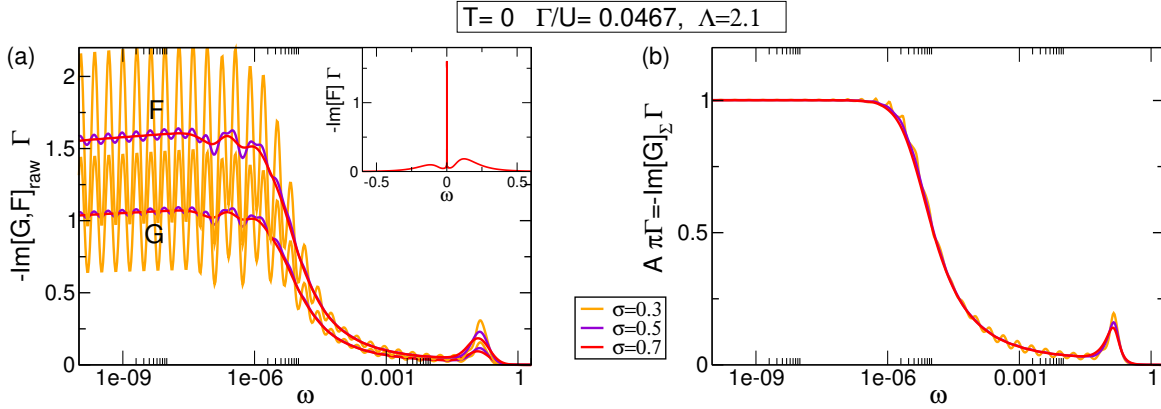

Figure A.3: Improvement of the spectral function with the self-energy representation for various broadening parameters σ. As for the previous Figures, we use $T = 0$, $\Lambda = 2.1$, $U = 0.3$ and $\Gamma = 0.014$. (a) $A\pi = \text{Im}[\mathcal{G}]$, $\text{Im}[F]$ as extracted directly from NRG. Both functions show the same "artefacts" due to the logarithmic discretization and broadening. Inset: $\text{Im}[F]$ on a linear scale. (b) $A(\omega)$ calculated using the self-energy representation of $\mathcal{G}$. The artefacts cancel and the result is improved significantly. Much smaller value of σ can be used. In this plot, the Friedel sum rule [21] (here: $A(0)\pi\Gamma = 1$) is fulfilled up to 0.15%.

Appendix B

Relation between the Anderson and the Kondo model

In the local moment regime of the Anderson model, the impurity level is fixed at $\varepsilon_d \ll E_F \ll \varepsilon_d + U$. Then the QD is approximately singly occupied; the empty or doubly occupied states of the QD are energetically highly unfavourable. As motivated in Sec. 2.5, it is intuitive to relate the Anderson model to an effective model of a local spin $\mathbf{S}$ interacting via a ferromagnetic Heisenberg interaction with the spin $\mathbf{s}$ provided by the reservoir. The mapping was done rigorously in 1966 by J.R. Schrieffer and P.A. Wolff [30]. They presented a canonical transformation, the Schrieffer-Wolff transformation, that relates the single-level Anderson model in the local moment regime with the Kondo model, the model J. Kondo had used in 1964 to explain the Kondo effect [1]. The existence of the transformation proves that the single-level Anderson model (for which perturbation theory cannot solve the Kondo problem) has similar low-temperature anomalies than the Kondo model [30] and shows Kondo physics. The idea of the Schrieffer-Wolff transformation can be summarized as follows: (i) Processes to first order in V are eliminated from the tunnelling amplitude by a canonical transformation and (ii) then the system is project onto the subspace of one local electron. The result is the Kondo model with an Heisenberg exchange interaction $J_{kk'}$.

In the first part of this Appendix we apply the Schrieffer-Wolff transformation to a two-channel Anderson-like model known to show Kondo physics [16]. We find no simple direct relation between the Anderson-like model and the Anderson-Kondo model studied in Chapter 6.2. In the second part we relate the Kondo temperatures of the single-level Anderson model and the Kondo model presented in Sec. 2.4.3 and 2.5.1, respectively.

B.1 Schrieffer-Wolff transformation for a two-channel model

Recently, Potok *et al.* [17] reported the experimental realization of the two-channel Kondo effect. Their setup was motivated by a proposal of Oreg *et al.* [16], where a two-channel

Anderson-like model was shown to lead to two-channel Kondo physics. The model consists of a local level, tunnel-coupled to reservoir 1 and 2. Reservoir 1 is realized by a big dot, modelled by a standard reservoir plus Coulomb energy U_1 which ensures that the number of particles in reservoir 1 is conserved. This results in two-channel Kondo physics, since due to energy conservation, particle exchange between reservoir 1 and 2 is suppressed.

In Chapter 6.2 we studied a quite similar model, where channel 1 is coupled to the impurity via antiferromagnetic Heisenberg coupling. At first glance one expects that, similar to the Anderson and Kondo model, also in this case a Schrieffer-Wolff transformation should provide a mapping between the two two-channel models. Following the original article [30], we apply the Schrieffer-Wolff transformation to the Anderson-like model. But, contrarily to the standard mapping where the state space of the impurity is projected to single occupancy, the number of particles in channel 1 is kept constant and not on the local level. We do not find a transformation directly relating the two models. Additional terms are generated and the coupling constants are infinite series in the occupation and Coulomb interaction of reservoir 1.

We start from the two-channel Anderson-like model proposed in [16],

$$
H \;=\; H_0 + H_1, \tag{B.1}
$$

$$
H_0 \;=\; \varepsilon_d n_d + U n_\uparrow n_\downarrow + \frac{U_1}{2}(\hat{N}_1 - n_C)^2 + \sum_{\alpha=1,2;k\sigma} \varepsilon_{\alpha k\sigma} n_{\alpha k\sigma} + \sum_{k\sigma} V_2(c^\dagger_{2k\sigma} d_\sigma + H.c.), \tag{B.2}
$$

$$
H_1 \;=\; V \sum_{k\sigma}(c^\dagger_{1k\sigma} d_\sigma + H.c.). \tag{B.3}
$$

H_1 is the tunnelling term we want to "eliminate" and replace by a Heisenberg interaction with coupling constant $J \propto V^2$. In the following, we drop the summation sign. Where necessary for clarity, variables or operators related to the impurity are denoted by an index d. $\hat{N}_1 = \sum_{k'\sigma'} n_{1k'\sigma'}$ counts the number of electrons on the big dot (reservoir 1). We consider $n_C = 0$, otherwise $-U_1\hat{N}_1 n_C$ can be included into the definition of ε_k.

B.1.1   Transformation of the Hamiltonian

We search a canonical transformation S such that the effective Hamiltonian

$$
\tilde{H} = e^S H e^{-S} \tag{B.4}
$$

is quadratic in V, i.e. it does not contain any terms of order V, V^3 or higher order. For

$$
e^S \approx 1 + S + \frac{1}{2}S^2 \tag{B.5}
$$

the effective Hamiltonian is given by

$$
\tilde{H} \approx H_0 + H_1 + [S, H_0] + [S, H_1] + \frac{1}{2}[S, [S, H_0]]. \tag{B.6}
$$

It is easy to check that the terms of order V vanish for

$$H_1 = -[S, H_0], \tag{B.7}$$

since under this condition $S \propto V$. Consequently, the transformed (and approximated) Hamiltonian reads

$$\tilde{H} = H_0 + \frac{1}{2}[S, H_1] \tag{B.8}$$

B.1.2 Appropriate transformation

We search a generator S such that $H_1 = [H_0, S]$ is fulfilled. We start from S_0, i.e. the transformation for the standard Anderson model [30]. As usual, potential scattering terms ($\propto VV_2 c_1^\dagger c_2$) are neglected. S is extended such that the term generated by the Coulomb interaction of the impurity vanishes[1]. But, contrarily to the standard Schrieffer-Wolff transformation, the equations do *not* close, because *many* electrons interact on the large dot via the Coulomb interaction U_1, and obviously $\hat{N}_1 \hat{N}_1 \neq \hat{N}_1$. The calculation yields

$$
\begin{aligned}
S \;=\;& S_0 + S_1 + \sum_{m=2}^{\infty} S_m \\
S_0 \;=\;& \sum_{k\sigma} \frac{V}{\bar{\varepsilon}_k - \varepsilon_d} \left(c_{1k\sigma}^\dagger d_\sigma - H.c. \right) + \sum_{k\sigma} \frac{V}{\bar{\varepsilon}_k - \varepsilon_d} \frac{U}{\bar{\varepsilon}_k - \varepsilon_d - U} \left(c_{1k\sigma}^\dagger d_\sigma n_{-\sigma}^d - H.c. \right), \\
S_1 \;=\;& -\sum_{k\sigma} \frac{V}{\bar{\varepsilon}_k - \varepsilon_d} \frac{U_1}{\bar{\varepsilon}_k - \varepsilon_d} \left(c_{1k\sigma}^\dagger d_\sigma \hat{N}_1 - H.c. \right), \\
& -\sum_{k\sigma} \frac{V}{\bar{\varepsilon}_k - \varepsilon_d} \left(\frac{UU_1}{\bar{\varepsilon}_k - \varepsilon_d - U} - \frac{UU_1}{\bar{\varepsilon}_k - \varepsilon_d} \right) \frac{1}{\bar{\varepsilon}_k - \varepsilon_d - U} \left(c_{1k\sigma}^\dagger d_\sigma n_{-\sigma}^d \hat{N}_1 - H.c. \right), \\
S_m \;=\;& \sum_{k\sigma} X_m^k c_{1k\sigma}^\dagger d_\sigma (\hat{N}_1)^m + \sum_{k\sigma} Y_m^k c_{1k\sigma}^\dagger d_\sigma n_{-\sigma}^d (\hat{N}_1)^m - H.c.,
\end{aligned}
\tag{B.9}
$$

where $Y_m^k \propto VUU_1^m$ and $X_m^k \propto VU_1^m$. Apart from $\bar{\varepsilon}_k = \varepsilon_k + \frac{U_1}{2}$, S_0 is the same than for the standard Anderson model. Actually, for $n_C \neq 0$ and $\frac{U_1}{2} = U_1 n_C$, it is exactly the same.

It is convenient to shorten the result to

$$S = \sum_n S_n = \sum_n \left[\left(\sum_{k\sigma} X_n^k c_{1k\sigma}^\dagger d_\sigma (\hat{N}_1)^n + \sum_{k\sigma} Y_n^k c_{1k\sigma}^\dagger d_\sigma n_{-\sigma}^d (\hat{N}_1)^n \right) - H.c. \right]. \tag{B.10}$$

B.1.3 The effective Hamiltonian

Let us now evaluate $\tilde{H} = H_0 + \frac{1}{2}[S, H_1]$. Operators with index d refer to the impurity, with index k to the big dot (reservoir 1). Notation: $\Psi_k^\dagger = (c_{1k\uparrow}^\dagger, c_{1k\downarrow}^\dagger)$, $\vec{s}^{kk'} = (\Psi_k^\dagger 1/2 \vec{\sigma} \Psi_{k'})$, with $\vec{\sigma}_i$ the Pauli matrix σ_i. Same for the dot.

---

[1] It vanishes since $n_\sigma n_\sigma = n_\sigma$.

The contribution of S_0 leads to the well known result for the standard Anderson model,

$$\frac{1}{2}[S_0, H_1] = 2J_{kk'}\vec{S}_d \cdot \vec{s}_{kk'} \tag{B.11a}$$

$$+ \ 2(W_{kk'} - \frac{1}{4}J_{kk'}(\Psi_d^\dagger\Psi_d))(\Psi_k^\dagger\Psi_{k'}) \tag{B.11b}$$

$$- \ 2(W_{kk} - \frac{1}{2}J_{kk}n_{d-\sigma})n_{d\sigma} \tag{B.11c}$$

$$- \ \frac{1}{2}J_{kk'}c_{k-\sigma}^\dagger c_{k'\sigma}^\dagger d_\sigma d_{-\sigma} + H.c. \tag{B.11d}$$

The coupling constants are given by

$$J_{k'k} = \frac{1}{2}UV_kV_{k'}\left[\frac{1}{(\varepsilon_k - (\varepsilon_d + U))(\varepsilon_k - \varepsilon_d)} + \frac{1}{(\varepsilon_{k'} - (\varepsilon_d + U))(\varepsilon_{k'} - \varepsilon_d)}\right], \tag{B.12}$$

$$W_{k'k} = \frac{1}{4}V_kV_{k'}\left[\frac{1}{\varepsilon_k - \varepsilon_d} + \frac{1}{\varepsilon_{k'} - \varepsilon_d}\right]. \tag{B.13}$$

In order to obtain the standard Kondo-model (when assuming a single-channel system), the contributions of Eq. (B.11) are evaluated for the subspace of one electron on the dot so that only the $\vec{S}\vec{s}$ term survives and the Kondo Hamiltonian

$$H_K = 2J_{kk'}\vec{S}_d \cdot \vec{s}_{kk'} + \varepsilon_{k\sigma}n_{k\sigma} \tag{B.14}$$

is obtained. For $k, k' \sim k_F = 0$, the coupling constant is given by

$$J = -\frac{UV^2}{\varepsilon_d(\varepsilon_d + U)}, \tag{B.15}$$

as motivated in Sec. 2.5. The coupling is antiferromagnetic, $J > 0$, for $-U < \varepsilon_d < 0$. Actually, the Schrieffer-Wolff transformation does not make sense out of that regime anyway.

In our case of the two-channel model, we focus on the subspace of constant number of electrons in reservoir 1, i.e. $< \Psi_k^\dagger\Psi_k > = < \hat{N}_1 > = N_1 = const$. Then the contribution of S_0 results in:

- The first term describes the Kondo coupling.

- $(\Psi_k^\dagger\Psi_{k'})$ is potential scattering and can be neglected.

- A term $(\Psi_d^\dagger\Psi_d)(\Psi_k^\dagger\Psi_{k'})$ is generated.

- In the third line the *impurity parameters* ε_d and U of H_0 are renormalized.

- The last term leads out of the subspace, thus cancels.

Therefore, already S_0 leads to a different Hamiltonian than studied in Chapter 6.2. But let us now evaluate $\tilde{H}$ in its general form:

$$\frac{1}{2}[S_n, H_1]|_{<\hat{N}_1>=N_1} = \tag{B.16}$$

$$\frac{1}{2}\sum_{kk'\sigma\sigma'}\{X_n^k V \quad [\quad (c_{1k\sigma}^\dagger c_{1k'\sigma} - n_\sigma^d)(N_1)^n$$

$$- (c_{1k\sigma}^\dagger c_{1k'\sigma'}d_\sigma d_{\sigma'}^\dagger)\left[\sum_{x=1}^{n-1}(N_1)^{n-x}(N_1-1)^x\right]]$$

$$+Y_n^k V \quad [\quad (c_{1k\sigma}^\dagger c_{1k'\sigma} - n_\sigma^d)\, n_{-\sigma}^d\,(N_1)^n$$

$$+ \quad (c_{1k\sigma}^\dagger c_{1k'-\sigma}d_\sigma d_{-\sigma}^\dagger)(N_1)^n$$

$$- \quad (c_{1k\sigma}^\dagger c_{1k'\sigma'}d_\sigma n_{-\sigma}^d d_{\sigma'}^\dagger)\left[\sum_{x=1}^{n-1}(N_1)^{n-x}(N_1-1)^x\right]]$$

$$\} + H.c.$$

Written in $SU(2)$ symmetric form, this reads

$$\frac{1}{2}[S_n, H_1] = \left[-Y_n^{kk'}(N_1)^n + (-X_n^{kk'} + Y_n^{kk'})(M_n)\right]\vec{S}_d\vec{s}_{kk'} \tag{B.17}$$

$$- \left[\frac{1}{2}(N_1)^n(X_n^{kk} - Y_n^{kk}\,n_{-\sigma}^d)\right]n_\sigma^d$$

$$+ \left[\frac{1}{2}X_n^{kk'}(N_1)^n + \frac{1}{2}X_n^{kk'}(M_n)\right](\Psi_k^\dagger\Psi_{k'})$$

$$+ \left[\frac{1}{4}Y_n^{kk'}(N_1)^n - \frac{1}{4}(X_n^{kk'} + Y_n^{kk'})(M_n)\right](\Psi_d^\dagger\Psi_d)(\Psi_k^\dagger\Psi_{k'})$$

$$+ \frac{1}{2}Y_n^{kk'}(M_n)\,c_{k\sigma}^\dagger c_{k'\sigma}n_\sigma^d n_{-\sigma}^d$$

were we used $Y_n^{kk'} = V(Y_n^k + Y_n^{k'})$, same for $X_n^{kk'}$. Therefore, $Y_n^{kk'} \propto \frac{V^2}{\hat{\varepsilon}_k}(U_1 N_1)^n$, $X_n^{kk'} \propto \frac{V^2}{\hat{\varepsilon}_k}(U_1)^n(M_n)$, with $(M_n) = \sum_{x=1}^{n-1}(N_1)^{n-x}(N_1-1)^x$. The terms for $n = 0, 1$ you can get from Eq. (B.9). Except for the last term, the Hamiltonian has the same structure than the S_0 contribution. But the coupling constants are infinite series in the occupation N_1 and Coulomb interaction U_1 of reservoir 1.

B.1.4 Some useful relations

$$-(\Psi_d^\dagger\frac{\sigma_z}{2}\Psi_d)(\Psi_k^\dagger\frac{\sigma_z}{2}\Psi_{k'}) = \frac{1}{4}[-n_{d\sigma}c_{k\sigma}^\dagger c_{k'\sigma} + n_{d\sigma}c_{k-\sigma}^\dagger c_{k'-\sigma}] \tag{B.18}$$

$$\frac{1}{4}(\Psi_d^\dagger\Psi_d)(\Psi_k^\dagger\Psi_{k'}) = \frac{1}{4}[n_{d\sigma}c_{k\sigma}^\dagger c_{k'\sigma} + n_{d\sigma}c_{k-\sigma}^\dagger c_{k'-\sigma}] \tag{B.19}$$

$$-2S_z^d s_z^{kk'} + \frac{1}{2}(\Psi_d^\dagger\Psi_d)(\Psi_k^\dagger\Psi_{k'}) = n_{d-\sigma}c_{k\sigma}^\dagger c_{k'\sigma} \tag{B.20}$$

B.2 Kondo temperature for the single-level Anderson and the Kondo model

Applying the Schrieffer-Wolff transformation to the standard single-level Anderson model [30], the coupling V of the Anderson model and the coupling J of the Kondo model are related by Eq. (B.15),

$$J(\Gamma) = -\frac{\Gamma}{\pi\rho}\frac{U}{(U+\varepsilon_d)\varepsilon_d},$$

with $\Gamma = \pi\rho V^2$. For the symmetric case, where $\varepsilon_d = -U/2$, the relation yields

$$J(\Gamma) = \frac{4\Gamma}{U\pi\rho}. \tag{B.21}$$

For the single-level Anderson model the scale of the Kondo temperature can be estimated by poor man's scaling [29] or by Bethe-Ansatz [28]

$$T_K^{AM} = \sqrt{\frac{U\Gamma}{2}}e^{-\frac{\pi}{2U\Gamma}\varepsilon_d(U+\varepsilon_d)}. \tag{B.22}$$

Note that, depending on convention, T_K is often multiplied by the Wilson number $w = 0.41071$ that can be extracted from the exact Bethe Ansatz.

For the Kondo model perturbation theory or poor man's scaling to second order in J lead to $T_K^{O(J^2)} \approx De^{-1/2J\rho}$, as derived in Sec. 2.5.1, see Eq. (2.20). Poor man's scaling to third order in J is more sophisticated,

$$T_K^{O(J^3)} \sim D_{KM}|2J\rho|^2\, e^{-1/2J\rho}. \tag{B.23}$$

This is the formula that agrees with the results of NRG for the Kondo model.

But it is known that relating the Anderson model and Kondo model, the effective bandwidth D_{KM} of the Kondo model is proportional to the Coulomb energy U of the Anderson model, $D_{KM} = cU$. Therefore, relating the symmetric Anderson model to the Kondo model, $T_K^{AM}(\Gamma) = T_K^{O(J^3)}(J(\Gamma))$, one finds the proportionality constant c to be $c = \frac{\sqrt{\pi}}{4}$.

It is important to keep this U-dependence of the Kondo bandwidth in mind when comparing NRG results obtained for the Anderson model and the corresponding Kondo model, see Fig. B.1. There the flow diagrams for a Kondo model with $J = 0.1$ and a symmetric Anderson model with $\Gamma(J = 0.1)$ and $U = 0.2$ are shown. Clearly the iteration where the system changes to the strong coupling limit differs for the two models. They are

well described by the Kondo temperatures given by Eq. (B.23) for the Kondo model with $D_{KM} = 1$ and Eq. (B.22) for the Anderson model, respectively. Both Kondo temperatures are indicated by a vertical line. The Figure also shows the Kondo temperatures for the effective couplings J_{eff} and $\Gamma(J_{eff})$, where $J_{eff}(\Lambda) = J/A(\Lambda)$ with $A(\Lambda) = \frac{1}{2}\ln\Lambda\frac{1+\lambda^{-1}}{1-\lambda^{-1}}$ takes the NRG intrinsic discretization with discretization parameter Λ into account [38].
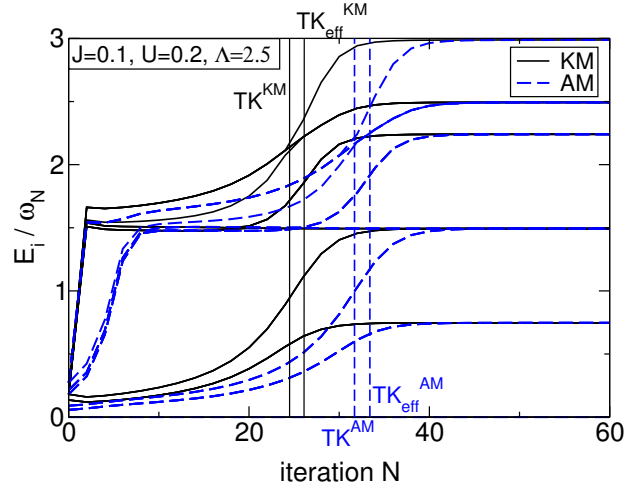

Figure B.1: NRG flow diagram for a Kondo model with $J = 0.1$ and the corresponding symmetric Anderson model with $\Gamma(J = 0.1)$ and $U = 0.2$. The NRG discretization parameter is chosen to be $\Lambda = 2.5$. The energy scale of the transition to the strong coupling regime differ by a factor of $\propto U$. The Kondo temperatures (for J as well as $J_{eff}(\Lambda)$, see text) are indicated by vertical lines. For the Kondo model $T_K^{O(J^3)}$ is given by Eq. (B.23) with $D_{KM} = 1$, for the Anderson model we use Eq. (B.22) multiplied by the Wilson number $w \approx 0.41071$.

Appendix C

Scattering phases and NRG flow diagrams

At $T = 0$, a Fermi liquid can be described by potential scattering. It is therefore fully characterized by the scattering matrix. Accordingly, the low lying energy levels of the converged NRG flow diagrams can be understood in terms of the scattering phases $\delta_{\nu\sigma}$ defined by the eigenvalues $e^{i\delta_{\nu\sigma}}$ of the scattering matrix, with $\nu = 1, 2$ denoting the two (spinful) eigenchannels.

Within the NRG method, the Hamiltonian of an impurity system like the Anderson or Kondo model is transformed to a chain Hamiltonian that can be solved iteratively by successively adding sites, thereby increasing the energy resolution. For details, see Sec. 3. Actually, with increasing chain length N, not only the energy resolution gets enhanced like $\sim \Lambda^{-(N-1)/2}$, but also the length scale of the system increases like $L \sim \Lambda^{(N-1)/2}$ [38]. $\Lambda > 1$ is an NRG parameter characterizing the logarithmic discretization of the conduction band.

Therefore, if the stable low-energy fixed-point is reached (i.e. at iterations where the system rescaled by $\Lambda^{-(N-1)/2}$ is self-similar and the resulting spectrum is invariant w.r.t. added sites), the rescaled spectrum is the spectrum of a system of size L in units of $2\pi v_F/L$, with v_F the Fermi velocity.

It can then be understood in terms of boundary conformal field theory [37]. In case of a Fermi liquid, the fixed-point spectrum is equal (within the accuracy of NRG) to the spectrum of the effective fixed-point Hamiltonian [37, 93]

$$H_{\mathrm{fp}} = \sum_{\nu\sigma} \Delta_\nu \left(q - \frac{\delta_{\nu\sigma}}{\pi} \right) c^\dagger_{q,\nu\sigma} c_{q,\nu\sigma}. \tag{C.1}$$

Here, q is integer (half-integer) for even (odd) NRG iterations and Δ_ν are Λ-dependent constants to be determined from the NRG spectrum.

The spectrum of H_{fp} is built of four equidistant free-particle spectra (labelled by ν), each shifted by the phase $\delta_{\nu\sigma}$. Actually, $\delta_{\nu\uparrow} = -\delta_{\nu\downarrow}$ for zero magnetic field, thus we use $\delta_\nu = \delta_{\nu\uparrow}$ for convenience. The phases can be extracted from the NRG flow diagrams by comparison

with the many-body spectrum constructed out of the four shifted single-particle spectra, see Chapter 5. To identify the states from the constructed and the NRG spectra with each other, labelling with quantum numbers is useful. Note that an exactly equidistant energy spectrum is only obtained in the limit $\Lambda \to 1$, where the NRG transformations are exact. With increasing Λ some of the degeneracies are lifted, compare for examples the flow diagrams of Fig. C.1(a) ($\Lambda = 2$) and Fig. B.1 ($\Lambda = 2.5$). Usually it is possible to extract the phases out of the lowest lying levels which are unconcerned of this effect.

The example of a flow diagram for the symmetric Anderson-model is shown in Fig. C.1(a). The low-energy fixed-point is characterized by an equidistant energy spectrum for the lowest levels. The ground state is non-degenerate. The equidistant levels are separated by $\Delta_1/2$. Thus, as expected for the symmetric Anderson model, the phase is given by $\delta_1 = \pi/2$. The second eigenchannel of the scattering matrix decouples from the impurity, thus $\delta_2 = 0$. It is not included in the NRG calculation. A NRG flow diagram of a non-Fermi liquid is given in Fig. C.1(b). It shows the case of a the two-channel Kondo model, see Eq. (6.1). The ground state is two-fold degenerate and the lowest energy levels are given by 1, 4, 5, 8 in units of the lowest excitation. Clearly the flow diagram cannot be explained by equidistant single-particle spectra.

Further flow diagrams are given in Figs. 6.3 and 6.10 for two-channel models that in a certain regime exhibit non-Fermi liquid behaviour. Not only the (non-)Fermi liquid character and the phases (if existent) can be extracted, but also the competition between the two disconnected channels can be seen.
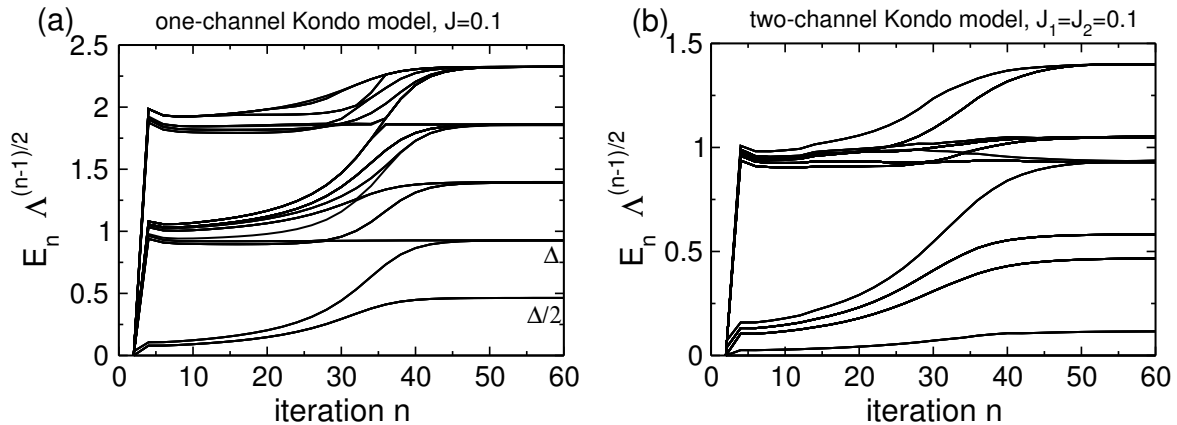

Figure C.1: NRG flow diagrams. The low-energy fixed point can be explained by boundary conformal field theory [37]. (a) One-channel Kondo model. The energy spectrum of the Fermi liquid is related to phase-shifted equidistant single-particle spectra with level distance Δ. Here $\delta_1 = \pi/2$. $J = 0.1$, $\Lambda = 2$. Note that for increasing Λ, some of the degeneracies are lifted, see e.g. Fig. B.1. (b) Two-channel Kondo model. In case of a non-Fermi liquid scattering theory does not apply, thus the energy levels cannot be related to scattering phases. The energy spectrum shows the typical $1 - 4 - 5 - 8$ pattern. $J_1 = J_2 = 0.1$, $\Lambda = 2$.

Appendix D

Some fermionic commutation relations

All fermionic operators obey the anti-commutation relations

$$\left[c_i, c_j^\dagger\right]_+ = \delta_{ij}, \tag{D.1}$$

$$\left[c_i^\dagger, c_j^\dagger\right]_+ = [c_i, c_j]_+ = 0. \tag{D.2}$$

For commutation relations, this results in

$$\left[c_i, c_j^\dagger\right] = 2c_i c_j^\dagger - \delta_{ij} = -2c_j^\dagger c_i + \delta_{ij}, \tag{D.3}$$

$$\left[c_i^\dagger, c_j^\dagger\right] = 2c_i^\dagger c_j^\dagger, \quad [c_i, c_j] = 2c_i c_j. \tag{D.4}$$

Useful commutator properties (independent on the operator statistics):

$$[ab, cd] = a[b, c]d + [a, c]bd + ca[b, d] + c[a, d]b \tag{D.5}$$

$$[a^\dagger, b^\dagger] = -([a, b])^\dagger \tag{D.6}$$

For composite operators these relations can be combined to

$$[n_i, c_j^\dagger] = c_i^\dagger \delta_{ij}, \tag{D.7}$$

$$[n_i, c_j] = -c_i \delta_{ij}, \tag{D.8}$$

$$\left[n_i, c_j^\dagger c_k\right] = c_j^\dagger c_k \delta_{ij} - c_j^\dagger c_k \delta_{ik}, \tag{D.9}$$

$$\left[n_\uparrow^i n_\downarrow^i, c_{j\sigma}^\dagger c_{k\sigma}\right] = c_{i\sigma}^\dagger c_{k\sigma} n_{i-\sigma} \delta_{ij} - c_{j\sigma}^\dagger c_{k\sigma} n_{k-\sigma} \delta_{ik}, \tag{D.10}$$

$$\left[n_i n_j, c_k^\dagger\right] = c_k^\dagger (n_i \delta_{jk} + n_j \delta_{ik}) + c_k^\dagger \delta_{ijk}, \tag{D.11}$$

$$[n_i n_j, c_k] = -c_k(n_i \delta_{jk} - n_j \delta_{ik}) + c_k \delta_{ijk}, \tag{D.12}$$

$$[(N_k)^m, c_k] = -\sum_{x=1}^{m-1} (N_{k'})^{m-x} c_{k'} (N_{k'})^x; \quad N_{k'} = \sum_{k'} n_{k'}, \tag{D.13}$$

$$\left[a^\dagger b, c^\dagger d\right] = a^\dagger d\delta_{bc} - c^\dagger b\delta_{ad} \tag{D.14}$$

and

$$\sum_{k'}\left[c_{k\sigma}, c^\dagger_{k'\uparrow}c^\dagger_{-k'\downarrow} + H.c.\right] = \sigma c^\dagger_{-k,-\sigma}, \tag{D.15}$$

$$\sum_{k'}\left[c^\dagger_{k\sigma}, c^\dagger_{k'\uparrow}c^\dagger_{-k'\downarrow} + H.c.\right] = -\sigma c_{-k,-\sigma}. \tag{D.16}$$

Part IV

Miscellaneous

Bibliography

[1] J. Kondo. *Resistance Minimum in Dilute Magnetic Alloys*. Prog. Theor. Phys. **32**, 37–49 (1964).

[2] K. G. Wilson. *The renormalization group: Critical phenomena and the Kondo problem*. Rev. Mod. Phys. **47**, 773–840 (1975).

[3] A. Yacoby, M. Heiblum, D. Mahalu and H. Shtrikman. *Coherence and Phase Sensitive Measurements in a Quantum Dot*. Phys. Rev. Lett. **74**, 4047–4050 (1995).

[4] R. Schuster, E. Buks, M. Heiblum, D. Mahalu, V. Umansky and H. Shtrikman. *Phase measurement in a quantum dot via a double-slit interference experiment*. Nature **385**, 417–420 (1997).

[5] M. Avinun-Kalish, M. Heiblum, O. Zarchin, D. Mahalu and V. Umansky. *Crossover from 'mesoscopic' to 'universal' phase for electron transmission in quantum dots*. Nature **436**, 529–533 (2005).

[6] L. Kouwenhoven and C. Marcus. *Quantum Dots*. Physics World **11**, 35–39 (1998).

[7] L. I. Glazman and M. E. Raikh. *Resonant Kondo transparency of a barrier with quasilocal impurity states*. JETP Lett. **47**, 452–455 (1988).

[8] T. K. Ng and P. A. Lee. *On-Site Coulomb Repulsion and Resonant Tunneling*. Phys. Rev. Lett. **61**, 1768–1771 (1988).

[9] D. Goldhaber-Gordon, H. Shtrikman, D. Mahalu, D. Abusch-Magder, U. Meirav and M. A. Kastner. *Kondo effect in a single-electron transistor*. Nature **391**, 156 – 159 (1998).

[10] W. G. van der Wiel, S. D. Franceschi, T. Fujisawa, J. M. Elzerman, S. Tarucha and L. P. Kouwenhoven. *The Kondo Effect in the Unitary Limit*. Science **289**, 2105 (2000).

[11] W. J. de Haas, J. H. de Boer and G. J. van den Berg. *The electrical resistance of gold, copper, and lead at low temperatures*. Physica (Ultrecht) **1**, 1115 (1934).

[12] Y. Ji, M. Heiblum, D. Sprinzak, D. Mahalu and H. Shtrikman. *Phase Evolution in a Kondo-Correlated System*. Science **290**, 779–783 (2000).

[13] Y. Ji, M. Heiblum and H. Shtrikman. *Transmission Phase of a Quantum Dot with Kondo Correlation near the Unitary Limit*. Phys. Rev. Lett. **88**, 076601 (2002).

[14] M. Zaffalon, B. Aveek, M. Heiblum, D. Mahalu and V. Umansky. *Transmission phase of a singly occupied quantum dot in the Kondo regime*. cond-mat/0711.1172 (2007).

[15] C. Karrasch, T. Enss and V. Meden. *Functional renormalization group approach to transport through correlated quantum dots*. Phys. Rev. B **73**, 235337 (2006).

[16] Y. Oreg and D. Goldhaber-Gordon. *Two-Channel Kondo Effect in a Modified Single Electron Transistor*. Phys. Rev. Lett. **90**, 136602 (2003).

[17] R. M. Potok, I. G. Rau, H. Shtrikman, Y. Oreg and D. Goldhaber-Gordon. *Observation of the two-channel Kondo effect*. Nature **446**, 167 – 171 (2007).

[18] A. W. Holleitner, R. H. Blick and K. Eberl. *Fabrication of coupled quantum dots for multiport access*. Appl. Phys. Lett. **82**, 1887–1889 (2003).

[19] Y. Aharonov and D. Bohm. *Significance of Electromagnetic Potentials in the Quantum Theory*. Phys. Rev. **115**, 485–491 (1959).

[20] P. W. Anderson. *Localized Magnetic States in Metals*. Phys. Rev. **124**, 41–53 (1961).

[21] D. C. Langreth. *Friedel Sum Rule for Anderson's Model of Localized Impurity States*. Phys. Rev. **150**, 516–518 (1966).

[22] J. Weis, R. J. Haug, K. v. Klitzing and K. Ploog. *Competing channels in single-electron tunneling through a quantum dot*. Phys. Rev. Lett. **71**, 4019–4022 (1993).

[23] F. B. Anders. *A Numerical Renormalization Group approach to Non-Equilibrium Green's Functions for Quantum Impurity Models*. cond-mat/0803.3004 (2008).

[24] Y. Meir, N. S. Wingreen and P. A. Lee. *Transport through a strongly interacting electron system: Theory of periodic conductance oscillations*. Phys. Rev. Lett. **66**, 3048–3051 (1991).

[25] M. Pustilnik, L. Borda, L. I. Glazman and J. von Delft. *Quantum phase transition in a two-channel-Kondo quantum dot device*. Phys. Rev. B **69**, 115316 (2004).

[26] A. Hewson. *The Kondo Problem to heavy Fermions*. Cambridge University Press Cambridge (1993).

[27] F. Marquardt. *Lecture notes on Mesoscopic Physics* (2006). Www.theorie.physik.uni-muenchen.de/∼florian/meso06.html.

[28] T. A. Costi, A. C. Hewson and V. Zlatic. *Transport coefficients of the Anderson model via the numerical renormalization group*. J. Phys.: Condens. Matter **6**, 2519–2558 (1994).

[29] F. D. M. Haldane. *Scaling Theory of the Asymmetric Anderson Model*. Phys. Rev. Lett. **40**, 416–419 (1978).

[30] J. R. Schrieffer and P. A. Wolff. *Relation between the Anderson and Kondo Hamiltonians*. Phys. Rev. **149**, 491–492 (1966).

[31] P. W. Anderson. *A poor man's derivation of scaling laws for the Kondo problem*. J. Phys.C: Solid State Phys. **3**, 2436–2441 (1970).

[32] P. G. Silvestrov and Y. Imry. *Towards an Explanation of the Mesoscopic Double-Slit Experiment: A New Model for Charging of a Quantum Dot*. Phys. Rev. Lett. **85**, 2565–2568 (2000).

[33] Y. Meir and N. S. Wingreen. *Landauer formula for the current through an interacting electron region*. Phys. Rev. Lett. **68**, 2512–2515 (1992).

[34] J. Rammer and H. Smith. *Quantum field-theoretical methods in transport theory of metals*. Rev. Mod. Phys. **58**, 323–359 (1986).

[35] W. Izumida, O. Sakai and Y. Shimizu. *Many Body Effects on Electron Tunneling through Quantum Dots in an Aharonov-Bohm Circuit*. JPSJ **66**, 717 – 726 (1997).

[36] R. Landauer. Philos. Mag. **21**, 863 (1970).

[37] I. Affleck, A. W. W. Ludwig, H.-B. Pang and D. L. Cox. *Relevance of anisotropy in the multichannel Kondo effect: Comparison of conformal field theory and numerical renormalization-group results*. Phys. Rev. B **45**, 7918–7935 (1992).

[38] H. R. Krishna-murthy, J. W. Wilkins and K. G. Wilson. *Renormalization-group approach to the Anderson model of dilute magnetic alloys. I. Static properties for the symmetric case*. Phys. Rev. B **21**, 1003–1043 (1980).

[39] R. Bulla, N.-H. Tong and M. Vojta. *Numerical Renormalization Group for Bosonic Systems and Application to the Sub-Ohmic Spin-Boson Model*. Phys. Rev. Lett. **91**, 170601 (2003).

[40] R. Bulla, H.-J. Lee, N.-H. Tong and M. Vojta. *Numerical renormalization group for quantum impurities in a bosonic bath*. Phys. Rev. B **71**, 045122 (2005).

[41] R. Bulla, T. A. Costi and T. Pruschke. *Numerical renormalization group method for quantum impurity systems*. Rev. Mod. Phys. **80**, 395 (2008).

[42] F. B. Anders and A. Schiller. *Real-Time Dynamics in Quantum-Impurity Systems: A Time-Dependent Numerical Renormalization-Group Approach*. Phys. Rev. Lett. **95**, 196801 (2005).

[43] F. B. Anders and A. Schiller. *Spin precession and real-time dynamics in the Kondo model: Time-dependent numerical renormalization-group study.* Phys. Rev. B **74**, 245113 (2006).

[44] A. Weichselbaum and J. von Delft. *Sum-Rule Conserving Spectral Functions from the Numerical Renormalization Group.* Phys. Rev. Lett. **99**, 076402 (2007).

[45] R. Peters, T. Pruschke and F. B. Anders. *Numerical renormalization group approach to Green's functions for quantum impurity models.* Phys. Rev. B **74**, 245114 (2006).

[46] A. I. Toth, C. P. Moca, O. Legeza and G. Zarand. *Density matrix numerical renormalization group for non-Abelian symmetries.* cond-mat/0802.4332 (2008).

[47] F. Verstraete, A. Weichselbaum, U. Schollwock, J. I. Cirac and J. von Delft. *Variational matrix product state approach to quantum impurity models.* cond-mat/0504305 (2005).

[48] O. Sakai, Y. Shimizu and T. Kasuya. *Single-Particle and Magnetic Excitation Spectra of Degenerate Anderson Model with Finite f?f Coulomb Interaction.* JPSJ **58**, 3666–3678 (1989).

[49] W. C. Oliveira and L. N. Oliveira. *Generalized numerical renormalization-group method to calculate the thermodynamical properties of impurities in metals.* Phys. Rev. B **49**, 11986–11994 (1994).

[50] R. Bulla, A. C. Hewson and T. Pruschke. *Numerical renormalization group calculations for the self-energy of the impurity Anderson model.* J. Phys.: Condens. Matter **10**, 8365–8380 (1998).

[51] R. Bulla, T. A. Costi and D. Vollhardt. *Finite-temperature numerical renormalization group study of the Mott transition.* Phys. Rev. B **64**, 045103 (2001).

[52] W. Hofstetter. *Generalized Numerical Renormalization Group for Dynamical Quantities.* Phys. Rev. Lett. **85**, 1508–1511 (2000).

[53] S. R. White. *Density matrix formulation for quantum renormalization groups.* Phys. Rev. Lett. **69**, 2863–2866 (1992).

[54] U. Schollwöck. *The density-matrix renormalization group.* Rev. Mod. Phys. **77**, 259 (2005).

[55] C. Raas, G. S. Uhrig and F. B. Anders. *High-energy dynamics of the single-impurity Anderson model.* Phys. Rev. B **69**, 041102 (2004).

[56] A. Holzner, A. Weichselbaum and J. von Delft. *Matrix product state approach for a two-lead, multi-level Anderson impurity model.* cond-mat/0804.0550 (2008).

[57] A. J. Daley, C. Kollath, U. Schollwck and G. Vidal. *Time-dependent density-matrix renormalization-group using adaptive effective Hilbert spaces*. J. Stat. Mech.: Theor. Exp. P04005 (2004).

[58] G. Vidal. *Efficient Simulation of One-Dimensional Quantum Many-Body Systems*. Phys. Rev. Lett. **93**, 040502 (2004).

[59] C. Bruder, R. Fazio and H. Schoeller. *Aharonov-Bohm Oscillations and Resonant Tunneling in Strongly Correlated Quantum Dots*. Phys. Rev. Lett. **76**, 114–117 (1996).

[60] Y. Oreg and Y. Gefen. *Electron scattering through a quantum dot: A phase lapse mechanism*. Phys. Rev. B **55**, 13726–13729 (1997).

[61] P. G. Silvestrov and Y. Imry. *Spin effects and transport in quantum dots with overlapping resonances*. Phys. Rev. B **65**, 035309 (2001).

[62] A. Silva, Y. Oreg and Y. Gefen. *Signs of quantum dot˘lead matrix elements: The effect on transport versus spectral properties*. Phys. Rev. B **66**, 195316 (2002).

[63] V. Meden and F. Marquardt. *Correlation-Induced Resonances in Transport through Coupled Quantum Dots*. Phys. Rev. Lett. **96**, 146801 (2006).

[64] D. I. Golosov and Y. Gefen. *Transmission through quantum dots: Focus on phase lapses*. Phys. Rev. B **74**, 205316 (2006).

[65] V. Kashcheyevs, A. Schiller, A. Aharony and O. Entin-Wohlman. *Unified description of phase lapses, population inversion, and correlation-induced resonances in double quantum dots*. Phys. Rev. B **75**, 115313 (2007).

[66] Y. Oreg. *Universal phase lapses in a noninteracting model*. New J. Phys. **9**, 122 (2007).

[67] G. Hackenbroich. *Phase coherent transmission through interacting mesoscopic systems*. Phys. Rep. **343**, 463 (2001).

[68] P. Nozieres. *A "fermi-liquid" description of the Kondo problem at low temperatures*. J. Low Temp. Phys. **17**, 31–42 (1974).

[69] U. Gerland, J. von Delft, T. A. Costi and Y. Oreg. *Transmission Phase Shift of a Quantum Dot with Kondo Correlations*. Phys. Rev. Lett. **84**, 3710–3713 (2000).

[70] P. G. Silvestrov and Y. Imry. *Enhanced Sensitivity of the Transmission Phase of a Quantum Dot to Kondo Correlations*. Phys. Rev. Lett. **90**, 106602 (2003).

[71] M. Büttiker. *Four-Terminal Phase-Coherent Conductance*. Phys. Rev. Lett. **57**, 1761–1764 (1986).

[72] A. G. Aronov and Y. V. Sharvin. *Magnetic flux effects in disordered conductors*. Rev. Mod. Phys. **59**, 755–779 (1987).

[73] M. Pustilnik and L. I. Glazman. *Kondo Effect in Real Quantum Dots*. Phys. Rev. Lett. **87**, 216601 (2001).

[74] U. Fano. *Effects of Configuration Interaction on Intensities and Phase Shifts*. Phys. Rev. **124**, 1866–1878 (1961).

[75] A. A. Clerk, X. Waintal and P. W. Brouwer. *Fano Resonances as a Probe of Phase Coherence in Quantum Dots*. Phys. Rev. Lett. **86**, 4636–4639 (2001).

[76] O. Entin-Wohlman, A. Aharony, Y. Imry and Y. Levinson. *The Fano Effect in Aharonov-Bohm Interferometers*. J. Low Temp. Phys. **126**, 1251–1273 (2002).

[77] H. A. andK. Kobayashi, A. Sano, S. Katsumoto and Y. Iye. *Interference Effect in Multilevel Transport through a Quantum Dot*. JPSJ **73**, 3235 (2004).

[78] R. H. Dicke. *The Effect of Collisions upon the Doppler Width of Spectral Lines*. Phys. Rev. **89**, 472–473 (1953).

[79] R. H. Dicke. *Coherence in Spontaneous Radiation Processes*. Phys. Rev. **93**, 99 (1954).

[80] R. Berkovits, F. von Oppen and J. W. Kantelhardt. *Discrete charging of a quantum dot strongly coupled to external leads*. EPL **68**, 699–705 (2004).

[81] K. Satori, H. Shiba, O. Sakai and Y. Shimizu. *Numerical Renormalization Group Study of Magnetic Impurities in Superconductors*. JPSJ **61**, 3239–3254 (1992).

[82] T. Yoshioka and Y. Ohashi. *Numerical Renormalization Group Studies on Single Impurity Anderson Model in Superconductivity: A Unified Treatment of Magnetic, Nonmagnetic Impurities, and Resonance Scattering*. JPSJ **69**, 1812–1823 (2000).

[83] Y. Tanaka, A. Oguri and A. C. Hewson. *Kondo effect in asymmetric Josephson couplings through a quantum dot*. New J. Phys. **9**, 115 (2007).

[84] J. S. Lim and M.-S. Choi. *Andreev Bound States in the Kondo Quantum Dots Coupled to Superconducting Leads*. cond-mat/0609333 (2006).

[85] J. Bauer, A. Oguri and A. Hewson. *Spectral properties of locally correlated electrons in a Bardeen-Cooper-Schrieffer superconductor*. J. Phys.: Condens. Matter **19**, 486211 (2007).

[86] A. Oguri, Y. Tanaka and A. C. Hewson. *Quantum Phase Transition in a Minimal Model for the Kondo Effect in a Josephson Junction*. JPSJ **73**, 2494–2504 (2004).

[87] C. Karrasch, A. Oguri and V. Meden. *Josephson current through a single Anderson impurity coupled to BCS leads*. Phys. Rev. B **77**, 024517 (2008).

[88] I. Affleck and A. Ludwig. *Exact conformal-field-theory results on the multichannel Kondo effect: Single-fermion Green's function, self-energy, and resistivity*. Phys. Rev. B **48**, 7297–7321 (1993).

[89] P. Nozieres and A. Blandin. *Kondo effect in real metals*. J. Phys. (Paris) **41**, 193 (1980).

[90] A. Zawadowski. *Kondo-like State in a Simple Model for Metallic Glasses*. Phys. Rev. Lett. **45**, 211–214 (1980).

[91] F. B. Anders, E. Lebanon and A. Schiller. *Coulomb blockade and non-Fermi-liquid behavior in quantum dots*. Phys. Rev. B **70**, 201306 (2004).

[92] E. Lebanon, A. Schiller and F. B. Anders. *Enhancement of the two-channel Kondo effect in single-electron boxes*. Phys. Rev. B **68**, 155301 (2003).

[93] W. Hofstetter and G. Zarand. *Singlet-triplet transition in lateral quantum dots: A numerical renormalization group study*. Phys. Rev. B **69**, 235301 (2004).

List of Publications

The results presented in this thesis have been published in the following papers:

1. *Mesoscopic to universal crossover of transmission phase of multi-level quantum dots*
   C. Karrasch, T. Hecht, A. Weichselbaum, Y. Oreg, J. von Delft and V. Meden
   Pys. Rev. Lett. **98**, 186802 (2007)

2. *Phase lapses in transmission through interacting two-level quantum dots*
   C. Karrasch, T. Hecht, A. Weichselbaum, J. von Delft, Y. Oreg and V. Meden
   New J. Phys. **9**, 123 (2007)

3. *Interplay of mesoscopic and Kondo effects for transmission amplitude of few-level quantum dots*
   T. Hecht, A. Weichselbaum, Y. Oreg and J. von Delft
   to be submitted to *Phys. Rev. B*, cond-mat/0805.3145

4. *Numerical renormalization group calculation of near-gap peaks in spectral functions of the Anderson model with superconducting leads*
   T. Hecht, A. Weichselbaum, J. von Delft and R. Bulla
   accepted for publication in J. Phys.: Condens. Matter, cond-mat/0803.1251

Deutsche Zusammenfassung

Die vorliegende Arbeit beschäftigt sich mit dem Transport durch Quantenpunkte. Systeme mit Quantenpunkten ermöglichen Studien des Quantentransportes, sowie der damit verknüpften grundlegenden physikalischen Effekte, wie z.B. dem Kondoeffekt, unter wohlkontrollierten Bedingungen. In dieser Arbeit behandeln wir Quantenpunkte, die sich gut durch Störstellenmodelle nach Anderson beschreiben lassen. In diesen Modellen sind die diskreten Niveaus des Quantenpunktes durch Tunnelprozesse an fermionische Bäder gekoppelt. Die Modellparameter, wie Energie und Breite der Niveaus, lassen sich im Experiment kontrolliert verändern. Hierdurch ermöglichen diese Systeme den direkten Test von Experiment gegenüber Theorie und umgekehrt. Um die Eigenschaften dieser stark korrelierten Systeme zu berechnen, verwenden wir die numerische Renormierungsgruppenmethode (NRG) [2].

Die Resultate dieser Arbeit sind in drei Projekte untergliedert. Das erste und umfangreichste Projekt beschäftigt sich mit der Transmissionsamplitude durch Quantenpunkte und insbesondere mit der Phase der Transmission. Messungen an Quantenpunkten mit vielen Elektronen, d.h. für kleine Niveauabstände, ergeben ein universelles Verhalten der Phase, d.h. die Phase ist unabhängig von den einzelnen Niveaus oder den verwendeten Proben [3, 4, 5]. Dieses experimentelle Resultat war fast zehn Jahre lang unverstanden. Neuere Experimente [5] hingegen zeigen, dass die Transmissionsphase bei Quantenpunkten mit wenigen Elektronen, d.h. grossen Niveauabständen, mesoskopisches Verhalten zeigt: Sie hängt von den Parametern der einzelnen Niveaus bzw. Quantenpunkte ab. Wir zeigen, dass das generische Verhalten durch ein Andersonmodell mit mehreren Niveaus reproduziert werden kann: Mesoskopisches bzw. universelles Phasenverhalten ergibt sich für wohlseparierte bzw. überlappende Niveaus. Eine Analyse der renormierten Einteilchenniveaus zeigt, dass sich in letzterem Fall ein überproportional breites Niveau in der Nähe der Fermikante bildet. Der universelle Phasencharakter ergibt sich dann aus Fano-Antiresonanzen dieses breiten mit den schmaleren renormierten Niveaus. Moderate Temperaturen verstärken den universellen Charakter der Phase. Für den Fall wohlseparierter Niveaus untersuchen wir weiters den Effekt von Kondokorrelationen auf die Transmissionsphase. Ein zweites Projekt beschäftigt sich mit einem Quantenpunkt mit einem Niveau, welcher an ein supraleitendes Bad gekoppelt ist. Wir zeigen, dass die Energieauflösung der NRG Methode nicht durch die Grösse der Energielücke des Supraleiters beschränkt ist, wodurch es möglich ist, auch scharfe Strukturen in der Spektralfunktion aufzulösen. Damit finden wir im Fall von kleinen Energielücken schmale Spitzen in der Spektralfunktion bei Energien nahe der Bandkante. In einem dritten Projekt untersuchen wir einen Quantenpunkt, der an zwei unabhängige Bäder gekoppelt ist, wodurch im Kondobereich Nichtfermiflüssigkeitsverhalten auftreten kann. Mittels zweier Modelle untersuchen wir den Übergang zum normalen Verhalten einer Fermiflüssigkeit. Unsere Untersuchungen ergeben, dass die Ausdehnung des Parameterbereiches in welchem Nichtfermifluessigkeitsverhalten vorliegt stark von den Kopplungsmechanismen zwischen Quantenpunkt und Bädern abhängt.

Acknowledgements

First and foremost I would like to gratefully thank my advisor Jan von Delft for the guidance and encouragement he has provided throughout the course of this thesis. His stimulating and critical questions have been crucial – both for gaining a deeper understanding of the physical problems as well as for my ambition to solve them. He taught me how to give a good presentation and how to write scientific publications. I am grateful for the possibility of going to conferences and visit my collaborators. Thanks for being always receptive for my opinion as well as for the open atmosphere at our chair. Thanks also to Nina, his wife, for her generous hospitality.

I am thankful to Michael Sindel who introduced me into the secrets of both life as a PhD student and the NRG method. He generously left his NRG code to me. So did Andreas Weichselbaum. Andreas was not only my matlab expert, but always took the time for discussing the physical and technical peculiarities of my projects. Thanks for the great waltz, too.

Most of the studies presented in this thesis greatly benefited from the knowledge, experience and ideas of my collaborators (and friends). I am deeply grateful to Ralf Bulla, the NRG expert who supported me during the course of my work. It was a pleasure to work together with Volker Meden and Christoph Karrasch. I thank Yuval Oreg for our lifely discussions and hospitality at the Weizman Institute of Science in Rehovot, as well as Michael Pustilnik for the even more lively discussions concerning the two-channel Kondo effect and energy saving. I am very happy that I could also collaborate with Slava Kashcheyevs, who still was a bundle of energy even after two great weeks in Windsor. I enjoyed stimulating discussions with Gergely Zaránd and Michele Zaffalon. Thanks to Moty Heiblum, Clemens Rössler and Andreas K. Hüttel for providing experimental figures for this thesis.

Thanks to all the group members, I had a great time together with you. I especially want to tell my gratitude to Rolf Helmes for the warm welcome in the group and at all the times we met. I further thank Benjamin Abel, my office mate, for that I could share with you all the joys but also sorrows during the last few years. Then, Michael Möckel for the discussions about the meaning of life. Andreas Holzner for keeping seagull alive. Geraldine Haack for staying in Munich a bit longer. Hamed Saberi for opening my eyes about what you really need to know if you are new somewhere. Florian Marquardt for the wonderful questions and explanations about physics. László Borda for the help with NRG problems. Peter Fritsch, Udo Hartmann and Markus Storcz for sweeties-supply. Stefan Kehrein for

his encouraging comments. Ralph Simmler for the Dachstein course and, together with his team, for the maintenance of the cluster. And, of course, the rest of the group, Wolfgang Münder, Florian Bauer, Maximilian Treiber, Björn Kubala, Max Ludwig, Clemens Neuenhahn, Ferdinand Helmer, Alexander Hoffmann, Alexander Buchner, Markus Heyl, Barbara Englert, Enrique Solano, Afif Siddiki, Oleg Yevtushenko, Vitaly Golovach, Pei Wang, Frank Wilhelm, Ioana Serban, Mikhail Kiselev, Johannes Ferber, Corinna Kollath, Henryk Gutmann, Robert Dahlke, Andreas Friedrich, Stéphane Schoonover and Sylvia Kaiser

I am very grateful for the friendship with Nikola Dudeck, Iris Messen, Inga Fischer, my cousin Sandra Sappl, Henning Christ and Dominique Gobert. Thanks also to my mentor Natascha Ecker.

I owe my loving thanks to my boyfriend Klemens Hammerer, who understands to make me smile.

My deepest gratitude goes to my sister and my parents. For the love, support and their believe in me from the first day of my life. It is to them that I dedicate this work.

Curriculum vitae

Theresa Hecht
Diplomphysikerin

born in Friedberg, Germany

Academic Education

08/2004–07/2008	Ph.D. studies in Theoretical Condensed Matter Physics supervised by Prof. Dr. von Delft Physics Department, Center of NanoScience and Arnold Sommerfeld Center for Theoretical Physics, Ludwig-Maximilians University, München
10/1998–05/2004	Study of General Physics, Technical University, München
05/2004	Diploma in General Physics (Technical University, München)
05/2003–05/2004	Diploma Thesis supervised by Prof. Dr. Cirac Max-Planck Institute for Quantum Optics, Garching "Quantum Computation with Bose-Einstein Condensates"
2001–2002	DAAD scolarship, Study of Physics (focus Quantum Optics) Ecole Doctorale de la Region Parisienne, Paris
09/2000	Vordiplom in General Physics (Technical University, München)
07/1998	Allgemeine Hochschulreife Deutschherren Gymnasium, Aichach